Monte Carlo Study of Biaxial Nematic Liquid Crystals

A thesis submitted for the award of the degree of
Doctor of Philosophy in Physics

By

B. Kamala Latha

School of Physics
University of Hyderabad
Hyderabad-500 046, India.
June 2014

To

My Family

Table of Contents

Table of Contents iii

List of Tables vi

List of Figures vii

Declaration xv

Certificate xvi

Acknowledgements xvii

Preface xix

1 Introduction- Biaxial Nematics 1

- 1.1 Introduction . . . 1
  - 1.1.1 Nematic Phases . . . 2
- 1.2 Microscopic Origin of Order Parameters . . . 7
- 1.3 Mean field Theories of Biaxial Nematic Phase . . . 12
  - 1.3.1 Molecular Potential for Biaxial Phase formed by Non-Cylindrically Symmetric Molecules . . . 12
  - 1.3.2 A Generalized Mean Field Model . . . 13
- 1.4 Phenomenological Theories of Biaxial Nematic Phase . . . 20
- 1.5 Models Studied . . . 21
  - 1.5.1 Lebwohl-Lasher Model . . . 22
  - 1.5.2 Dispersion Model . . . 22
  - 1.5.3 General Hamiltonian in Cartesian Coordinates . . . 24
- 1.6 Review of Experiments . . . 25

Bibliography 29

2 Introduction to Monte Carlo Simulation Methods 35

- 2.1 Introduction . . . 35
- 2.2 Canonical Monte Carlo Methods . . . 37
  - 2.2.1 Metropolis Algorithm . . . 39

2.3 Non-Boltzmann Sampling 41
    2.3.1 Entropic Sampling 42
    2.3.2 Wang-Landau Algorithm 43
2.4 Periodic Boundary Conditions 45
2.5 Calculation of Observables 46
2.6 Review of Simulations of Biaxial Nematics 50

Bibliography **52**

3 A Wang-Landau Monte Carlo Investigation of the Mean Field Phase Diagram of Biaxial Liquid Crystals **56**

3.1 Introduction 56
3.2 Hamiltonian Model 59
3.3 Details of Simulation 61
    3.3.1 Sampling Technique 61
    3.3.2 Simulation Details 63
3.4 Simulation Results 64
    3.4.1 Segment OI 65
    3.4.2 Segment OI : Range of λ^* = (0.1-0.25) 69
    3.4.3 Segment OI: Range of λ^*= (0.26 - 0.33) 76
    3.4.4 Segment IV 78
    3.4.5 Segment IV: Range of λ^* = ($1/3$,0.53) 78
    3.4.6 Segment IV: Range of λ^* = (0.54 - 0.733) 79
    3.4.7 Segment IV: Range of λ^* = (0.733 - 0.93) 86
3.5 Phase Diagram from MC Simulations 89
3.6 Discussion of Results 91
3.7 Conclusions 97

Bibliography **99**

4 A Wang-Landau Monte Carlo Investigation of the Essential Triangle **102**

4.1 Introduction 102
4.2 Segment IW 103
    4.2.1 Segment IZ: Range of λ' = (0.33 - 0.691) 107
    4.2.2 Segment ZW: Range of λ' = (0.691 - 0.747) 113
4.3 Dispersion Parabola OT 120
4.4 Conclusions 127

Bibliography **129**

5 A Study of Pretransitional Behaviour of Biaxial Nematics **130**

5.1 Introduction 130
5.2 Model used and System studied 133
5.3 Simulation Details 135
5.4 Results and Discussions 136

5.4.1 $I - N_U$ transition . . . 137
5.4.2 $N_U - N_B$ transition . . . 138
5.4.3 Temperature Variation of Correlation Lengths . . . 140
5.4.4 Effect of the Biaxiality Parameter λ_Z . . . 142
5.5 conclusions . . . 143

Bibliography **146**

6 Structures and Transitions in a Hybrid Biaxial Nematic Film **148**
6.1 Introduction . . . 148
6.2 System under study . . . 152
6.2.1 Model Hamiltonian . . . 154
6.2.2 Simulation Details . . . 154
6.3 Results and Discussion . . . 155
6.3.1 Type of Film . . . 156
6.3.2 Effect of variation of thickness . . . 170
6.3.3 Effect of variation of anchoring strength . . . 172
6.4 Conclusions . . . 176

Bibliography **179**

7 Anchoring Transitions in Biaxial Nematic Droplets **182**
7.1 Introduction . . . 182
7.2 Model and details of simulations . . . 185
7.3 Results and discussion . . . 188
7.4 Conclusions . . . 199

Bibliography **201**

8 Conclusions **204**

List of Publications **209**

List of Tables

3.1 Comparison of transition temperatures at some points along OI 71

4.1 Coordinates of points B1-B7 and Z along the segment IW of the essential triangle (Fig.2) 107
4.2 (γ, λ) values corresponding to λ_Z 120

5.1 Critical exponents and estimated T_{C1} values from angular correlations of different molecular axes (λ_Z=0.35) 139
5.2 Critical exponents and estimated T_{C1} values from angular correlations of different molecular axes (λ_Z=0.275) 139
5.3 Critical exponents and estimated T_{C1} values from angular correlations of different molecular axes (λ_Z=0.2) 139
5.4 Correlation lengths for various λ_Z at the $I - N_U$ transition 140

List of Figures

1.1 Schematic of a biaxial molecule 14

1.2 Schematic of a biaxial phase 14

1.3 The domain of stability for the interaction Hamiltonian in the plane ξ=1: G. De Matteis *et al*, *Continuum Mech. Thermodyn.* **19** 1-23 (2007) 16

1.4 Essential triangle OIV: C_1 and C_3 are tricritical points. C_2 is a triple point. The dispersion parabola meets the side IV at the point T, the Landau point: F. Bisi *et al*, *Phys. Rev. E* **73** 051709 (2006). 16

1.5 Mean field phase diagram along the upper boundary OIV of the essential triangle. The scaled transition temperature $1/\beta^*$ is plotted as function of the interaction parameter λ^*. Solid lines represent first order transitions. Broken lines represent second order transitions: G. De Matteis $et\ al$, *Continuum Mech. Thermodyn.* **19** 1-23 (2007). 20

1.6 Phase diagram obtained from canonical Monte Carlo simulations along the dispersion parabola of the essential triangle. The scaled transition temperature T^* is plotted as function of the interaction parameter λ (λ_Z). Solid lines represent mean-field results and symbols represent MC results: F. Biscarini $et\ al$,*Phys. rev. Lett.***75**, 1803 (1995) 23

3.1 Essential triangle : Region of biaxial stability 57

3.2 Experimental parameters from the present simulation at λ^* = 0.1 (a)Representative density of states (b)Energy histogram of the entropic ensemble 66

3.3 Experimental parameters from the present simulation at λ^* = 0.1. Temperature variation of (a)Average energy per particle (b) specific heat (per particle)and energy cumulant V_4 66

3.4 Experimental parameters from the present simulation at λ^* = 0.1. Temperature variation of (a) uniaxial and biaxial orders along with their susceptibilities χ. (b) phase biaxiality parameter and molecular biaxiality parameters with their susceptibilities χ 67

3.5 Comparison of data obtained from RW- and B- ensembles.Temperature variation of: (a) Specific heat (b) Uniaxial order and (c) Biaxial order, at λ^*=0.12 68

3.6 Temperature variation of: (a) Specific heat; (b) Uniaxial order; and (c) Biaxial order, obtained from RW- and B-ensembles at λ^*=0.20 (Deviations observed at very low temperatures ($\leq$ 0.25), common to all plots, have their origin from inadvertent inadequate sampling of microstates comprising the entropic ensemble, at these very low energy values. As these deviations do not interfere with the interesting nature of the graphs, recomputations were not attempted to correct for this, to save computing time) 68

3.7 Temperature variation of (a)Specific heat(b) Uniaxial order (c) Biaxial order, obtained from RW- and B-ensembles at λ^*=0.33 (please see the explanatory note of Fig.(3.4), for low temperature variations. 69

3.8 Temperature variation of experimental parameters for different values of λ^* (0.1 to 0.25) 70

3.9 Energy cumulant for λ^* = (a) 0.18 (b) 0.19 and (c) 0.2 71

3.10 Experimental parameters at λ^*=0.22 72

3.11 Experimental parameters at λ^*=0.26 72

3.12 Variation of free energy at the $I - N_U$ transition as a function of (a) Energy per particle (b) R^2_{00} (c) R^2_{22} for λ^*=0.12 73

3.13 Variation of the free energy at the $N_U - N_B$ transition as a function of (a) Energy per particle (b) R^2_{00} (c) R^2_{22} for λ^*=0.12 74

3.14 Variation of the free energy as a function of (a)Energy per particle (b) R^2_{00} (c) R^2_{22} for λ^*=0.22 75

3.15 Temperature variation of experimental parameters for different values of λ^* in the range (0.26, $1/3$) 76

3.16 (a) Specific heat profile with (inset) energy cumulant (b) Order parameters with (inset)susceptibility profiles for λ^*=0.33 77

3.17 Free energy as a function of biaxial order at temperature (a) T = 1.402 (b) T = $T_{N_{BI}}$ = 1.4 (c) T = 1.398 for λ^*=0.33 (L=15) 77

3.18 Temperature variation of order parameters for values of λ^* in the range ($1/3$, 0.53) 79

3.19 (a) Specific heat profile with (inset) energy cumulant V_4 (b) Order parameters with (inset) susceptibility profiles for λ^*=0.47 80

3.20 Temperature variation of the specific heat for values of λ^* in the range (0.53, 0.733) 80

3.21 (a) Temperature variation of (a) Specific heat C_v (with energy cumulant V_4 as an inset), and (b) order parameters (with their susceptibilities (χ') as an inset), obtained from RW- and B-ensembles at λ^* = 0.65 (0.264, 0.158). The susceptibility of R^2_{00} shows the signatures of both transitions whereas the susceptibility of R^2_{22} shows a single peak at T_{C2}. Clear signature of the second transition, and its first order nature, may also be inferred from the V_4 data. 81

3.22 (a) Specific heat profile with (inset) energy cumulant V_4 (b) Order parameters with (inset) susceptibility profiles at λ^*=0.54 82

3.23 (a) Specific heat profile with (inset) energy cumulant V_4 (b) Order parameters with (inset) susceptibility profiles at λ^*=0.58 83

3.24 (a) Specific heat profile with (inset) Binder's cumulant V_4 (b) Order parameters with (inset)susceptibility profiles for λ^*=0.62 83

3.25 (a) Specific heat profile with (inset) energy cumulant V_4 (b) Order parameters with (inset) susceptibility profiles at λ^*=0.66 84

3.26 (a) Specific heat profile with (inset) energy cumulant V_4 (b) Order parameters with (inset) susceptibility profiles at λ^*=0.69 84

3.27 (a) Specific heat profile with (inset) energy cumulant V_4 (b) Order parameters with (inset) susceptibility profiles at λ^*=0.72 85

3.28 Variation of representative free energy as a function of (a) Energy (b) R^2_{00} (c) R^2_{22} at I - N_{B1} transition (T_{C1}), for various λ^* values in region C_3T of the essential triangle. 87

3.29 Variation of Landau Free energy as a function of (a) Energy (b) R^2_{00} (c) R^2_{22} at $N_{B1} - N_B$ transition (T_{C2}), for various λ^* values in region C_3T of the essential triangle. 88

3.30 Temperature variation of order parameters for values of λ^* in the range (0.733, 0.93), based on B-ensembles 89

3.31 Phase diagram as a function of λ^* from RW-ensembles. The transition temperature $1/\beta^*$ is scaled to conform to mean - field values as indicated in the text. Points along OIV in Fig. 3.1 are mapped onto the λ^* - axis for reference. An additional biaxial - biaxial transition is observed in the region KTV in place of a single transition (to the biaxial phase) predicted by the mean-field theory. 90

3.32 MF phase diagram along the upper boundary of the essential triangle. (Giovanni De matteis *et al Continuum. Mech. Thermodyn.* **19**, 1-23 (2007) . . . 91

3.33 (a) Temperature variation of (a)Specific heat C_v (with energy cumulant V_4 as an inset), and (b) order parameters (with their susceptibilities (χ's) as an inset), obtained from RW- and B-ensembles at λ^* = 0.733 (1/3, 1/9). The results obtained from RW- and B-ensembles are indicated by black and lines respectively. 92

3.34 Contour plots of the distribution of microstates in the entropic ensemble at $\lambda^* \simeq 0.73$: (a) Microstate energy versus its uniaxial order and (b) microstate energy versus its biaxial order. The superimposed red and black lines are thermal averages from RW- and B-ensembles respectively. 93

3.35 Contour plots of the distribution of microstates in the entropic ensemble at $\lambda^* \simeq 0.73$: (a) Microstate energy versus its uniaxial order and (b) microstate energy versus its biaxial order . The contour maps of the distributions from RW- and B-ensembles equilibrated at temperature close to T_{C2} are superposed. The thick red and black lines are corresponding plots of thermal averages obtained from these ensembles respectively. 94

3.36 Micro-canonical data at $\lambda^* = 0.65$ as a function of energy per site (a) Microstate energy distribution (b) G_{11}-distribution (c) G_{22}-distribution (d) G_{33}-distribution (e) order parameters versus G_{22} (f) index of the eigenvector of maximum order of the microstates, Δ. 96

3.37 The long range order of the three molecular axes $(\boldsymbol{e}, \boldsymbol{e}_\perp, \boldsymbol{m})$ at $\lambda^* = 0.65$, as a function of temperature. The $\boldsymbol{e}$-axes show a dramatic increase in their ordering at the second transition. 97

4.1 The essential triangle, depicting the two interior trajectories along which detailed simulations have been carried out. (i) IZW (b) OZT 103

4.2 Essential triangle, depicting typical values of (γ, λ) along IW (also see Table.(5.1)) 104

4.3 Comparison of (a) specific heat (b) order parameter profiles obtained from B- and RW- ensembles for $\lambda^{'}$ = 0.477 (B_1 in Fig.4.2): Deviations observed at very low temperatures ($\leq$ 0.25), common to all plots, have their origin from inadvertent inadequate sampling of microstates comprising the entropic ensemble, at these very low energy values. As these deviations do not interfere with the interesting nature of the graphs, recomputations were not attempted to correct for this, to save computing time. 105

4.4 Comparison of (a) specific heat (b) order parameter profiles obtained from B- and RW- ensembles for $\lambda^{'}$ = 0.5666 (B_2 in Fig.4.2) 105

4.5 Comparison of (a) specific heat (b) order parameter profiles obtained from B- and RW- ensembles for $\lambda^{'}$ = 0.6105 (B_3 in Fig.4.2) 106

4.6 Comparison of (a) specific heat (b) order parameter profiles obtained from B- and RW- ensembles for $\lambda^{'}$ = 0.709 (B_5 in Fig.4.2, in the partly repulsive region of the triangle.) 106

4.7 Comparison of (a) specific heat (b) order profiles for values of $\lambda^{'}$ from 0.33 to 0.455 108

4.8 Comparison of (a) Specific heat (b) order parameter profiles for values of $\lambda^{'}$ from 0.463 to 0.610 108

4.9 Comparison of (a) specific heat (b) order parameter profiles for values of $\lambda^{'}$ from 0.639 to 0.691 109

4.10 Susceptibilities (χ 's) of the order parameters for values of $\lambda^{'}$ from 0.462 to 0.610 110

4.11 energy cumulant V_4 for values of $\lambda^{'}$ from 0.345 to 0.45 111

4.12 Energy cumulant V_4 for values of $\lambda^{'}$ from 0.463 to 0.610 111

4.13 energy cumulant V_4 for values of $\lambda^{'}$ from 0.64 to 0.691 112

4.14 Phase diagram inside the essential triangle along path OIW 113

4.15 Representative free energy plotted as a function of (a) energy (b)R^2_{00} (c) R^2_{22} at the point B3 ($\lambda^{'}$ = 0.610, Fig. 4.2) 114

4.16 Representative free energy plotted as a function of (a) energy (b)R^2_{00} (c) R^2_{22} at the point B4 ($\lambda^{'}$ = 0.674, Fig.4.2) 115
4.17 Representative free energy plotted as a function of (a) energy (b) R^2_{00} (c) R^2_{22} at the point Z ($\lambda^{'}$ = 0.692, Fig.4.2) 116
4.18 Representative free energy plotted as a function of (a) energy (b) R^2_{00} (c) R^2_{22} at the point B5 ($\lambda^{'}$ = 0.709, Fig.4.2) 117
4.19 Comparison of (a) specific heat (b) order parameter profiles for values of $\lambda^{'}$ in the range 0.709 - 0.747 (L=15) 118
4.20 Energy cumulant V_4 for values of $\lambda^{'}$ in the range 0.709 - 0.747 (L=15) . . . 119
4.21 Representative free energy plotted as a function of (a) energy (b)R^2_{00} (c) R^2_{22} at point B6 ($\lambda^{'}$ = 0.740, Fig.4.2) 119
4.22 Comparison of (a) specific heat (b) order parameter profiles from B- and RW- ensembles for λ_Z = 0.2 121
4.23 Comparison of (a) specific heat (b) order parameter profiles from B- and RW- ensembles for λ_Z = 0.35 122
4.24 Specific heat for λ_Z values (a) Range: (0.15, 0.4085) (b) Range: (0.42, 0.65) (L=15, RW-ensembles) 122
4.25 Order parameter profiles for λ_Z values (a) Range: (0.15, 0.4085) (b) Range: (0.42, 0.65) (L=15, RW-ensembles) 123
4.26 Susceptibilities (χs) of the order parameters for λ_Z values: (a)0.2 (b) 0.25 . 124
4.27 Susceptibilities (χs) of the order parameters for λ_Z values : (a)0.3 (b) 0.35 . 124
4.28 Susceptibilities (χs) of the order parameters for λ_Z value 0.4085 125
4.29 Energy cumulants V_4 at various λ_Z values along the path OT (L=15, RW-ensembles) 125
4.30 Phase diagram along the dispersion parabola from RW-ensembles (L=15) . 126

5.1 Spatial variation of angular correlations of different molecular axes near the $I - N_U$ transition temperature ($T^{'}$ = 1.12) for λ_Z=0.35 137
5.2 Fits of correlation lengths of different molecular axes to the power law behaviour (Eqn.5.3.3 near the $I - N_U$ transition (λ_Z=0.35) 138
5.3 Spatial variation of angular correlations of different molecular axes near the $N_U - N_B$ transition temperature ($T^{'}$ = 0.51) for λ_Z=0.35 141
5.4 Spatial variation of angular correlations of different molecular axes near the $N_U - N_B$ transition temperature ($T^{'}$ = 0.15) for λ_Z=0.2 142

5.5 Variation with temperature of correlation lengths of different molecular axes covering both transitions for λ_Z = 0.275 143

5.6 Variation with temperature of correlation lengths of different molecular axes covering both transitions for λ_Z = 0.35 144

5.7 comparison of correlation lengths at $I - N_U$transition for different λ_Z . . . 145

6.1 (a)Type A Film (b) Type C Film 153

6.2 Variation with temperature of system properties in Type C film (a) Specific heat C_V (b) Two major order parameters R^2_{00}, R^2_{22} (c)- (f) The four order parameters along with their susceptibilities 157

6.3 Layerwise variation of different properties of the Type C film, with tempertaure: (a) R^2_{00} (b) R^2_{02} (c) R^2_{20} (d) R^2_{22} (e) Angle θ (f) Angle ϕ (see text) 159

6.4 Variation with temperature of system properties in Type A film (a) Specific heat C_V (b) Two major order parameters R^2_{00}, R^2_{22} (c)- (f) The four order parameters along with their susceptibilities 161

6.5 Layer-wise variation of different properties of the Type A film, with temperature: (a) R^2_{00} (b) R^2_{02} (c) R^2_{20} (d) R^2_{22} (e) Angle θ (f) Angle ϕ (see text) 162

6.6 Variation of maximum eigen values associated with each of the ordering tensors of the three molecular axes (x, y, z), as a function of temperature for (a) Type C film (b) Type A film 163

6.7 Variation with temperature of system properties in CY film (a)- (d) The four order parameters along with their susceptibilities (e) Angle θ (f) Angle ϕ 167

6.8 Variation with temperature of system properties in AY film (a)- (d) The four order parameters along with their susceptibilities (e) Angle θ (f) Angle ϕ 168

6.9 Variation of maximum eigen values asociated with each of the ordering tensors of the three molecular axes (x, y, z), as a function of temperature for (a) CY film (b) AY film 169

6.10 Variation with temperature of system for different thickness of Type C film (a) C_V; (b) R^2_{00}; (c) R^2_{02}; (d) R^2_{20} (e) R^2_{22} 171

6.11 Variation with temperature of system for different thickness of Type A film (a) C_V; (b) R^2_{00}; (c) R^2_{02}; (d) R^2_{20} (e) R^2_{22} 173

6.12 Variation of order parameters with temperature for different anchoring strengths (ϵ_{nz}) in Type C film: (a) R^2_{00} (b) R^2_{02} (c) R^2_{20} (d) R^2_{22} 174

6.13 Variation with temperature for different anchoring strengths (ϵ_{nz}) in Type A film: (a) R^2_{00} (b) R^2_{02} (c) R^2_{20} (d) R^2_{22} 175

7.1 Spatial dependence of order parameters and susceptibilities at λ_Z = 0.35, at different temperatures 190

7.2 Spatial dependence of order parameters and susceptibilities at λ_Z = 0.3, at different temperatures 191

7.3 Spatial dependence of order parameters and susceptibilities at λ_Z = 0.25, at different temperatures 192

7.4 Spatial dependence of order parameters and susceptibilities at λ_Z = 0.2, at different temperatures 193

7.5 Effect of variation of λ_Z on the spatial dependence of (a) R^2_{22} (b) R^2_{00} at T=0.1 and anchoring strength ϵ_s = 0.25 194

7.6 Spatial dependence of fluctuations in R^2_{00} for different λ_Z at (a) T = 0.7 and (b) T = 0.6 195

7.7 Variation of (a) order parameters and (b) susceptibility in $< R^2_{22} >$, bracketing the anchoring transition for various values of ϵ_s at λ_Z = 0.35, T = 0.4 196

7.8 Variation of (a) order parameters and (b) susceptibility in $< R^2_{22} >$, bracketing the anchoring transition for various values of ϵ_s at λ_Z = 0.35, T = 0.2 198

Declaration

I hereby declare that the work presented in this thesis titled **‘Monte Carlo Study of Biaxial Nematic Liquid Crystals’** has been carried out by me under the supervision of Prof. V.S.S. Sastry, School of Physics, University of Hyderabad, Hyderabad, India, as per the Ph.D ordinances of the University. I declare, to the best of my knowledge, that no part of this thesis has been submitted for the award of a research degree of any other University.

B. Kamala Latha

Registration No: 06PHPH25.

Date:

Hyderabad.

Certificate

This is to certify that the thesis work titled “**Monte Carlo Study of Biaxial Nematic Liquid Crystals**” being submitted to the University of Hyderabad by **Ms. B. Kamala Latha** (Registration No:06PHPH25), for the award of the degree of Doctor of Philosophy in Physics, is a record of *bona fide* work carried out by her under my supervision.

The matter embodied in this report has not been submitted to any other University or Institution for the award of any degree or diploma.

Dean,
School of Physics,
University of Hyderabad,
Hyderabad–500 046

Prof. V. S. S. Sastry,
Supervisor,
School of Physics,
University of Hyderabad,
Hyderabad–500 046

Acknowledgements

First and foremost, I express my profound sense of gratitude and indebtedness to my teacher and thesis advisor Prof. V. S. S. Sastry, for his supervision and guidance. Prof. Sastry has been extremely supportive throughout this research work and I appreciate his contributions of time, knowledge and invaluable suggestions without which this dissertation would not have been possible. He has been a tremendous mentor to me. His joy and enthusiasm for research was contagious and motivational to me, even during tough times in the Ph.D. pursuit. His constant support with continual and persuasive efforts has made me to understand the nuances of the subject. It has been certainly a memorable experience to have worked with him.

I sincerely thank Prof. K. P. N. Murthy for his advice and support during the course of this work. I take this opportunity to sincerely thank the faculty of the school who taught me physics during my M.Sc, M.Phil and pre-Ph.D studies at this university. Their passion for the subject and zeal to impart knowledge made them the role models for the student community and they continue to inspire me in my chosen profession.

I am grateful to the Dean, School of Physics for providing the necessary facilities and support during my research days.

I am thankful to Prof. N. Satyavathi (formerly with Osmania University) for her support and encouragement.

It is wonderful to have Ms. Regina Jose, Dr. G. Sai Preeti, Dr. D. Jayasri, Dr. M. Rajeswari, Mr. J. Anantaiah, Mr. Siva Chari, Mr. Suman Kalyan, Dr. T. Arun Kumar and Dr. P. Satyanarayana as my co-workers and colleagues providing much needed help. Special thanks are due to Ms. Regina Jose for her assistance and constant support. I wish them all success in their future endeavours.

It is my pleasure to thank the Director, Centre for Molecular Simulation and Design (CMSD), University of Hyderabad, for providing the computing facilities.

I am grateful to University Grants Commission (UGC) for providing scholarships, namely, Research Fellowship for Meritorious Students (RFSMS) and Basic Science Research (BSR) during 2010-13.

Thanks are also due to Mr. T Abraham and other office staff (School of Physics) who helped me in one or the other way.

I take this opportunity to specially thank my family. My dream to pursue research would not have been possible without their unending and loving support. My husband K.C.Kumar stood by me like a rock and constantly encouraged me in this pursuit I undertook a little late in life. His faith in my abilities helped me to undertake this most memorable and cherished journey in life. My children Karthik and Virinchi supported me with their unconditional love and understanding. I also owe thanks to my in-laws and my mother for their blessings and support. It was the dream of my (late) father that his children achieve great heights in their lives. This dissertation thesis is dedicated to all the members of my family who encouraged me to realise this dream.

B. Kamala Latha

Preface

Molecular organization and ordering behavior in thermotropic biaxial liquid crystals has been the subject of many experimental as well as theoretical investigations, including computer simulations. Though macroscopic biaxial phase is an expected consequence of the shape anisotropy of many realistic liquid crystal molecules, their non -cylindrical symmetry of the molecular distribution is effectively averaged out due to thermal motions. As a consequence, this manifestation of molecular biaxiality is more often not evident in experiments, and theoretical models employing uniaxial constituents are profitably used to compare with experiments.

Introduction of biaxial tensor components in the model Hamiltonians leads to theoretical predictions regarding the existence of a biaxial nematic phase, under suitable choices of the model parameters. Analysis of these models based on molecular field theories as well as on phenomenological considerations, captures the essential features of the phase diagram. Predicted condensation of thermally driven spontaneous biaxial order is an important attraction of this effort, due its perceived technological implications. However the experimental scenario has not been that encouraging, with very few unambiguously accepted biaxial phases in realistic systems being reported to date. In this context, computer simulation of the phase sequences of a general Hamiltonian model, especially focusing on the relevant parameter space holding promise for a direct formation of a biaxial nematic from isotropic phase, seems to be topical as well as academically interesting. This thesis summarizes such an effort employing the state-of-the-art Markov Chain Monte Carlo (MCMC) methods, reporting on the macroscopic equilibrium behavior of a general quadratic biaxial Hamiltonian model (and its dispersion-approximation variant). The entropic sampling technique employed enables one to compute density of states and hence examine the free energy profiles of the system under differing experimental conditions, - besides of course yielding equilibrium properties with desired temperature resolution, from the canonical ensembles constructed through suitable reweighting procedures.

Biaxial nematics are often modeled, partly for its simplicity, within the so-called dispersion approximation (with one model parameter, say λ_Z). Here, each molecule is associated with a single fluctuating dipole (oscillator), which in turn interacts with those of the surrounding neighbouring molecules. The mean field phase diagram of this model predicts a sequence which includes a low temperature biaxial phase ($I - N_U - N_B$), and suggests a specific value of λ_Z where the isotropic phase is slated to make a direct transition to the biaxial phase, called the Landau point (LP). A more general model endows each molecule with two distinct oscillators, leading to a Hamiltonian with two adjustable parameters (γ, λ), allowing for a richer parameter space and presumably more closer to realistic systems. Analysis of this model within mean-field approximation is of recent origin, and such investigations employing bifurcation methods and mini-max principle provide useful insights into the role of the various interactions in different regions of the parameter space. One unsavory feature of this analysis, as was noted in the literature, is the unsatisfactory asymptotic behavior of the phase sequence in the limit of vanishing coupling between the intermolecular biaxial-biaxial tensor components, i.e. as $\lambda \to 0$. The mini-max analysis in this partly repulsive region (where the Hamiltonian is indefinite) maintains that a direct $I - N_B$ transition is to be expected to continue in this limit, even though the biaxial phase stability is known to be assured only if $\lambda > 0$. One of the objectives of the present work is to analyze the simulation data in this regime of intriguing analytical result. Further, the studies are extended to revisit the extensively investigated dispersion model, and examine the spatial correlation functions of the three molecular axes at different values of λ_Z as a function of temperature. Finally the thesis reports simulation results on two confined biaxial systems (hybrid planar films with variable anchoring conditions, and a micro-droplet with homeotropic boundary conditions at the interface), to provide interesting comparisons with similar work with uniaxial constituents. The presentation of this work is spread over eight chapters in the thesis.

The first chapter presents model Hamiltonians developed to account for interactions among the biaxial constituents in the liquid crystal system, and a brief summary of the mean field theories proposed to describe bulk biaxial nematic systems, as well as the details of predicted phase diagrams. The second chapter summarizes principles of different sampling techniques (canonical and entropic) based on MCMC, used for simulations on these liquid crystal systems.

The third chapter is concerned with simulation results, and the phase diagram so obtained, of a bulk biaxial nematic system based on a general quadrupolar interaction Hamiltonian, which permits two variable interaction parameters describing the uniaxial-biaxial (γ) and biaxial-biaxial (λ) coupling between the molecular tensor components of neighbouring molecules, after setting the temperature scale. Predictions regarding the phase behavior were made earlier based on mean-field theoretic arguments, along a chosen trajectory in (γ, λ) space (the so-called essential triangle) and a direct transition from the isotropic to a biaxial phase is expected over a major portion of the perimeter of this triangle. One open question in this analysis seems to be the predicted condensation of a low temperature biaxial phase $vis - a - vis$ the limit of biaxial nematic stability, as $\lambda \rightarrow 0$ and particularly in the presence of appreciable γ. The work reported in this chapter focuses on simulations carried out along the same trajectory as that of the mean-field analysis (the perimeter of the essential triangle, referred to as the arc λ^*), so as to enable a direct comparison of the simulational predictions with expectations from bifurcation methods. Briefly stated, the Monte Carlo results progressively differ qualitatively from the earlier predictions in the regime of large and vanishing λ. Based on the micro-canonical data in this interesting region (i.e. in the regime of vanishing attractive coupling of one molecular minor axes compared to the other axes couplings), it is argued that the onset of macroscopically observable biaxial order is inhibited due to inherent barriers to fluctuations of energy components comprising the total energy. The lack of concomitant development of long range order of the molecular axes (inhomogeneity), which gives rise to these barriers, can be overcome only on further cooling to very low temperatures. The chapter in this respect makes an attempt to possibly explain the difficulty in experimentally realizing the biaxial phase in a direct second order transition from the isotropic phase of a biaxial liquid, as predicted by mean-field treatments.

The fourth chapter presents the simulation results inside the essential triangle along two chosen trajectories, in order to examine the relative interplay between γ and λ terms. The first trajectory is chosen such that a path in (γ, λ) space is traversed which could make a connection to experimentally realizable systems. It also covers the partly repulsive regions of the mean field Hamiltonian. The second chosen trajectory is along the dispersion parabola, which is embedded in the essential triangle as a boundary separating the fully attractive regime from partly repulsive region in the (γ, λ) space. The examination of free energy profiles obtained in these simulation experiments provides a pointer to the possible barriers to macroscopic biaxial order, which could develop in real systems.

The fifth chapter focuses on the computation of the correlation lengths associated with the three molecular axes and critical exponents associated with the phase transitions. The dispersion parabola is chosen as the trajectory of study for a systematic variation of the parameters, with the two parameters being replaced by single variable, say λ_Z. Such data was collected as a function of temperature bracketing the two transitions, for various values of molecular biaxiality λ_Z. The results show strong influence of the biaxiality on the correlation lengths, and the exponents. The case of λ_Z = 0.2 seems to be curious and perhaps is a manifestation of the fact that a minimum degree of biaxiality is needed in practical terms before the biaxial model could differ qualitatively from the uniaxial (Lebwohl-Lasher) model (represented by the origin of the (γ, λ) space.

The sixth chapter presents the simulation study of planar films of a biaxial liquid crystal embedded between substrates which induce hybrid anchoring conditions. Extending the earlier work on one such film (which yielded rather curious behavior with temperature) two such films with same anchoring conditions, but with differing interactions at the surface, were studied based on canonical sampling methods. In order to obtain a better appreciation of the different director structures in different phases, different order parameters are computed layer-wise, as also their director directions. A detailed analysis of the data in these films shows that the onset of the low temperature transition to the biaxial phase makes the order parameter of one of the minor axes dominant (over that of the molecular long axis) and the corresponding direction of the dominant director is perpendicular to the plane containing the bent director structure. This seems to be an interesting result since we find that in the biaxial phase, one can generate an in-plane order of high degree involving one of the minor axes of the molecules, while the bent director from the long axis alignment is locked within the plane due to influence from the substrates. The effect of varying the relative anchoring strengths of the substrates, as well as the thickness of the films, on the development of this in-plane order, is also probed.

The seventh chapter is concerned with the simulation results for another confined system within the dispersion approximation, a biaxial nematic droplet. Canonical sampling methods are employed to compute the equilibrium order parameters and their susceptibilities in the uniaxial and biaxial regime, and based on this data the sizes of the bulk-like core at the centre of the droplet are estimated. The results indicate that uniaxial phases formed at high temperatures for different λ_Z values are quantitatively different in their elastic behavior. For example, it is known that for a uniaxial medium the core size increases as the order increases, owing to an increase in elastic energy density. However in the case of a biaxial nematic droplet, the biaxial core size seems to decrease with increasing biaxial order.

The last chapter summarizes the salient features of the work indicated above, and stresses on the relative advantages of employing entropic sampling methods over the conventional canonical techniques, while constructing equilibrium ensembles. It is demonstrated that the former seeks out some of the (rare) microstates missed by the latter, and in our present context, that seems to have made a qualitative difference in assigning the nature of a given phase, as well as in predicting the onset of a new transition. Also, the advantage of examining the free energy profiles as a function of temperature, energy, as well as order parameters, - afforded by the estimation of the density of states -, is clearly brought out through this study. In summary, the thesis makes a modest attempt at exploring biaxial liquid crystals, both in bulk as well as in confined geometries, with a detailed Monte Carlo study.

Chapter 1

Introduction- Biaxial Nematics

1.1 Introduction

Thermodynamic phases of condensed matter which exhibit unique ordering properties intermediate between a crystalline solid and an isotropic liquid are called liquid crystals (LCs) or mesophases. They possess many of the mechanical properties of a liquid like fluidity, formation and coalescence into droplets and exhibit simultaneously anisotropy in their physical properties, like a crystal. The characteristic feature of liquid crystals is the presence of long range orientational order in the arrangement of their constituent molecules while having quasi long-range translational or positional degrees of freedom.

The discovery of liquid crystalline state is credited to Friedrich Reintzer, a botanist, who described his experiments with cholestryl ester in a paper published in 1888. The term liquid crystal was coined by the physicist Otto Lehmann. Georges Friedel [1] classified the liquid crystals, according to their structural properties, into nematic, smectic and cholestric phases. However, liquid crystals remained as pure scientific curiosity till the 1960's till the advent of their possible usage in flat panel displays, owing to their elctro-optical properties. The response of phases to external stimuli such as electric,magnetic and chemical environments lead to many technological application of liquid crystals in display devices [2] - [7]. Recent technological advances include their usage in photonics [8] and biochemical sensors [9].

Liquid crystals can be broadly classified in two categories namely thermotropic and lyotropic liquid crystals. Single component systems that show mesomorphic behaviour as a function of temperature are called thermotropic. A lyotropic liquid crystal consists of two or more components that exhibit liquid-crystalline properties in certain concentration ranges. This Thesis is mainly concerned with the study of thermotropic liquid crystal phases.

Thermotropic phases are exhibited by a) elongated (calamitic) molecules, b) disk-like (discotic) molecules, and c) banana shaped molecules or bent-core molecules. The central part of such molecules comprises typically a rigid core (phenyl groups) connected to flexible (aliphatic) chains. The phase sequences of these materials are strongly correlated to the structure of the constituent (groups of) molecules. The calamitic molecules usually form nematic, smectic and cholestric phases whereas the discotic molecules form columnar phases. Excellent introductions to the typical molecular structure and their role in condensing into a variety of rich mesomorphic phases are available [10, 11].

Nematic phase is the simplest mesophase into which the an isotropic liquid could condense, and differs from it by the presence of unique direction along which the anisotropic molecules tend to develop an orientational order. The preferred direction of orientation is called the 'director' and is denoted by a (headless) unit vector $\hat{\boldsymbol{n}}$. If the molecules of the LC phase lack inversion symmetry, then the nematic phase develops chirality (cholestric phase), in which the director rotates in a helical fashion about an axis perpendicular to the director. A smectic phase is formed when the phase has orientational order and the centre of mass of molecules are arranged in layers giving rise to positional order. When smectic and nematic phases are found in one compound, the nematic phase nearly always exists at a higher temperature than the smectic (except in reentrant nematic phases).

1.1.1 Nematic Phases

The two interesting orientationally ordered liquid crystalline phases are the uniaxial and biaxial nematics [12], which possess long range orientational order, but no positional order. The uniaxial nematic phase has the $D_{\infty h}$ symmetry, where as the biaxial nematic phase exhibits D_{2h} symmetry. Both thermotropic and lyotropic liquid crystals exhibit these phases.

Uniaxial nematic phase

The name, uniaxial nematic phase, derives from the property that the system possesses a single axis along which a plane polarized light beam can travel without undergoing a change in the state of polarization. When liquid crystal molecules which are rod-like with an elongated appearance are cooled from the isotropic phase, a uniaxial nematic phase (N_U) is typically obtained. It is customary, for theoretical description, to treat the molecules as ellipsoids of revolution possessing cylindrical symmetry about the long axis. The director $\widehat{\boldsymbol{n}}$ is now defined as the average direction along which the symmetry axes of the molecules tend to point, representing the axis of symmetry of the phase. Obviously the isotropic symmetry of the medium is lost in this process. Hence any observable tensorial property of the nematic phase, such as dielectric constant, has two distinct principal components and the difference between them is a measure of anisotropy of the medium. This macroscopic anisotropy is a manifestation of the microscopic anisotropic interactions at the molecular level.

Two Uniaxial liquid crystal phases can be identified, called the N_{U+} and N_{U-} phases. N_{U+} is formed from prolate (rod) shaped molecules and N_{U-} is formed from oblate (disc) shaped molecules. In a rod-shaped molecule the director is along the the long-axis, whereas in disc-shaped molecules the director is normal to the disc.

The symmetry of a simple nematic liquid crystal can be best described in terms of the order parameter, which is defined to non-zero in the ordered phase and zero in the disordered phase. The main difference between the isotropic and nematic phases is the the presence of long-range orientational order in the nematic phase, while positional order is absent in both the phases. Macroscopically the amount of orientational order in the nematic phase is described by two scalar order parameters S and D. S signifies the contributions to the order from orienting the long molecular axes along the director. A finite D means that there is a difference in tendency of the two transeverse molecular axes to project on the director.

The onset of the nematic phase in anisotropic liquids can be accounted for based on two methodologies: molecular statistical theory and phemenological Landau-de Gennes theory. In the molecular statistical approach, the physical behaviour of these materials is explained at the molecular level. Anisotropic interaction forces between the molecules are responsible for the development of long range order at the phase transition to the nematic phase. In a mean field approach, a single molecule is assumed to be in an average field produced by surrounding molecules. Long range order in the nematic phase occurs due to contributions from the anisotropic part of the pair potential between two molecules. The Onsagar approach [13] ascribes the nematic ordering as arising due to short range intermolecular repulsive force between molecules in the shape of hard rods. Another approach due to Cotter and Gelbart [14, 15] assumes a Van der Waals type of interaction between the molecules. The Maier-Saupe approach [2] assumes that anisotropic dispersion forces are responsible for nematic order among the molecules. The attractive interaction arises from electrostatic interaction between induced dipoles of the molecules. The theory predicts a first order transition from a isotropic state to uniaxial nematic state and is successful in explaining the observed pretransitional effects in a qualitative manner.

Phenomenological Landau theory of second order phase transitions [16] was successfully applied to study the first order isotropic-uniaxial nematic phase transition by de Gennes [17]. In this formalism, the free energy is expanded in terms of order parameters and its gradients, compatible with the system under consideration. The coefficients of the expansion generally depend on the temperature and other thermodynamic parameters. The signs of the coefficients are chosen such that expansion is stable against an unlimited growth of order parameter. Depending on the symmetry of the phases involved, a suitable parametrisation of the order tensor is employed. The absolute minima of resultant free energy are explored to obtain the possible topologies of the phase diagrams.

Biaxial Nematic Phase

In all above theories of the nematic phase, the constituent nematogenic molecules are assumed to possess cylindrical symmetry. However in reality all molecules are intrinsically biaxial and flexible and very rarely have true cylindrical symmetry. The macroscopically observed uniaxial phase is a result of rotational disorder around the long molecular axis [18]. A biaxial nematic phase strictly implies that there are two axes along which a plane polarized light beam can travel without the state of polarization being altered. The two orthogonal directions are denoted by the principal director $\widehat{\boldsymbol{n}}$ and minor director $\widehat{\boldsymbol{m}}$. It implies that at the macroscopic level the three principal components of a observable property like refractive index, which is a second rank tensor, will have three different values.

Conventionally the biaxial nematic molecule is represented as a rectangular parallelepiped with D_{2h}symmetry [19]. The point symmetry group consists of an identity, a two fold rotation axis (principal axis) with a perpendicular mirror plane, and two two-fold rotation axes perpendicular to the principal axis. The molecular (x, y, z) axes are taken to coincide with these rotation axes. The molecular z axis is assumed to be the long axis of the molecule with dimension L and the y, z are identified with the the breadth B and width W respectively. For both cases of flat plates $(L = B > W)$ and long rods $(L > B = W)$ an ordering of Maier-Saupe type is expected to occur. However in the case of flat plates the W axes tend to align parallel whereas in the case of rods the ordering is due to the L axes. A complete mutual alignment of the respective axes corresponds to the biaxial ground state.

The biaxial nematic phase was predicted theoretically by Freiser [20] using a molecular field approximation. He generalised the Maier-Saupe interaction potential to include the interaction between asymmetrical molecules which constitute a real nematic. By assuming that each molecule interacts with its z nearest neighbours, the minimisation of the resulting free energy lead to the prediction of a first order transition from a isotropic state to a uniaxial nematic. However the uniaxial state is not the ground state of the system. Further cooling leads to second order transition from a uniaxial to a biaxial state where the molecules are completely aligned. He proposed a biaxial order parameter in addition to the uniaxial order parameters S. However the possibility of a intervening crystalline or smectic phase is not ruled out in reality.

Subsequently the Landau-de Gennes formalism was employed by Alben [21] to study the phase transitions in a fluid of biaxial particles.The predicted phase diagram contained a special critical point where two second order lines meet the first order phase boundary in a sharp cusp. An 'accidental' second order transition between the isotropic-biaxial phases takes place at that point, denoted as Landau point in later literature.

A mean field phase diagram for such a fluid of interacting particles was obtained by Straley [19] by assuming the biaxial particles to rectangular blocks. He identified the four order parameters necessary to describe the resulting uniaxial and biaxial phases. The phase diagram obtained was similar to the one predicted by Alben [21] using the phenomenological Landau theory.

Although the biaxial phase resulting from non-cylindrical symmetry of the molecules was yet to be discovered, the effect of the deviation from cylindrical symmetry on the uniaxial phase was investigated by Luckhurst et al [22]. A molecular field theory was proposed for uniaxial liquid crystals formed by non-cylindrically symmetric molecules assuming that only dispersive forces contribute to the intermolecular potential. Subsequently an extension of the Maier-Saupe theory for biaxial nematics was proposed by Bocara $et\ al$ [23] who using a system of asymmetric ellipsoids, obtained a phase diagram for biaxial nematic phase. This phase diagram was similar to phase diagram obtained by Straley. Subsequently Remler and Haymet [24] solved Freiser's model exactly within the mean field approximation over the full range of biaxiality. It confirmed the order of transitions $I - N_U = N_B$ over a range of biaxiality and a single $I = N_B$ transition at a value of biaxiality equal to $\frac{1}{\sqrt{6}}$. However it was concluded that mean-field theory does not provide an adequate description of the biaxial phase transition even in realistic models which incorporate actual nematogenic behaviour. The phase diagram predicted in all the above studies was qualitatively confirmed in a simulation of the lattice model of a Biaxial Hamiltonian in the dispersion approximation [25].

The phase diagram for the biaxial liquid crystal was also reconfirmed using phenomenological Landau-de Gennes formalism [26–28] and theory was also suitably modified to include local fluctuations of the order parameter and applied to explain the experimentally observed critical opalescence within the nematic phase [27, 29, 30].

The number of order parameters required, to describe uniaxial and biaxial phases resulting from interacting biaxial particles, can be obtained by considering the orientational distribution function.

1.2 Microscopic Origin of Order Parameters

From the molecular point of view, phase transitions are described by the modifications produced by the order parameters in the singlet distribution functions [10]. The order parameters form the expansion coefficients of the singlet distribution in a suitable basis set. The order of an ensemble of molecules is specified by a distribution function $P(r, \Omega)$ which gives the probability of finding a molecule at a particular position r and with a particular orientation Ω, where Ω denotes the set of three Euler angles α, β, γ which describe the molecular orientation with respect to the Laboratory-frame.

For a nematic phase only orientational degrees of freedom are important and the distribution function can be written as

$$P(r, \Omega) = \rho f(\Omega)$$

where ρ = uniform mass density and $f(\Omega)$ is the orientational distribution function which is normalized i.e $\int f(\Omega) d\Omega = 1$.

Any well behaved function of the three Euler angles $f(\Omega)$ can be expanded in a basis of Wigner rotation matrices [31]. A complete expansion of the orientational distribution function is

$$f(\Omega) = \sum_{L,m,n} \langle D^L_{m,n}(\Omega) \rangle D^L_{m,n}(\Omega) \tag{1.2.1}$$

where $D^L_{m,n}(\Omega)$ are Wigner matrices or generalized spherical harmonics. The expansion coefficients $\langle D^L_{m,n}(\Omega)\rangle$ which are the averages of $D^L_{m,n}(\Omega)$ are the required orientational order parameters. In principle there are $(2L+1)^2$ order parameters. These can be reduced depending on the symmetry of the molecules and the mesophase.

A uniaxial phase formed by cylindrically symmetric molecules

This is the simplest example of the nematic phase which is formed by molecules having shape of rigid rods, prolate spheroids, cylinders or spherocylinders. Both the phase and the constituent molecules have $D_{\infty h}$ symmetry. Due to head tail symmetry of the nematic phase ($\widehat{n}$ and $-\widehat{n}$ are equivalent), it immediately implies that only terms with even L are allowed in the expansion of the orientational distribution function in Eqn.1.2.1.

Assuming the axis of cylindrical symmetry, the director, to be along laboratory Z-axis, no observable property will change on rotation around the Z-axis. Then $f(\Omega)$(=$f(\alpha,\beta,\gamma)$) is independent of the angle α, since it describes a rotation about laboratoty Z-axis. This implies that $m = 0$ in $D^L_{m,n}$. Further since the molecules are cylindrically symmetric, the distribution is independent of angle γ, which describes the rotation around molecular z-axis. Hence $n = 0$ in $D^L_{m,n}$. Therefore

$$f(\Omega) = f(\beta) = \sum_{L=0}^{\infty} \frac{2L+1}{2} \langle D^L_{00}\rangle D^L_{00};\ L = even; \tag{1.2.2}$$

where

$$D^L_{00} = P_L(cos\beta)$$

Therefore

$$f(\Omega) = f(\beta) = \frac{1}{2} < D^0_{00} > + \frac{5}{2} < D^2_{00} > D^2_{00} + \frac{9}{4} < D^4 2_{00} > D^4_{00} + -- \tag{1.2.3}$$

The first three expansion coefficients are

$$\langle D^0_{00}\rangle = 1; \langle D^2_{00}\rangle = \frac{1}{2}\langle 3cos^2\beta - 1\rangle; \langle D^4_{00}\rangle = \frac{1}{8}\langle 35cos^4\beta - 30cos^2\beta + 3\rangle; \tag{1.2.4}$$

$< D^0_{00} >$ being a constant is unsuitable as an order parameter. The first nontrivial term $< D^2_{00} >$ = S (by convention) can be taken as the scalar order parameter which describes the degree of order of the molecules about the average orientation. This is also confirmed by experimental evidence that second rank interactions are dominant in a nematic LC.

It can be seen from the definition in eqn (1.2.4) that when all molecules point in the same direction as the director in the nematic phase i.e when $\theta = 0$, $S = 1$. $S = 0$ in isotropic phase and S is minimum when all molecules lie perpendicular to the director and there is no preferred direction in this plane. Thus value of S lies in interval $[-\frac{1}{2}, 1]$. In tensorial notation the order parameter can be expressed as

$$\boldsymbol{Q} = \frac{1}{2} S(3\widehat{\boldsymbol{n}} \otimes \widehat{\boldsymbol{n}}) - \boldsymbol{I})$$

which is a symmetric, traceless second rank spherical tensor. It represents the quadrupolar moment of the distribution .

Alternatively if the orientational distribution function is expanded in terms of the direction cosines of the director with a molecule fixed frame, then the Saupe ordering matrix is obtained. It is a symmetric traceless cartesian tensor of rank 2 and contains 5 independent elements. It is called the ordering supertensor and is defined as

$$\boldsymbol{S}_{ab}^{AB} = \frac{< 3\boldsymbol{l}_{Aa}\boldsymbol{l}_{Bb} - \boldsymbol{\delta}_{AB}\boldsymbol{\delta}_{ab} >}{2} \tag{1.2.5}$$

where the superscripts A and B can be any one of the principal axes X, Y or Z of the phase and the subscripts a and b can be any of the principal axes, x, y, or z of the molecules. l_{Aa} denotes the cosine of the angle between axes A and a while δ_{AB} denotes the kronecker delta.

Applying the symmetry conditions of the uniaxial mesophase, the matrix $\boldsymbol{S}_{zz}^{ZZ}$ becomes diagonal with only one independent component $\boldsymbol{S}_{zz}^{ZZ} = S$, the nematic order parameter, introduced by Tsvetkov [32]. The co-ordinate system in which $\boldsymbol{S}_{zz}^{ZZ}$ becomes diagonal is called the Principal axis system of S or the ordering matrix frame.

Uniaxial and Biaxial phases formed by non cylindrical molecules

When the constituent molecules of the phase are noncylindrical (like prolate ellipsoid,rectangular parallelepiped) the other axes of the molecules may have tendency to mutually align along with the calamitic axis of the molecule.The cylindrical symmetry of the phase is then broken and the next lower point group symmetry is the D_{2h} symmetry.

Uniaxial phase Here since the phase is uniaxial, the resulting distribution function is independent of angle α.

$$f(\Omega) = \sum_{L,n} \langle D^L_{0,n}(\Omega)\rangle D^L_{0,n}(\beta,\gamma).$$

Applying the orthogonality condition of Wigner matrices we have

$$f(\beta,\gamma) = \frac{1}{4\Pi}\sum_{0}^{\infty}\sum_{n=-L}^{L}(2L+1)\langle D^L_{0,n}\rangle D^L_{0,n}(\beta,\gamma). \tag{1.2.6}$$

There are $(2L+1)$ order parameters for each L given by $\langle D^L_{0,n}\rangle$. Since the molecules are non cylindrical, a molecular frame with axes along the three C_2 axes, can be chosen. Such a choice gives rise to three mutually perpendicular mirror planes which are perpendicular to the x, y, z axes of the molecule. Using this symmetry condition and the fact that the spherical harmonics $D^L_{0,n}(\beta,\gamma)$ are multiplied by $(-1)^L$ under the same operation, we only need to expand in Wigner matrices of even rank L. The first few are

$$D^0_{00}(\beta,\gamma) = 1; \tag{1.2.7a}$$

$$D^2_{00}(\beta,\gamma) = P_2(\cos\beta); \tag{1.2.7b}$$

$$D^2_{0,\pm 2}(\beta,\gamma) = \sqrt{\frac{3}{8}}\sin^2\beta\exp(\mp i2\gamma). \tag{1.2.7c}$$

Hence at the second rank level there are 2 order parameters $< D^2_{00} >$ and $Re < D^2_{02} >$. $< D^2_{00} >$, the uniaxial order parameter S, gives the degree of alignment of the z-molecular axis with the director. The order parameter $Re < D^2_{02} >$ is denoted conventionally as D. The phase is not biaxial.

In the Principal axis system of the Saupe ordering matrix, this corresponds to $S = \boldsymbol{S}^{ZZ}_{zz}$ and $D = \boldsymbol{S}^{ZZ}_{xx} - \boldsymbol{S}^{ZZ}_{yy}$. These two order parameters are sufficient to describe the uniaxial phase formed by non cylindrical molecules.

Biaxial phase The orientational distribution function depends on the three Euler angles α, β, γ and can be expanded in terms of the Wigner matrices as

$$f(\Omega) = f(\alpha, \beta, \gamma) = \sum_{L,m,n} \langle D^L_{m,n} \rangle D^L_{m,m}(\alpha, \beta, \gamma). \tag{1.2.8}$$

where $\langle D^L_{m,n} \rangle$ are the required order parameters, which can be obtained by applying the symmetry conditions of the molecule and phase, as done above. This results in four second rank order parameters $< R^L_{mn} >$ which are Wigner functions $< D^{mn}_L >$ symmetry adapted for the D_{2h} group of particles and phase [25, 33]. For the even terms they are ,

$$R^L_{mn}(\Omega) \equiv \frac{1}{2} Re(D^L_{mn} + D^L_{m-n}).$$

These are called symmetry adapted basis functions and the only functions whose thermodynamic averages do not vanish. They are expressed explicitly as

$$R^2_{00}(\Omega) = \frac{3}{2}\cos^2\beta - \frac{1}{2}; \tag{1.2.9a}$$

$$R^2_{02}(\Omega) = \sqrt{\frac{3}{8}}\ \sin^2\beta \cos 2\gamma; \tag{1.2.9b}$$

$$R^2_{20}(\Omega) = \sqrt{\frac{3}{8}}\ \sin^2\beta \cos 2\alpha; \tag{1.2.9c}$$

$$R^2_{22}(\Omega) = \frac{1}{4}(\cos^2\beta + 1)\cos 2\alpha\ \cos 2\gamma - \frac{1}{2}\cos\beta\ \sin 2\alpha. \tag{1.2.9d}$$

The order parameters are defined in terms of these composite functions as

$$S =< R^2_{00} >,\ D =< R^2_{02} >,\ P =< R^2_{20} >,\ C =< R^2_{22} >$$

The four order parameters expressed in terms of the cartesian form are [34]

$$S =< R^2_{00} > = \boldsymbol{S}^{ZZ}_{zz}; \tag{1.2.10a}$$

$$D =< R^2_{02} > = \boldsymbol{S}^{ZZ}_{xx} - \boldsymbol{S}^{ZZ}_{yy}; \tag{1.2.10b}$$

$$P =< R^2_{20} > = \frac{\boldsymbol{S}^{XX}_{zz} - \boldsymbol{S}^{YY}_{zz}}{\sqrt{6}}; \tag{1.2.10c}$$

$$C =< R^2_{22} > = \frac{(\boldsymbol{S}^{XX}_{xx} - \boldsymbol{S}^{XX}_{yy}) - (\boldsymbol{S}^{YY}_{xx} - \boldsymbol{S}^{YY}_{yy})}{3}. \tag{1.2.10d}$$

$$\tag{1.2.10e}$$

As can be seen from above definitions, S and D measure the ordering of the major and minor molecular axes with respect to the major phase axis whereas P and C measure the ordering of the major and minor molecular axes with respect to the minor axes of the phase.

Thus the biaxial phase formed by non-cylindrical molecules is described by four order parameters S, D, P, C. This notation is usually employed by experimentalists by convention. However we shall be using the notation of the symmetry adapted basis functions as our order parameters. The various notations of the order parameters and the relations between different notations adapted in literature on biaxial nematics is discussed by Rosso [35].

1.3 Mean field Theories of Biaxial Nematic Phase

Two mean field treatments have been proposed at the molecular level to understand the physical properties of the biaxial nematic. The earlier one, due to Luckhurst [22], takes only the dispersion forces between the molecules into account while calculating the intermolecular pair potential. A recent mean field model proposed by Sonnet $et\ al$ [18], on the other hand, takes shape dispersion of the biaxial dielectric susceptibility into account while proposing a mean field model for biaxial liquid crystals. We discuss below both the mean field theories in detail.

1.3.1 Molecular Potential for Biaxial Phase formed by Non-Cylindrically Symmetric Molecules

This model, called the dispersion model, extends the Maier-Saupe theory for uniaxial molecules, to include lathe-like molecules. Starting from a intermolecular potential for particles of a general shape, the potential of mean torque experienced by a given molecule is obtained after averaging over the intermolecular distance, all possible orientations of the second molecule with respect to the first and over all intermolecular separations. Limiting the summation to those terms with L=2 we have

$$U(\beta\gamma) = -kT(a\ d^2_{00}(\beta) + b\ d^2_{02}(\beta)\cos 2\gamma); \tag{1.3.1}$$

where

$$a = -(c_{200}\ d^2_{00} + 2c_{220}\ d^2_{02}\cos 2\gamma)/kT;$$

$$b = -(2c_{220}\ d^2_{00} + 4c_{222}\ d^2_{02}\cos 2\gamma)/kT;$$

and c_{Lmn} are expansion coefficients.

A simple case results when the molecules are interacting via dispersion forces. c_{220} is then given by the geometric mean approximation

$$c_{220} = \sqrt{c_{222}c_{200}}$$

Defining $\lambda = \dfrac{c_{220}}{c_{200}}$ which is a measure of deviation from cylindrical symmetry and substituting in above equations for a and b we get

$$a = -\alpha[\langle d^2_{00}\rangle + 2\lambda\ d^2_{02}\cos 2\gamma]$$

$$b = 2\lambda a$$

where $\alpha = -c_{200}/kT$; On substituting for a, b, λ and α in Eqn.(1.3.1) and expressing in terms of above R^L_{mn} we get the simplest rotationally invariant attractive pair potential in the dispersion approximation as [22]

$$U = -\epsilon_{ij}\{P_2(\cos(\beta_{ij})) + 2\lambda[R^2_{02}(\omega_{ij}) + R^2_{20}(\omega_{ij})] + 4\lambda^2 R^2_{22}(\omega_{ij})\} \tag{1.3.2}$$

This λ will be referred to as λ_Z in our subsequent discussion of dispersion model, in order to introduce consistency of notation with reference to the discussion on the generalized mean filed model, which has a interaction parameter λ.

1.3.2 A Generalized Mean Field Model

This model is proposed by Sonnet $et\ al$ [18] and developed in a series of papers by various authors [34, 36–40]. It is a model which builds on a more general theory, originally proposed by Straley [19]. He proposed a mean field model for interacting particles lacking an

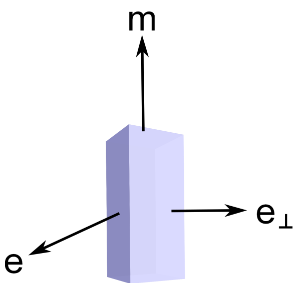

Figure 1.1: Schematic of a biaxial molecule

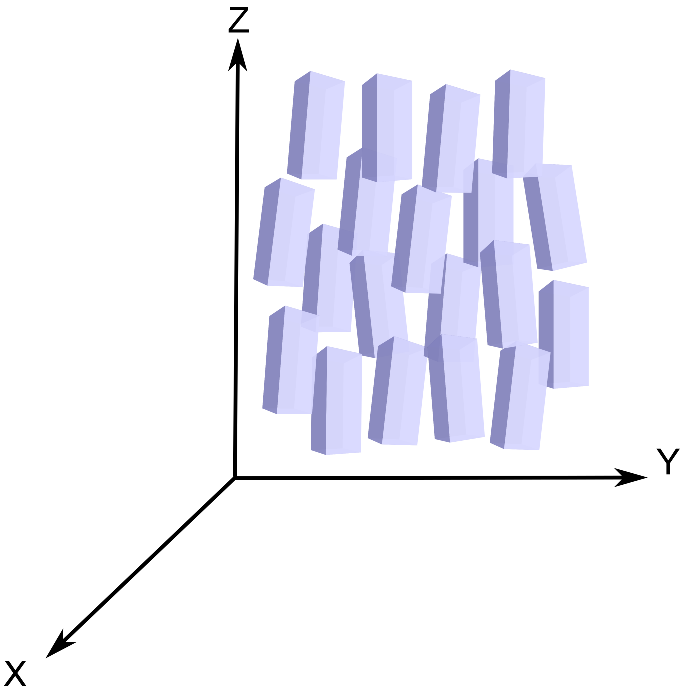

Figure 1.2: Schematic of a biaxial phase

axis of rotational symmetry using four order parameters, instead of the conventional two order parameters.

In this model, a biaxial molecule is schematically represented as a platelet, in an eigen frame $(\boldsymbol{e}, \boldsymbol{e}_\perp, \boldsymbol{m})$ where $\boldsymbol{m}$ is the major axis, $\boldsymbol{e}$ and $\boldsymbol{e}_\perp$ are the minor axes. $(\boldsymbol{e}, \boldsymbol{e}_\perp, \boldsymbol{m})$ can be thought of as the eigen vectors of any molecular polarizability tensor.

A schematic of the molecule and the biaxial phase is shown in Figs. 1.1 and 1.2. Each molecule can be described in terms of two orthogonal traceless tensors $\boldsymbol{q}$ and $\boldsymbol{b}$ defined as

$$\boldsymbol{q} = \boldsymbol{m} \otimes \boldsymbol{m} - \frac{\boldsymbol{I}}{3};$$

$$\boldsymbol{b} = \boldsymbol{e} \otimes \boldsymbol{e} - \boldsymbol{e}_\perp \otimes \boldsymbol{e}_\perp;$$

The tensor $\boldsymbol{q}$ is uniaxial around $\boldsymbol{m}$ and has two equal eigen values. The tensor $\boldsymbol{b}$ is biaxial and has three unequal eigen values. If $\boldsymbol{m}$ is assumed to be the long molecular axis, then $\boldsymbol{q}$ represents a uniaxial tensor describing the dominant geometric feature of the molecules, while tensor $\boldsymbol{b}$ represents their biaxiality. A biaxial molecule can then be fully described by the pair ($\boldsymbol{q}, \boldsymbol{b}$), representing the uniaxial and biaxial components. The orientational interaction energy between any two biaxial molecules represented by $(\boldsymbol{q}, \boldsymbol{b})$ and $(\boldsymbol{q}', \boldsymbol{b}')$ can be written as

$$U = U_0[\xi \boldsymbol{q} \cdot \boldsymbol{q}^{'} + \gamma(\boldsymbol{q} \cdot \boldsymbol{b}^{'} + \boldsymbol{q}^{'} \cdot \boldsymbol{b}) + \lambda(\boldsymbol{b} \cdot \boldsymbol{b}^{'}] \tag{1.3.3}$$

where U_0= scaling energy, ξ = ± 1, and γ and λ are dimensionless interaction parameters, whose values determine the relative importance of the uniaxial-biaxial coupling and biaxial-biaxial coupling interactions between the molecules.

The above interaction can be understood in terms of an electrostatic model for the biaxial molecule. The anisotropic part of dielctric polarizability tensor can be assumed to be composed of uniaxial and biaxial components with different polarisabilities. The fluctuating dipole on one molecule interacts with the corresponding dipole on the other molecule, resulting in more than one molecular absorption frequency. In other words a biaxial molecule can be thought of as composed of three independent orthogonal oscillators.

It can be noted that the interaction reduces to that of Maier-Saupe when both γ=λ=0, representing a uniaxial coupling between the molecules. When either γ or λ differ from zero, the biaxial components contribute to the total interaction. When λ=γ^2 Eqn.(1.3.3) reduces to

$$U = -U_0(\boldsymbol{q} + \gamma \boldsymbol{b}) \cdot (\boldsymbol{q}^{'} + \gamma \boldsymbol{b}^{'}) \tag{1.3.4}$$

which can be interpreted in terms of the London dispersion approximation. Eqn.(1.3.4) is the interaction energy as proposed by Luckhurst $et\ al$ [22] for the case of dispersion interactions. Thus the interaction energy in Eqn.(1.3.3) which includes a uniaxial-biaxial coupling and a biaxial-biaxial coupling in addition to the uniaxial-uniaxial coupling represents a generalized interaction Hamiltonian. It attains its absolute minimum when the

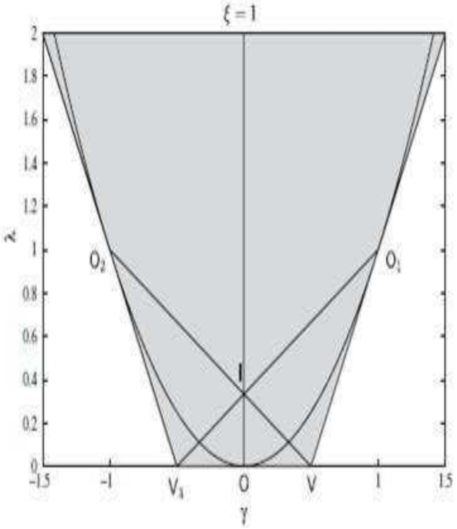

Figure 1.3: The domain of stability for the interaction Hamiltonian in the plane ξ=1: G. De Matteis *et al*, *Continuum Mech. Thermodyn.* **19** 1-23 (2007)

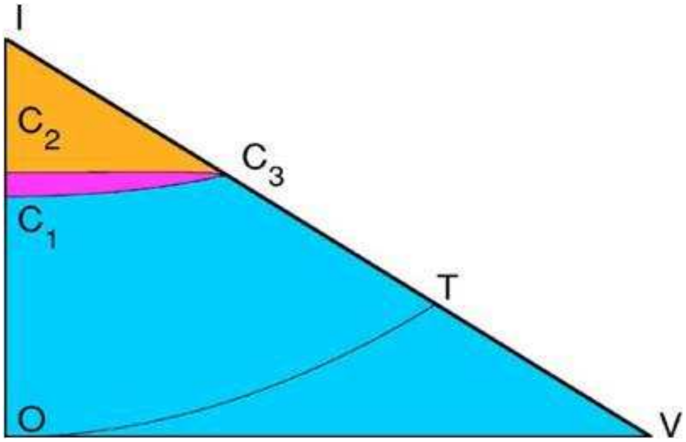

Figure 1.4: Essential triangle OIV: C_1 and C_3 are tricritical points. C_2 is a triple point. The dispersion parabola meets the side IV at the point T, the Landau point: F. Bisi *et al*, *Phys. Rev. E* **73** 051709 (2006).

molecular vectors $(\boldsymbol{e}, \boldsymbol{e}_{\perp}, \boldsymbol{m})$ and $(\boldsymbol{e}', \boldsymbol{e}'_{\perp}, \boldsymbol{m}')$ coincide i.e when $\boldsymbol{q} = \boldsymbol{q}'$ and $\boldsymbol{b} = \boldsymbol{b}'$. This ground stability condition restricts the admissible values of the parameters γ, λ to

$$\lambda > 0;\ \xi - |2\gamma| + \lambda > 0$$

which is a fan shaped region for $\xi\ = +1$ and an angular region for $\xi\ = -1$ in the (γ, λ) plane. Due to the repulsive nature of the $\boldsymbol{q}$-$\boldsymbol{q}'$ interaction, the angular region is included in the fan shaped region, shown in Fig1.3. The corresponding restoring torque is uniaxial about $\boldsymbol{e}$, $\boldsymbol{e}_{\perp}$,$\boldsymbol{m}$ along three straight lines O_2V, O_1V_3 and OI respectively inside the fan shaped region.These are defined by

$$1 - 2\gamma - 3\lambda = 0;\ \ 1 + 2\gamma - 3\lambda = 0;\ \ \gamma = 0$$

respectively. These lines intersect at the point $I = (0, \frac{1}{3})$.

On extending the local stability analysis to other critical points of H and further applying permutation symmetries it is concluded that there exists a triangular region OIV in the (γ, λ) plane which represents the whole domain of stability of H. All choices of model parameters can be reproduced by suitable permutation of the molecular axes within the triangular region, which is aptly called the Essential Triangle [39,40], shown in Fig.1.4. The sides OI and IV form part of the uniaxial torque lines and thus exhibit D_{4h} invariance of the pair-wise interaction in addition to the D_{2h} invariance exhibited by H everywhere inside the triangle. The dispersion parabola $\lambda = \gamma^2$ intersects the Essential Triangle at the point T.

In the mean field treatment, an ensemble of biaxial molecules is considered, within which the orientation $\omega = (\alpha, \beta, \gamma)$ of each molecule is specified with respect to a fixed reference frame $(\boldsymbol{E}_x, \boldsymbol{E}_y, \boldsymbol{E}_z)$ such that

$$\boldsymbol{m} = \cos\alpha\sin\beta\boldsymbol{E}_x + \sin\alpha\sin\beta\boldsymbol{E}_y + \cos\beta\boldsymbol{E}_z; \tag{1.3.5a}$$

$$\boldsymbol{e} = (\cos\gamma\cos\alpha\cos\beta - \sin\gamma\sin\alpha)\boldsymbol{E}_x + (\cos\gamma\sin\alpha\cos\beta\beta + \sin\gamma\cos\alpha)\boldsymbol{E}_y - \cos\gamma\sin\beta\boldsymbol{E}_z; \tag{1.3.5b}$$

$$\boldsymbol{e}_{\perp} = -(\sin\gamma\cos\alpha\cos\beta + \cos\gamma\sin\alpha)\boldsymbol{E}_x - (\sin\gamma\sin\alpha\cos\beta - \cos\gamma\cos\alpha)\boldsymbol{E}_y + \sin\gamma\sin\beta\boldsymbol{E}_z; \tag{1.3.5c}$$

Macroscopically the liquid crystal phase is described by the order parameters introduced by Straley [19] which are represented by two independent second rank tensors $\boldsymbol{Q}$ and $\boldsymbol{B}$ defined as the ensemble averages of $\boldsymbol{q}$ and $\boldsymbol{b}$. Assuming that they have a same eigen frame $(\boldsymbol{E}_x, \boldsymbol{E}_y, \boldsymbol{E}_z)$ in the absence of any external distorting cause, they can be represented as

$$\boldsymbol{Q} = \langle \boldsymbol{q} \rangle = S(\boldsymbol{E}_z \otimes \boldsymbol{E}_z - \frac{\boldsymbol{I}}{3}) + T(\boldsymbol{E}_x \otimes \boldsymbol{E}_x - \boldsymbol{E}_y \otimes \boldsymbol{E}_y); \quad (1.3.6a)$$

$$B = \langle \boldsymbol{b} \rangle = S^{'}(\boldsymbol{E}_z \otimes \boldsymbol{E}_z - \frac{\boldsymbol{I}}{3}) + T^{'}(\boldsymbol{E}_x \otimes \boldsymbol{E}_x - \boldsymbol{E}_y \otimes \boldsymbol{E}_y); \quad (1.3.6b)$$

where $S, T, S^{'}, T^{'}$ are the order parameters of the system. $\boldsymbol{Q}$ represents the average quadrupolar distribution of the long molecular axis. Its degree of biaxiality measured by T reflects the lack of axial symmetry of the orientational distribution function. $\boldsymbol{B}$ represents the macroscopic manifestation of the intrinsic molecular biaxiality of the molecules and the role it plays in the molecular interaction. Its uniaxial and biaxial components are described by the scalar order parameters $S^{'}$ and $T^{'}$. When these two tensors are employed, a uniaxial phase occurs whenever both $\boldsymbol{Q}$ and $\boldsymbol{B}$ are uniaxial i.e when $T = T^{'}$=0. A general biaxial state is described by all four scalar order parameters. An extrinsic biaxial phase exhibited by cylindrically symmetric molecules is represented by single tensor $\boldsymbol{Q}$.

In the notation employed in the above section,the relation between the order parameters is

$$S^{'} = D, T = \frac{1}{3}P, \ T^{'} = \frac{1}{3}C$$

the uniaxial parameter S being the same. In the mean field approximation adopted in ref [18] a single molecule experiences a pseudo potential

$$U(\boldsymbol{q}, \boldsymbol{b}) = -U_0[\xi \boldsymbol{Q} \cdot \boldsymbol{q} + \gamma(\boldsymbol{Q} \cdot \boldsymbol{b} + \boldsymbol{B} \cdot \boldsymbol{q}) + \lambda \boldsymbol{B} \cdot \boldsymbol{b}]. \quad (1.3.7)$$

The partition function *Z* [37] given by

$$Z(\boldsymbol{Q}, \boldsymbol{B}, \beta, \lambda, \gamma) = \int_T exp(\beta[\xi \boldsymbol{Q} \cdot \boldsymbol{q} + \gamma(\boldsymbol{Q} \cdot \boldsymbol{b} + \boldsymbol{B} \cdot \boldsymbol{q}) + \lambda \boldsymbol{B} \cdot \boldsymbol{b}]). \quad (1.3.8)$$

and the free energy *F* is

$$F(\boldsymbol{Q}, \boldsymbol{B}, \beta, \lambda, \gamma) = U_0\{\frac{1}{2}\boldsymbol{Q} \cdot \boldsymbol{Q} + \gamma \boldsymbol{Q} \cdot \boldsymbol{B} + \frac{\lambda}{2}\boldsymbol{B} \cdot \boldsymbol{B} - \frac{1}{\beta} ln(\frac{Z}{8\pi^2}) \quad (1.3.9)$$

where T is the manifold described by all possible molecular orientations $(\boldsymbol{e}, \boldsymbol{e}_\perp, \boldsymbol{m})$, $\beta = \frac{U_0}{k_B t}$, k_B is the Boltzmann constant and t is the absolute temperature.

The analysis of this free energy function for tricriticality [37] predicts a second tricritical point in addition to the tricritical point already predicted for the case when γ=0 by Sonnet $et\ al$ [18]. Application of bifurcation analysis [38] to the consistency conditions for the order parameters confirmed the presence of the second tricritical point.

The quadratic Hamiltonian in Eqn(1.3.3) can be diagonalized [39] and can be written as the superposition of two quadratic components as

$$H = -U(a^+\boldsymbol{q}^+ \cdot \boldsymbol{q}^{+'} + a^-\boldsymbol{q}^- \cdot \boldsymbol{q}^{-'})$$

where $\boldsymbol{q}^+$ and $\boldsymbol{q}^-$ orthogonal molecular tensors are represented as

$$\boldsymbol{q}^\pm = \boldsymbol{q} + \gamma^\pm \boldsymbol{b}$$

with

$$\gamma^\pm = \frac{3\lambda - 1 \pm \sqrt{(3\lambda - 1)^2 + 12\gamma^2}}{6\gamma}$$

$$a^+ = \frac{\gamma^- - \gamma}{\gamma^- - \gamma^+}$$

and

$$a^- = \frac{\gamma - \gamma^+}{\gamma^- - \gamma^+}$$

For

$$\gamma = 0, \boldsymbol{q}^+ = q, \boldsymbol{q}^- = b; \frac{a^-}{a^+} = \lambda$$

Whenever $\lambda > \gamma^2$ the quadratic components are attractive and when $\lambda < \gamma^2$ one of them turns repulsive. Thus it can be concluded that H is fully attractive when $\lambda > \gamma^2$ and partly repulsive when

$$\lambda > 0; \;\; \lambda < \gamma^2; \;\; \lambda - |2\gamma| + 1 > 0;$$

The dispersion parabola thus forms the boundary between the regions where the Hamiltonian is eitheer fully attractive or partly repulsive. For the fully attractive Hamiltonian,the associated free energy is minimised with respect to four scalar order parameters, whereas

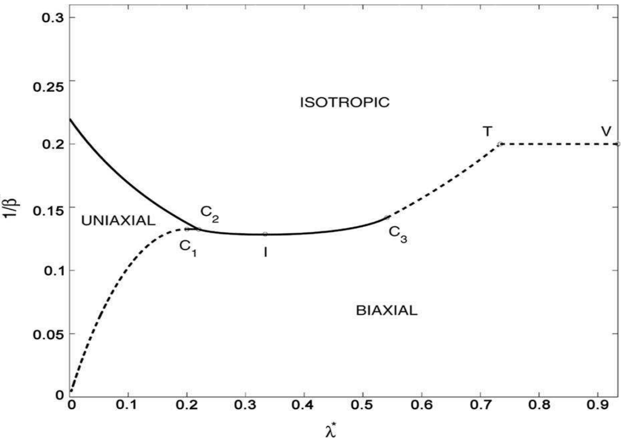

Figure 1.5: Mean field phase diagram along the upper boundary OIV of the essential triangle. The scaled transition temperature $1/\beta^*$ is plotted as function of the interaction parameter λ^*. Solid lines represent first order transitions. Broken lines represent second order transitions: G. De Matteis $et\ al$, *Continuum Mech. Thermodyn.* **19** 1-23 (2007).

for the partly repulsive Hamiltonian the stationary points of the free energy are calculated which are in fact its saddle points. There the free energy has maxima with respect to two scalar variables and minima with respect to two others. The phase sequences predicted by the associated free energy using numerical bifurcation and continuation analysis of the stationary points of free energy lead to the prediction of a universal mean field phase diagram [39], as function of arclength OIV of the essential triangle. A further constrained stability analysis of the mean field free energy in the reduction classes for the order parameters revealed a sequence of triple points in the repulsive region [40]. The phase diagram obtained from the above mean field analysis is shown in Fig.1.5.

1.4 Phenomenological Theories of Biaxial Nematic Phase

Recent experimental interest in the thermotropic biaxial nematic phase after its discovery in bent-core systems and tetrapodes has led to the renewed theoretical interest in the biaxial phase. The topological properties of the phase diagrams of liquid crystals with achiral molecules were studied for transitions from isotropic to uniaxial and biaxial phases using LDG theory [41].The stability of the biaxial nematic phase was reexamined and analytical solutions for all the distinct classes of the allowed phase diagrams were presented [42].

In view of the generalized mean field theory (described in the previous section) which considered the two major order tensors, a phenomenological Landau potential in the two macroscopic order tensors has been proposed by the authors [43] to describe the various phases predicted by the universal mean field phase diagram. In a very recent paper [44], a molecular field theory approach has been adopted to the Landau theory of uniaxial and biaxial nematics. The magnitude of the coefficients in the Landau expansion was related to the molecular biaxial parameters which occur in molecular field theories.

1.5 Models Studied

Computer simulation studies of liquid crystals have played a crucial role in confirming the theoretical predictions concerning the phase transitions behaviour, bulk physical properties and response to external stimuli. Molecular level simulations complement the observed experimental behaviour and act as bridge between the theoretical predictions and the macroscopic world of the Laboratory [45, 46]. Generic models have been developed to simulate liquid crystal bulk behaviour based on mean field and phenomenological theories. Nematic phases can be simulated using lattice spin models [25], off lattice hard particle models [47] and soft particle models where Gay-Berne potential is used.The Gay-Berne model is a more realistic model since translational degrees of freedom are incorporated along with orientational degrees of freedom. However the computational costs are high and hence only small systems can be simulated. This restriction can be overcome with lattice spin models where the (classical)spins are fixed on lattice sites and possess only orientational degrees of freedom. These are highly configurable and suitable choice of inter-site potential led to the simulation of biaxial liquid crystals, LC dimers, LC mixtures ,and LC ordering in aerogels etc [48, 49].

In this thesis lattice spin models have been employed to simulate bulk uniaxial and biaxial nematic phases and also the effect of confinement on their behaviour.

1.5.1 Lebwohl-Lasher Model

The earliest and most widely used lattice spin model for study of uniaxial nematics is the Lebowhl-Lasher model [50]. The molecules (or a cluster of molecules) are represented by vectors (or 3 dimensional spins) on a cubic lattice of dimensions $L \times L \times L$ and are assumed to have uniaxial symmetry. Interactions are restricted only to the nearest neighbours, and the potential between two such spins located at i and j is given by

$$U_{ij} = -\epsilon P_2(cos\theta_{ij}). \tag{1.5.1}$$

where ϵ_{ij} is a positive constant ($= \epsilon$) for nearest neighbours and zero otherwise, θ_{ij} is the angle between the spins and $P_2(\cos\theta_{ij})$ is the Legendre Polynomial. The energy is minimised when the angle between the spins is 0° or 180°. Starting from a random configuration of spins which indicate the isotropic phase of the liquid crystal, the spins orient parallel or antiparallel to each other as the temperature is lowered. A sudden jump in the ordering occurs at a weak first order transition at a critical temperature T^*_{NI} and the amount of order can be measured by the order parameter $S = P_2(\cos\theta)$ in the nematic phase. The transition temperature can be estimated accurately with this model.

1.5.2 Dispersion Model

This lattice model is used to simulate a biaxial liquid crystal and is based on the interaction potential proposed by Luckhurst *et al* [22, 51–53] for biaxiality exhibited by noncylindrically symmetric molecules, in the dispersion approximation. The biaxial particles on a three dimensional lattice interact through an attractive pair potential of the form

$$H = -\epsilon_{ij}\{P_2(\cos(\beta_{ij})) + 2\lambda_Z[R^2_{02}(\omega_{ij}) + R^2_{20}(\omega_{ij})] + 4\lambda^2_Z R^2_{22}(\omega_{ij})\}. \tag{1.5.2}$$

Here, $\omega(\alpha, \beta, \gamma)$ is the set of Euler angles specifying the orientation of the molecule, and ω_{ij} represents the relative orientation of the $ijth$ pair of molecules. R^L_{mn} are combinations of Wigner functions, symmetry-adapted for the D_{2h} group of the two interacting particles. ϵ_{ij} is the strength of interaction between the molecules, which sets the scale of the energy.

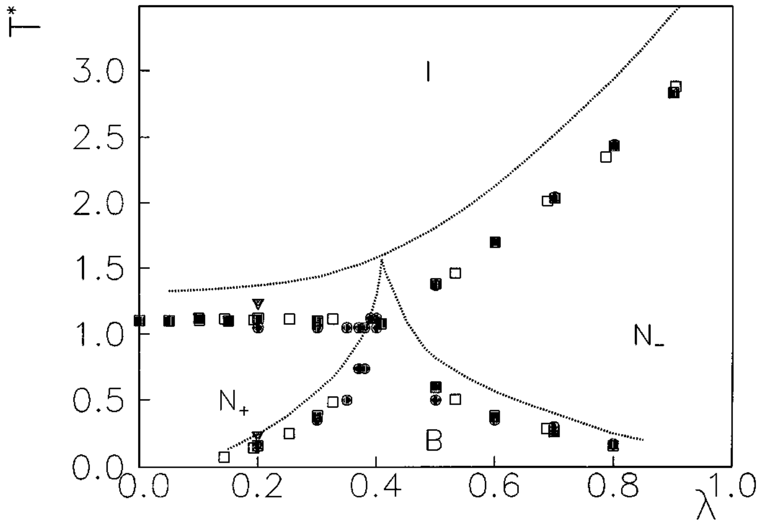

Figure 1.6: Phase diagram obtained from canonical Monte Carlo simulations along the dispersion parabola of the essential triangle. The scaled transition temperature T^* is plotted as function of the interaction parameter λ (λ_Z). Solid lines represent mean-field results and symbols represent MC results: F. Biscarini $et\ al$,*Phys. rev. Lett.***75**, 1803 (1995)

The biaxiality parameter λ_Z measures the amount of deviation from cylindrical symmetry. When λ_Z=0, the potential reduces to the well known Lebhowl-Lasher potential for uniaxial molecules [50] while for $\lambda_Z \neq 0$ the molecules not only align their major axis but also their faces. The value $\lambda_Z = \frac{1}{\sqrt{6}}$ forms the boundary between a system of prolate ($\lambda_Z < \frac{1}{\sqrt{6}}$) and oblate ($\lambda_Z > \frac{1}{\sqrt{6}}$) molecules.

The above expression is conveniently recast as a function of inner products of different vectors specifying the orientations of different molecules (x_i, y_i, z_i) with those of the chosen laboratory frame, and is expressed as [54]

$$U_{ij} = -\epsilon\{\frac{3}{2}V_{33} - \sqrt{6}\lambda_Z(V_{11} - V_{22}) + \lambda_Z^2(V_{11} + V_{22} - V_{12} - V_{21}) - \frac{1}{2}\} \qquad (1.5.3)$$

Here $V_{ab} = (u_a.v_b)^2$, and the unit vectors u_a, v_b, $[a, b = 1, 2, 3]$, are the three axes of the two interacting neighbouring molecules.

Monte Carlo simulations of this biaxial lattice model for various values of biaxiality parameter λ_Z [25, 54], shown in Fig.1.6, confirmed the predicted mean field phase diagram [19, 21]. On cooling from a isotropic phase, a biaxial fluid undergoes a first order isotropic-uniaxial nematic phase transition at a higher temperature followed by a second order uniaxial-biaxial transition at a lower temperature. Depending on the biaxility parameter, prolate or oblate uniaxial phases are formed. However, at a limiting value of $\lambda_Z = \dfrac{1}{\sqrt{6}}$ a direct second order isotropic-biaxial phase transition takes place. This value of λ_Z marks the cross-over region between the prolate and oblate uniaxial phases. This point is denoted as a Landau bicritical point or a Landau triple point. The MC estimate of the uniaxial-biaxial transition temperature is found to be lower than the predicted mean field value.

1.5.3 General Hamiltonian in Cartesian Coordinates

The two parameter general lattice model can be described in terms of Legendre polynomials involving the three angles between the corresponding molecular axes, as proposed in [55]. Simple geometric identities are used to specify the interaction between identical particles of D_{2h} symmetry associated with a three-dimensional simple cubic lattice. The orientation of each particle is specified by an orthonormal triplet of 3-component vectors $(\omega_{\lambda\mu}$ where ω_λ= $(\phi_\lambda, \theta_\lambda, \psi_\lambda)$ are an ordered triplet of Euler angles [56]. Here the orientations be defined with respect to an arbitrary Cartesian frame. The two interacting particles on neighbouring sites j and k are labelled as(using simpler notation) v_j and u_k. Let the set of Euler angles $\Omega = \Omega_{\mu\nu}$ define the rotation transforming u_j into v_j. A transformation f_{jk} is defined as

$$f_{jk} = (v_j.u_k), G_{jk} = P_2(f_{jk})$$

where $P_2(...)$ denotes second Legendre polynomial. The continuous interaction potential proposed by Sonnet et al [18] can be reset using appropriate linear combinations of the terms G_{jk} as

$$U = -\epsilon\{G_{33} - 2\gamma(G_{11} - G_{22}) + \lambda[2(G_{11} + G_{22}) - G_{33}]\}. \tag{1.5.4}$$

where $G_{ll}$are defined with respect to the director frame, ϵ is a positive quantity setting the reduced temperature scale $T^{'}$=K_BT/ϵ in the simulation. $|\gamma|$ and $|\lambda|$ are dimensionless quantities, which are smaller than one. Since a simple cubic lattice with coordination number 6 has been used here, the above pair potential differs from the generalised mean field potential in eqn(1.3.3) by a factor of $\frac{3}{2}$. The reduced temperature then differs from the mean field reduced temperature by a factor of 9 [57].

when $|\gamma| = 0$ and $|\lambda| = 0$, Eqn.(1.5.4) reduces to the well known and extensively studied Lewbowhl-Lasher (LL) model. Simulation results suggest that when $|\gamma| \neq 0$ and $|\lambda| = 0$, biaxial order disappears in the system [51]. When $\gamma \propto \lambda^2$ the special case of dispersion model can be obtained from the above equation. The parameter λ_Z appearing in the dispersion model and the present γ appearing in this model are related as

$$\lambda_Z = \sqrt{\frac{3}{2}}\,\gamma.$$

This model has been extensively used in our simulation studies of the universal mean field phase diagram.

1.6 Review of Experiments

The ongoing quest for a stable thermotropic biaxial nematic phase has been aptly named 'the holy grail' of liquid crystal research [58] since the prediction of the phase nearly 40 years ago by Freiser [20]. The intense search has led to a development of experimental, theoretical and computational techniques in order to synthesize and characterise the phase.

The experimental detection of biaxial phase is based on the fact that three principal components of any second rank tensorial property of the nematic are different. Several experimental techniques were developed in the last few years to detect biaxial order arising from molecular biaxiality in liquid crystalline phases. Polarized optical microscopy and conoscopy readily provide indications of biaxial ordering in the system. A uniaxial nematic is identified by Schliern texture showing four-brush disclinations whereas a biaxial nematic has two-brush disclinations. A conoscopic observation of the sample detects birefringence. In this method, an interference pattern is obtained giving two dark lines called isogyres. The isogyres form a cross for a uniaxial nematic whereas they open up for a biaxial nematic.

Deuterium NMR methods involving either directly deuteriated nematic molecules or deuteriated probe molecules are widely used for the determination of biaxiality in bulk nematic samples, the main advantage being that biaxiality due to surface alignment is ruled out. However,the possibility of induced biaxiality due to strong applied magnetic field or sample spinning is present. The small amount of transversal orientational ordering is hard to detect as effects due to surface anchoring cannot be ruled out.

Experimentally the biaxial phase was first obtained in a lyotropic, ternary mixture of potassium laurate, 1-Decanol and D_2O in 1980 [59]. Initial approaches to the design of biaxial molecules were based on high shape biaxiality in line with the theoretical predictions, which predict a biaxial phase in broadest temperature range when the shape biaxiality $\lambda_Z \simeq (1/\sqrt{6})$ [21, 23], supported by simulations [25]. This corresponds to a length: breadth: width ratio of $5 : 3 : 1$. Assuming the average width of molecules to be $W = 0.45nm$, the molecular length and breadth should be $2.2nm$ and $1.3nm$ respectively, which translates to a significant size of molecule. A small change from this optimal ratio leads to the formation of uniaxial phase of rods (N_{U+}) or discs (N_{U-}). Conoscopy and optical texture were used for characterisation of molecules synthesized with the above criteria [60–62]. However these claims were questioned with NMR spectroscopy [63]. Another problem associated with large rigid molecules which do not exactly fit the $\lambda_Z = 1/\sqrt{6}$ criterion is crystallization into a smectic phase before the N_B phase is formed.

Mixtures of rods and disk-like LC molecules were considered as candidates for the formation of the N_B phase [21], in which the molecular symmetries would permit the individual self alignment of rods and discs in mutually perpendicular directions. However experimentally such mixtures tended to demix into two uniaxial phases, one rich in rods and other rich in discs [64]. Though recent experiments [65, 66] point to low transition enthalpies for such rod-disc systems, an unambiguous biaxial phase has not been reported in such systems.

According to theoretical predictions [63, 67, 68], macroscopic biaxiality could also be achieved through a bend in the molecular shape through an angle α. A direct $I - N_B$ transition is predicted when the bending angle α is close ($\pm 1 - 2^\circ$) to the tetrahedral angle 109°. Most of the known bent-core mesogens prefer formation of smectic or modulated smectic phases rather than a nematic phase [69]. However more recently the thermotropic biaxial nematic phase was discovered in rigid bent core mesogens based on mesogenic oxidiazole core with apex angle $\sim 140^\circ$ [70], which was further characterised by X-ray diffraction [71], polarized microscopy, conoscopy and deuterium NMR spectroscopy [72]. The biaxial nematic phase was found to occur at a high temperature range of $\sim 200^\circ$. Subsequently, polarized Raman spectroscopy was used to estimate the order parameters in the uniaxial and biaxial phases of bent-core ODBP mesogens [73, 74]. Polarising optical microscopy found evidence of a reversible $N_U - N_B$ transition in a quiscent melt of bent-core mesogens [75].

The evidence of thermotropic biaxial nematic phase has also been found in liquid crystalline organosiloxane tetrapodes using infrared absorbance measurements [76], deuterium NMR [77], dynamic light scattering methods [78]. Biaxiality was also confirmed in LC polymers [79], after the prediction of the phase in polymer systems [80] The biaxial nematic and biaxial smectic phases were found recently in colloidal systems of Goethic particles with simple board like shape and short range repulsive interaction [81].

Among the various type of molecules which exhibit the biaxial nematic phase, bent-core molecules appear to the contenders for use in fast switching optical devices. A major setback in the experimental field appears to be the lack of consistency in experimental findings. A recent report suggests that application of electro-optic techniques to a the compound A131 (reported to be biaxial based on small angle X-ray diifraction and Deuterium NMR method) has proved that the compound is uniaxial in the entire nematic range [82]. Application of the same technique to another bent-core compound C_6- BAN [83] has shown that the macroscopic biaxiality exhibited is induced by the electric field and points to the presence of biaxial clusters in a macroscopically uniaxial nematic phase. Another recent structure study of bent-core compounds suggests that the low-angle X-ray diffraction pattern used to characterise a biaxial phase is due to Smectic-C fluctuations ('cybotactic' groups) in the uniaxial nematic phase. As per more recent study, surface effects and anchoring transitions sometimes lead to a false positive identification of a uniaxial-biaxial phase transition [84]. A summary of the existing experimental techniques and design of materials [85,86] can be found in a recent review [69]. Achieving spontaneous, observable macroscopic biaxiality in nematic liquid crystal phases before transition to higher ordered phases or crystallization seems to be rather difficult.

The ongoing quest for a thermodynamically stable biaxial nematic phase is also fuelled by the possibility of potential application in liquid crystal display devices. Recently it was found that [87] on the application of an electric field, the switching of a minor director is faster compared to the major director. The possible in-plane switching of the minor director is hoped to lead to faster response times.

Bibliography

[1] G. Freidel, *Ann. Physique* **18**, 273 (1922).

[2] G. Vertogen and W. H. de Jeu,*Thermotropic Liquid Crystal Fundamentals*, Springer-Verlag, Berlin, 1988.

[3] N. V. madhusudana,*Theories of liquid crystals*, in: B.Bahadur (Ed.), *Liquid Crystals: Apllications and Uses*, Vol 1, world Scientific, Singapore, 1990, p.37 (chapter2).

[4] S. Chandrasekhar. *Liquid Crystals*. Cambridge University Press, 2nd edition, January 29, 1993.

[5] Peter. J. Collings and Michael Hird,*Introduction to Liquid Crystals Chemistry and Physics*, Taylor& Francis, 1997.

[6] Ronald. Y. Dong,*Nuclear magnetic resonance of Liquid Crystals*, 2nd Ed., Springer-Verlag, 1997.

[7] D. Demus,J. W. Goodby,G. W. Gray,H. W. Spiess and V. Vill(ed.),*Handbook of Liquid Crystals*, Wiley-VCH, Weinheim, 1998.

[8] M. J. Escuti, Jun Qi and G. P. Crawford,*Appl. Phys. Lett.***83**, 1331 (2003).

[9] S. J. Woltman, G. D. jay and G. P. Crawford,*Nat. Mater.* **6**, 929 (2007).

[10] G. R. Luckhurst and G. W. Gray (Eds.), *The Molecular Physics of Liquid Crystals*, Acad. Preaa, new York, 1979.

[11] Dunmur. D, Fukuda. A. Luckhurst. G. R. (Eds.) *Physical Properties of Liquid Crystals*, 2001, London, UK: Institute of Electrical Engineers.

[12] P. G. De Gennes and J. Prost.*The Physics of Liquid Crystals*, 2nd ed, Clarendon, Oxford, 1993.

[13] L. Onsagar,*Ann. N. Y. Acad. Sci.* **51**, 627 (1949).

[14] M. A. Cotter,*J. Chem. Phys.* **66**, 4710 (1977).

[15] W. M. Gelbart and B. A. Baron,*J. Chem. Phys.* **66**, 207 (1977).

[16] L. D. Landau and E. M. Lifshitz, *Statistical physics,* 2nd Ed., Pergamon, Oxford, 1969.

[17] P. G. De Gennes, *Mol. Cryst. Liq. Cryst.* **12**, 193 (1971).

[18] A. M. Sonnet, E. G. Virga, G. E. Durand ,*Phys. Rev. E.* **67***,* 061701 (2003).

[19] J. P. Straley, *Phys. Rev. A* **10**, 1881 (1974).

[20] M. J. Freiser. *Phys. Rev. Lett.***24**, 1041 (1970).

[21] R. Alben, *Phy. Rev. Lett.***30**, 17, 778 (1973).

[22] G. R. Luckhurst, C. Zannoni, P. L. Nordio and U. Segre, *Mol. Phys.* **30**, 1345 (1975).

[23] N. Bocara, R. Mejdani and L. de Seze,**J. de. Phys. 7**, 149 (1977).

[24] D. K. Remler and A. D. J. Haymet, *J. Phys. Chem.* **90**, 5426 (1986).

[25] F. Biscarini, C. Chiccoli, P. Pasini, F. Semeria and C. Zannoni. *Phys. Rev. Lett.***75**, 1803(1995).

[26] D. W. Allender and M.A.Lee, *Mol. Cryst. Liq. Cryst.* **110**, 331 (1984).

[27] E. F. Gramsbergen, L. Longa and W. De Jeu, *Phys. Rep.* **135**, 195 (1986).

[28] P. K. Mukherjee, *J. Chem. Phys.* **109**, 2941 (1998).

[29] Z. H. Wang, P. H. Keyes, *Phy. Rev. E* **54(5)**, 5249 (1996).

[30] S. singh, *Phys. rep.* **324**, 107 (2000).

[31] C. Zannoni, *The Molecular Dynamics of Liquid Crystals*, G. R. Luckhurst and C. A. Veracini, (Eds.), Kluwer, pages 11-36 (1994).

[32] V Tsvetkov *Acta Physicoch USSR* **10**, p557 (1939).

[33] Bela Mulder, *Phys. Rev. A* **39**, 360 (1989).

[34] F. Bisi, G. R. Luckhurst, E. G. Virga, *Phy. Rev. E*, **78**, 021710 (2008).

[35] R. Rosso, *Liq. Cryst.* **34**, 737 (2007).

[36] Lech Longa, P. Grzybowski, S. Romano and E. Virga, Phy. Rev. E **71**, 051714 (2005).

[37] G. De Matteis and E. G. Virga, *Phys. Rev. E* **71** 061703 (2005).

[38] G. De Matteis, S. Romano, and E. G. Virga, *Phys. Rev. E* **72** 041706 (2005).

[39] F. Bisi, E. G. Virga, Jr. E. C. Gartland, G. De Matteis, A. M. Sonnet, and G. E. Durand, *Phys. Rev. E* **73** 051709 (2006).

[40] G. De Matteis, F. Bisi and E. G. Virga, *Continuum Mech. Thermodyn.* **19** 1-23 (2007).

[41] A. E. prostakov, E. S. Larin and M. B. Stryukov, *Crystallogr. Rep.* **47**, 1041 (2002).

[42] David Allender, L. Longa, *Phy. Rev. E* **78**, 011704 (2008).

[43] G. De Matteis,A. M. Sonnet and E. G. Virga, *Continuum. Mech. Thermodyn.* **20** 347 (2008).

[44] G. R. Luckhurst, S. Naemura,T. J. Sluckin, Kenneth.S. Thomas and Stefano. S. Turzi,*Phy. Rev. E* **85**,031705(2012).

[45] C. M. Care and D. J. Cleaver, *Reports on Progress in Physics* **68** 2665 (2005).

[46] M. R. Wilson, *Int. Rev. Phys. Chem.* **24** 421 (2005).

[47] M. P. Allen, *Liq. Cryst.* **8** 499 (1990).

[48] M. R. Wilson, *Chem. Soc. Rev.* **36**, 1881 (2007).

[49] R. Berardi, L. Muccioli, S. Orlandi, M. Ricci, C. Zannoni, *J. Phys.: Condens. Matter.*,**20**, 463101.1 (2008).

[50] P. A. Lebwohl and G. Lasher, *Phys. Rev. A* **6**, 426 (1972).

[51] G. R. Luckhurst and S. Romano, *Mol. Phys.* **40** 129 (1980).

[52] R. Hashim, G. R. Luckhurst and S. Romano. *Mol. Phys.* **53**, 1535 (1984).

[53] R. Hashim, G. R. Luckhurst, F. Prata and S. Romano *Liq. Cryst.* **15**, 283 (1993).

[54] C. Chiccoli, P. Pasini, F. Semeria, C. Zannoni, *Int. J. Mod. Phys. C.* **10**,469(1999).

[55] S. Romano, *Physica A* **337**, 505 (2004).

[56] D. M. Brink, G. R. Satchler, *Angular Momentum*, 2nd Ed. , Oxford University Press, Oxford, UK.

[57] F. Bisi, S. Romano, and E. G. Virga, *Phys. Rev. E*, **75**, 041705 (2007).

[58] G. R. Luckhurst, *Nature* **430**, 413 (2004).

[59] L. J. Yu and A. Saupe, *Phy. Rev. Lett.* **45**, 1000 (1980).

[60] K. Praefcke, B. Kohne, B. Gndog Diele, G. Pelzl, and U. Bakowsky, *Mol. Cryst. Liq. Cryst.* **198**, 393 (1991).

[61] S. Chandrasekhar,*Mol. Cryst. Liq. Cryst. Sci. Technol., Sect. A* **243**, 1 (1994).

[62] S. Chandrasekhar, G. G. Nair, D. S. Shankar Rao, S. Krishna Prasad, K. Praefcke, and D. Blunk, *Curr. Sci.* **75**, 1042,(1998).

[63] G. R. Luckhurst, *Thin solid Films* **393**, 40 (2001).

[64] A. Cuetos, A. Galindo and G. Jackson, *Phy. Rev. Lett.* **101**, 237802 (2008)

[65] R. W. Date and G. W. Bruce,*J. Am. Chem. Soc.* **125**, 9012 (2003).

[66] P.H. J. Kouwer and G. H. Mehl, *J. Mater. Chem.* **19**, 1564 (2009).

[67] P. I. C. Teixeira, A. J. Masters and B. M. Mulder, *Mol. Cryst. Liq. Cryst.* **323**, 167 (1998).

[68] P. J. Champ, M. P. Allen and A. J. Masters, *J. Chem. Phys.* **111**, 9871 (1999).

[69] Carsten Tschierske and D. J. Photinos, *J. Mat. Chem.***20**, 4263 (2010).

[70] B. R. Acharya, A. Primak, T. J. Dingemans, E. T. Samulski, and S. Kumar, *Pramana* **61**,231(2003).

[71] B. R. Acharya, A. Primak, and S. Kumar, *Phy, Rev. Lett.* **92**, 1455061 (2004).

[72] L. A. Madsen, T. J. Dingemans, M. Nakata, E. T. samulski, Phy. Rev. Lett, **92**, 145505 (2004).

[73] C. D. Southern, P. D. Brimicombe, S. D. Siemianowski, S. Jaradat, N. Roberts, V. Gortz, J. W. Goodby, H. F. Gleeson, *Euro. Phy. Lett.***82**, 56001 (2008).

[74] Min Sang Park $et\ al$, *Phys. Rev. Lett.* **105**, 027801 (2010).

[75] Joseph Picken $et\ al$, *Liq. Cryst.* **39**, 1, 19(2012).

[76] K. Merkel, A. Kocot, J. K. Vij, R. Korlacki, G. H. Mehl, T. Meyer, *Phys. Rev. Lett.* **93**, 237801 (2004).

[77] J. L. Figueirinhas, C. Cruz, D. Filip, G. Feio, A. C. Ribeiro, Y. Frere, T. Meyer, G. H. Mehl, *Phys. Rev. Lett.* **94**, 107802 (2005).

[78] K. Neupane, S. W. Kang, S. Sharma, D. Carney, T. Meyer, G. H. Mehl, D. W. Allender, Satyendra Kumar, and S. Sprunt, *Phys. Rev. Lett.* **97** 207802 (2006).

[79] K. Severing, K. Saalwachter,*Phy. Rev. Lett.* **92**, 125501 (2004).

[80] F. Hessel and H. Finkelmann, *Polym. Bull.* **15**, 1996, DOI:10.1007/BF00254854.

[81] E. Van den Pol, A. V. Petukhov, D. M. E. Thies-Weesie, D. V. Byelov, G. J. Vroege, *Phys. Rev. Lett* **103**, 258301 (2009).

[82] K. Van Le *et al*, *Phys. Rev. E.* **79**, 030701(R) (2001).

[83] Mamatha Nagaraj, Y. P. Panarin, U. Manna, J. K. Vij, C. Keith and C. Tschierske. *Appl. Phys. Lett.***96**, 0111106 (2010).

[84] T. Ostapenko, C. Zhang, S. N. Sprunt, A. J kli, and J. T. Gleeson, *Phy. Rev. E* **84**, 021705 (2011).

[85] Lori L. Cooper, E. T. Samulski and Eric Scherrer, *Mol. Cryst. Liq. Cryst.* **511**,2003 (2009).

[86] Matthias Lehmann, *Liq. Crys* **38**, 1389 (2011).

[87] J. H. Lee, T. K. Lim, W. T. Kim, and J. I. Jin, *J. Appl. Phys.* **101** 034105 (2007).

Chapter 2

Introduction to Monte Carlo Simulation Methods

2.1 Introduction

Computer simulation studies of physical phenomena can be considered as an independent tool in their own right, complementing the other two established methodologies, namely experimental investigations in the laboratory and theoretical analysis based on physical laws. The advent of fast and affordable computers has led to an exponential increase in scientific investigations using various novel simulation techniques in contemporary research. There are many situations where exact solution of a theoretical model is not feasible, or a particular experimental situation where a necessary spatial/temporal resolution is not achievable. It is in such scenarios that a computer simulation helps in understanding the complex physical system and provide a useful perspective. A simulation can be viewed as a computer based experiment on a generic model, which helps one to assess the range of validity of any approximate analytic work based on the model. On the other hand, it can also bridge the gap in interpreting experiments involving real systems with typically complicated interactions. In general, a computer simulation approach dealing with problems of statistical physics requires the setting up of appropriate molecular models of interest and determination of the equilibrium state of a sufficiently large system of these particles at the chosen external (thermodynamic), like conditions of temperature, pressure etc. by numerical simulation methods [1–5].

The role of computer simulations in liquid crystal research is well established [6].

Simulations enable one to relate the microscopic molecular properties to macroscopic behaviour, to study the spontaneous formation of liquid crystalline phases, and to determine their response to external fields. The many body correlations which exist in a condensed phase, are automatically taken into consideration in a simulation experiment. The advances in the field using hard and soft particle models, molecular and atomistic models is well documented [7–9].

The purpose of a simulation experiment is to measure the macroscopically observed properties which are exhibited by the system under study. These are the expectation values of the physical observables. The average or expectation value can be regarded as a time average over the states that the system passes through or a simple average over a large number of microstates in equilibrium. According to probabilistic view employed in statistical mechanics, the phase space probability density can be used to determine the equilibrium properties which emerge as the averages of physical variables of the stationary probability density. A crucial part of a simulation is the generation of a equilibrium ensemble for the given Hamiltonian of a system, under the chosen equilibrium conditions.

Accordingly, let the probability of a system to be in a state μ be $\omega_\mu(t)$. Defining the transition probability (per unit time) for the system to transit from a state μ to a state ν to be $R(\mu \to \nu)$, the evolution of the probabilities is defined by the following Master equation [1] as

$$\frac{d\omega_\mu}{dt} = \sum_\nu [\omega_\nu(t) R(\nu \to \mu) - \omega_\mu(t) R(\mu \to \nu)]. \tag{2.1.1}$$

The probabilities must naturally obey the rule

$$\sum_\mu \omega_\mu(t) = 1.$$

When the system reaches equilibrium, the left hand side of Eqn.(2.1.1) becomes zero and the evolution of microstates is stationary with time. Any system in equilibrium is governed by transition probabilities obeying Eqn (2.1.1) characterised by a (unique) transition probability matrix R. Development of appropriate microstates for a given Hamiltonian and generation of equilibrium ensembles can be done using two powerful techniques namely, Monte Carlo technique and Molecular Dynamics method [1,6]. In the molecular dynamics method the net force and/or torque acting on each interaction site are used to determine the consequent accelerations. By applying Newton's laws of motion over short and discretized intervals, the evolution of the many-body system can be numerically tracked and consequently the dynamic properties can be calculated along with static equilibrium properties. Monte Carlo methods, on the other hand, use stochastic methods to generate new configurations using importance sampling techniques. In this Thesis we adopt the Monte Carlo technique to simulate biaxial liquid crystal behaviour in bulk and confinement.

2.2 Canonical Monte Carlo Methods

The goal of Monte Carlo simulations is to estimate the expectation value

$$< O >= \frac{\sum_C O(C)exp(-\beta E(C))}{Z(\beta)} \tag{2.2.1}$$

of an observable O defined by the Hamiltonian H at inverse temperature $\beta = \dfrac{1}{k_B T}$ (k_B is the Boltzmann constant, T is the absolute temperature). $E(C)$ is the energy of the microstate (configuration) C. The factor $exp(-\beta E(C))$ is the Boltzmann weight for the microstate C at temperature T. The normalization constant is the canonical partition function given by

$$Z(\beta) = \sum_C exp(-\beta E(C)). \tag{2.2.2}$$

The sum runs over all possible microstates of the system.

Importance sampling is used to sample the microstates from a Markov chain generated according to the given equilibrium distribution

$$P(C) = \frac{exp[-\beta E(C)]}{Z}. \tag{2.2.3}$$

This constitutes a canonical ensemble governed by the Boltzmann weight $exp(-\beta E(C))$. A Markov chain is defined by the transition probability

$$P(C_{k+1} = C_i | C_k = C_j) = W_{ij} \ \forall k \tag{2.2.4}$$

where W_{ij} is the probability for transition from microstate C_i to C_j in a single step. This implies that the transition probability W_{ij} for a given microstate C_i to evolve into another microstate C_j depends only on the present state C_i and not on the history of the trajectory in whole state space. To ensure that after an initial equilibration period, the microstates occur with the given probability Eqn.(2.2.3), the transition probability should satisfy the three conditions:

$$W_{ij} \geq 0 \; \forall \; i, j; \tag{2.2.5a}$$

$$\sum_j W_{ij} = 1 \; \forall \; i; \tag{2.2.5b}$$

$$W_{ij}\pi_j = W_{ji}\pi_i; \tag{2.2.5c}$$

where π_i is the equilibrium probability of the microstate C_i i.e

$$\pi_i = exp[\beta E(C_i)]/Z.$$

Eqn.(2.2.5c) is the detailed balance condition, which implies that

$$\frac{W_{ij}}{W_{ji}} = \frac{\pi_i}{\pi_j} = \exp[-\beta\{(E(C_i) - E(C_j)\}]. \tag{2.2.6}$$

It may be noted that only the ratios of the equilibrium probabilities appear in the above equation. The ratio can be computed since it involves a ratio of the Boltzmann weights. The knowledge of the partition function is not necessary to calculate the transition probabilities.

The canonical partition function in eqn(2.2.2) can also be expressed in terms of the density of states $\Omega(E)$ as

$$Z(\beta) = \int \Omega(E) exp(-\beta E) \; dE \tag{2.2.7}$$

where the density of states $\Omega(E)$ is a measure of the states contributing to a given energy E. Here the probability density for a closed system to have an energy E is given by

$$P_B(E) = \Omega(E) exp(-\beta E) \tag{2.2.8}$$

where the the suffix B indicates that it is a Boltzmann-Gibbs distribution. The function $\Omega(E)$ is an increasing function of energy whereas the Boltzmann factor decreases exponentially with energy. For a given temperature ($1/\beta$), their product yields a probability distribution peaked in a narrow region centred around the mean value of E appropriate to that temperature. The microstates which have the probability distribution in eqn(2.2.8) comprise the canonical ensemble and the method of sampling is called canonical sampling. The average of any macroscopic variable can be obtained by averaging over these sampled microstates in the canonical ensemble. Monte Carlo method based on Eqn.(2.2.5) is referred to as the Boltzmann sampling method.The sampling method Eqn.(2.2.5) implemented very elegantly, without requiring the prior knowledge of the partition function, is the Metropolis algorithm [10].

2.2.1 Metropolis Algorithm

The Metropolis algorithm gives a simple prescription for the generation of Markov chain of microstates, starting from a initial state C_0, as shown:

$$C_0 \rightarrow C_1 \rightarrow C_2 \rightarrow .....C_k \rightarrow C_{k+1} \rightarrow .....$$

It uses the principle of importance sampling and asymptotically generates equilibrium configurations of the canonical ensemble. Assume a lattice of size $L \times L \times L(=V)$ on which spins are placed at each lattice site. Start with a random configuration of spins, called the initial microstate C_i. Select a spin in the current configuration at random and with equal probability. Flip the spin and get a trial configuration C_t. Calculate the energy difference between the configurations $\Delta E = E(C_t) - E(C_i)$. Accept the trial state according to the acceptance probability given by

$$p = min(1, exp(-\beta\Delta E))$$

or in other words,

• If $\Delta E \leqslant 0$ accept the trial configuration;

- If $\Delta E > 0$, generate a random number ξ in the interval (0,1).

a)If $\xi \leqslant exp(-\beta\Delta E)$, accept the trial state;

b)If $\xi > exp(-\beta\Delta E)$,reject the trial state and include the current microstate in the ensemble.

This is called a single Monte Carlo step (MCS). The system switches from a state C_k to a state C_{k+1} at the end of each MCS. A consecutive set of V number of MCS constitute a Monte Carlo step per spin (MCSS) (lattice sweep, in our parlance). Microstates are colected at the end of each MCSS. Iterating the above procedure we get a Markov chain of microstates. The microstates at the beginning of the chain are discarded (during the process of equilibration) and the microstates in the asymptotic part of the chain constitute the canonical ensemble. The required properties can then computed for each microstate and the average over the canonical ensemble over a large number of equilibrated states) yields the expectation value of an observable quantity of the system. The associated statistical error is inversely proportional to the sample size and fairly accurate measurements can be made on increasing sample size.

The Metropolis algorithm has been very successful in simulating a wide range of phenomena in condensed matter physics. However it is not very effective near phase transitions since the statistical error in measurements increases in the vicinity of a phase transition, due to critical fluctuations. An attempt made to decrease the errors by increasing the sample size results in an increase of the correlation time. It is observed [11] that if successive microstates in the sampled Markov chain are correlated, the statistical errors increase by a factor of $\sqrt{1+2\tau^*}$ where τ^* is the integrated auto-correlation time. The increase in correlation time is called critical slowing down. It is observed, in glassy systems and spin glasses, the configuration space consists of certain low energy regions occur surrounded by high energy regions. Since the algorithm samples states according to their Boltzmann weights, the probability of reaching a high energy region becomes exponentially low. Hence at low temperatures the algorithm gets stranded in these low energy basins (or metastable states) for a long time leading to larger computational times [1]. The single flip dynamics of the algorithm leads to critical slowing down near second order phase transitions where domain formation hinders the dynamics. Cluster flipping algorithms like Swendsen and Wang algorithm [12], Wolff algorithm [13] have been used to reduce the critical slowing down near continuous phase transitions.

The applicability of the above algorithms is limited in systems exhibiting first order transitions where super critical slowing down occurs in the critical region. This is due to the fact that microstates which represent the interface between ordered and disordered states have a low probability of occurrence in a closed system and are consequently sampled less. Hence free energy interface between the ordered and disordered states develops a barrier which cannot be easily overcome with canonical sampling methods. The tunneling time between the metastable regions increases with the system size, leading to critical slowing down. Hence non-Boltzmann sampling methods like umbrella sampling [14–16], multicanonical method [12, 17–19], entropic sampling method [20] have been proposed to overcome the barriers between coexisting phases at first order transitions. The basic idea behind these methods is to sample regions of configuration space which have low probability of occurrence with relative ease, along with the most probable ones.

2.3 Non-Boltzmann Sampling

The canonical partition function in Eqn. (2.2.2) can be expressed in terms of microcanonical entropy as

$$Z(\beta) = \sum_{E} exp(\frac{S(E)}{k_B} - \beta E). \tag{2.3.1}$$

The probability for the macroscopic system to have an energy E in the canonical ensemble is given by

$$P(E) \propto exp(\frac{S(E)}{k_B} - \beta E). \tag{2.3.2}$$

The above is a Boltzmann distribution the sampling from which enables us to obtain microstates at a particular energy. However, if sampling from an arbitrary distribution

$exp(-\alpha(E))$ is desired then the probability density is

$$P_{\alpha(E)}(E) \propto exp(\frac{S(E)}{K_B} - \alpha(E)). \tag{2.3.3}$$

Apart from ergodicity, the detailed balance condition which has to be imposed now is given by

$$\frac{W(\mu \to \nu)}{W(\nu \to \mu)} = \frac{p_\nu}{p_\mu} = exp[-(\alpha(E_\nu) - \alpha(E_\mu))]. \tag{2.3.4}$$

The acceptance probability for a trial state C_t obtained on updating from a current state $C_i$is then given by

$$p = min[1, exp[-(\alpha(E(C_t) - \alpha(E(C_i))]. \tag{2.3.5}$$

The sampling with the above acceptance probability with an arbitrary chosen distribution is called non-Boltzmann sampling. When $\alpha(E) = \beta E$ in eqn(2.3.3) the conventional Boltzmann sampling is recovered.

2.3.1 Entropic Sampling

Entropic sampling [20] is obtained when $\alpha(E)$ is chosen such that $\alpha(E) = \frac{S(E)}{K_B}$ in Eqn.(2.3.3). Then the resultant probability density is constant for all E. Consequently the system performs a random walk in one dimensional energy space and visits all energies with equal probabilities. All microstates which connect ordered and disordered states, (for e.g.near a first order transition) are sampled equally. The histogram of energy obtained would then be a flat in the entire energy range. In order to implement this algorithm, information of the density of states is needed, which is however $apriori$ unknown. So, the basic strategy of entropic sampling is first to estimate it during the simulation process using an iterative method until a flat histogram of energy is obtained.

Reweighting Canonical ensemble average of any observable quantity $O(C)$ is obtained by unweighting and reweighting of $O(C)$ for each microstate C sampled from the entropic ensemble $(C_i, i = 1, n)$. For unweighting we divide by the factor $exp[\alpha(E(C_i)]$

and for reweighting we multiply with a factor $exp(-\beta E(C_i))$. The weight factor associated with each microstate C belonging to the entropic ensemble is thus

$$W(C,\beta) = [exp(\alpha E(C) - \beta E(C))] \tag{2.3.6}$$

Therefore the equilibrium value of any observable $< O >$ is given by

$$< O >= \frac{\sum_C O(C)W(C,\beta)}{\sum_C W(C,\beta)} \tag{2.3.7}$$

where the summation over C indicates that the sum runs over all the available microstates in the ensemble.

2.3.2 Wang-Landau Algorithm

Wang-Landau algorithm [21] is a powerful, flexible and iterative algorithm to estimate $\alpha(E)$ directly such that the estimate is very close to the true value of density of states $\frac{S(E)}{k_B}$. This method is a variant of the entropic sampling technique and is related in spirit to the mulicanonical Monte Carlo and umbrella sampling techniques and their variations [22,23]. This algorithm has been applied to systems with a discrete energy spectrum [24, 25] and also continuous energy spectrum [26, 27] with certain modifications on application to off-lattice simulations [28], protein folding [29]. However for continuous systems, i.e systems in which the random walk is performed with continuous step sizes, it is observed that this technique requires modifications to overcome the problem of slow dynamics. In particular, the WL algorithm has been suitably modified to study liquid crystal behaviour [30]. A further modified version of the algorithm using entropic frontier sampling techniques [31] has been successfully employed to study the isotropic-nematic transition in liquid crystals and liquid crystal elastomers. We describe this modified algorithm below, as applicable to our biaxial liquid crystal system.

The energy range of interest is divided into a large number if bins of equal width $g_i(i = 1, M_E)$ where M_E is the maximum number of bins depending on the system size. Initialise g_i to an array $g_i = e^2(i = 1, M_E)$. Let C_c be the initial microstate with energy E_c and let the energy belong to the μ^{th} energy bin. Let C_t denote the trial microstate with energy E_t and let its energy belong to the ν^{th} bin. If $g_\nu \leq g_\mu$ then accept trial state and set $C_1^{'} = C_t$; If $g_\nu > g_\mu$ then calculate $g_\mu/g_\nu = p$. Generate a random number r in the range $(0, 1)$. If $r \leqslant p$ accept the trial microstate $C_1^{'} = C_t$, otherwise reject the microstate and $C_1^{'} = C_0$. This constitutes a single step. L^3 such steps constitute one Monte Carlo sweep (MCS). In the first MCS every move gets accepted because g_i is the same for all i. The acceptance probability in terms of the entropy $\alpha_i = log\ g(E_{i)}$ is given by

$$p = 1\ if\ \alpha_t \leq \alpha_c;\ p = exp[-(\alpha_t - \alpha_c)]\ if\ \alpha_c < \alpha_t. \tag{2.3.8}$$

To avoid overflow errors all computations are done on a logarithmic scale. The logarithm of entropy is denoted as $\xi_i = log(\alpha_i)$ and the acceptance probability in terms of ξ is given by [32]

$$p = min\{1, exp[-exp[\xi_t + log(1 - exp(-(\xi_t - \xi_c)))]]\}. \tag{2.3.9}$$

After one MCS, ξ_i is updated with a Gaussian Kernel function

$$\xi_i = \xi_i + \gamma_0 exp(\frac{|x - x_0|}{\delta})^2 \tag{2.3.10}$$

where $|x - x_0|$ is the difference in energy in current state and the previous energy values in each bin. γ and δ denote the height and width of the Gaussian respectively. For example in some of the simulations, initial values of (γ_0, δ) are chosen to be 0.1 and 640 $(0.002{*}nbins)$ respectively. After every 10,00 MCS, γ_0 is reduced to $\gamma_0 \rightarrow 0.95\gamma_0$. This is continued till γ_0 reaches a preset value of 0.001. This entire computation constitutes one iteration.

Frontier sampling technique is an algorthmic guidance, provided in addition to the WL routine, by which the system is forced to sample from low entropic regions. The basic idea is to set a cut-off $\xi_T(x)$ on the energy axis where $\xi_T(x) \geq k$ and all $\xi(x)$ to the higher energy side (T region) are boosted with a positive value. The cut-off bin is called the frontier. Initially a cut-off bin number is chosen corresponding to 0.95% of the difference $\xi_i^k - \xi_i^{k-1}$, where k is the iteration index and i is the bin index at the highest energy which is typically close to zero in our system. This cut-off bin acts as the frontier for the next two iterations. After two successive iterations, the cutoff bin is calculated again, by checking if there is any other bin j in the lower energy range at which the difference is greater than the cut-off. If it exists, then the cut-off is reset to 0.95% of $\xi_j^k - \xi_j^{k-1}$. The bin j then acts as the frontier above which there is an uniform growth of $\xi_T(x)\ \forall\ x = j, N$. The ξ values of all the bins to the right of j are then boosted with a value such that a entropic barrier is set. The system is then unable to cross the barrier and consequently samples the lower energy regions leading to an accumulation of states near the frontier which are otherwise not visited. The number of iterations are continued till the $\xi_T(x)$ covers the entire energy range.

After $\xi_T(x)$ covers the entire energy range, a long smoothing run is performed to remove any discontinuities in the density of states (DOS) ξ and it converges to its true asymptotic value within computational limits. The smoothing run starts with initial values of (γ_0, δ) set to (0.001, 640) and the value of γ_0 is progressively decreased during this part until it reaches a value of $\simeq 10^{-9}$. A production run is then performed using the computed density of states and a large entropic ensemble of microstates C_i is collected. The relevant thermodynamic quantities are computed at each temperature by computing appropriate canonical ensemble of states using the reweighting technique described previously.

2.4 Periodic Boundary Conditions

Computer simulations are performed typically on a relatively limited number of particles N of the order of $10^3 - 10^6$ which is a very small number in comparison to the actual number of molecules in a bulk system which is of the order of Avagadro's number [4]. Applying boundary conditions helps in minimising the finite size effect and the effect of the surface and the edges on the bulk system. A most widely used condition is the periodic boundary condition where a spin in the i^{th} row at the edge of the lattice sees a spin at the beginning of the i^{th} row as it's neighbour, or equivalently a lattice is assumed to be surrounded by identical lattices on all sides. However one drawback is that the transition temperatures tend to get overestimated due to correlation between sites. Applying free boundaries, on the other hand,leads to underestimation of the transition temperature. We used such boundary conditions for studies on bulk samples.

2.5 Calculation of Observables

The macroscopic observables which are calculated in a simulation are the average energy E, specific heat C_v, the four order parameters which quantify the biaxial phase and their susceptibilities as well as fourth order energy cumulant, measuring the kurtosis of the distribution [33]. We briefly describe the procedure used to compute these variables as averages over canonical ensembles.

Average energy and specific heat The average energy is calculated by taking the average over a large number of microstates in a canonocal ensemble extracted from the entropic ensemble by reweighting procedure. The average energy is obtained from the entropic ensemble of states as

$$< E >= \frac{\sum_{i=1}^{n} E_i exp(-\beta E + \alpha E)}{\sum_{i=1}^{n} exp(-\beta E + \alpha E)}. \tag{2.5.1}$$

The specific heat at constant volume is obtained from the mean square fluctuations of energy given by

$$C_v = \frac{(< E^2 > - < E >^2)}{k_B T^2} \tag{2.5.2}$$

where k_B is the Boltzmann constant. The temperature is always represented in reduced units as

$$T^{'} = \frac{k_B T}{\epsilon}$$

where ϵ represents the coupling between neighbouring spins in the Hamiltonian model and sets the scale of computation and T is the actual temperature.

Order Parameters Four order parameters are necessary to describe the liquid crystal phases obtained in a system comprising of molecules with D_{2h} symmetry. These are the uniaxial order $< R^2_{00} >$, the phase biaxiality parameter $< R^2_{20} >$, the biaxial order parameters $< R^2_{02} >$ and $< R^2_{22} >$ arising due to molecular biaxiality. The uniaxial nematic phase is characterised by two orientational order parameters $< R^2_{00} >$ and $< R^2_{02} >$ whereas the biaxial symmetry requires inclusion of other two orientational parameters as well. These are computed using the method proposed by Robert Low [34] and Allen [35].

Consider a system of N liquid crystal molecules. Let an orthonormal triad of unit vectors $\{e^{(i)}_x, e^{(i)}_y, e^{(i)}_z\}$ be associated with each of the the molecules $(i = 1, N)$. These may refer to the semi-axes of an ellipsoid which models the shape of the molecule or its moment of inertia tensor. The laboratory frame of reference is denoted by (E_x, E_y, E_z). The order parameters are calculated from ordering tensors $\boldsymbol{Q}^{xx}$, $\boldsymbol{Q}^{yy}$ and $\boldsymbol{Q}^{zz}$ constructed from the unit vectors $\{e^{(i)}_x, e^{(i)}_y, e^{(i)}_z\}$. They are defined as

$$\boldsymbol{Q}^{xx} = \frac{1}{N}\sum_{i=1}^{N}\begin{pmatrix} e^{(i)}_{xx}e^{(i)}_{xx} - 1/3 & e^{(i)}_{xx}e^{(i)}_{xy} & e^{(i)}_{xx}e^{(i)}_{xz} \\ e^{(i)}_{xy}e^{(i)}_{xx} & e^{(i)}_{xy}e^{(i)}_{xy} - 1/3 & e^{(i)}_{xy}e^{(i)}_{xz} \\ e^{(i)}_{xz}e^{(i)}_{xx} & e^{(i)}_{xz}e^{(i)}_{xy} & e^{(i)}_{xz}e^{(i)}_{xz} - 1/3 \end{pmatrix}.$$

$$\boldsymbol{Q}^{yy} = \frac{1}{N}\sum_{i=1}^{N}\begin{pmatrix} e^{(i)}_{yx}e^{(i)}_{yx} - 1/3 & e^{(i)}_{yx}e^{(i)}_{yy} & e^{(i)}_{yx}e^{(i)}_{yz} \\ e^{(i)}_{yy}e^{(i)}_{yx} & e^{(i)}_{yy}e^{(i)}_{yy} - 1/3 & e^{(i)}_{yy}e^{(i)}_{yz} \\ e^{(i)}_{yz}e^{(i)}_{yx} & e^{(i)}_{yz}e^{(i)}_{yy} & e^{(i)}_{yz}e^{(i)}_{yz} - 1/3 \end{pmatrix}.$$

$$\boldsymbol{Q}^{zz} = \frac{1}{N}\sum_{i=1}^{N}\begin{pmatrix} e^{(i)}_{zx}e^{(i)}_{zx} - 1/3 & e^{(i)}_{zx}e^{(i)}_{zy} & e^{(i)}_{zx}e^{(i)}_{zz} \\ e^{(i)}_{zy}e^{(i)}_{zx} & e^{(i)}_{zy}e^{(i)}_{zy} - 1/3 & e^{(i)}_{zy}e^{(i)}_{zz} \\ e^{(i)}_{zz}e^{(i)}_{zx} & e^{(i)}_{zz}e^{(i)}_{zy} & e^{(i)}_{zz}e^{(i)}_{zz} - 1/3 \end{pmatrix}.$$

We note from the definitions of the $\boldsymbol{Q}$ dyadics that they are symmetric and traceless, since the sum of diagonal elements of the $\boldsymbol{Q}$ tensors are zero. Hence the eigen values of these matrices are real and the eigen vectors are mutually orthogonal. It is known from Linear algebra that if a symmetric matrix M has eigen vector v associated with a eigen value λ then $v^T M v = \lambda$. The order parameters of a liquid crystal system, which signify the amount of order in preferred directions of orientation, can be obtained using the above property.

We find the eigen values of each of the tensors $\boldsymbol{Q}^{xx}, \boldsymbol{Q}^{yy}$ and $\boldsymbol{Q}^{zz}$ and the associated eigen vectors. By comparing the eigen values of the three tensors we identify the tensor with the maximum eigen value as $\boldsymbol{Q}_{max}$, with minimum eigen values as $\boldsymbol{Q}_{min}$ and the third one as $\boldsymbol{Q}_{mid}$. The eigen vector associated with the maximum eigen value of all the eigen values is the system director labelled as Z axis, which corresponds to the laboratory Z-direction (E_z). To complete the orthonormal triad of the laboratory axes, we pick the largest positive eigen value from among the eigen values of $\boldsymbol{Q}_{mid}$ and $\boldsymbol{Q}_{min}$ and project it's eigen vector in a plane perpendicular to the system director. The projection forms the Y direction and the eigenvector is labeled as Y (laboratory E_y). The remaining X-direction (laboratory E_x) of the orthonormal triad can be computed using the Y and Z unit vectors. This orthonormal triad forms the principal axis system in which measurements are made.

Taking the molecular z axis to be the long axis for the molecules, the most dominant eigen value $\lambda_{max}$is a measure of the molecular long axis to be oriented along the system director. The uniaxial order parameter is defined as

$$R^2_{00} = \frac{3}{2}\lambda_{max} = \frac{3}{2}Z^T\boldsymbol{Q}_{max}Z.$$

The phase biaxiality parameter R^2_{20} is a measure of the difference in ordering of the x and y molecular axes along the system director and is given as the difference between the other two eigen values of $\boldsymbol{Q}_{max}$ i.e

$$R^2_{20} = \sqrt{\frac{3}{8}}(f_2^T\boldsymbol{Q}_{max}f_2 - f_3^T\boldsymbol{Q}_{max}f_3).$$

. where f_2 and f_3 are the other two eigen vectors of Q_{max}.

If value of $< R^2_{20} >= 0$ then the system is unchanged by a rotation about the Z axis; A nonzero $< R^2_{20} >$ indicates that even in a system of uniaxial molecules, there could be an orienational order without cylindrical symmetry.

The ordering along the primary director arising from the noncylindrical shape of the molecules is the molecular biaxiality parameter $< R^2_{02} >$. It is given by

$$R^2_{02} = \sqrt{\frac{3}{8}}(Y^T\boldsymbol{Q}_{mid}Y - X^T\boldsymbol{Q}_{min}X).$$

. where $Y^T\boldsymbol{Q}_{mid}Y$ denotes how the molecular y axes is aligned with respect to the laboratory E_y direction and so on. A measure of the ordering in the X and Y directions originating from the molecular biaxiality is given by the biaxiality parameter R^2_{22} defined as

$$R^2_{22} = \frac{1}{4}(Y^T \boldsymbol{Q}_{mid} Y + X^T \boldsymbol{Q}_{min} X - X^T \boldsymbol{Q}_{mid} X - Y^T \boldsymbol{Q}_{min} Y)$$

which is normally taken as an effective monitoring parameter of the biaxial transition.

The averages of the above quantities are computed using the same method as for energy as in eqn(2.5.1) during reweighting. The fluctuations in the order parameter values is measured by the susceptibility χ defined as

$$\chi = \frac{1}{k_B T}(< R^2 > - < R >^2)$$

where R is any the above order parameter.

Both specific heat C_V and χ show divergence near transition temperatures. The location of the peaks is used to determine the transition temperature. The peak in the R^2_{00} susceptibility indicates the isotropic-nematic transition temperature whereas the peak in the R^2_{22} is indicative of uniaxial nematic - biaxial nematic phase transition.

Energy Cumulant The fourth order cumulant of the energy gives a measure of the kurtosis of its probability distribution [33]. It is used as a measure of the order of the transition. It is defined as

$$V_4 = 1 - \frac{< E^4 >}{3 < E^2 >^2}$$

For first order transitions

$$V_4 = \frac{2}{3} \; for \; T < T_C; \tag{2.5.3a}$$

$$= 0 \; for \; T > T_C; \tag{2.5.3b}$$

wheras for second order transitions the cumulant always vanishes regardless of the size of lattice. The scaling behaviour of these quntities with system size is often used to estimate the transition temperatures.

2.6 Review of Simulations of Biaxial Nematics

In the last few decades, computer simulations of liquid crystals has emerged as a powerful tool to investigate the mesogenic behaviour which is a result of interplay of various competing mechanisms which operate over a wide range of length and time scales [7, 9] . Nematic phases have been simulated using continuous attractive potentials, hard core potentials and Gay-Berne potential models. The simplest model to describe the biaxial nematic phase is the lattice model based on attractive potential with a single parameter used to describe biaxiality [36, 37]. Monte Carlo methods were successfully employed to investigate and confirm the theoretical predictions of spontaneous thermotropic biaxial ordering for a value of biaxiaity parameter [37]. The complete phase diagram for this dispersion model and the associated order parameters were obtained [38, 39]. A two parameter lattice model [40] was developed to study the interaction between two molecules with D_{2h} symmetry interacting through pair potential [41], which confirmed the predictions qualitatively. Lattice models were also used to simulate biaxial phases produced by V-shaped molecules [42].

The effect of changing the molecular shape and interaction parameters on the phase behaviour and structure of liquid crystalline phases was studied by Allen [35] using hard ellipsoids of revolution with translational and rotational degrees of freedom. The resulting phase diagram from the off-lattice simulation provided evidence for isotropic,nematic, discotic and biaxial liquid crystal phases. A subsequent detailed study of the phase diagram [43] reported a narrow range of shape anisotropies which give rise to the biaxial nematic phase. MC simulations of biaxial ellipsoids modelled with generalised Gay-Berne potential [44] hint at the competition between shape and interaction anisotropies for a biaxial GB particle. The molecular dynamics simulation of a Gay Berne fluid under the influence of an electric field [45] confirmed the experimental observation of the fast switching times associated with the secondary director as compared to the primary director.

The phase behaviour of bent-core mesogens was also studied concurrent to their prediction by Camp $et\ al$ and Lansac $et\ al$ [46, 47]. These were modelled using rigid rods joined at one end, and the resulting phase diagrams revealed N_U ordering for large apex angles. The phase behaviour of a fluid made of a real N_B molecules [48, 49] was simulated using a full-atomistic potential with electrostatic interactions by Palaez $et\ al$ [50]. A spontaneous ordering to a N_B phase was observed on cooling from the isotropic state. An excellent review of the progress made in the simulations of biaxial nematics can be found in a recent review by Berardi *et al* [9]. As noted by these the field of computer simulations of biaxial nematics has kept pace with the theoretical predictions, and presents a peculiar case where design and syntehesis of molecules follow the theoretical and simulation results.

Bibliography

[1] M. E. J. Newman and G. T. Barkema, *Monte Carlo methods in statistical physics* , Clarendon press, London(2002).

[2] D. P. Landau and K. Binder, *A guide to Monte Carlo simulations in statistical physics*, Cambridge University Press, 2nd edition(2005).

[3] K. P. N. Murthy, *Monte Carlo methods in statistical physics* Universities Press, India(2004).

[4] M. P. Allen and D. J. Tildesley, *Computer simulation of liquids*, Clarendon, Oxford(1991).

[5] B. A. Berg, *Markov chain Monte Carlo-Innovations and Applications*, (ed.) W. S. Kendall, F. Liang and J. S. Wang, World Scientific, Singapore(2005).

[6] P. Pasini, C. Chiccoli and C. Zannoni, *Advances in computer simulations of liquid crystals*, (ed.) P. Pasini and C. Zannoni, Kluwer Acad. Publishers (2000).

[7] C. M. Care and D. J. Cleaver, *Reports on Progress in Physics*, **68**, 2665 (2005).

[8] M. R. Wilson, Progress in computer simulations of liquid crystals. *Int. Rev. Phys. Chem.* **24**, 421 (2005).

[9] R. Berardi, L. Muccioli, S. Orlandi, M. Ricci, C. Zannoni, *J. Phys.: Condens. Matter.* **20**, 463101.1 (2008).

[10] N. Metropolis, A. W. Rosenbluth, M. N. Rosenbluth, A. H. Teller, and E. Teller, *J. Chem. Phys.* **21**, 1087 (1953).

[11] H. Muller Krumbhaar and K. Binder, *J. Stat. Phys.* **8**, 1 (1973).

[12] R. H. Swensden and J. S. Wang, *Phy. Rev. Lett.* **58**, 2 (1987).

[13] Ulli wolff, *Phy. Rev. Lett.* **62**, 361 (1989).

[14] G. Torrie and J. P. Valleau, *Chem. Phys. Lett.* **28**, 578 (1974).

[15] G. M. Torrie and J. P. Valleau, *J. Comp. Phys.* **23**, 187 (1977).

[16] Z. W. Salzburg $et\ al$, *J. Chem. Phys.* **30**, 65 (1959).

[17] B. A. Berg and T. Neuhas, *Phys. Lett. B* **267**, 249 (1991).

[18] B. A. Berg and T. Neuhaas, *Phys. Rev. Lett.* **68**, 9 (1992).

[19] W. Janke, *Physica A* **254**, 164 (1998).

[20] J. Lee, *Phys. Rev. Lett* **71**, 211 (1993); **71**, 2352 (1993).

[21] F. Wang and D. P. Landau, *Phys. Rev. Lett.* **86**, 2050 (2001); F. Wang and D. P. Landau, *Phy. Rev. E* **64**, 056101 (2001).

[22] P. M. C. de Olivera, T. J. P. Penna, H. J. Herrmann, *Braz, J. Phys.* **26**, 677 (1996).

[23] P. M. C. de Olivera, *Eur. Phys. J. B* **6**, 111 (1998); P. M. C. de Olivera, T. J. P. Penna and H. J. Herrmann, *Eur. Phys. J. B***1**, 205 (1998).

[24] D. P. Landau and F. Wang, *Braz. J. Phys* **34**, 2A (2004).

[25] D. T. Seaton, T. Wust and D. P. Landau, *Phys. Rev. E* **81**, 011802 (2010).

[26] P. Poulain, F. Calvo, R. Antoine, M. Broyer, P. Dugourd, *Phys. Rev. E* **73**, 056704 (2006).

[27] S. Sinha, S. K. Roy, *Phys. Lett. A* **373**, 308 (2009).

[28] M. S. Shell, P. G. Debenedetti and A. Z. Panagiotopoulos, *Phys. Rev. E* **66**, 056703 (2002).

[29] N. Rathore, T. A. Knotts and J. J. de Pablo, *Biophysics. J.* **85**, 3963 (2003).

[30] D. Jayasri, V. S. S. Sastry and K. P. N. Murthy, *Phy. Rev. E* **72**, 036702 (2005).

[31] D. Jayasri, Ph. D Thesis, *Non-Boltzmann Monte Carlo study of Confined Liquid Crystals and Liquid Crystal Elastomers*, University of Hyderabad, India(2009).

[32] B.A. Berg, arxiv: con-mat/0206333v2 (2002).

[33] K.Binder and D. P. Landau, *phys. Rev. B* **30**,1477 (1984).

[34] Robert J Low. *Eur. J. Phys.* **23**, 111 (2002).

[35] M. P. Allen, *Liq. Cryst.* **8** 499 (1990).

[36] G. R. Luckhurst, C. Zannoni, P. L. Nordio and U. Segre, *Mol. Phys.* **30**, 1345 (1975).

[37] G. R. Luckhurst and S. Romano, *Mol. Phys.* **40**, 129 (1980).

[38] F. Biscarini, C. Chiccoli, P. Pasini, F. Semeria, C. Zannoni. *Phys. Rev. Lett.***75**, 1803 (1995).

[39] C. Chiccoli, P. Pasini, F. Semeria, C. Zannoni. *Int. J. Mod. Phys. C.* **10**, 469 (1999).

[40] S. Romano, *Physica A* **337**, 505 (2004).

[41] A.M.Sonnet, E.G.Virga, G.E.Durand .*Phys. Rev. E.*, **67**,061701(2003).

[42] M. A. Bates and G. R. Luckhurst, *Phy. Rev. E 72*, 051702 (2005).

[43] P. J. Camp and M. P. Allen, *J. chem. phys.* **106**, 6681 (1997).

[44] R. Berardi and C. Zannoni, *J. chem. phys.* **113**, 5971 (2000)

[45] R. Berardi, L. Muccioli and C.Zannoni, *J. Chem. Phys* **128**, 024905 (2008).

[46] P.J. Camp, M. P. Allen and A. J. Masters, *J. chem. phys.* **111**, 9871 (1999).

[47] Y. Lansac, P. K. Maiti, N.A. Clark and M. A. Glaser, *Phy. Rev. E* **67**, 011703 (2003).

[48] B. R. Acharya, A. Primak, and S. Kumar, *Phy. Rev. Lett.* **92**, 145506 (2004).

[49] L. A. Madsen, T. J. Dingemans, M. Nakata, E. T. Samulski,*Phy. Rev. Lett.* **92**, 145505 (2004).

[50] J. Palaez and M. R. Wilson, *Phys. Rev. Lett.***97**, 267801 (2006).

Chapter 3

A Wang-Landau Monte Carlo Investigation of the Mean Field Phase Diagram of Biaxial Liquid Crystals

In this chapter we investigate the phase sequence of biaxial liquid crystals, based on the general quadratic model Hamiltonian introduced in chapter 1, using a simulation technique which combines entropic and frontier sampling techniques. We review the necessary background and the recent developments in the field in section 3.1. The WL-simulation technique is introduced in section 3.2. The simulation results are discussed in section 3.3. Conclusions drawn from the novel simulation techniques are presented in section 3.4.

3.1 Introduction

The biaxial nematic phase has attracted considerable attention recently for various reasons, starting from a fundamental question about the conducive experimental conditions for its existence to its envisaged applications in display devices. Though predictions made by various mean-field (MF) theoretic treatments [1]- [7], Landau free energy based analyses [8] - [12] and computer simulations [13] - [20] support the feasibility of such a phase, the progress on the experimental front [21,22] has been rather modest. Questions regarding the existence and subsequent experimental identification of a biaxial phase in the synthesized compounds persist in the literature [23] - [26].

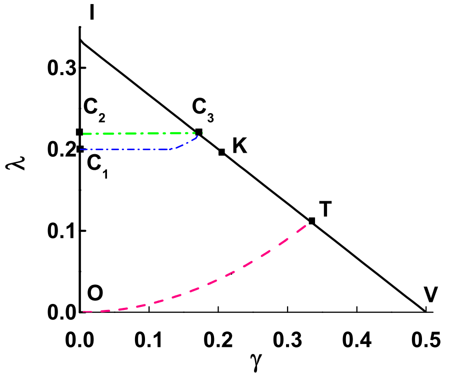

Figure 3.1: Essential triangle : Region of biaxial stability

The recent generalised MF analysis, as outlined in chapter 1, identifies a triangular region of biaxial stability in the Hamiltonian parameter space, denoted as the 'Essential Triangle', OIV, shown in Fig.(3.1). All realizable biaxial nematic systems can be represented as appropriate points in this triangle, by suitable choice of symmetry axes and consequent rescaling of the temperature. All possible phase sequences predicted by the Hamiltonian model can be obtained by choosing a corresponding point on the triangle. In particular, a mean field phase diagram was predicted [7] as a function of the arc length OIV, denoted by λ^*, defined as $\lambda^* = \lambda$ on the segment OI, and

$$\lambda^* = \frac{(1+\sqrt{13}\gamma)}{3},$$

with

$$\gamma = \frac{(1-3\lambda)}{2}$$

covering the segment IV. The MF phase diagram predicts for $\lambda^* \lesssim 0.22$ $(\gamma = 0, \lambda \lesssim 0.22)$ a two stage transition from the isotropic to a biaxial phase, with an intervening uniaxial nematic phase. The uniaxial-biaxial transition is second order $(N_B = N_U - I)$ upto point C_1 $(\gamma = 0, \lambda \simeq 0.2)$ and then changes to first order $(N_B - N_U - I)$ upto C_2 $(\gamma = 0, \lambda \simeq 0.22)$. For the rest of the range of λ^*, a direct transition is expected, extending upto V in Fig. (3.1). This transition is predicted to be first order $(N_B - I)$ for $\lambda^* \leq 0.54$ $(\gamma = 5/29, \lambda = 19/27)$ and second order $(N_B = I)$ upto the point V $(\gamma = 0.5, \lambda = 0.0)$. Hence C_1 and C_3 are tricritical points and C_2 is a triple point.

The above scenario from MF analysis implies that a biaxial nematic phase should be condensing over a significant region of the parameter space [7]. The biaxial phase should occur as a rule and not as an exception raising experimental expectations, contrary to the laboratory observations. The recent example of readily observable deviation between mean field predictions [7] and the experimental observations is the tetrapode system [22] investigated by Bisi et al [27]. Taking the ratio $\rho = (N_B - N_U)/(N_U - I)$ as the quantitative criterion to identify the Hamiltonian parameters corresponding to the data of the tetrapode, it is found the tetrapode data corresponds to the value $(\gamma = 0.174, \lambda = 0.193)$, a point which falls below the tricritical line C_1C_3 in the essential triangle. The experimental observation deviates from MF expectations in this system in that after the onset to the biaxial phase, the macroscopic biaxiality order parameter of the the real system tapers off to about $\sim 7\%$ of the MF predicted value. In other words, in real system development of significant macroscopic biaxial order is for some reason, inhibited.

It is also interesting to observe that the asymptotic behaviour in the limit of vanishing value of the biaxial - biaxial tensorial interaction strength, $\lambda \to$ 0, leads to a conflicting result at the point V in the phase diagram, as was noted in [7]. The mini-max analysis in this 'partly repulsive region' predicts a direct isotropic - biaxial transition to occur at this point, whereas the biaxial phase stability criterion requires $\lambda > 0$ for the onset of a biaxial phase.

An attempt was made by De Matteis *et al* [28] to resolve this discrepancy in the partly repulsive region by using minimax principle. Taking into consideration the D_{4h} symmetry of the Hamiltonian along uniaxial torque lines, the μ-model was proposed (in the repulsive region in the essential triangle). The parameter μ is defined such that $\mu \leq 0$ corresponds to the attractive interactions and $0 < \mu \leq 1$ corresponds to the partly repulsive interactions. The μ model predicts a direct $I - N_B$ transition for upto μ= 0.43, after which a series of first order $I - N_U - N_B$ transitions and biaxial - biaxial transitions are predicted in the region for $0.43 < \mu \leq 1$ (a region close to the point V in the essential triangle). An isolated tricritical point is predicted in the limit $\mu \to 1$ corresponding to the point 'V' in mean field phase diagram (see Fig.3.1). It may also be noted that these predictions were only partly confirmed by the conventional Monte Carlo simulations [28].

Keeping in view these issues between the mean field results and experiments and also the unsatisfactory mean field predictions in the asymptotic limit of biaxial stability ($\lambda \to 0$), we have attempted to carry out a systematic simulation study along the sides of the essential triangle OIV to facilitate a direct comparison between simulations and mean field results. We note that the earlier simulation studies which largely support the mean field theoretical predictions (but do not necessarily answer the absence of macroscopic biaxial order) were all carried out using conventional Boltzmann sampling based on metropolis algorithm (see chapter 2). This procedure however has known limitations with systems possibly encountering free energy barriers. In this context, we felt the need to apply a different sampling technique and look for possible new features.

We combine both entropic sampling and frontier sampling techniques (which can effectively overcome free energy barriers) to study the phases predicted by the general quadratic Hamiltonian model. We employ Wang-Landau algorithm [29] suitably modified for liquid crystal simulations [30], and augment it with frontier sampling.

3.2 Hamiltonian Model

The general quadrupolar orientational Hamiltonian was originally suggested by Straley [2], subsequently phrased in tensorial formalism [5]. Accordingly, the interacting biaxial molecules can be represented by two pairs of symmetric, traceless tensors ($\boldsymbol{q}$, $\boldsymbol{b}$) and ($\boldsymbol{q}^{'}$, $\boldsymbol{b}^{'}$). The tensors $\boldsymbol{q}$ and $\boldsymbol{q}^{'}$ are uniaxial around the unit molecular vectors $\boldsymbol{m}$ and $\boldsymbol{m}^{'}$, whereas both $\boldsymbol{b}$ and $\boldsymbol{b}^{'}$, orthogonal to $\boldsymbol{q}$ and $\boldsymbol{q}^{'}$, respectively, are biaxial. $\boldsymbol{q}$ and $\boldsymbol{b}$ are the irreducible components of the anisotropic parts of any molecular susceptibility tensor and can be represented in the eigen frame $(\boldsymbol{e}, \boldsymbol{e}_{\perp}, \boldsymbol{m})$ of the tensor as

$$\boldsymbol{q} := \boldsymbol{m} \otimes \boldsymbol{m} - \frac{\boldsymbol{I}}{3} I \qquad (3.2.1)$$

$$\boldsymbol{b} := \boldsymbol{e} \otimes \boldsymbol{e} - \boldsymbol{e}_{\perp} \otimes \boldsymbol{e}_{\perp} \tag{3.2.2}$$

where $\boldsymbol{I}$ is the identity tensor. Similar representations hold for $\boldsymbol{q}'$ and $\boldsymbol{b}'$ in the eigen frame $(\boldsymbol{e}', \boldsymbol{e}'_{\perp}, \boldsymbol{m}')$. The interaction energy can now be written as

$$H = -U_0[\xi\, \boldsymbol{q} \cdot \boldsymbol{q}' + \gamma(\boldsymbol{q} \cdot \boldsymbol{b}' + \boldsymbol{q}' \cdot \boldsymbol{b}) + \lambda\, \boldsymbol{b} \cdot \boldsymbol{b}'] \tag{3.2.3}$$

where U_0 is the scale of the energy, ξ = ± 1, γ and λ are dimensionless interaction parameters, whose values determine the relative importance of the uniaxial-biaxial coupling and biaxial-biaxial coupling interactions between the molecules. We focus on the region of biaxial stability with the long molecular axes providing the definition of the primary director. Accordingly, we chose $\xi = +1$ in Eqn. (3.2.3).

For simulation purposes, the above Hamiltonian in Eqn. (3.2.3) is conveniently recast as a biaxial mesogenic lattice model, where particles of D_{2h} symmetry, represented by unit vectors u_a, v_b on lattice sites a and b interact through a nearest neighbour pair potential [31]

$$U = -\epsilon\{G_{33} - 2\gamma(G_{11} - G_{22}) + \lambda[2(G_{11} + G_{22}) - G_{33}]\}. \tag{3.2.4}$$

Here f_{ab}= ($v_a.u_k$), G_{ab}=$P_2(f_{ab})$, ξ = +1 and ϵ (set to unity in simulations) is a positive quantity setting the reduced temperature T'=$K_B T/\epsilon$.

The pair-wise interaction in Eqn. (3.2.3) is particularly transparent when expressed in terms of tensors appropriate to the symmetry of the diagonal IV (uniaxial torque along $\boldsymbol{e}$) as [7, 28]

$$H = U'[\,\mu(\boldsymbol{e} \otimes \boldsymbol{e} - \frac{\boldsymbol{I}}{3}) \cdot (\boldsymbol{e}' \otimes \boldsymbol{e}' - \frac{\boldsymbol{I}}{3}) - (\boldsymbol{e}_{\perp} \otimes \boldsymbol{e}_{\perp} - \boldsymbol{m} \otimes \boldsymbol{m}) \cdot (\boldsymbol{e}'_{\perp} \otimes \boldsymbol{e}'_{\perp} - \boldsymbol{m}' \otimes \boldsymbol{m}')] \tag{3.2.5}$$

where

$$U' = U(1 - \lambda)/2$$

and

$$\mu = \frac{(1-9\lambda)}{(1-\lambda)}$$

In this format, $\mu = -3$ corresponds to the point I (0, 1/3) in Fig. 3.1, $\mu = 0$ to the Landau point T $(1/3, 1/9)$ (LP), and $\mu = +1$ to V (0.5, 0.0). In particular we observe that $\mu = -1$ corresponds to $\lambda^* \backsimeq 0.57$ located at K in Fig. 3.1.

3.3 Details of Simulation

3.3.1 Sampling Technique

Wang-Landau sampling is a Monte Carlo technique initially developed for discrete models as a temperature independent, iterative method with the ability to sample rough energy landscapes. In order to perform simulations of a continuous model like the Lebwohl - Lasher model which describes the isotropic - nematic transition, a modified Wang - Landau algorithm was developed [30], in order to sample rare microstates in the phase space, as the span of the total energy increases with size. This modified algorithm (JSM) augmented with frontier sampling [32] is used to simulate the biaxial model.

The Wang-Landau sampling is based on calculating the density of states g(E) where E is the energy of the system. To avoid numerical problems like overflow truncation errors, the simulation is done using a log-log scale i.e g_i is calculated as $\xi = log(\alpha) = log(log(g_i))$. The acceptance probability, updation of ξ_i, unweighting and reweighting are done on the same scale as suggested by Berg [33].

Initially the cubic lattice (of size L) of the biaxial liquid crystal with random configuration of headless spins is initialised. The energy range (E_{min}, E_{max}) is divided into $40 * L^3$ (=nbins)bins. Let the current microstate belong to an energy bin c. Orientation of a chosen spin is changed randomly and the trial microstate obtained belong to a bin t. The acceptance probability of the trial microsatet is calculated using the Eqn.

$$p = min\{1, exp[-exp[\xi_t + log(1 - exp(-(\xi_t - \xi_c)))]]\}.$$

This constitutes a Monte Carlo step. A Monte Carlo sweep (MCS) consists of L^3 such steps. Once a MCS is completed the value of ξ_i is updated with a Gaussian kernel function

$$\xi(i) \rightarrow \xi_i + \gamma_0 exp(-\frac{|x - x_0|}{\delta})^2$$

The values γ_0 and δ are the scaling parameters to adjust the height and width of the Gaussian kernel, respectively. The initial values of (γ_0, δ) are taken as $(0.1, 0.002 * nbins)$. After every 10000 MCS, the value of γ_0 is reduced to $\gamma_0 \rightarrow 0.95\gamma_0$. This updation of γ_0 is continued till it reaches a predetermined minimum value of typically, 0.001. This entire procedure is called an iteration. After every two successive iterations, the difference between the updated values of ξ is calculated at each bin.

The cut off bin number is chosen as that corresponding to 95% of the difference of

$$\xi^k(i) - \xi^{k-1}(i),$$

where k is the iteration index and the bin index i corresponds to the highest energy of interest.The cut off bin acts as the frontier, and the algorithm continues the iterations. The frontier is the bin j above which all $\xi(x)$ to the higher energy side (T region) are boosted with a positive value and there is an uniform growth of $\xi_T(x) \ \forall \ x = j, N$. A boost = 0.5 is added to the values of $\xi_T(x)$ which are at the right of j. Thus a high entropic barrier is created for the random walker to enter the high energy regions.

Consequently, an accumulation of states occurs near the frontier till the height becomes equal to the boosted area. This pushes the explored region towards the lower energy region. In other words, as more higher entropic regions are adequately sampled, the frontier is pushed to lower energy regions, so as to make the system sample beyond the frontier. The simulation is performed until $\xi_T(x)$ covers the entire energy range. This takes typically about 200 iterations. Then a long smoothing run is performed with initial values of (γ_0, δ) set to $(0.001, 0.002 * nbins)$, so as to remove any discontinuities in the density of states (DoS) profile. In this run, the values of γ_0 are progressively reduced till it reaches a value 10^{-9}. This ensures that the final ξ converges to its asymptotic value and is as close to the representative density of states of the system as possible. within computing errors.

The final DoS is then used in a long production run to collect an entropic ensemble of 4×10^7 microstates. Once the DoS and physical parameter values of the microstates belonging to the entropic ensemble are available, reweighting can be done at any desired temperature resolution. The macroscopic value of any physical property O, in thermal equilibrium at temperature T (β=$\frac{1}{k_B T}$) is then computed from the collection of microstates in the entropic ensemble C_i by a reweighting procedure as

$$\langle O \rangle = \frac{\sum O(C_i) g(E_i) exp[-\beta E(C_i)]}{\sum g(E_i) exp[-\beta E(C_i)]} \tag{3.3.1}$$

3.3.2 Simulation Details

Simulations were carried out on a cubic lattice (L=20) with periodic boundary conditions. The biaxial molecules on each lattice site interact with the nearest neighbours based on the potential in Eqn.(3.2.4). The parameters γ and λ were chosen such that we traverse along the boundary of the essential triangle 'OIV' (encompassing line segments OI and IV) which amounts to varying the arclength λ^* from 0 to 1(0.933). Simulations were carried out at closely spaced values of λ^* for nearly 60 points on this arc.

Initially, conventional Monte Carlo sampling techniques (Boltzmann ensembles) were employed to study the phase behaviour on the essential triangle at select values of λ^*. In each simulation, the reduced temperature is varied from 2.0 to 0.04 in steps of 0.002 units and at each temperature, the sample is equilibrated for 6.5×10^5 MC runs before collecting the canonical averages of all relevant physical parameters in a production run of 6.5×10^5 MC runs. Thus the averaging is done over 6.5×10^5 microstates at each temperature. The canonical ensembles collected at a given temperature with this sampling will henceforth be denoted as B-ensembles.

The simulations were then carried out using modified Wang-Landau (WL) algorithm augmented by frontier sampling, at each of the above value of λ^* ($0 < \lambda^* < 1$). At each value, the g(E) which is the estimate of the density of states was obtained and an entropic ensemble of 10^7 microstates (C_i) was generated, by making an effectively uniform random walk in energy space guided by the DoS. Equilibrium ensembles at any desired (reduced) temperature ($T^{'}$) are consequently extracted by a suitable reweighting procedure (RW-ensembles) [32, 34]. These encompass all permissible microstates consistent with the equilibrium conditions, overcoming any inherent free energy barriers, unlike their Boltzmann counterparts (B-ensembles). The average value of physical properties at any desired temperature were calculated using Eqn.(3.3.1).

The physical parameters of interest in this system which were calculated at each λ^* are average energy $< E >$, specific heat $< C_v >$, Binder's energy cumulant V_4 (= $1- < E^4 > /(3 < E^2 >^2)$) which is a measure of the kurtosis [35], the four order parameters of the phase calculated according to the method in ref [36]. They are the uniaxial order $< R^2_{00} >$ (along the primary director), the phase biaxiality $< R^2_{02} >$, and the molecular contribution to the biaxiality of the medium $< R^2_{22} >$, $< R^2_{20} >$, and their susceptibilities. All the physical parameters are collected at a high temperature resolution of 0.002 units.

In the case of WL simulation, representative free energy profiles are also computed making use of the DoS data as a function of the two order parameters R^2_{00} and R^2_{22} at various temperatures.

The reduced temperature scale ($T^{'}$) used in the simulations differs from mean field temperature scale($T^{''}$) by a factor of 9 [19]. A further scaling was done to obtain compatibility with mean field temperature $1/\beta^*$ [7] by dividing $T^{''}$ with the condensation energy U^* of the biaxial phase,which is the minimum of H, i.e

$$T^{''} = \frac{T^{'}}{9}, T^* = \frac{T^{''}}{U^*}$$

where

$$U^* = \frac{2U(1+3\lambda)}{3} \, and \, U = \epsilon = 1.$$

3.4 Simulation Results

Each λ^* value represents a biaxial system represented by the Hamiltonian parameters γ and λ, which are closely related to the molecular anisotropy and hence to the shape of the molecules comprising the biaxial liquid crystal. The WL simulation carried out for each such point provides rich information about the phase sequence and nature of the orientational ordering in the system, and data can be extracted at the desired temperature resolution, once the entropic ensemble is constructed. Taking into account the D_{4h} invariance of the Hamiltonian along OI and IV, two scalar order parameters R^2_{00} and R^2_{22} suffice to describe the condensed phases. The simulation results are presented, for purposes of clarity, by dividing the arc OIV (λ^*-axis) into three convenient parts: OI,IC_3 and C_3TV.

3.4.1 Segment OI

This region corresponds to the segment of the λ axis defining the essential triangle, and the value of λ^* is tha same as the value of λ, i.e $\lambda^* = \lambda$. The interaction between the intermolecular uniaxial tensors involving the '$\boldsymbol{m}$' axis is decoupled from that between biaxial tensors involving the other two minor axes $\boldsymbol{e}$ and $\boldsymbol{e}_\perp$. The Hamiltonian is totally attractive and admits free energy solutions which attain global minima. The biaxial systems represented have a special dispersion of the dielectric shape susceptibility and are an extreme case of the real molecules represented by the general Straley interaction. Initially we present the data obtained from a typical WL simulation at say, $\lambda^* = 0.1$ as an example to introduce notation and relevant parameters, referring to Figs. 3.2- 3.4.

Fig.3.2(a) depicts the density of states (DOS) $g(E)$ plotted as a function of energy per particle E. It is a smooth function of energy monotonically increasing in the relevant energy region. The energy histogram shown in Fig.3.2(b) is approximately flat in the energy range relevant to the temperature range of interest. The energy per particle E shown in Fig.3.3(a) shows two sharp kinks which are the indications of two transitions. The fluctuations in energy at these transitions show up as peaks at T_{C1} and T_{C2} in specific heat profile shown in Fig.3.3(b)(i). The C_V profile shows that as the liquid crystal is cooled from high temperature isotropic state (I) a uniaxial (N_U) phase is formed at the transition at temperature $T_{C1} = 1.146$. On further cooling from the uniaxial phase, a transition to a biaxial (N_B) phase occurs at temperature $T_{C2} = 0.706$. The significant dip in the energy

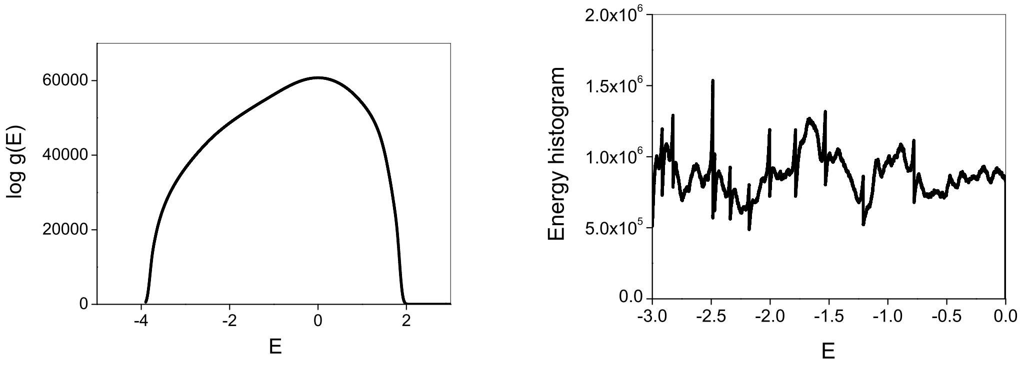

(a) (b)

Figure 3.2: Experimental parameters from the present simulation at $\lambda^* = 0.1$ (a)Representative density of states (b)Energy histogram of the entropic ensemble

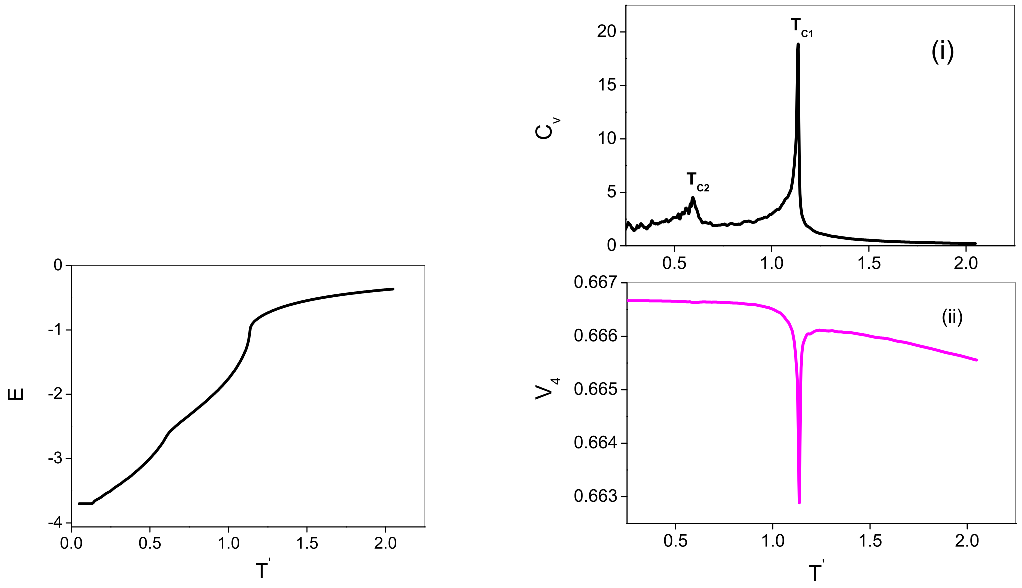

(a) (b)

Figure 3.3: Experimental parameters from the present simulation at $\lambda^* = 0.1$. Temperature variation of (a)Average energy per particle (b) specific heat (per particle)and energy cumulant V_4

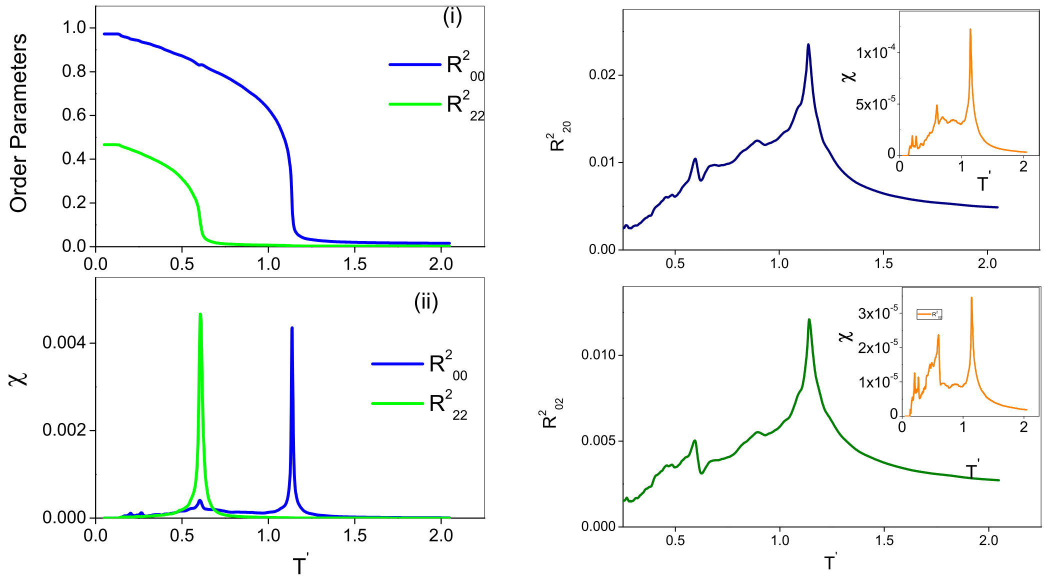

(a) (b)

Figure 3.4: Experimental parameters from the present simulation at $\lambda^* = 0.1$. Temperature variation of (a) uniaxial and biaxial orders along with their susceptibilities χ. (b) phase biaxiality parameter and molecular biaxiality parameters with their susceptibilities χ

cumulant V_4 in Fig.3.3(b) (ii) at T_{C1} indicates the first order nature of the I-N_U transition. The $N_U - N_B$ transition at T_{C2} is expected to be of second order, and V_4 does not show any first order signature. The order parameter and susceptibility profiles shown in Fig.3.4(a) confirm the nature of the phases obtained. The growth of the uniaxial order parameter R^2_{00} at T_{C1} (Fig.3.4(a)(i)) and the associated susceptibility peak confirms the $I - N_U$ transition, whereas the subsequent growth of biaxial order parameter R^2_{22} and the corresponding susceptibility peak, point to the low temperature transition from uniaxial to the biaxial phase.The phase biaxiality parameter R^2_{20} and molecular biaxiality parameter R^2_{02} are also shown along with the respective susceptibilities in Fig.3.4(b) for completeness of the presented data.Their susceptibilities also show the signatures of the two transitions. A comparison of the results from entropic sampling with those from the standard Metropolis-based Boltzmann sampling is shown in Fig.(3.5) under identical conditions of lattice size, and averages over comparable ensemble sizes. It is observed that the ensemble averages of the

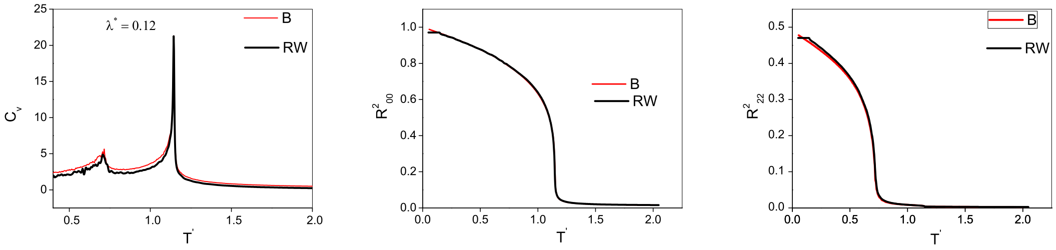

(a) (b) (c)

Figure 3.5: Comparison of data obtained from RW- and B- ensembles.Temperature variation of: (a) Specific heat (b) Uniaxial order and (c) Biaxial order, at λ^*=0.12

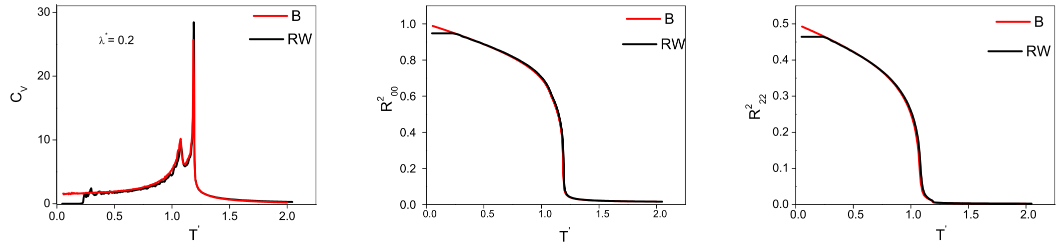

(a) (b) (c)

Figure 3.6: Temperature variation of: (a) Specific heat; (b) Uniaxial order; and (c) Biaxial order, obtained from RW- and B-ensembles at λ^*=0.20 (Deviations observed at very low temperatures ($\leq$ 0.25), common to all plots, have their origin from inadvertent inadequate sampling of microstates comprising the entropic ensemble, at these very low energy values. As these deviations do not interfere with the interesting nature of the graphs, recomputations were not attempted to correct for this, to save computing time)

observables obtained from averaging over the microstates present in the B-ensembles coincide exactly with averages over the microstates in RW-ensembles in the entire temperature range for λ^*=0.12.

A similar comparison at two other λ^* values (0.20 and 0.33) which are shown in Figs.(3.6) and (3.7)) confirms this observation. This implies the sampled states in both type of sampling procedures are similar along the λ - axis in the essential triangle.

The results obtained from entropic sampling (WL simulation) along OI are now presented for convenience in two segments. The results for λ^* values ranging from 0.1 to 0.25 are presented first, followed by data covering the rest of values 0.26-0.33.

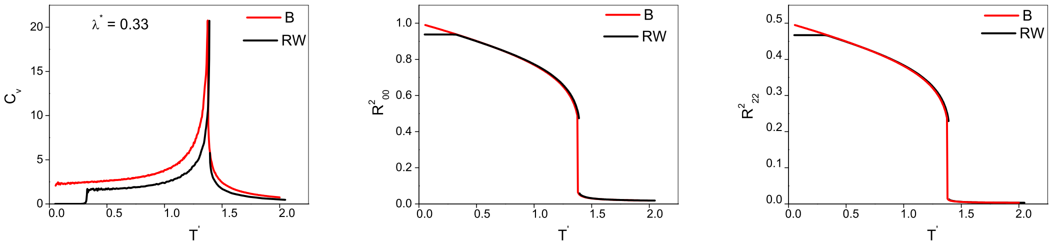

(a) (b) (c)

Figure 3.7: Temperature variation of (a)Specific heat(b) Uniaxial order (c) Biaxial order, obtained from RW- and B-ensembles at λ^*=0.33 (please see the explanatory note of Fig.(3.4), for low temperature variations.

.

3.4.2 Segment OI : Range of λ^* = (0.1-0.25)

The specific heat and order profiles for nine values of λ^* in this range are grouped together for comparison purposes and shown in Fig.3.8. The temperature variations of specific heat C_V, uniaxial order R^2_{00}, biaxial order R^2_{22} and energy cumulant V_4 obtained from RW-ensembles are depicted in Figs.3.8(a)-(c). It may be noted from Fig.3.8(a) that for all values of λ^*, two transition peaks are observed in the specific heat. As the biaxial system is cooled from the high temperature isotropic phase, a $I - N_U$ transition occurs at a high temperature T_{C1} followed by a second transition $N_U - N_B$ at lower temperature T_{C2}. The $I - N_U$ transition temperature remains fairly constant with the variation in λ^*, whereas $N_U - N_B$ transition shifts towards higher temperatures as λ^* increases from 0.1 to 0.25. This behaviour is also reflected in the order parameter profiles shown in Figs.3.8(b) and (c). This implies that on increasing λ^*(=λ in this segment) the biaxial phase is more favoured, which is as expected from the mean field predictions.

Supplementing the results on C_V and order parameters to determine the transition temperatures and symmetries of the phases so condensed, we focus on the temperature variations of the fourth order cumulant (V_4) representing the kurtosis of the ensemble distribution to look at the nature of the transitions. It is known that [35] the stronger the shape of the transition, the more significant will be the dip of V_4 at that transition, By examining the Figs. 3.9(a) - 3.9(c), depicting V_4 variation with T' at λ^* = 0.18, 0.19 and 0.20, respectively,

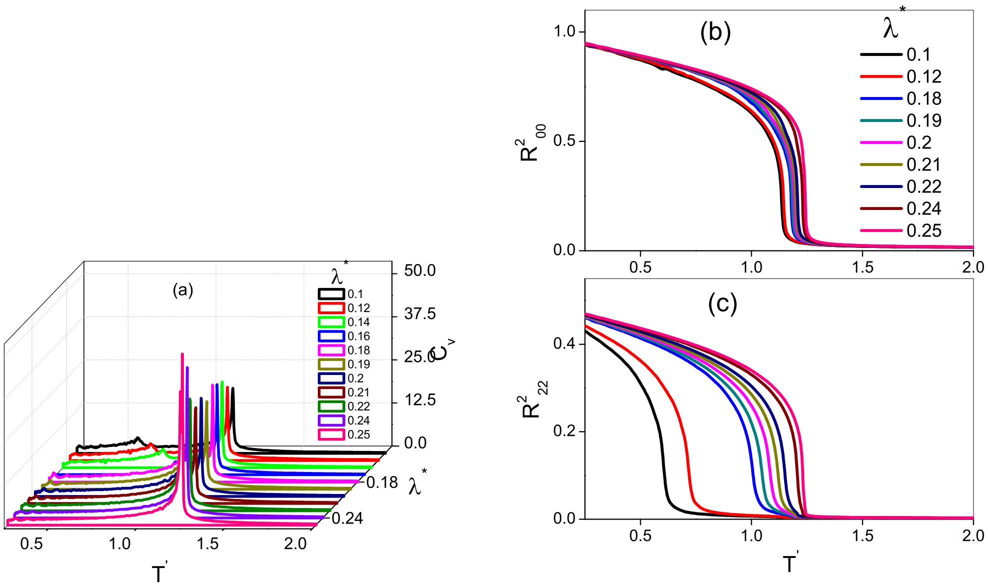

Figure 3.8: Temperature variation of experimental parameters for different values of λ^* (0.1 to 0.25)

with specific reference to its variation at $\lambda^* = 0.1$ (3.3(b)), we find evidences of the nature of $N_B - N_U$ transition becoming weakly first order at $\lambda^* = 0.18$. The mean field prediction for this cross-over tricritical point (point C_1 in the essential triangle on the λ axis) is at $\lambda^* = 0.2$, Such quantitative differences between the MF predictions and simulations based on hamiltonian models are not uncommon. A similar difference also seems to exist with respect to the second interesting point C_2 on the triangle, where the two transitions coalesce, and a triple point results. MF predictions suggest $\lambda^* = 0.22$ as the point of such merger, whereas the present simulations put this value at a slightly larger value , at $\lambda^* = 0.26$. The corresponding transition temperatures $T^{'}$in reduced units are given in Table.5.1 along with the mean field temperatures $T_1^{''}$, $T_2^{''}$, T_1^* and T_2^*.

Secondly, mean field predicts a triple point designated C_2 at λ^*=0.22 at inverse temperature β_c = 6.81. The simulation results, shown in Figs.(3.10) and (3.11), show that the triple point exists at λ^* = 0.26.

Within the caveat that simulation results pertaining to phase transitions are subject to finite size effects - like the known limitations on MF predictions -, these comparisons simply show that the general behaviour of the phase sequences in this interesting Hamiltonian

Table 3.1: Comparison of transition temperatures at some points along OI

λ^*	$T_1^{'}$	$T_2^{'}$	$T_1^{''}$	$T_2^{''}$	T_1^*	T_2^*
0.18	1.1753	0.9919	0.1305	0.1102	0.1272	0.1074
0.2	1.1937	1.077	0.1326	0.1196	0.1243	0.1122
0.22	1.211	1.149	0.1346	0.1276	0.1216	0.1153
0.26	1.2516		0.13917			0.1172

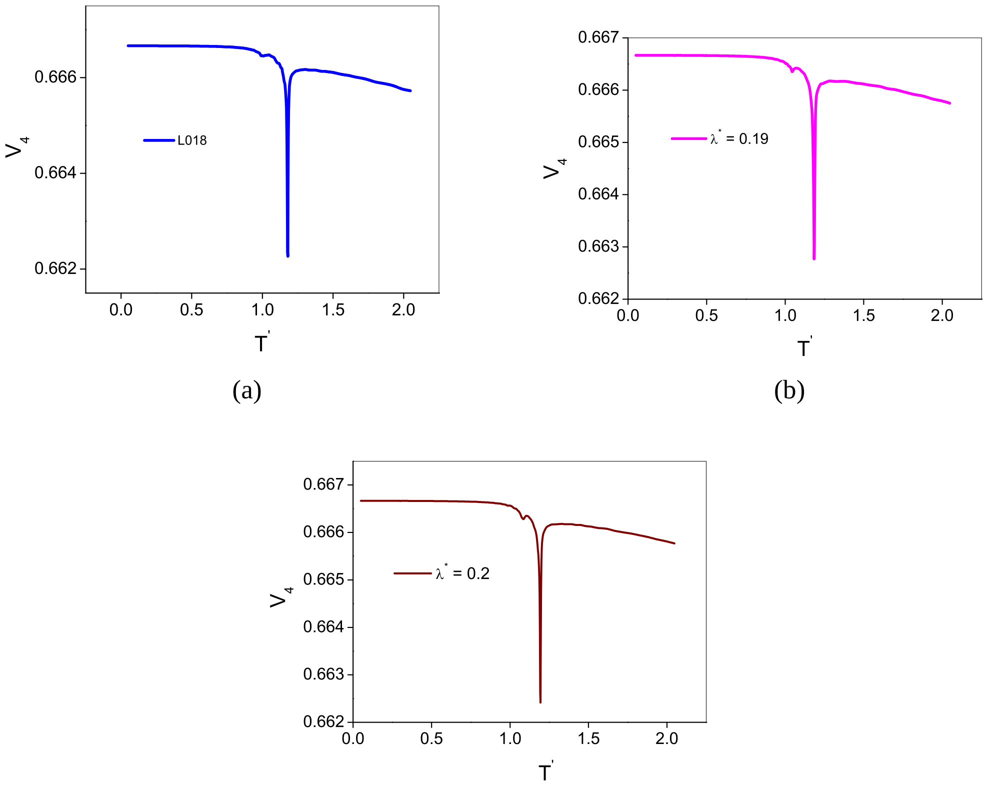

(a) (b)

(c)

Figure 3.9: Energy cumulant for λ^* = (a) 0.18 (b) 0.19 and (c) 0.2

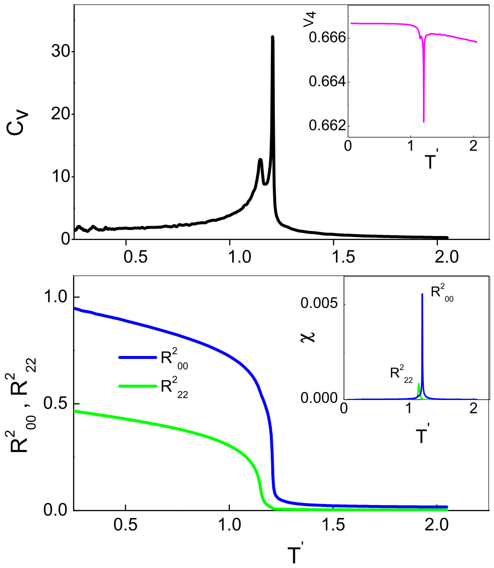

Figure 3.10: Experimental parameters at λ^*=0.22

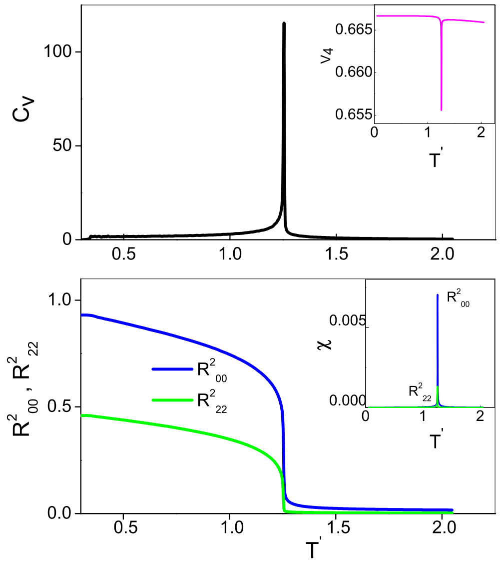

Figure 3.11: Experimental parameters at λ^*=0.26

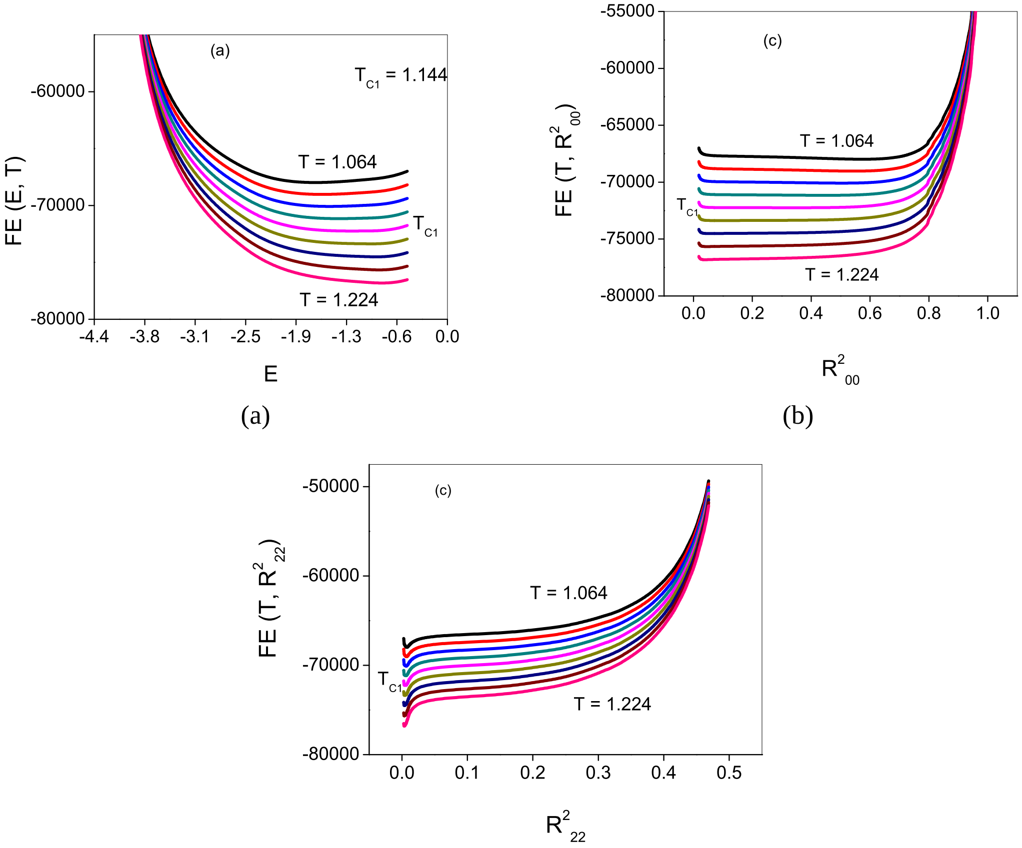

(a) (b)

(c)

Figure 3.12: Variation of free energy at the $I - N_U$ transition as a function of (a) Energy per particle (b) R^2_{00} (c) R^2_{22} for λ^*=0.12

parameter region are on the expected lines of MF theory qualitatively, though certain quantitative differences could be clearly seen.

Figs.3.12(a) - 3.12(c) depict the variation of free energy as the temperature is decreased from T=1.224 in the isotropic phase through the transition temperature T_{C1}=1.144 to the uniaxial phase at T=1.064,for $\lambda^* = 0.12$. The free energy is plotted as a function of energy in Fig.3.12(a) and as a function of order parameters in Figs.3.12(b) and 3.12(c). It can be observed that at any given temperature the free energy attains a minimum value for a small energy range. As the temperature is lowered, this free energy minimum shifts towards lower energies and also broadens. While the shifting to lower energy regions is expected, the broadening is due to contributions from more number of states in the specified energy range. The free energy curves w.r.t R^2_{00} in fig3.10(b) for the same temperatures show the

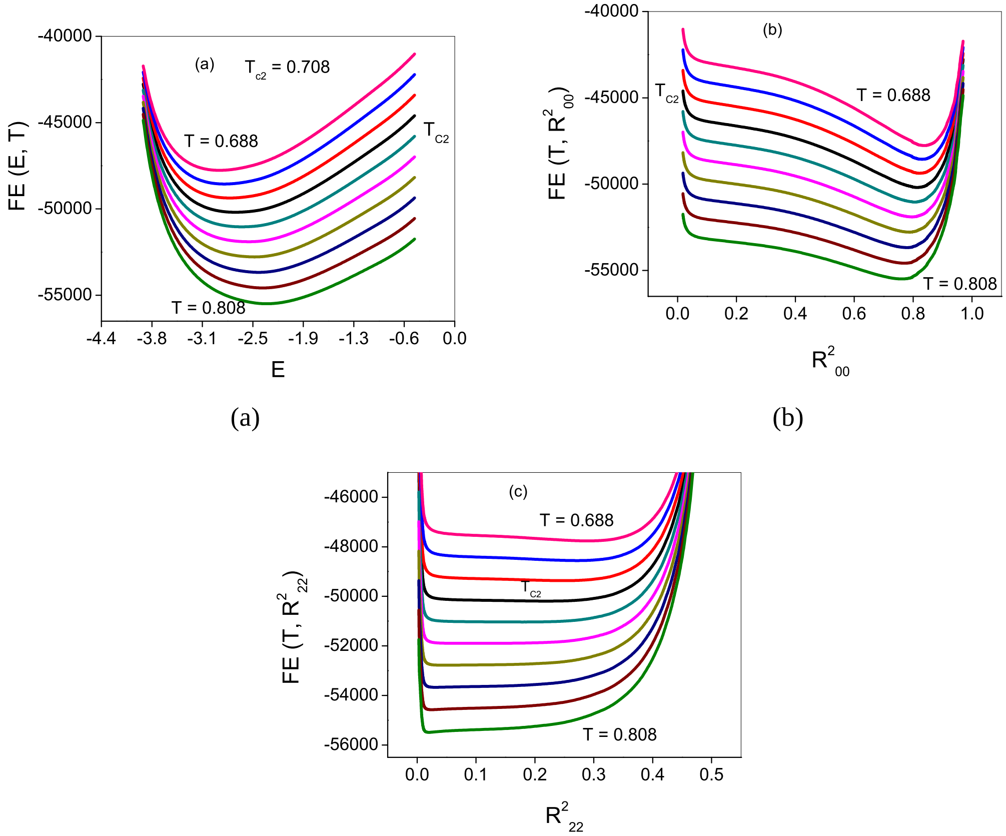

(a) (b)

(c)

Figure 3.13: Variation of the free energy at the $N_U - N_B$ transition as a function of (a) Energy per particle (b) R^2_{00} (c) R^2_{22} for λ^*=0.12

shifting of free energy minimum from $R^2_{00} \sim 0.05$ to $R^2_{00} \sim 0.58$ as the temperature is lowered through the transition. This implies that more uniaxially ordered states contribute to the broad minimum of free energy. The free energy w.r.t R^2_{22} in fig3.10(c) shows that the free energy minimum resides at $R^2_{22} \sim 0.0$ in the neighbourhood of the $I - N_U$ transition. Thus the free energy minimisation at the I-N_U transition arises entirely from development of uniaxial order.

Similar free energy curves plotted in the neighbourhood of the $N_U - N_B$ transition are shown in Figs.(3.13). It can be observed from Fig.3.13(a) that the free energy minimum shifts towards lower energies as the temperature is lowered from $T^{\cdot}$ = 0.808 to $T^{'}$ = 0.688 passing through the uniaxial - biaxial transition temperature $T^{'}$ = 0.708. The free

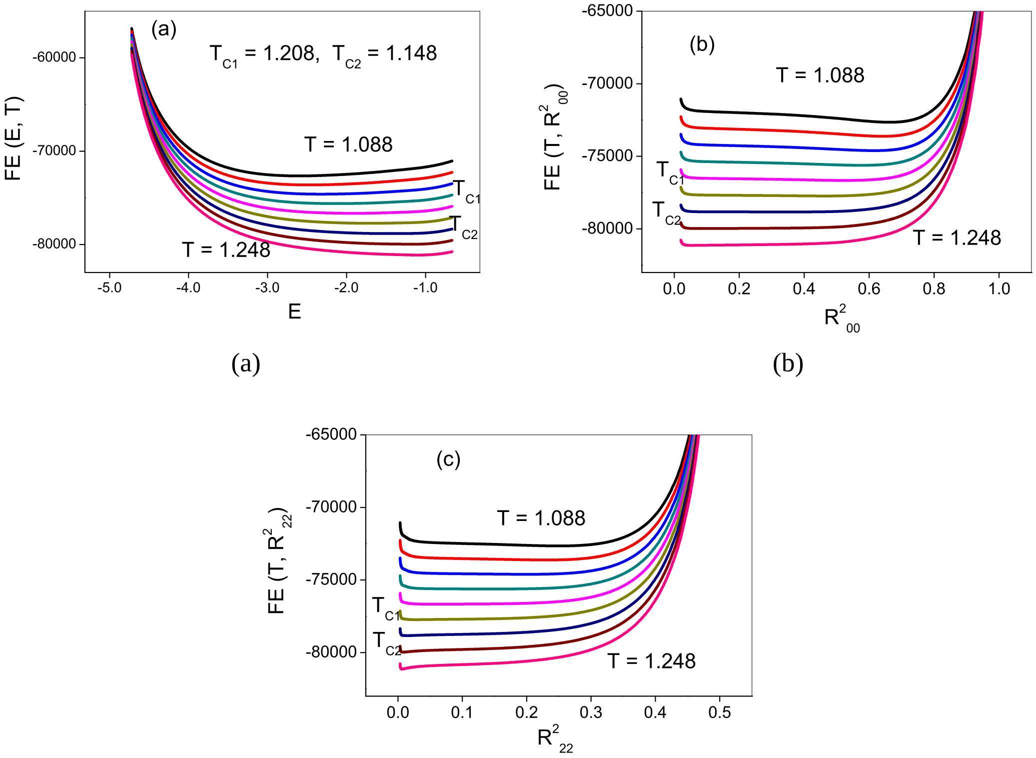

(a) (b)

(c)

Figure 3.14: Variation of the free energy as a function of (a)Energy per particle (b) R^2_{00} (c) R^2_{22} for λ^*=0.22

energy curves with respect to R^2_{00} (Fig.3.13(b))have deep minima throughout this temperature range indicating that long axis ordering continues to increase as the temperature is lowered. The free energy curves w.r.t. R^2_{22} (Fig.3.13(c)) on the other hand are relatively shallow and the minimum shifts to higher values of R^2_{22} as the temperature is lowered into the biaxial phase. The free energy curves reflect the building of biaxial order in both phases at these temperatures close to the transition at T_{C2}. The gradual increase of biaxial ordering at the $N_U - N_B$ transition comes from contributions from large number of microstates with a range of biaxial ordering.

The free energy plots for λ^* = 0.22 encompassing both the transition temperatures are shown in Figs.3.14(a) - 3.14(c). These display essentially the same features as described for λ^* = 0.12.

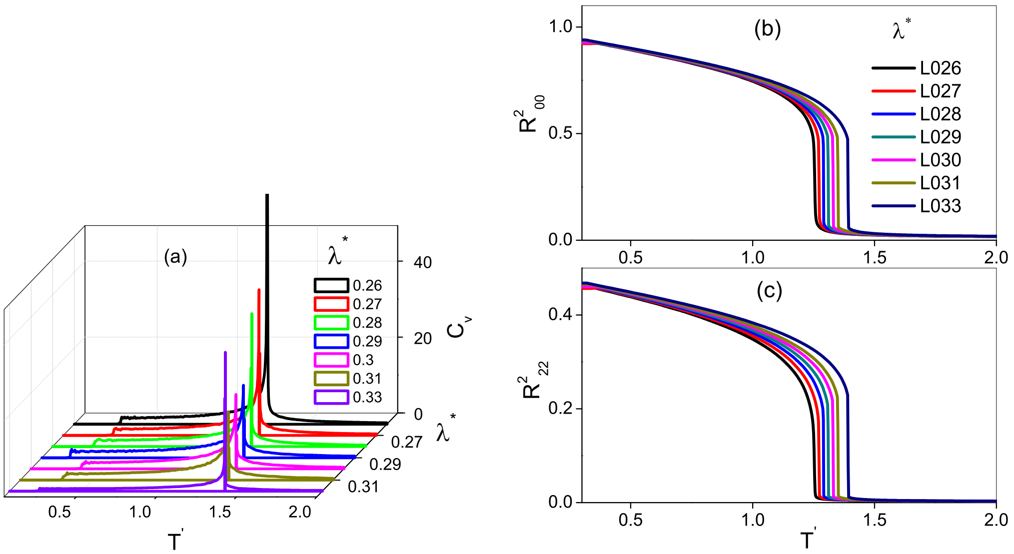

Figure 3.15: Temperature variation of experimental parameters for different values of λ^* in the range (0.26, $1/3$)

3.4.3 Segment OI: Range of λ^*= (0.26 - 0.33)

The simulation results for values of λ^* from 0.26 to 0.33 are shown in Figs.3.15 (a) - (c). These results point to direct $I - N_B$ transition in this region in accordance with the mean field predictions. As λ^* value increases the first order nature of the transition stronger. The results obtained at λ^* = 0.26 were already shown in Fig.(3.11). Fig.(3.16) shows the simulation results at λ^* = 0.33, located at the apex point I in the triangle. According to MF, this point is the intersection of three self conjugated lines in the essential triangle and the phase sequence is described by a single scalar order parameter. The symmetry requires a single first order isotropic - biaxial phase transition to occur at this point.

The simulation results agree with these predictions as evident from the strong C_V peak in Fig.(3.16). The energy cumulant shown in the inset suggests unambiguously this expectation. The sharp and concurrent increase of the biaxial order along with the uniaxial order indicates the onset of the biaxial phase from the isotropic phase, and the susceptibilities (inset) is also indicative of the nature of this transition. The free energy profile plotted as a function of the biaxial order R^2_{22} is shown in Fig.(3.17). It may be observed that two free energy minima exist at the transition which substantiates the first order nature of the

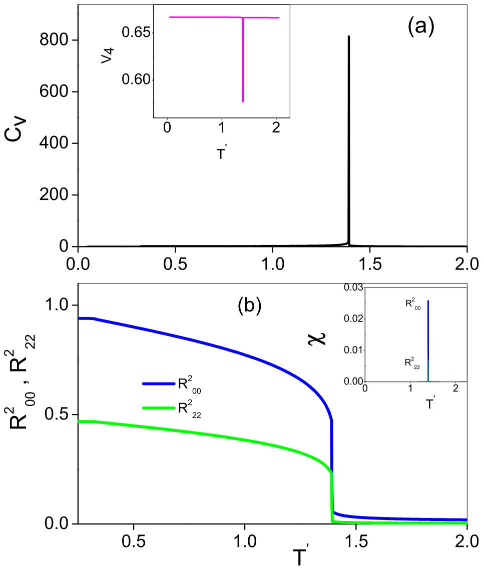

Figure 3.16: (a) Specific heat profile with (inset) energy cumulant (b) Order parameters with (inset)susceptibility profiles for λ^*=0.33

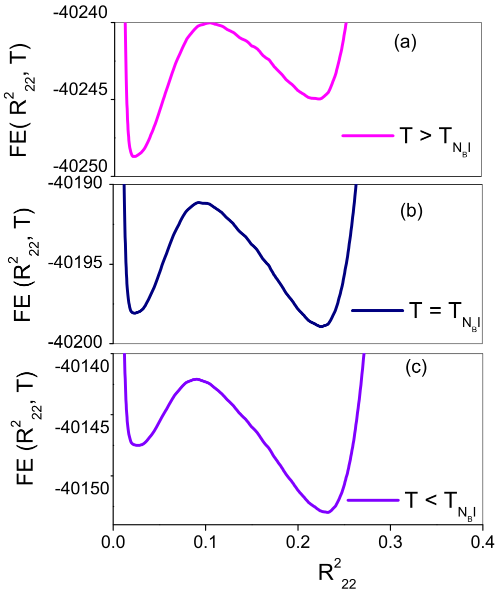

Figure 3.17: Free energy as a function of biaxial order at temperature (a) T = 1.402 (b) T = $T_{N_{BI}}$ = 1.4 (c) T = 1.398 for λ^*=0.33 (L=15)

transition. Similar minima exist in the free energy profile plotted with respect to uniaxial order R^2_{00}. The strong nature of the transition is clearly brought out by the explicit features of the free energy profile at the transition with respect to the order parameters: the large free energy barrier separating the two states, their coexistence at the transition temporary. It is to be noted that this feature is explicitly evident even at the modest lattice size L= 15. The point I is special in the sense that it is the intersection of three uniaxial torque axes - each around the each of the molecular axes -, and at this point the interaction is purely biaxial [7].

3.4.4 Segment IV

This line segment is the self conjugated line IV in the essential triangle, wherein the Hamiltonian is globally attractive till the point T and then becomes partly repulsive along segment TV. The value of λ^* increases from $1/3$ to 0.933 as we traverse from I to V on the triangle. According to mean field model, IV is a uniaxial torque line, along which the restoring torque is uniaxial around the molecular $\boldsymbol{e}$-axis. Mean field predicts a first order isotropic-biaxial transition along this line segment till a tricritical point C_3 $(5/29, 19/27)$ corresponding to λ^* = 0.54, at which nature of the isotropic-biaxial transition changes to second order. C_3V is a line of Landau triple points where a biaxial phase continuously branches off from the uniaxial phase. Point T on the segment C_3V is special: on one hand it is a bounding point where the fully attractive Hamiltonian turns partly repulsive: and it is also on the dispersion parabola defining a unique point where a single transition from isotropic to the biaxial phase predicted by MF [6] and confirmed by earlier Monte Carlo simulations [15]. Discusiion of the results in this section is again divided into three subsections for convenience.

3.4.5 Segment IV: Range of λ^* = ($1/3$,0.53)

The specific heat, uniaxial order and biaxial order profiles for values of λ^*=$1/3$ to 0.53 are presented in Figs.3.18 (a)-(c). It may be seen that our results confirm with the mean field

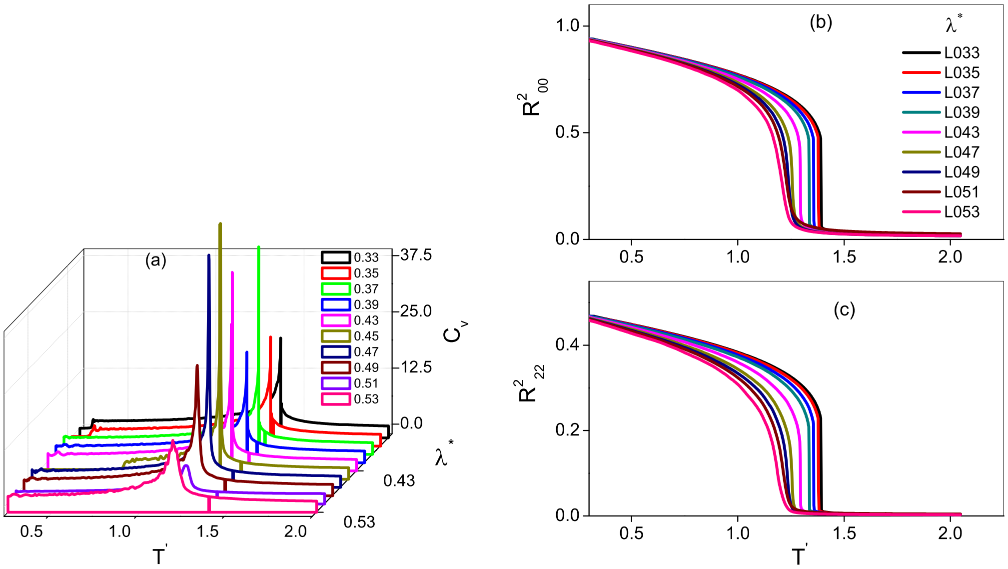

Figure 3.18: Temperature variation of order parameters for values of λ^* in the range $(1/3$, 0.53)

results along this line segment. It is to be noted from fig. 3.18(a) that the $I - N_B$ transition temperature remains fairly constant in this region. In addition we present the results at one of the values of λ^*(= 0.47) included in this region, separately for bringing out salient features of this transition, in Fig.3.19.

3.4.6 Segment IV: Range of λ^* = (0.54 - 0.733)

The specific heat profiles obtained for λ^* values ranging from 0.53 to 0.733 are presented in Fig.(3.20). We find that these clearly show the evidence of two transitions starting from λ^*=0.54, deviating qualitatively from men field prediction of a single $I = N_B$ transition. The transition peaks split gradually on increasing λ^*, and within this range, have a maximum temperature difference between the transitions at λ^* = 0.733 (T on the triangle). This is the landau point on the dispersion parabola with coordeinates $(1/3, 1/9)$ .Mean field theory predicts that the Landau point should host a direct isotropic - biaxial transition. We also find that the simulations based on Metropolis sampling (constituting the B-ensembles) in this region differ qualitatively from the current results from the entropic sampling data.

A comparative study of the specific heat profiles derived from the B- and RW-ensembles

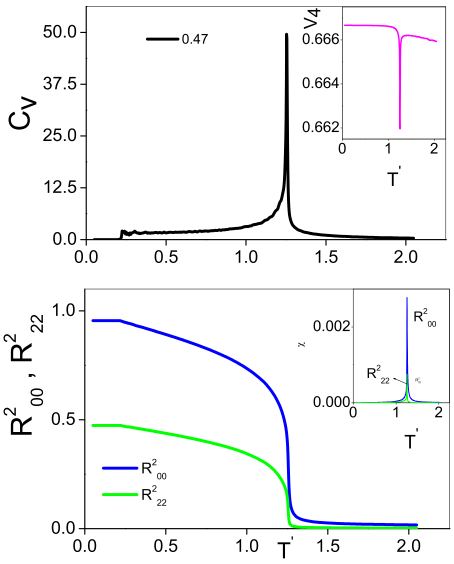

Figure 3.19: (a) Specific heat profile with (inset) energy cumulant V_4 (b) Order parameters with (inset) susceptibility profiles for λ^*=0.47

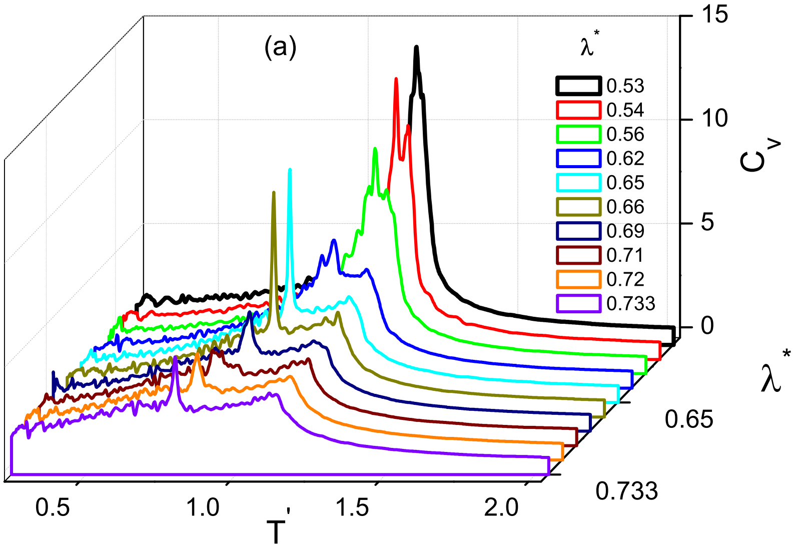

Figure 3.20: Temperature variation of the specific heat for values of λ^* in the range (0.53, 0.733)

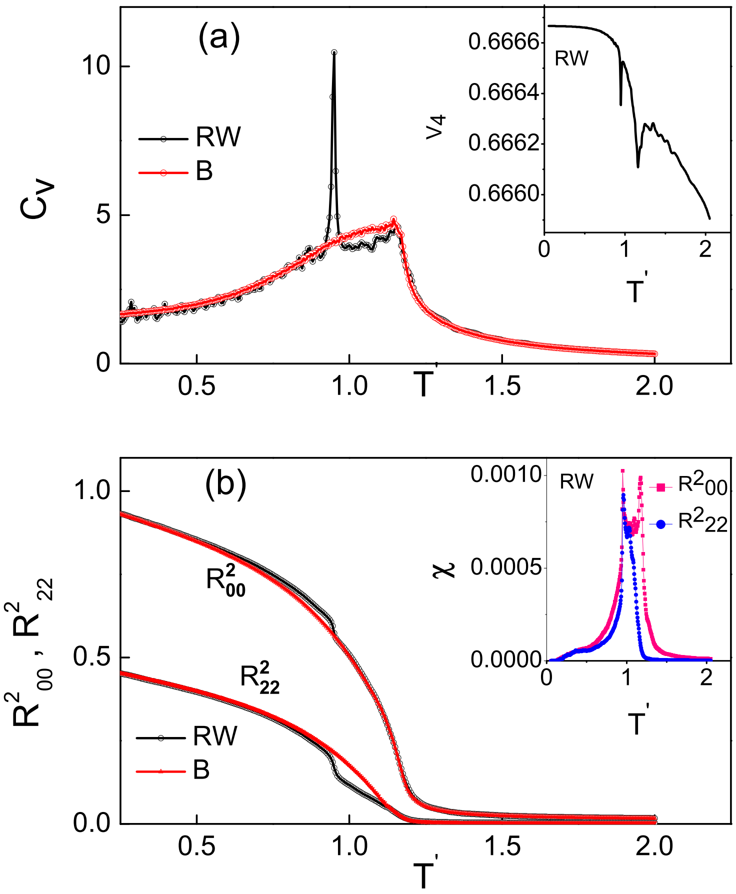

Figure 3.21: (a) Temperature variation of (a) Specific heat C_v (with energy cumulant V_4 as an inset), and (b) order parameters (with their susceptibilities (χ') as an inset), obtained from RW- and B-ensembles at λ^* = 0.65 (0.264, 0.158). The susceptibility of R^2_{00} shows the signatures of both transitions whereas the susceptibility of R^2_{22} shows a single peak at T_{C2}. Clear signature of the second transition, and its first order nature, may also be inferred from the V_4 data.

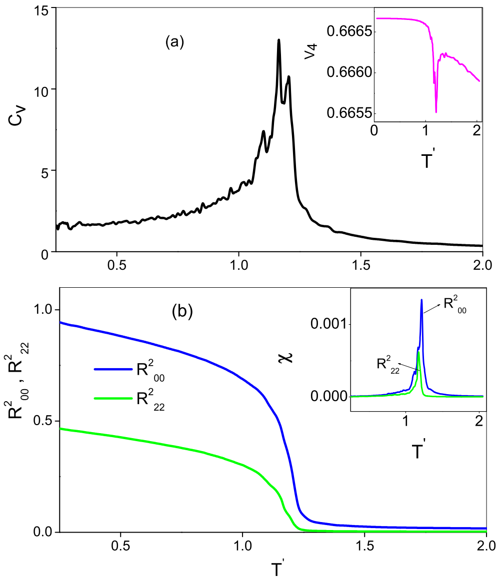

Figure 3.22: (a) Specific heat profile with (inset) energy cumulant V_4 (b) Order parameters with (inset) susceptibility profiles at λ^*=0.54

is depicted in Fig. 3.21(a), along with V_4 as an inset at λ^*= 0.65 (0.264, 0.158). The corresponding order parameters, and their susceptibilities are shown in Fig. 3.21(b). It may be observed from Fig. 3.21(a) that specific heat profile derived from the RW-ensembles exhibits two transitions whereas that derived from the B-ensembles in contrast exhibits a broad hump below the high-temperature C_v peak. The two order parameters obtained from RW-ensembles exhibit a jump in their values coincident with the second low - temperature C_v peak, whereas the orders obtained from the B - ensembles show a monotonic increase, as shown in Fig.3.21(b). The susceptibility of R^2_{00} (from RW-ensembles) shows the signatures of both the transitions whereas the susceptibility of R^2_{22} shows a single peak at T_{C2}. The WL simulation results for specific λ^* values(0.54, 0.58, 0.62, 0.66, 0.69 and 0.72) are shown in Figs.(3.22) - (3.27). These depict the specific heat with energy cumulant V_4 (inset) and order parameter profiles along with respective susceptibilities χ (inset) .

The data presented in Figs.(3.22) - (3.27) have some common features. The energy cumulant V_4 shown in the inset of each of the figures indicates the onset of a second dip at a lower temperature indicating the progression of first order nature of the second transition. It may be observed that the dip in the cumulant at the second transition is maximum at λ^*=

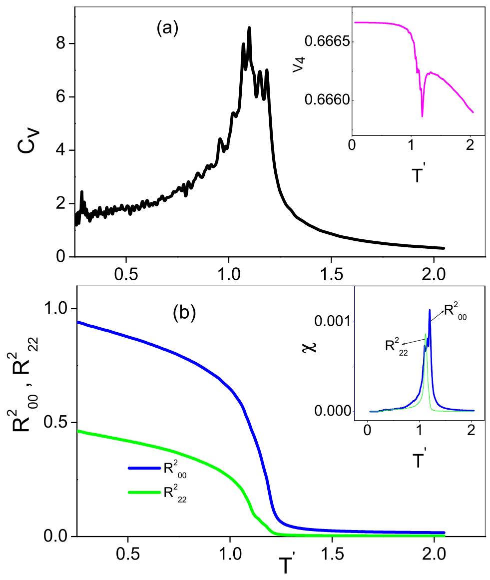

Figure 3.23: (a) Specific heat profile with (inset) energy cumulant V_4 (b) Order parameters with (inset) susceptibility profiles at λ^*=0.58

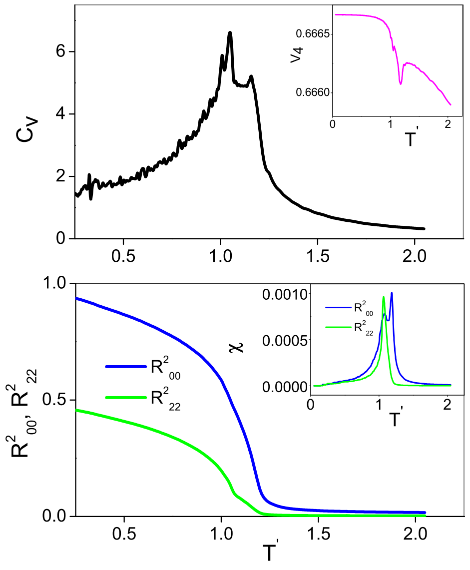

Figure 3.24: (a) Specific heat profile with (inset) Binder's cumulant V_4 (b) Order parameters with (inset)susceptibility profiles for λ^*=0.62

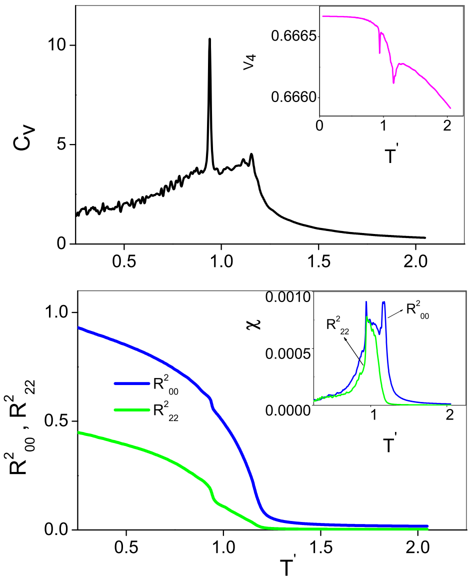

Figure 3.25: (a) Specific heat profile with (inset) energy cumulant V_4 (b) Order parameters with (inset) susceptibility profiles at λ^*=0.66

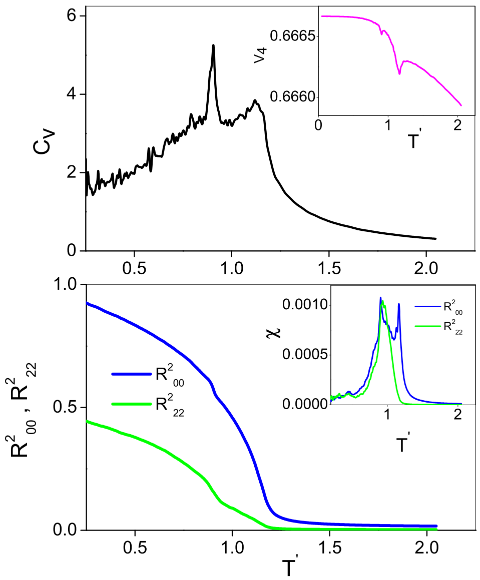

Figure 3.26: (a) Specific heat profile with (inset) energy cumulant V_4 (b) Order parameters with (inset) susceptibility profiles at λ^*=0.69

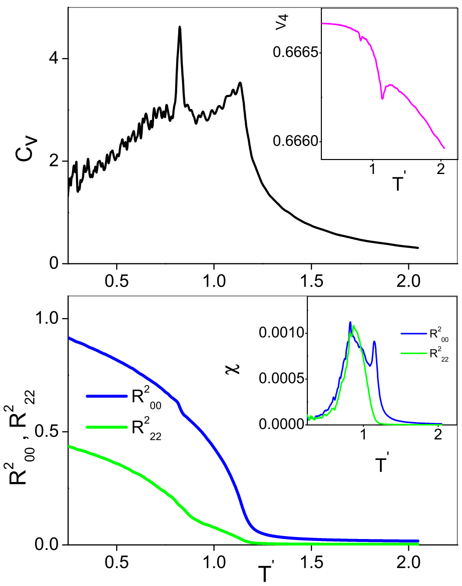

Figure 3.27: (a) Specific heat profile with (inset) energy cumulant V_4 (b) Order parameters with (inset) susceptibility profiles at λ^*=0.72

0.66 and it decreases for higher values of λ^*.

The nature of the phases underlying below the isotropic phase is obtained from the order parameter profiles and the susceptibility peaks. The order profiles indicate the onset of a biaxial phase at T_{C1} itself in which the growth of the biaxial order is only marginal, as compared to uniaxial order. However, both the uniaxial and biaxial order parameters display a sudden jump signalling the low temperature transition at T_{C2}, and subsequently increase rapidly (particularly R^2_{22}) as the temperature is lowered further. This behaviour is prominent for λ^* in the neighbourhood of λ^* 0.66. The susceptibility of the order parameters shows two peaks for R^2_{00} at both the transitions, whereas the susceptibility of R^2_{22} shows only a single peak at T_{C2}, for all values of λ^*.

We conclude from the above observations that an initial biaxial phase N_{B1} is formed on cooling from the isotropic phase in this range of λ^* values. It appears to be a weak biaxial phase sustaining only low intrinsic biaxial order. On cooling further a second biaxial phase N_B appears to form at T_{C2}, and this phase supports development of significant , and normal (as per expectations of MF theory), biaxial order R^2_{22} as evident from the figures above. Since the symmetry of both phases is the same, the transition is expected to be first order, and the energy cumulant data corroborate this argument convincingly.

Representative free energy profiles computed making use of the DoS data as a function of energy and two order parameters at the isotropic - biaxial phase (N_{B1}) transition temperature (T_{C1}) are shown in Figs.3.28 (a)-(c). It is observed that these profiles with respect to R^2_{00} show the presence of a slight kink whose height seems to increase as λ^* value increases from 0.54 to 0.733. Similar behaviour is also observed in the free energy curves with respect to R^2_{22}. These kinks perhaps are pointers to the presence of free energy barriers inherent in the system inhibiting the growth of the biaxial ordering in the N_{B1} phase. Interestingly, and perhaps satisfactorily, such graphs with respect to the energy of the system are however devoid of such curiosities. Similar free energy curves were plotted at the $N_{B1} - N_B$ transition and are shown in Figs 3.29(a) - (c). It can be observed that these curves do not show any kinks with respect to order parameters. These curves indicate that onset of ordering takes place rapidly and smoothly at the low temperature transition.

3.4.7 Segment IV: Range of λ^* = (0.733 - 0.93)

The partly repulsive region, TV in Fig.3.1) proved to be prohibitively expensive computationally for purposes of entropic sampling, and even for smaller systems (like L=10), satisfactory convergence of the population histogram to qualify to be the DoS could not be achieved in realistic time frames. Thus no data could be extracted in this region from WL sampling procedure. Failure of this algorithm, even assisted by frontier sampling, normally points to the preponderance of microstates in the higher energy region, at the exclusion of low energy (highly ordered states). Perhaps we could conjuncture at this point that the presence of partly repulsive contributions to the Hamiltonian (which also demands mini-max principle in carrying out mean field analysis in this region) is not allowing the algorithm to exhaust (in the sense of sampling) the high energy regions regions adequately thereby inhibiting the normal development of DoS.

We therefore rely on the data obtained from conventional Metropolis sampling in this region. It is interesting to note that the broad hump observed in the specific heat profiles

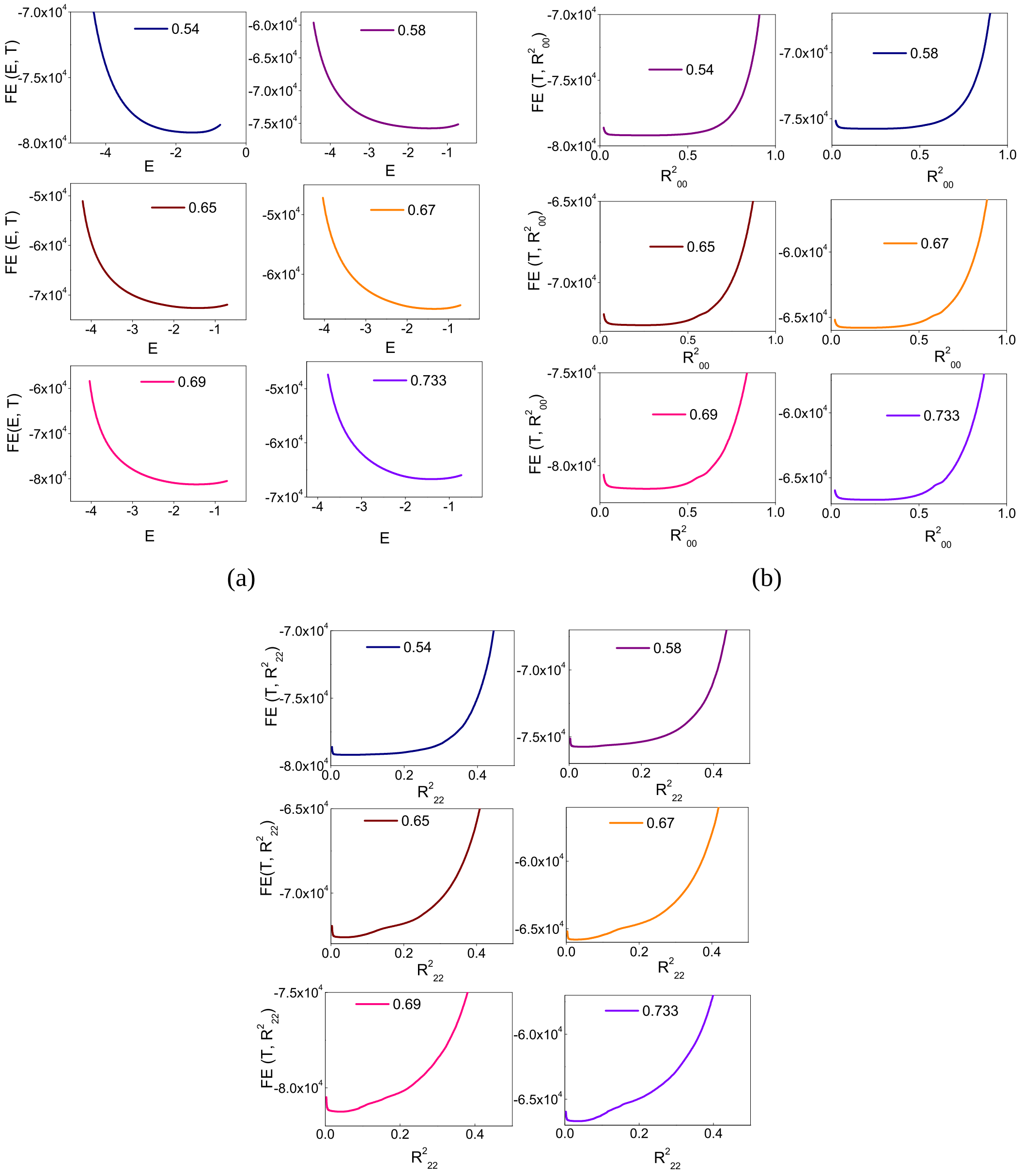

(a)

(b)

(c)

Figure 3.28: Variation of representative free energy as a function of (a) Energy (b) R^2_{00} (c) R^2_{22} at I - N_{B1} transition (T_{C1}), for various λ^* values in region C_3T of the essential triangle.

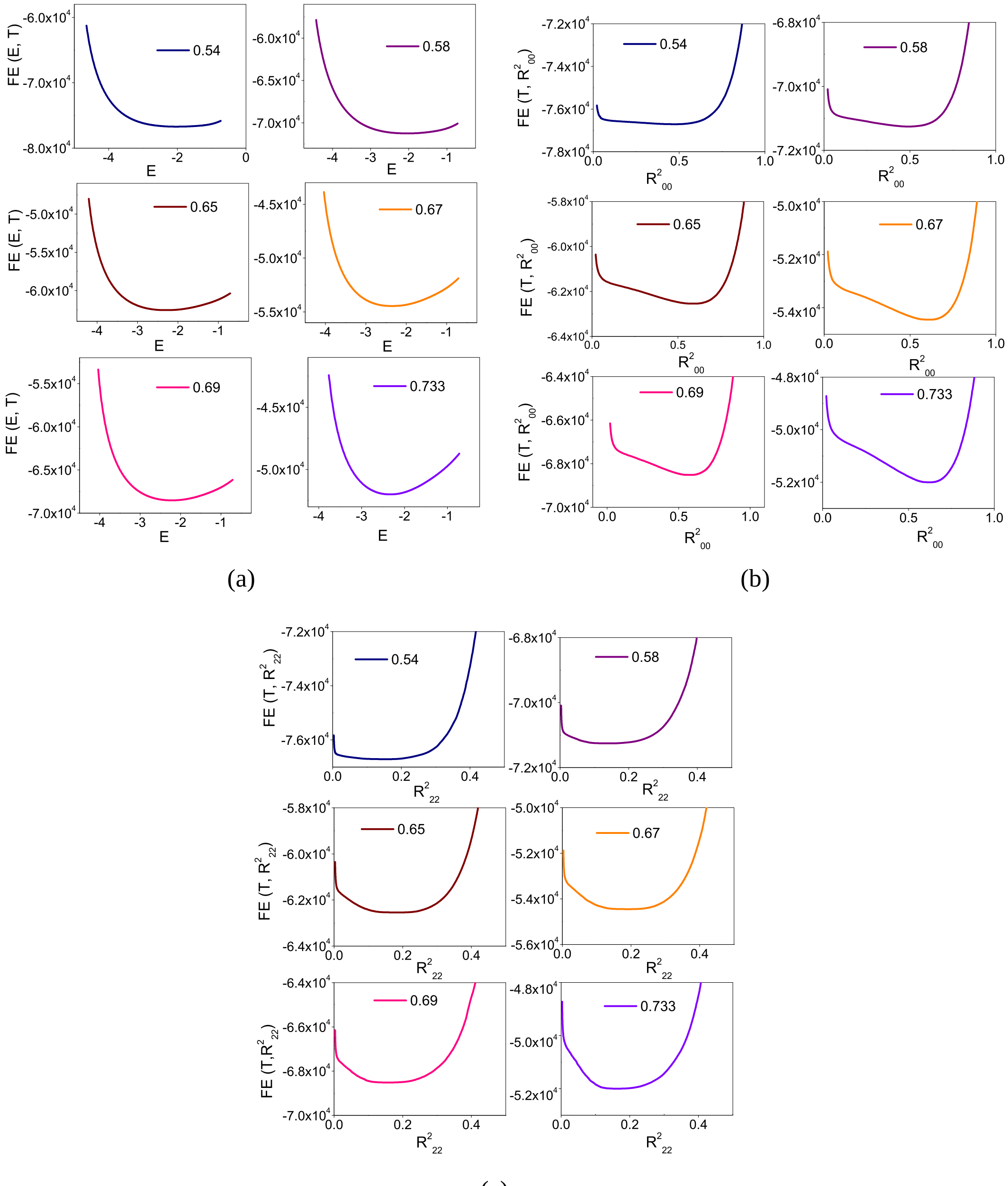

(a) (b) (c)

Figure 3.29: Variation of Landau Free energy as a function of (a) Energy (b) R^2_{00} (c) R^2_{22} at $N_{B1} - N_B$ transition (T_{C2}), for various λ^* values in region C_3T of the essential triangle.

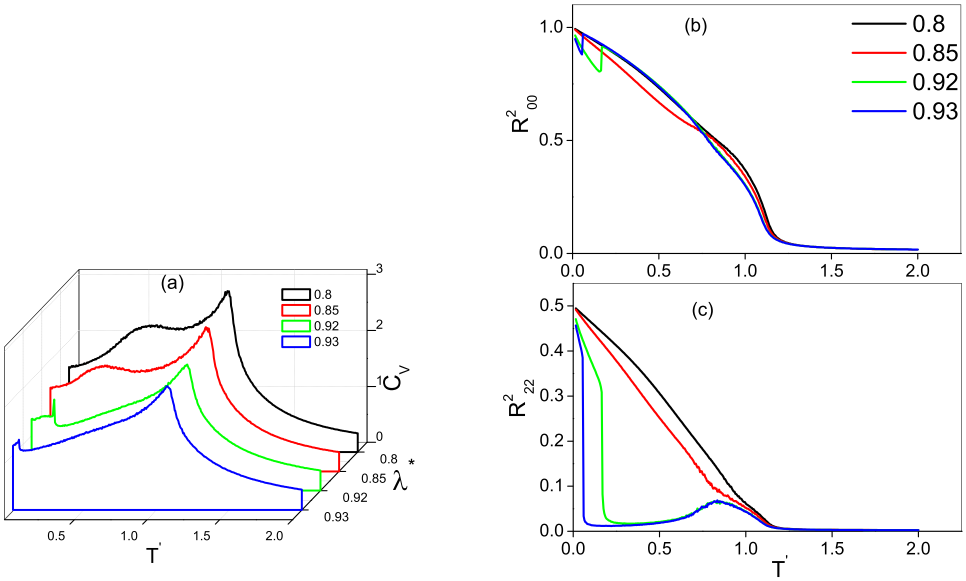

Figure 3.30: Temperature variation of order parameters for values of λ^* in the range (0.733, 0.93), based on B-ensembles

at $\lambda^* \lesssim 0.733$ decreases as the $\lambda^* \rightarrow 0.933$. We also observe that the phase underlying the isotropic phase is biaxial as indicated by the growth of biaxial order. For $\lambda^* \geqslant 0.9$ the degree of this order starts decreasing in this phase. The fact that the biaxial order tends to be low as $\lambda^* \rightarrow 0.933$, and corresponding transition temperature is suppressed towards zero progressively are rather satisfactory, in the sense that in this asymptotic limit biaxial stability terminates at V, and these simulations need to consistent with that requirement. These observations are consistent with the earlier Monte Carlo data (the so called μ - model($0 < \mu < 1$) [28]).

3.5 Phase Diagram from MC Simulations

We plotted the phase diagram from the above data by choosing 56 values of λ^* distributed over the arc OIV (Fig.(3.1)). Temperature location of the peaks of C_v profiles and of energy cumulant V_4 at different λ^* values, and identification of the liquid crystal phases from the corresponding order parameter variations (assisted by their susceptibilities), result in the phase diagram shown in Fig. 3.31 [37]. The temperature $T^{'}$ of the simulation is scaled to conform to the values $1/\beta^*$ used in the mean field treatment as discussed in section 3. We

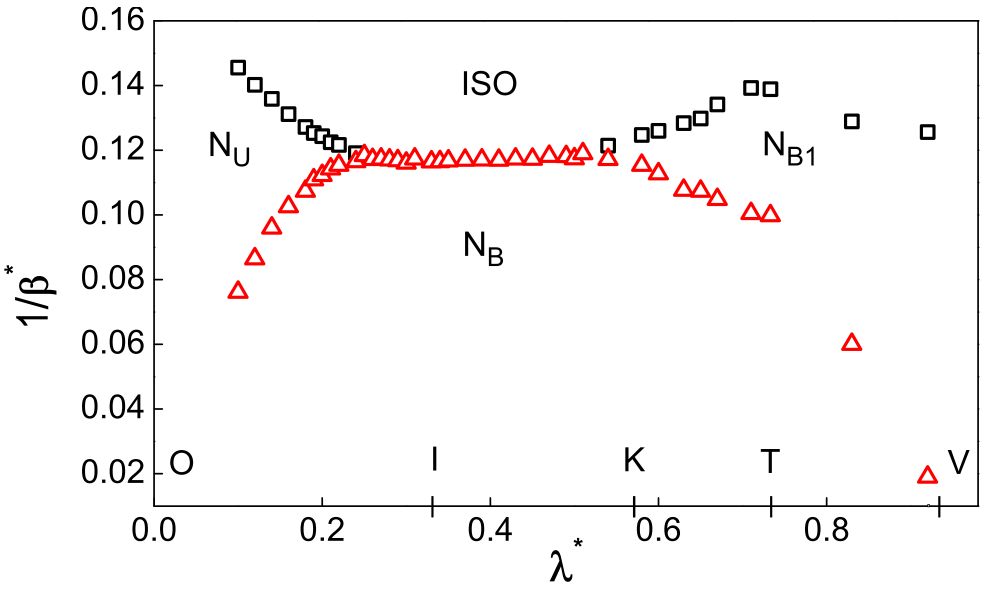

Figure 3.31: Phase diagram as a function of λ^* from RW-ensembles. The transition temperature $1/\beta^*$ is scaled to conform to mean - field values as indicated in the text. Points along OIV in Fig. 3.1 are mapped onto the λ^* - axis for reference. An additional biaxial - biaxial transition is observed in the region KTV in place of a single transition (to the biaxial phase) predicted by the mean-field theory.

present the MF predicted phase diagram in Fig.3.36, for ready comparison.

We find that these two phase diagrams differ qualitatively in the region C_3TV of the essential triangle. We observe that the direct transition from the isotropic to biaxial phase is replaced by two transitions in which an intermediate biaxial phase occurs between these two phases. Also we observe that Monte Carlo simulations based on Metropolis algorithm (constituting B-ensembles) largely support the mean-field observations in the region IT. The MF and the current MC phase diagrams differ qualitatively beyond $\lambda^* \gtrsim 0.54$, very close to the point K (Fig. (3.1). Apart from the isotropic to biaxial transition at T_{C1}, the appearance of a second C_v peak at T_{C2} indicates a second biaxial-biaxial first-order transition, as mentioned above.

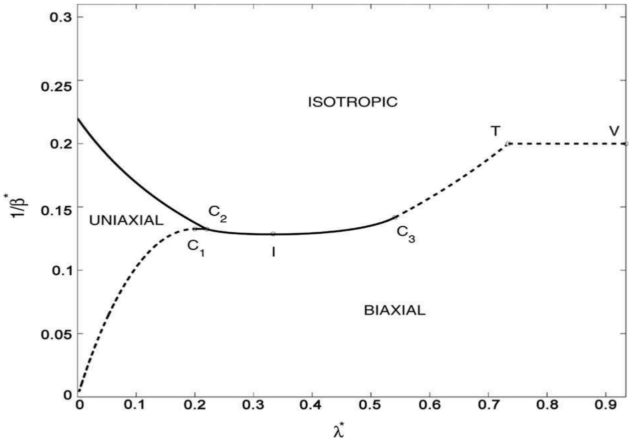

Figure 3.32: MF phase diagram along the upper boundary of the essential triangle. (Giovanni De matteis *et al Continuum. Mech. Thermodyn.* **19**, 1-23 (2007)

3.6 Discussion of Results

In order to determine the origin of the additional low temperature specific heat peak observed in the region C_3TV, we examined the microstates obtained from the B- and RW-ensembles at representative λ^* values. The Landau triple point (LP) T which, according to the mean field analysis, hosts a direct $I = N_B$ transition, is a point of great interest. It also lies on the dispersion parabola which forms a boundary between attractive and repulsive Hamiltonians.

A comparative study of the averages calculated from B- and RW- ensembles at the Landau point (λ^*=0.733) is shown in Fig 3.33. The specific heat profile obtained from the RW-ensemble exihibits an additional peak at T_{C2} (= 0.801) in addition to a high temperature transition peak at T_{C1} (= 1.121), for size L=20.

We depict the contours of the distribution of microstates in the entropic ensemble collected at the Landau point T, plotted as a function of their energy (per site) and order parameters in Figs. 3.31 (a) and (b). Fig. 3.34(a) depicts the entropic ensemble for uniaxial order on which the thermal averages of R^2_{00} obtained from WL simulation (RW-ensemble) and the Boltzmann simulation (B-ensemble) are superposed. The traversal path of the B-ensemble average is seen to be encompassing regions corresponding to contour peak positions, whereas the RW- ensemble average traverses a path which encompasses a larger

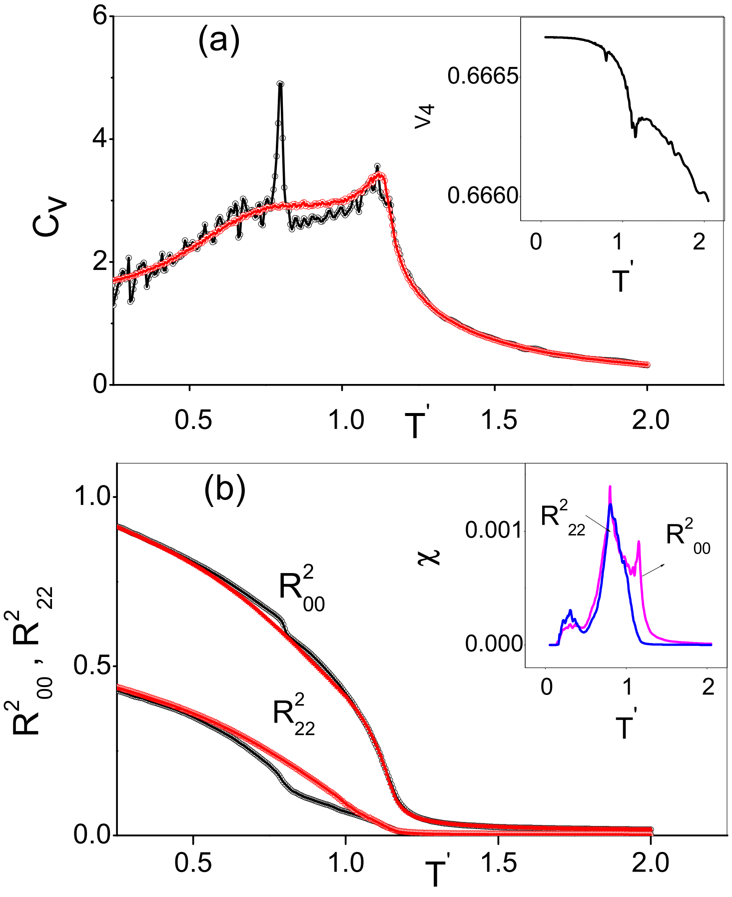

Figure 3.33: (a) Temperature variation of (a)Specific heat C_v (with energy cumulant V_4 as an inset), and (b) order parameters (with their susceptibilities (χ's) as an inset), obtained from RW- and B-ensembles at λ^* = 0.733 (1/3, 1/9). The results obtained from RW- and B-ensembles are indicated by black and lines respectively.

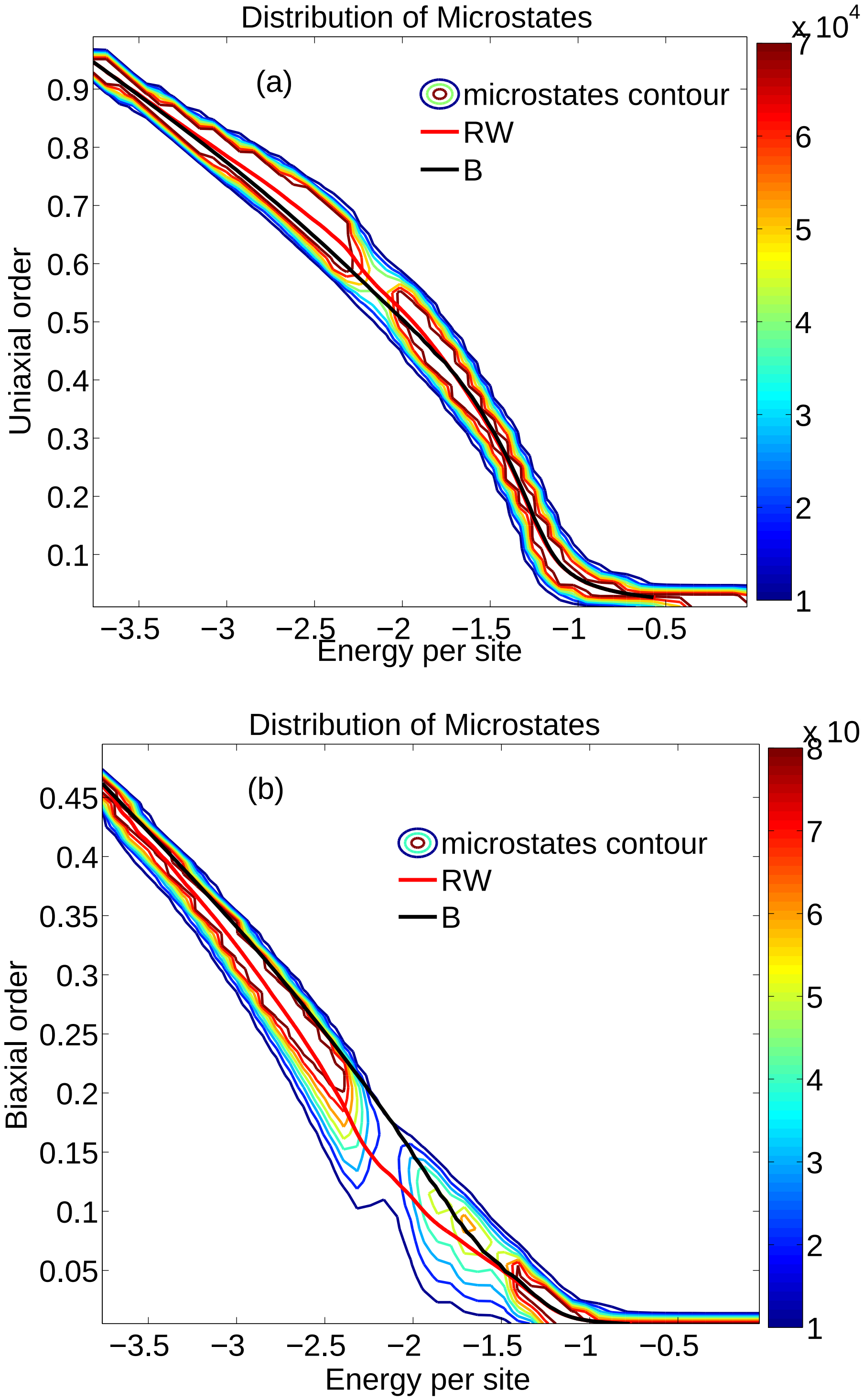

Figure 3.34: Contour plots of the distribution of microstates in the entropic ensemble at $\lambda^* \simeq 0.73$: (a) Microstate energy versus its uniaxial order and (b) microstate energy versus its biaxial order. The superimposed red and black lines are thermal averages from RW- and B-ensembles respectively.

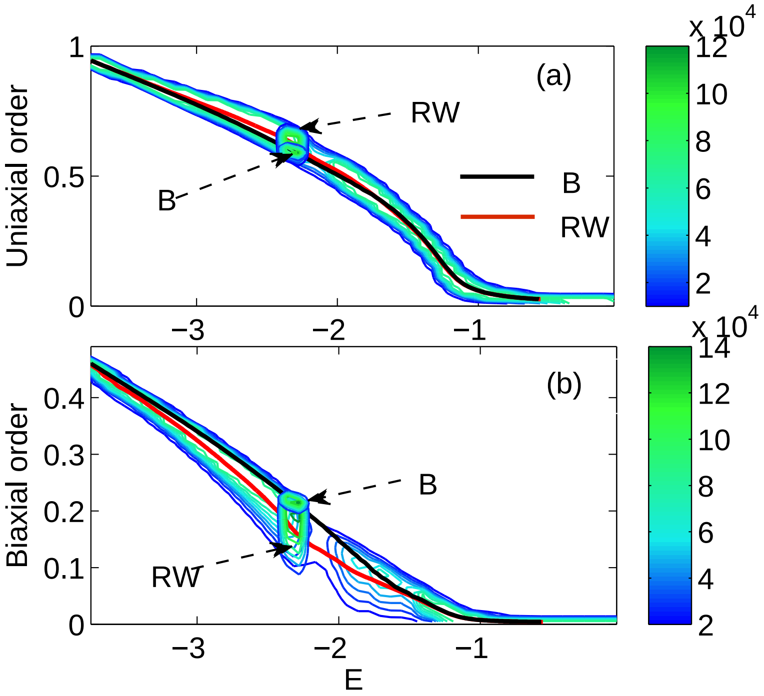

Figure 3.35: Contour plots of the distribution of microstates in the entropic ensemble at $\lambda^* \simeq 0.73$: (a) Microstate energy versus its uniaxial order and (b) microstate energy versus its biaxial order . The contour maps of the distributions from RW- and B-ensembles equilibrated at temperature close to T_{C2} are superposed. The thick red and black lines are corresponding plots of thermal averages obtained from these ensembles respectively.

collection of microstates even from sparse regions. This is a manifestation of the process of collection of microstates of the entropic ensembled in accordance with the estimated DoS, and subsequent reweighting which now permits within the equilibrium (canonical) ensemble even very rare states which are normally missed by Metropolis sampling. Subsequently, the averages from RW and B ensembles differ in this region, as they should. A similar scenario is observed in Fig. 3.34(b) which depicts the entropic ensemble and thermal averages for R^2_{22}. It is observed that the reweighted average starts differing starting at a point in higher energy region, and traverses a path which is qualitatively different, extending even into the region of deep biaxial phase.

We collected the microstates from B- and RW-ensembles equilibrated at the same temperature very close to T_{C2} . The contours of these canonical ensembles were plotted as a function of energy (per site) and order parameters. These were then superposed on the entropic ensemble (see Figs. 3.31(a) and (b)). The resulting composite contour plots are shown in Figs. 3.33 (a) and (b). While the average values and widths of the energy distributions from the two canonical ensembles are seen to be comparable, distributions of the microstates with respect to the order parameters are very different. Relative to the B-ensemble, the microstates belonging to the RW-ensemble have different contour peak positions with larger fluctuations, with R^2_{00} visiting much higher values and R^2_{22} correspondingly much lower values. The observed differences in the thermal behaviour of their respective averages are also shown (black and red solid lines in Figs. 3.35(a) and (b)).

We examined the decomposition of the total energy of an approximate micro-canonical ensemble into its components in the neighbourhood of the second transition. For purposes of analysis, we now rewrite the Hamiltonian in terms of contributions from pair-wise interactions between corresponding molecular axes [28], as

$$H = \epsilon[\mu G_{11} + (-2G_{33} - 2G_{22} + G_{11})] \tag{3.6.1}$$

Here, the indices N = 1, 2 and 3 represent the molecular axes $\boldsymbol{e}, \boldsymbol{e}_\perp, \boldsymbol{m}$ respectively, and $G_{jk} = P_2(f_{jk})$ where $P_2(.)$ denotes the second Legendre polynomial. In a lattice model, f_{jk} represents the inner product of the j^{th} axis of a molecule with the k^{th} axis of a nearest neighbouring molecule. We present our analysis of this ensemble in Figs. 3.34(a)-(f).

The distribution of the total energy (per site) of the microstates within a narrow range (-2.25 ± 0.0015) is shown in Fig. 3.34(a), while distributions of energy components G_{11} (0.37 ± 0.01), G_{22} (0.60 ± 0.07) and G_{33} (0.60 ± 0.07) are successively shown in Figs. 3.36(b)-(d). Clearly the fluctuations of these components occur so as to conserve the total energy within its width. The interaction energies of the two molecular axes, $\boldsymbol{e}_\perp$ and $\boldsymbol{m}$, with the corresponding axes of the neighbouring molecules are seen to fluctuate more widely relative to the $\boldsymbol{e}$ - axes coupling energies. Fig. 3.36(e) shows the variation of uniaxial and biaxial order parameter values of the microstates with respect to G_{22} (similar plots result with respect to G_{33} as well). Interestingly, the fluctuations on either side of G_{22} about its average lead to an increase in the uniaxial order of the microstates, with

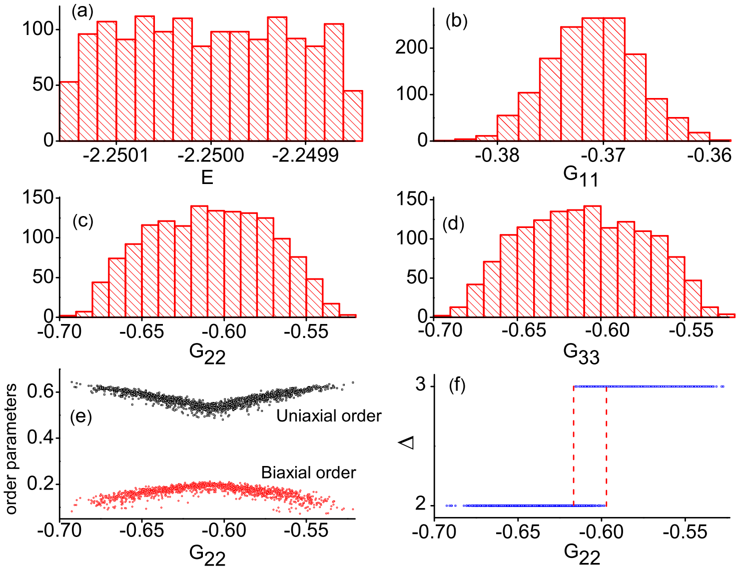

Figure 3.36: Micro-canonical data at $\lambda^* = 0.65$ as a function of energy per site (a) Microstate energy distribution (b) G_{11}-distribution (c) G_{22}-distribution (d) G_{33}-distribution (e) order parameters versus G_{22} (f) index of the eigenvector of maximum order of the microstates, Δ.

simultaneous decrease in their biaxial order. This observation led to an examination of the ordering tensors $(\boldsymbol{Q}_{\boldsymbol{ee}}, \boldsymbol{Q}_{\boldsymbol{e}_\perp \boldsymbol{e}_\perp}, \boldsymbol{Q}_{\boldsymbol{mm}})$ of the three molecular axes, determining their respective maximum eigen values [15]. The eigen vector corresponding to the maximum of these maxima is then taken as the primary order direction (calamitic axis). Indexing its direction as Δ (Δ = 1, 2 and 3) for the three possibilities of the ordering tensors of $(\boldsymbol{e}, \boldsymbol{e}_\perp, \boldsymbol{m})$ defining the calamitic axis of the sample, respectively, we show the variation of Δ with G_{22} in Fig. 3.36(f) (a complimentary plot obtains with G_{33}). In a small central region of G_{22} (0.60 ± 0.01) a degeneracy of the top two eigen values (corresponding to the ordering tensors of $\boldsymbol{e}_\perp$ and $\boldsymbol{m}$ axes) is observed, and hence the calamitic direction seems to fluctuate with equal probabilities within this narrow band between the corresponding eigen vectors (as an artefact of the inevitable rounding off errors during computation). For fluctuations outside this region, Fig. 3.36(f) shows that this degeneracy is lifted, and one of the eigen vectors (of tensors of $\boldsymbol{e}_\perp$ or $\boldsymbol{m}$) remains the unique calamitic axis depending on the sign of the fluctuation, indicating that the corresponding eigen value determines the dominant order, which is mapped to R^2_{00} by definition. Observed decrease of the biaxial

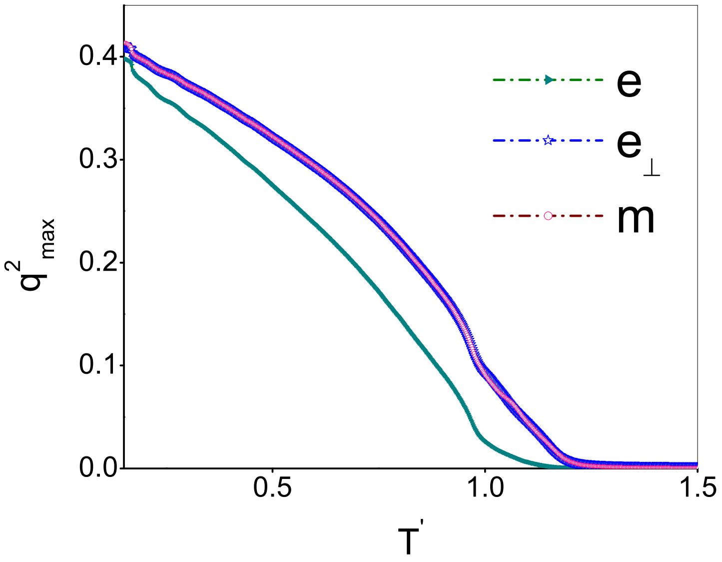

Figure 3.37: The long range order of the three molecular axes $(\boldsymbol{e}, \boldsymbol{e}_\perp, \boldsymbol{m})$ at $\lambda^* = 0.65$, as a function of temperature. The $\boldsymbol{e}$-axes show a dramatic increase in their ordering at the second transition.

order on both sides of the fluctuation (Fig. 3.36(e)) is a result of this circumstance.

Further insight into the nature of the second transition could be gained by plotting the temperature variation of the long range order of the three axes, represented by square of the maximum eigen values of the corresponding ordering tensors (Fig. 3.37). As expected on this diagonal, these values match well for $\boldsymbol{e}_\perp$ and $\boldsymbol{m}$ axes, and progressively increase on cooling. The long-range order of the $\boldsymbol{e}$-axes on the other hand increases significantly only at the onset of the second low temperature transition. It is this enhancement that seems to be promoting the onset of the second biaxial phase with observable macroscopic biaxiality.

3.7 Conclusions

In conclusion, we argue that, starting from the point K in Fig. (3.1), the initial biaxial phase condensing from the isotropic phase is the manifestation of the cooperative modes induced by the biaxial coupling of the $\boldsymbol{e}_\perp - \boldsymbol{m}$ axes (second term in Eqn. (3.2.5)). The subsequent biaxial-biaxial transition is mediated by the stabilizing effect of the long-range order of the molecular $\boldsymbol{e}$-axes (first term in Eqn. (3.2.5)) brought into play at a lower temperature. In this context K $(\mu = -1)$ appears to be a unique point where the strength of the effective attractive coupling of $\boldsymbol{e}$-axes becomes lower than the attractive biaxial coupling of the other two molecular axes, a phenomenon which continues as λ^* progresses on the diagonal. As the LP is reached, the former interaction progressively disappears, thereby pushing the corresponding transition temperature to lower values and weakening the first-order transition. The existence and description of the intermediate phase with no long-range order of the $\boldsymbol{e}$-axes seem naturally to be out of the valid regime of the MF theory. The absence of the signature of the second transition from the B-ensembles and limited fluctuations of the order parameters (Fig. 3.35(a) and 3.35(b)), seem to be correlated. The observed trajectory in the configuration space derived from RW-ensembles is qualitatively different beyond K and is not accessible to the standard Metropolis sampling apparently due to the onset of barriers to the energy component fluctuations, originating from the lack of concomitant onset of long-range order of the three axes (inhomogeneity).

The interesting discussions on antinematic interactions, covering the curious parameter region TV [28, 38, 39] provide complementary arguments as the Landau point is reached from the opposite side. Finally, the existence of an in-principle intermediate biaxial phase of inherently low order (inhibited by inhomogeneities) seems to be a pointer to the difficulties in experimentally realizing a stable, macroscopic biaxial nematic phase. The MF treatment also predicts the phase sequences expected along the trajectory interior to the triangle as well, - at least in the fully attractive region bounded by the dispersion parabola. In view of the observation in this chapter pointing to deviations beyond point 'K' on the essential triangle (which translates to increase of γ beyond a specified value, that too at the expense of λ), we carried out similar simulational analysis along two trajectories inside the triangle. These results are presented in next chapter.

Bibliography

[1] M. J. Freiser, *Phys. Rev. Lett.* **24**, 1041 (1970).

[2] J. P. Straley, *Phys. Rev. A* **10**, 1881 (1974).

[3] D. K. Remler and A. D. J. Haymet, *J. Phy. Chem.* **90**, 5426 (1986).

[4] G. R. Luckhurst, C. Zannoni, P. L. Nordio and U. Segre, *Mol. Phys.* **30**, 1345 (1975).

[5] A. M. Sonnet, E. G. Virga and G. E. Durand, *Phys. Rev. E.* **67**, 061701 (2003).

[6] F. Bisi, E. G. Virga, E. C. Gartland Jr., G. De Matteis, A. M. Sonnet, and G. E. Durand, *Phys. Rev. E.* **73**, 051709 (2006).

[7] G. De Matteis, F. Bisi, and E. G. Virga, *Continuum. Mech. Thermodynamics.* **19**, 1 (2007).

[8] R. Alben, *Phys. Rev. Lett.* **30**, 778 (1973).

[9] N. Bocara, R. Mejdani and L. De Seze, *J. Phys (Paris)* **38**, 149 (1976).

[10] E. F. Gramsbergen, L. Longa and W. H. de Jeu, *Phys. Rep.* **135**, 195 (1986).

[11] P. K. Mukherjee, *J. Chem. Phys.* **109**, 2941 (1998).

[12] David Allender and L. Longa, *Phy. Rev. E* **78**, 011704 (2008).

[13] G. R. Luckhurst and S. Romano, *Mol. Phys.* **40**, 129 (1980).

[14] M. P. Allen. *Liq. Cryst.* **8** 499(1990).

[15] F. Biscarini, C. Chiccoli, P. Pasini, F. Semeria and C. Zannoni, *Phys. Rev. Lett.* **75**, 1803 (1995).

[16] C. Chiccoli, P. Pasini, F. Semeria and C. Zannoni, *Int. J. Mod. Phys. C.* **10**, 469 (1999).

[17] R. Berardi and C. Zannoni, *Mol. Cryst. Liq. Cryst.* **396** 177 (2003).

[18] R. Berardi, L. Muccioli, S. Orlandi, M. Ricci and C. Zannoni, *J. Phys.: Condens. Matter.* **20**, 463101 (2008).

[19] Giovanni De Matteis, S. Romano and E.G.Virga, *Phy. Rev. E* **72**, 041706 (2005).

[20] G. Sai Preeti, K. P. N. Murthy, V. S. S. Sastry, C. Chiccoli, P. Pasini, R. Berardi and C. Zannoni, *Soft Matter* **7**, 11483 (2011).

[21] K. Severing, K. Saalwachter, Phy. Rev. Lett. **92**, 125501 (2004); L. A. Madsen, T. J. Dingemans, M. Nakata, E. T. Samulski, Phy. Rev. Lett. **92**, 145505 (2004); B. R. Acharya, A. Primak and S. Kumar, Phy. Rev. Lett. **92**, 145506 (2004); J. L. Figueirinhas, C. Cruz, D. Filip, G. Feio, A. C. Ribeiro, Y. Frere, T. Meyer, G. H. Mehl, Phys. Rev. Lett. **94**, 107802 (2005)

[22] K. Merkel, A. Kocot, J. K. Vij, R. Korlacki, G. H. Mehl and T. Meyer, *Phys. Rev. Lett.* **93**, 237801 (2004).

[23] N. Vaupotic, J. Szydlowska, M. Salamonczyk, A. Kovarova, J. Svoboda, M. Osipov, D. Pociecha and E. Gorecka, *Phy. Rev. E.* **80**, 030701 (R) (2009).

[24] K. Van Le, M. Mathews, M. Chambers, J. Harden, Quan Li, H. Takezoe and A. Jakli, Phys. Rev. E. **79**, 030701 (R) (2009).

[25] T. Ostapenko, C. Zhang, S. N. Sprunt, A. Jakli and J. T. Gleeson, *Phy. Rev. E.* **84**, 021705 (2011).

[26] Mamatha Nagaraj, Y. P. Panarin, U. Manna, J. K. Vij, C. Keith and C. Tschierske, Appl. Phys. Lett. **96**, 0111106 (2010).

[27] F. Bisi, G. R. Luckhurst, E. G. Virga, *Phy. Rev. E.* **78**, 021710 (2008)

[28] G. De Matteis and S. Romano, Phys. Rev. E. **78**, 021702 (2008).

[29] F. Wang and D. P. Landau,*Phys. Rev. Lett.* **86**, 2050 (2001); F. Wang and D. P. Landau,*Phy. Rev. E* **64**, 056101 (2001).

[30] D. Jayasri, V. S. S. Sastry and K. P. N. Murthy, *Phys. Rev. E.* **72**, 036702 (2006).

[31] S. Romano, *Physica A* **337**, 505 (2004).

[32] C. Zhou, T. C. Schulthess, S. Torbrugge and D. P. Landau, Phys. Rev. Lett. **96**, 120201 (2006).

[33] B.A. Berg, *cond-mat* 0206333.

[34] R. H. Swendsen and J. S. Wang, *Phys. Rev. Lett.* **58**, 86 (1987).

[35] K. Binder, *Z. Physik. B.* **43**, 119 (1981); K. Binder, Phys. Rev. Lett. **47**, 693 (1981).

[36] Robert J Low,*Eur. J. Phys.***23**, 111 (2002).

[37] B. Kamala latha, Regina Jose, K. P. N. Murthy, V. S. S. Sastry, *Phys. Rev. E* **89**, 050501(R) (2014) .

[38] G. De Matteis and S. Romano, Phys. Rev. E. **80**, 031702 (2009).

[39] S. Romano and G. De Matteis, Phys. Rev. E. **84**, 011703 (2011).

Chapter 4

A Wang-Landau Monte Carlo Investigation of the Essential Triangle

4.1 Introduction

The results reported in the previous chapter bring out certain interesting aspects of the phase sequences predicted by mean field theory and WL-based simulations, as a function of the arc length λ^* (along OIV of the essential triangle). The simulated phase sequence involving I, N_U and N_B phases is qualitatively confirming with the mean-field phase diagram proposed earlier, and the averages over equilibrium ensembles of microstates from the two sampling procedures (B- and RW- ensembles) are comparable within computational errors upto a certain value of λ^*. The deviations of the present results from the proposed mean-field phase diagram [1] are qualitative for values of $\lambda^* \geq 0.57$ (point K on the diagonal). A detailed analysis of this deviation, argued to be the consequence of increasing γ (at the expense of λ) in the interaction Hamiltonian, was possible thanks to the MF analysis already carried out on the trajectory.

However the Hamiltonian parameters corresponding to real systems are more likely to be in the interior of the triangle: the arc OIV serving as a very interesting boundary of this space hosting pair-wise interactions supporting D_{4h} symmetry. It may also be pointed out that qualitative picture of the phase sequences expected within the MF approximation can be gleaned in the interior of the essential triangle [2]. In view of this information for ready qualitative comparison, and because of the relevance of the interior trajectory to actual experiments, we carried out simulations, and similar detailed analysis as in the earlier chapter, along two trajectories: (i) segment IW where W is the midpoint of OV and (ii) segment of the parabola OZT (see Fig. 4.1).

4.2 Segment IW

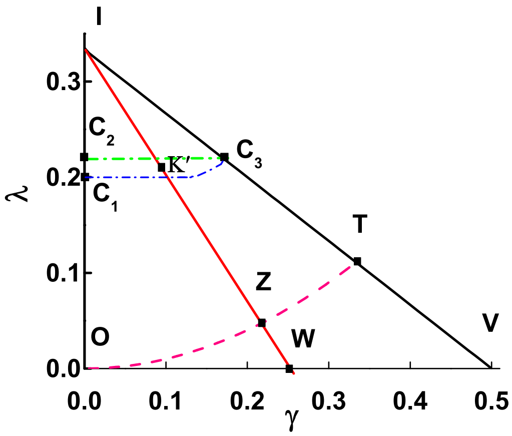

Figure 4.1: The essential triangle, depicting the two interior trajectories along which detailed simulations have been carried out. (i) IZW (b) OZT

The path IW inside the essential triangle at which simulations were done are shown in the schematic in Fig 4.1. The uniaxial - biaxial coupling coefficient γ on IW is half of the the value on the diagonal IV, for identical λ values. We denote the arclength of the path OIW as $\lambda^{'}$, given by $\lambda^{'} = \lambda$ on segment OI, and

$$\lambda^{'} = \frac{1}{3}(1 + 5\gamma)$$

where

$$\gamma = \frac{(1 - 3\lambda)}{4}$$

on the segment IW.

Initially Monte Carlo simulations (for L=20) were performed at chosen points B1, B2, B3, B4, Z and B5 along the trajectory IW (Fig. 4.2) and the results from the two different sampling procedures (B- and RW- ensembles) were compared. The Table 5.1 lists the values of (γ, λ) and corresponding arc lengths $\lambda^{'}$ at these points for ready reference. Fig. 4.2

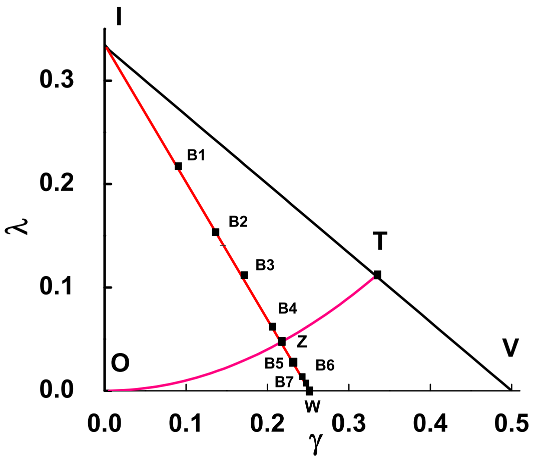

Figure 4.2: Essential triangle, depicting typical values of (γ, λ) along IW (also see Table.(5.1))

shows the location of these designated points schematically inside the essential triangle. The comparisons of the average values of observables obtained from B- and RW-ensembles at some of these points are shown in Figs.4.3-4.6. To keep the discussion somewhat simple, and more tractable, we present the data on the two major order parameters (R^2_{00} and R^2_{22}) only, even though the corresponding variations of the R^2_{20} and R^2_{02} and their susceptibilities are also computed and examined. It may be observed from Figs. 4.3 - 4.6 that the specific heat peaks and the order profiles obtained from the both ensembles coincide exactly (within computational errors) for values of $\lambda^{'}$ (e.g. at points B1, B2) which fall well within the attractive region for the Hamiltonian (above the parabola). A slight difference is observed in the low temperature transition peak positions for $\lambda^{'}$ values 0.6105 (B_3 in Fig.4.2). The order parameter profiles also betray this disparity (Fig.4.5(b)). It may be noted that B_3 has the same λ-coordinate as the Landau point T, but half the value of its γ-coordinate. To complete this preliminary examination of the ensembles, we present the results for $\lambda^{'}$ = 0.709 (B_5 in Fig.4.2), which is in the partly repulsive region of the triangle, as shown in Figs.4.6(a) and 4.6(b). The disparities between the predictions based on the two differently sampled equilibrium ensembles are even more prominent for this value of $\lambda^{'}$.

In the light of above observations, we carried out a systematic simulation study using the entropic sampling technique (WL algorithm) along the segment IW in order to obtain a

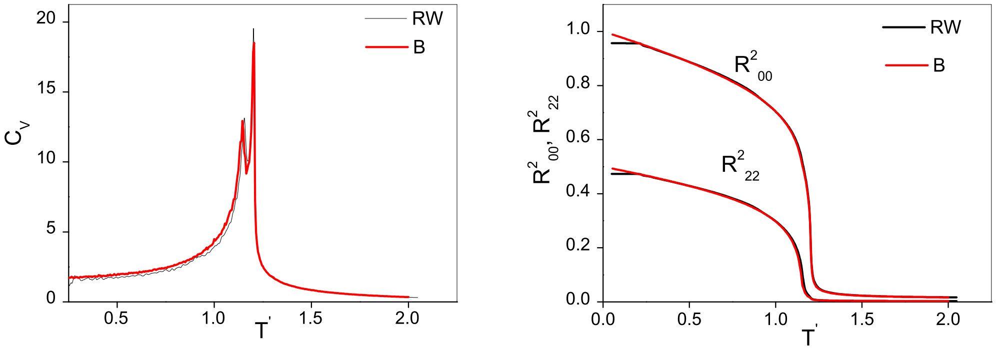

(a) (b)

Figure 4.3: Comparison of (a) specific heat (b) order parameter profiles obtained from B- and RW- ensembles for $\lambda^{'}$ = 0.477 (B_1 in Fig.4.2): Deviations observed at very low temperatures ($\leq$ 0.25), common to all plots, have their origin from inadvertent inadequate sampling of microstates comprising the entropic ensemble, at these very low energy values. As these deviations do not interfere with the interesting nature of the graphs, recomputations were not attempted to correct for this, to save computing time.

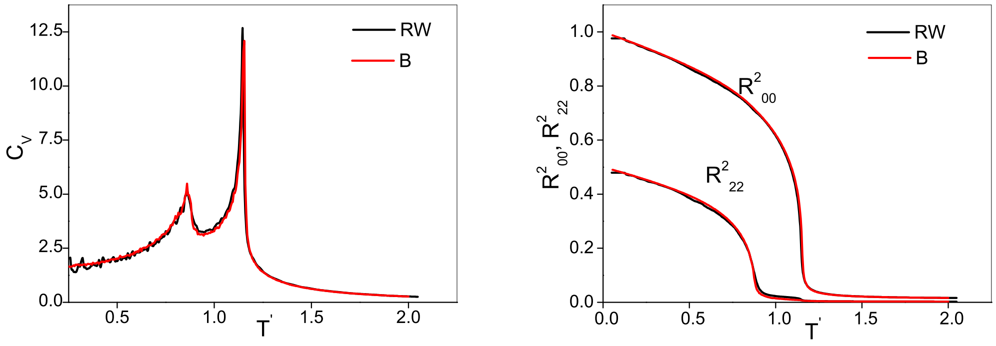

(a) (b)

Figure 4.4: Comparison of (a) specific heat (b) order parameter profiles obtained from B- and RW- ensembles for $\lambda^{'}$ = 0.5666 (B_2 in Fig.4.2)

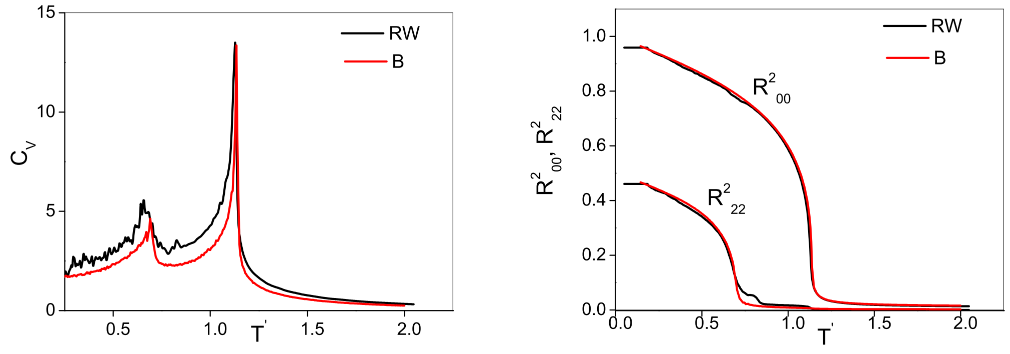

(a) (b)

Figure 4.5: Comparison of (a) specific heat (b) order parameter profiles obtained from B- and RW- ensembles for $\lambda' = 0.6105$ (B_3 in Fig.4.2)

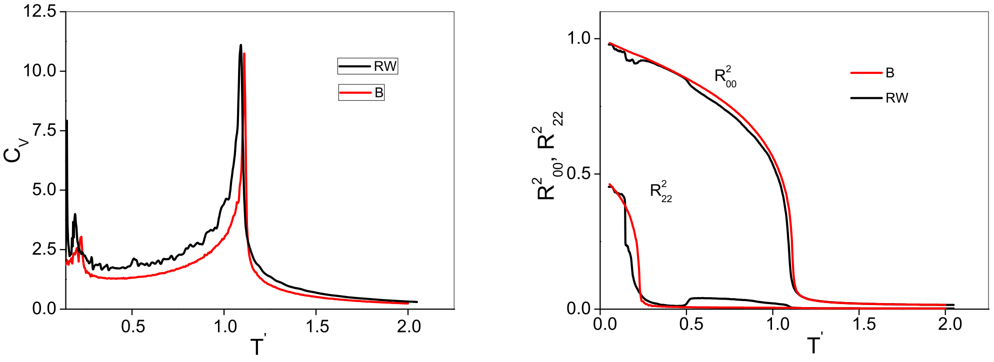

(a) (b)

Figure 4.6: Comparison of (a) specific heat (b) order parameter profiles obtained from B- and RW- ensembles for $\lambda' = 0.709$ (B_5 in Fig.4.2, in the partly repulsive region of the triangle.)

Table 4.1: Coordinates of points B1-B7 and Z along the segment IW of the essential triangle (Fig.2)

Point	γ	λ	$\lambda^{'}$
B1	0.0859	0.1719	0.4766
B2	0.1405	0.14658	0.5666
B3	0.1663	0.1116	0.6105
B4	0.2045	0.0606	0.674
Z	0.2149	0.0467	0.691
B5	0.2253	0.0328	0.709
B6	0.2440	0.0079	0.740
B7	0.2482	0.0024	0.747

generic phase diagram inside the essential triangle.

4.2.1 Segment IZ: Range of $\lambda^{'}$ = (0.33 - 0.691)

WL simulations were carried out at 30 values of $\lambda^{'}$ on the segment IW, where the arc length $\lambda^{'}$ ranges from 0.33 to 0.75. Temperature variation of the specific heat, and the two order parameters (R^2_{00} and R^2_{22}) in different ranges of $\lambda^{'}$, covering the segment IW, are presented in Figs. 4.7 - 4.9. It may be observed from Figs. 4.7(a) and 4.7(b) that for $\lambda^{'}$ values in the range 0.33 - 0.456, a single isotropic-biaxial transition takes place on cooling from the isotropic phase. This transition splits into two for higher values of $\lambda^{'}$, (e.g. see Fig.4.8(a) covering $\lambda^{'}$ range from 0.462 t0 0.610), with the low temperature transition peak point being progressively depressed with increase in $\lambda^{'}$ value. The variation of the order profiles in this region, shown in Fig. 4.8(b), reveals an intervening phase which is not strictly uniaxial since the system exhibits a low value of R^2_{22} at the onset of the transition. By performing simulations at different sizes (L=10, 15, 20), the possibility that this could

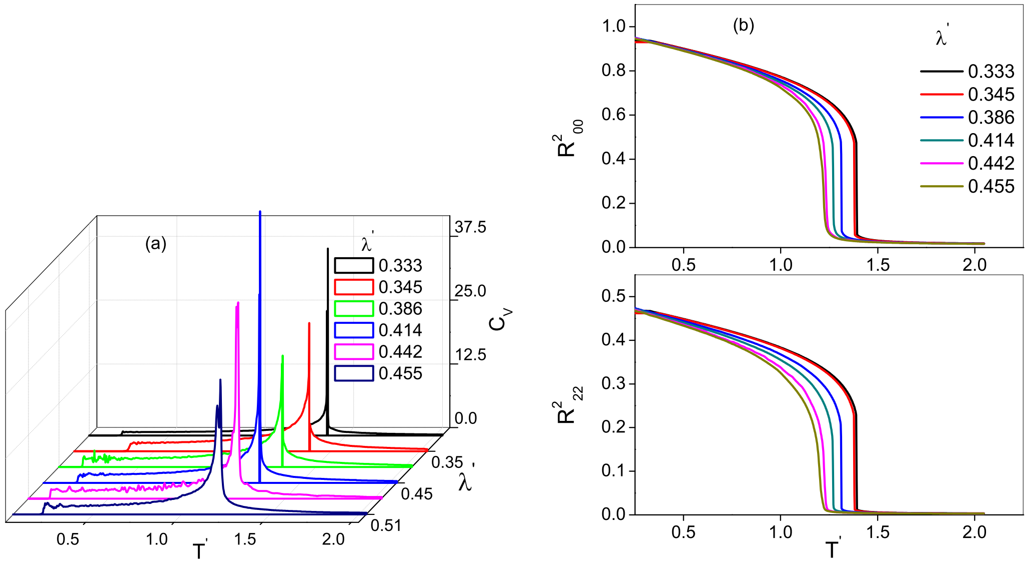

(a) (b)

Figure 4.7: Comparison of (a) specific heat (b) order profiles for values of λ' from 0.33 to 0.455

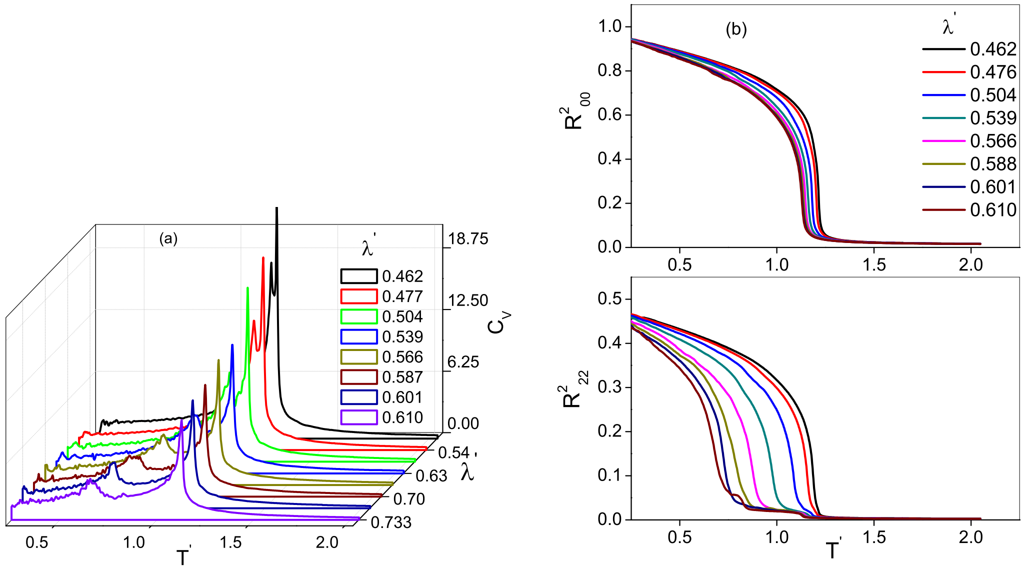

(a) (b)

Figure 4.8: Comparison of (a) Specific heat (b) order parameter profiles for values of λ' from 0.463 to 0.610

be a finite size effect is ruled out. (It may be noted that for these system sizes a pure uniaxial phase condenses on the λ-axis). The notable difference in the case of path IW, relative to IV, is that the degree of biaxiality (value of R^2_{22}) remains fairly independent of temperature, and the degree is the same for all subsequent values of λ' beyond this threshold, until interrupted by a second low temperature transition leading to an onset of appreciable biaxial order (Fig.4.8). The results of simulation for λ' values in the range

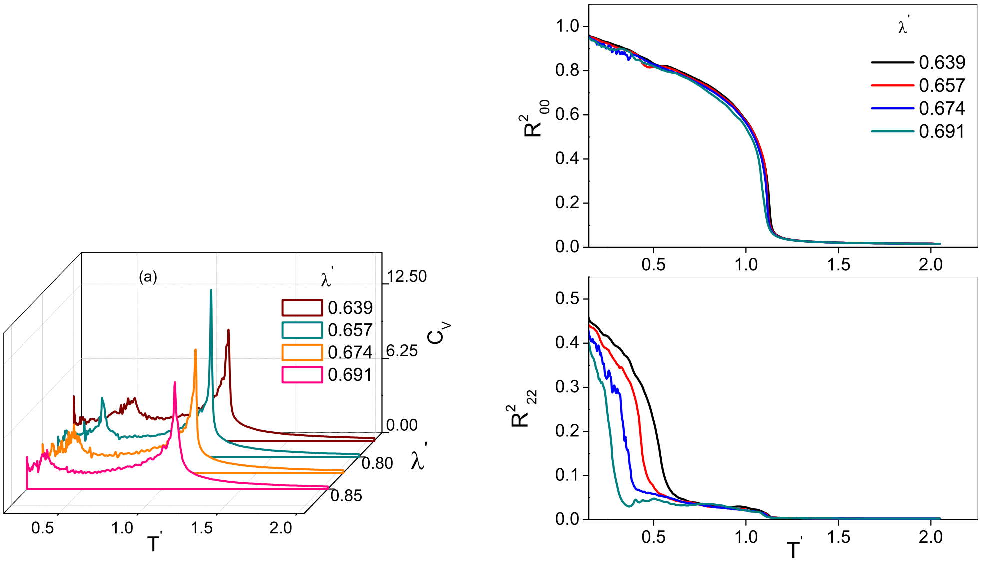

(a) (b)

Figure 4.9: Comparison of (a) specific heat (b) order parameter profiles for values of λ' from 0.639 to 0.691

0.639 - 0.691 are depicted in Fig. 4.9. Though these points lie very close to the parabola, they are still in the attractive region for the interaction Hamiltonian. It is observed from Fig. 4.9(a) that the second specific heat peak shifts progressively to lower temperatures as the value of λ' increases. Corresponding variations in the order parameters, shown in Fig.4.9(b) confirm the shift of the second transition temperature to lower values. However it is observed that the equilibrium averages of order parameters in this region of λ' are not as smooth, and show discernible fluctuations in the low temperature biaxial phase.

It is interesting to note that the intermediate phase persists to have a small degree of biaxial order ($\sim\ 0.05$) which (a) is not a finite size effect; (b) is fairly independent of temperatures within the liquid crystal phase; and (c) does not depend on the values of λ'. This phase with temperature dependence typical of uniaxial order, but having a small and constant biaxial symmetry (≤ 0.05)) , is designated as $N_{U'}$ phase in our notation. On subsequent lowering of temperature from this phase, the biaxial order increases rapidly at the second transition at T_{C2} and the lower temperature phase has macroscopically observable biaxial order, for all values of λ'. The susceptibility profiles of the order parameter in this region are depicted in Fig. 4.10. It may be observed that the R^2_{22} susceptibility starts increasing in the intermediate phase before showing a peak at the low temperature transition at T_{C2}. The fourth order energy cumulant (V_4) data obtained along the path OIW are shown in Figs. 4.11 - 4.13. It is observed that the $I - N_B$ transition remains strongly first order for values of λ' from 0.345 to 0.45. In the range of λ' from 0.463 to 0.691 (i,e upto the point Z in Fig.4.1), the high temperature transition at T_{C1} from the isotropic phase (I) to the ordered $N_{U'}$ phase shows a first order nature. Subsequently, the low temperature $N_{U'} - N_B$ transition seems to change gradually from first order to continuous nature, as seen from V_4 profiles in Figs.4.11 and 4.13.

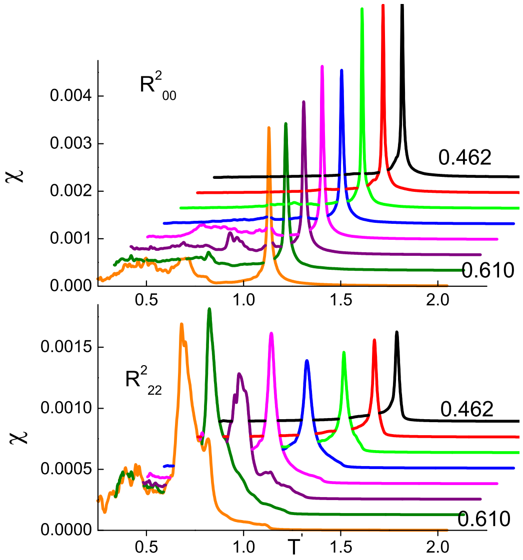

Figure 4.10: Susceptibilities (χ 's) of the order parameters for values of λ' from 0.462 to 0.610

An analysis of the above simulation data leads to the proposal of a phase diagram along

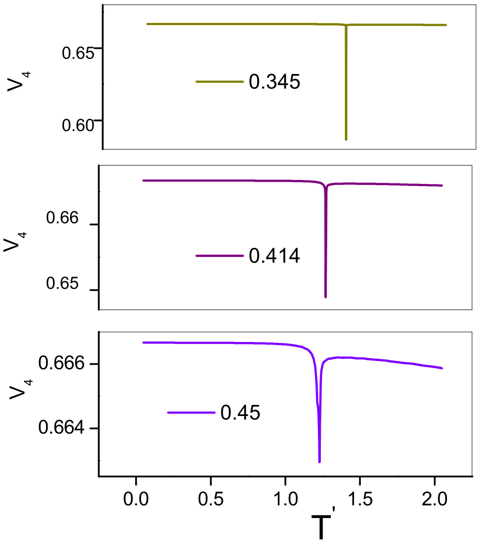

Figure 4.11: energy cumulant V_4 for values of $\lambda^{'}$ from 0.345 to 0.45

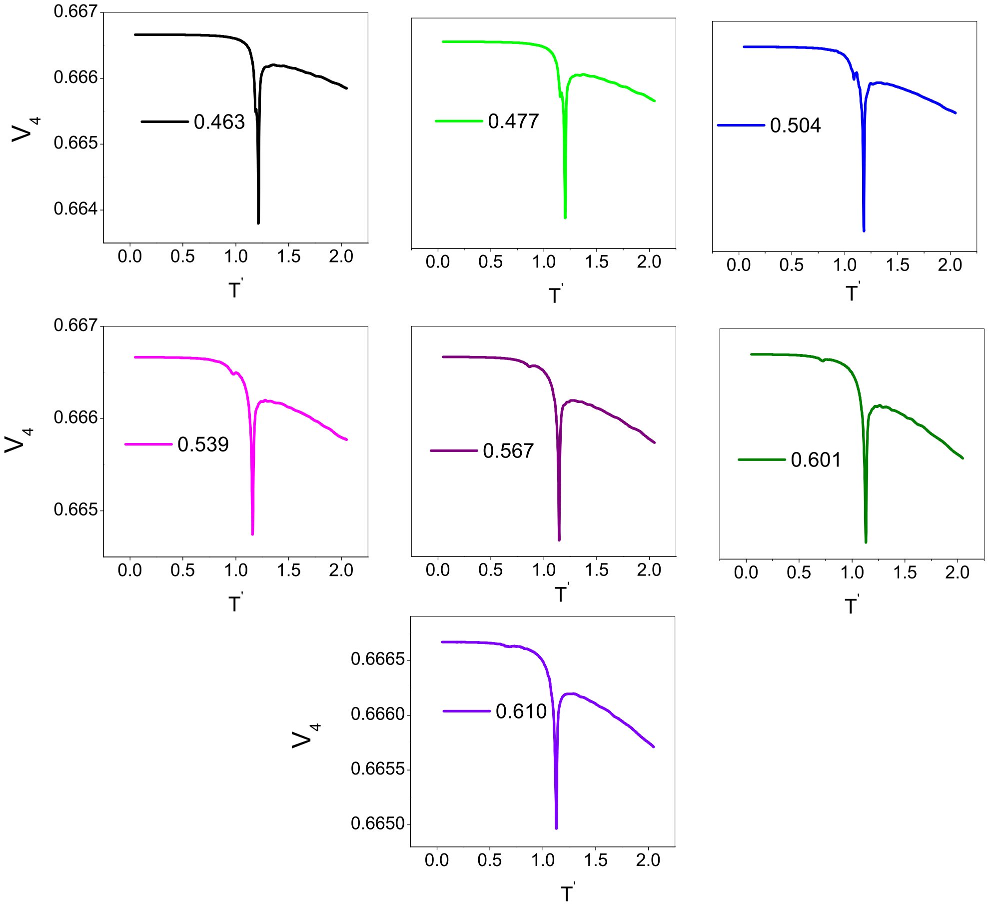

Figure 4.12: Energy cumulant V_4 for values of $\lambda^{'}$ from 0.463 to 0.610

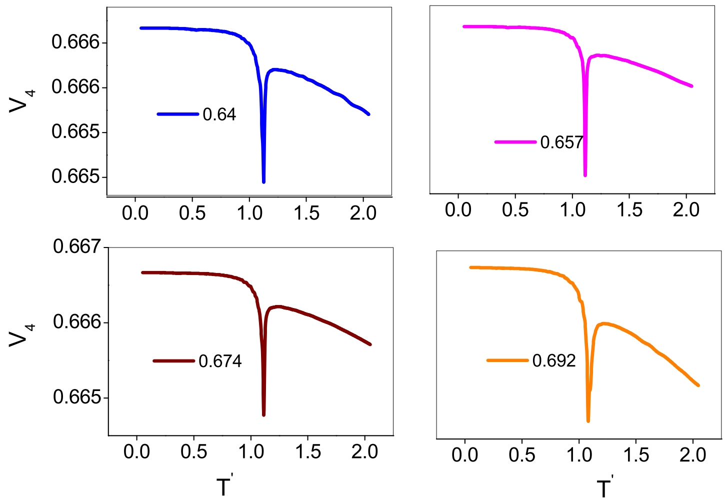

Figure 4.13: energy cumulant V_4 for values of $\lambda^{'}$ from 0.64 to 0.691

the path OIW, shown in Fig.4.14. We could report the data only upto the value $\lambda^{'} = 0.709$, as beyond this value (which falls into the partly repulsive region under the parabola) the computational times for the convergence of DoS are impractical. We observe from the temperature variation of order parameters that the growth of biaxial order appears to be progressively inhibited as $\lambda^{'}$ value increases within the attractive region, and enters the party repulsive region on crossing the parabola at the point Z. The free energy profiles, plotted as a function of energy and order parameters (computed from the DOS data), reflect the rationale for the impediments for the growth of the biaxial order as the base of the triangle OIW is reached. The free energy curves obtained for $\lambda^{'}$= 0.610 (B_3in the attractive region) are shown in Fig. 4.15. These curves depict the smooth variation of free energy as a function of energy and uniaxial order parameter. However, its variation with respect to R^2_{22} shows a small sharp well, (the edge being located at $R^2_{22} \simeq 0.02$), and the family of curves in Fig.4.15(c), as a function of temperature, shows that it required significant variation of temperature before the system could shift its free energy minimum away from this restricted region. It appears that during this temperature range, the system accesses microstates with rather small but nonzero degree of biaxiality, constrained however by free energy barriers to attain higher degree of biaxiality for considerable range of temperature.

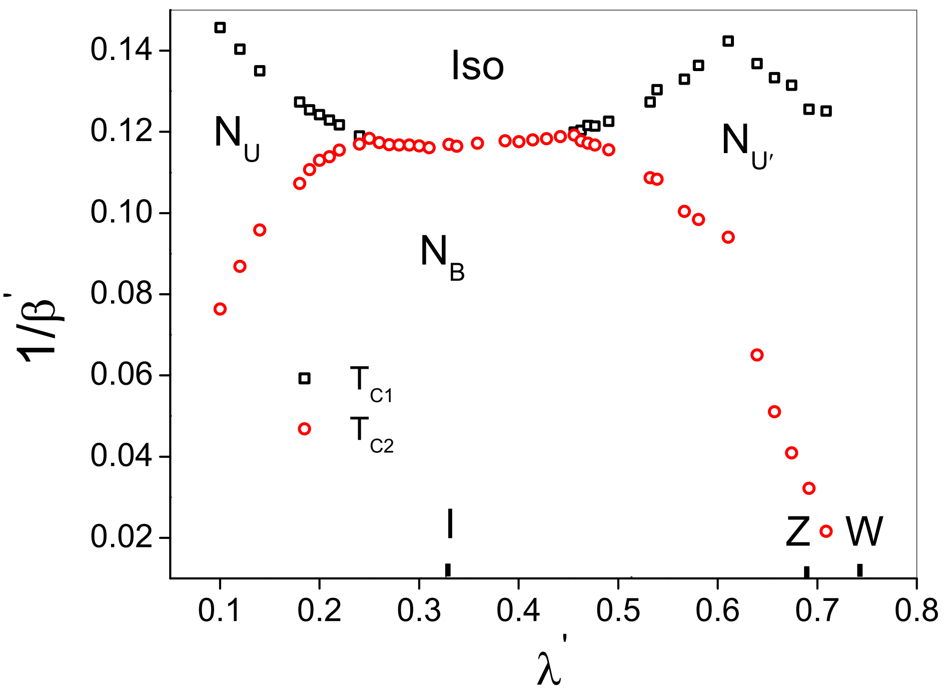

Figure 4.14: Phase diagram inside the essential triangle along path OIW

This circumstance seems to be manifesting as a corresponding curious variation of R^2_{22} at $\lambda^{'}$= 0.610, as in Fig.4.5(b). We find that the development of such free energy barriers (with respect to R^2_{22} at low values) and the requirement of the system to cool sufficiently to overcome them before accessing higher macroscopically observable values, is generic. All the data collected in this region supports and corroborates the simulated order parameter profiles reported in the previous figures. It is very interesting that such barriers are exhibited only along the path of biaxial order, but not along energy or uniaxial order. This implies a complex free energy surface in the 2-d space of order parameter, offering initial barriers to a significant development of biaxial order, until the system is sufficiently cooled. Figs. 4.16 - 4.18 demonstrate this view point.

4.2.2 Segment ZW: Range of $\lambda^{'}$ = (0.691 - 0.747)

We now present data obtained at B5, B6 and B7 (Fig.4.2), beyond the point Z. In this region, the biaxial-biaxial tensorial coupling term $\lambda \to 0$ asymptotically, leading to a special case of the interaction Hamiltonian. The case for λ = 0 was studied earlier through

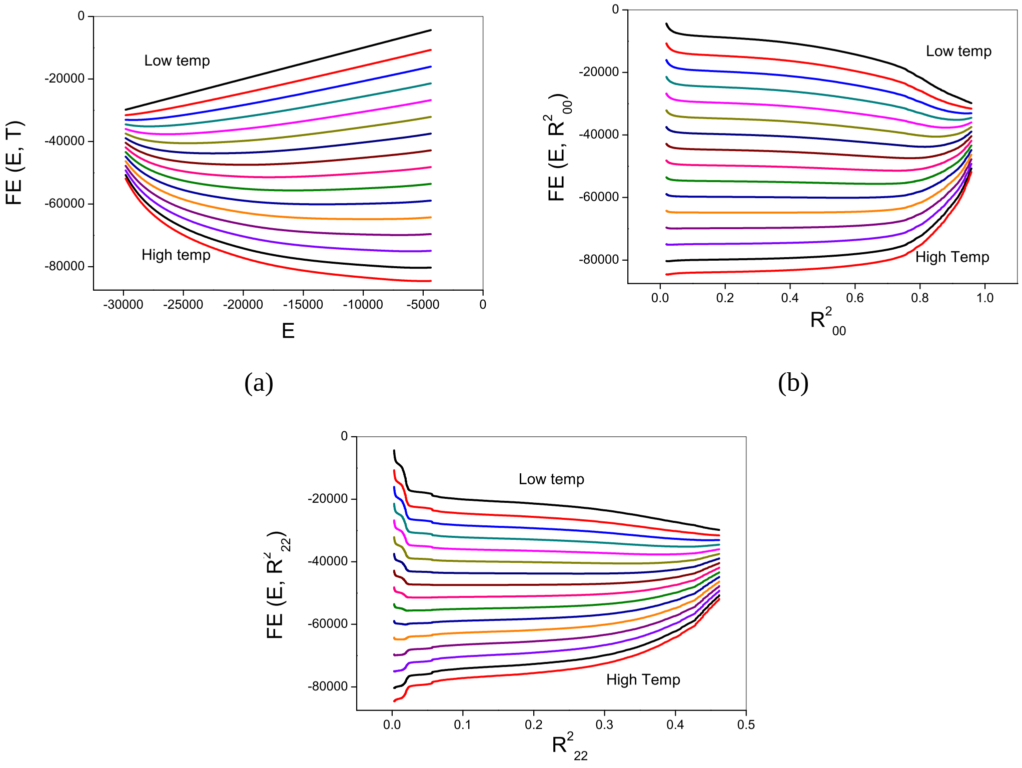

(a) (b)

(c)

Figure 4.15: Representative free energy plotted as a function of (a) energy (b)R^2_{00} (c) R^2_{22} at the point B3 (λ' = 0.610, Fig. 4.2)

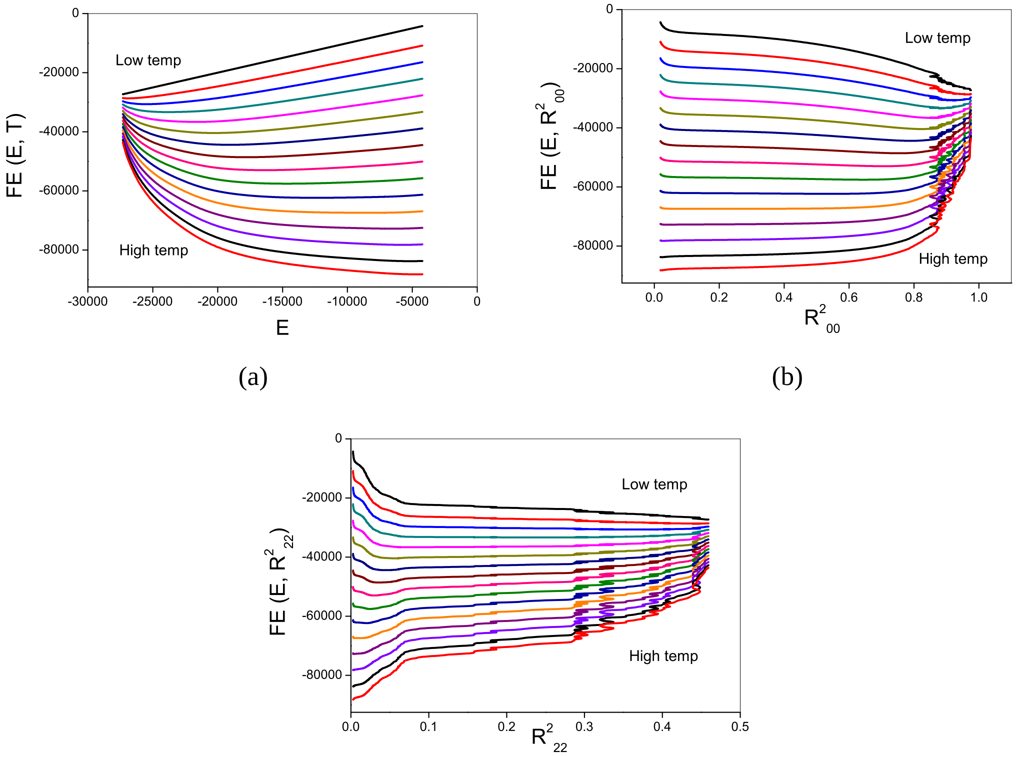

(a)

(b)

(c)

Figure 4.16: Representative free energy plotted as a function of (a) energy (b)R^2_{00} (c) R^2_{22} at the point B4 ($\lambda^{'}$ = 0.674, Fig.4.2)

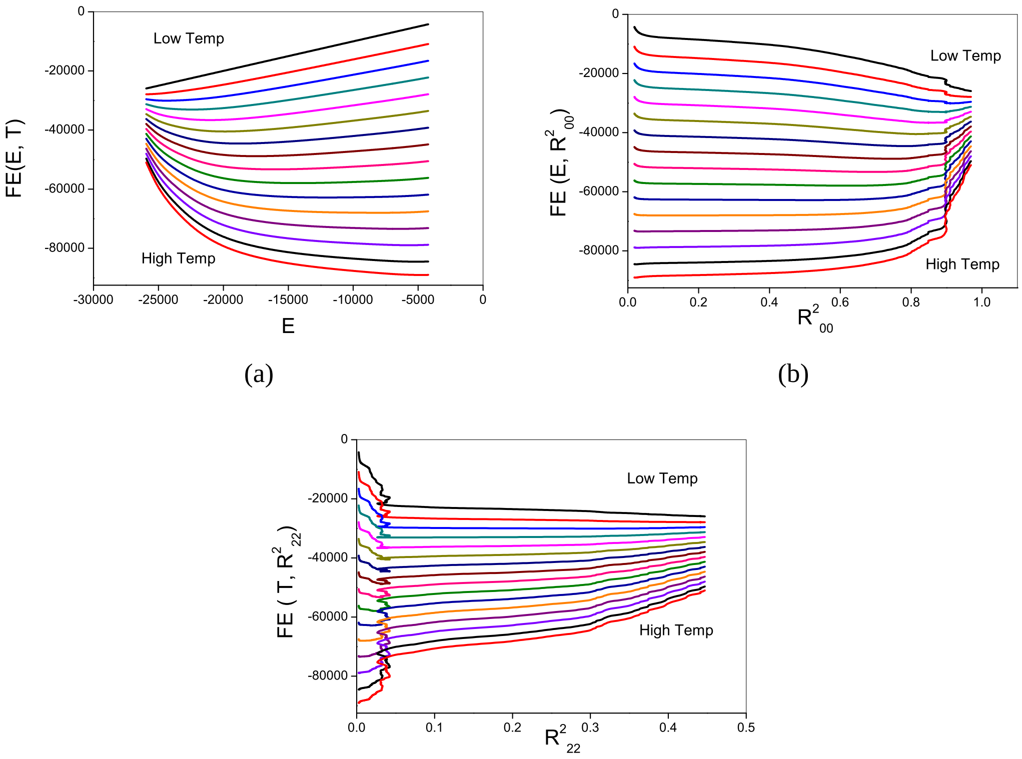

(a)

(b)

(c)

Figure 4.17: Representative free energy plotted as a function of (a) energy (b) R^2_{00} (c) R^2_{22} at the point Z ($\lambda^{'}$ = 0.692, Fig.4.2)

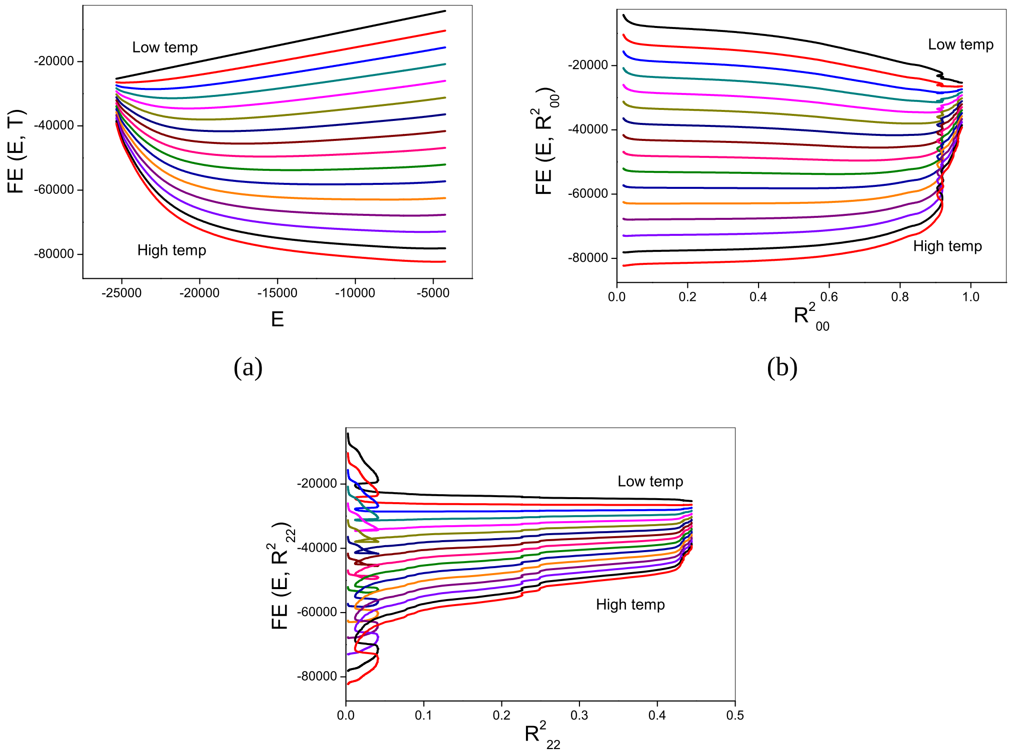

(a)

(b)

(c)

Figure 4.18: Representative free energy plotted as a function of (a) energy (b) R^2_{00} (c) R^2_{22} at the point B5 (λ' = 0.709, Fig.4.2)

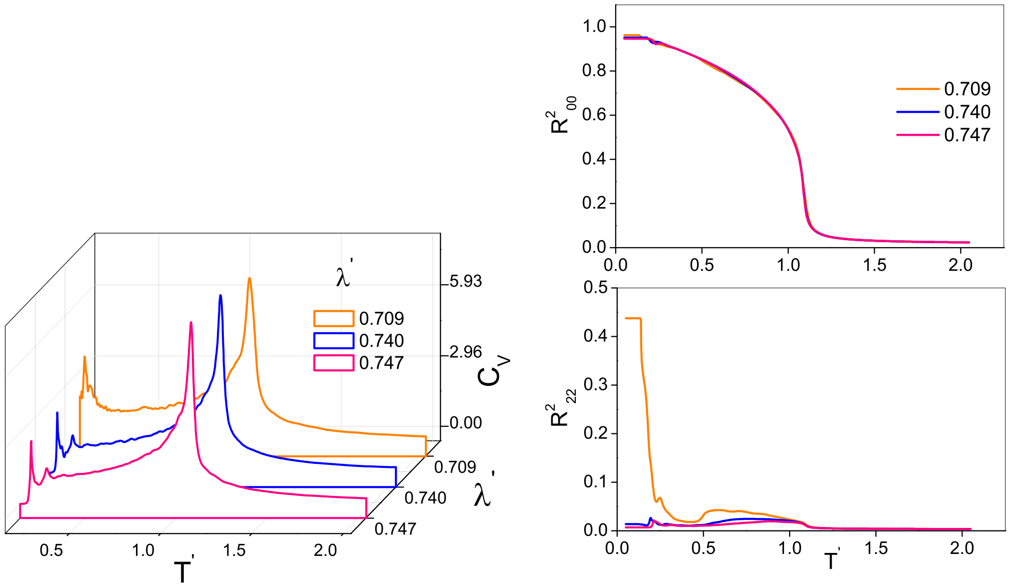

(a) (b)

Figure 4.19: Comparison of (a) specific heat (b) order parameter profiles for values of $\lambda^{'}$ in the range 0.709 - 0.747 (L=15)

simulations [3]. It was found that in the absence of the biaxial-biaxial interaction term, only a uniaxial phase could be obtained on condensation from the isotropic phase. We present here the simulation results in the case of $\lambda \to 0$. The mean field analysis predicts that the Hamiltonian is partly repulsive in this region and excluded volume effects play a major role [4]. Due to the constraints imposed by computational time, we could obtain data in this range of $\lambda^{'}$ only for a smaller system, with L=15. (instead of L=20, as in the earlier case). The specific heat and order parameter profiles are depicted in Figs. 4.19(a) and 4.19(b). The energy cumulants V_4 are shown in Fig. 4.20. It may be observed that the specific heat profiles show evidences of two transitions. The order parameter profiles depict the onset and growth of uniaxial order at T_{C1} for all values of $\lambda^{'}$. The biaxial order parameter increases at T_{C2} (in the biaxial phase) for $\lambda^{'}$ = 0.709, but remains close to zero for $\lambda^{'}$ = 0.740 and 0.747. This behaviour is as expected from mean field considerations at such values of $\lambda^{'}$, very close to the base OW. The free energy plots for λ = 0.740 are shown in Figs. 4.21(a) - 4.21(c). The free energy variation with respect to R^2_{22} for $\lambda^{'}$ = 0.740 again confirms the presence of barriers for the growth of biaxial order at points close to the base

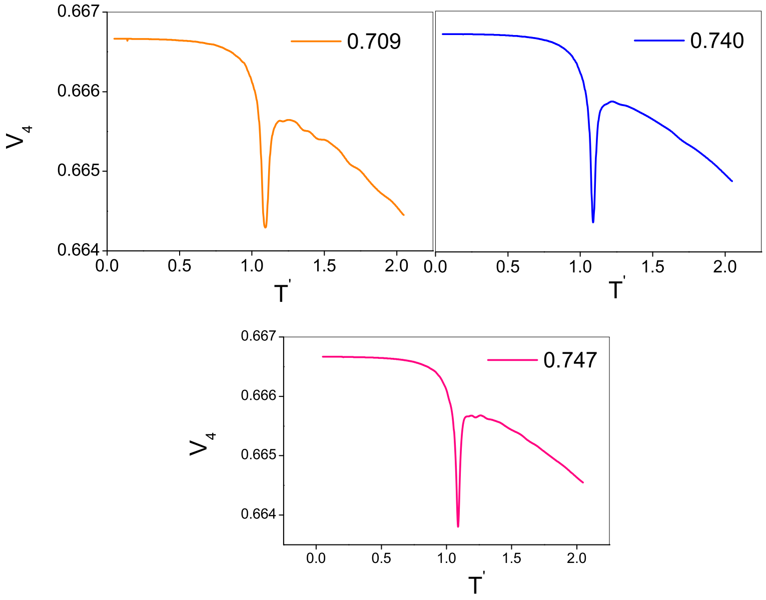

Figure 4.20: Energy cumulant V_4 for values of $\lambda^{'}$ in the range 0.709 - 0.747 (L=15)

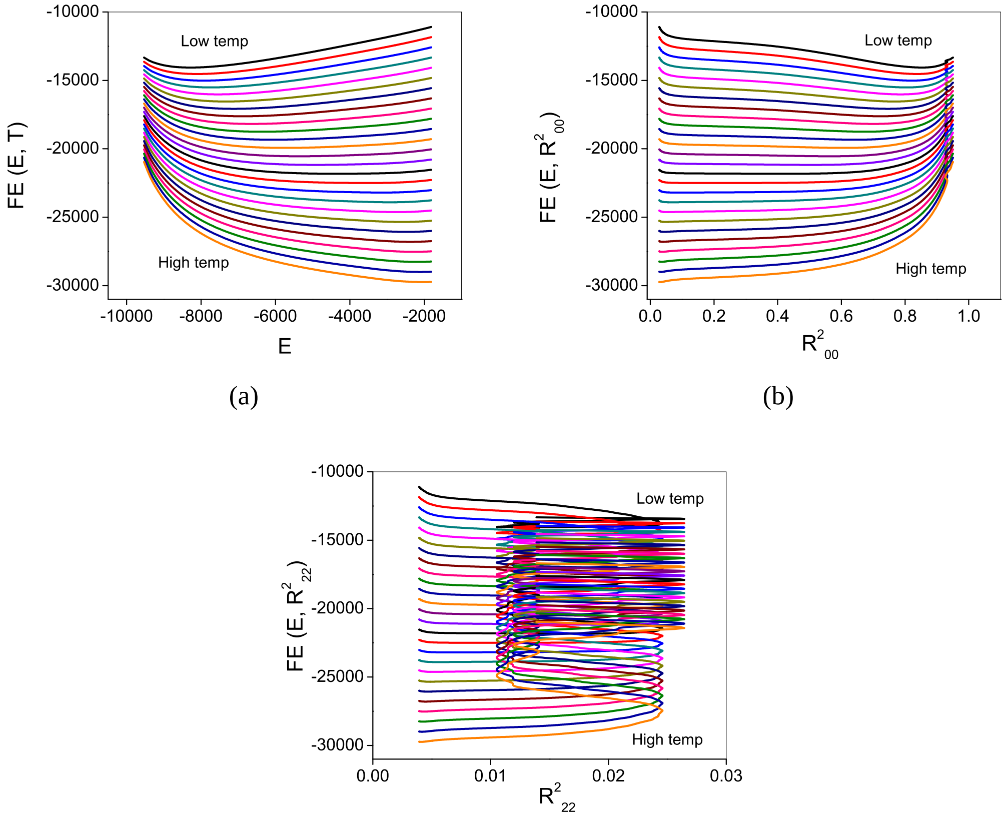

(a) (b)

(c)

Figure 4.21: Representative free energy plotted as a function of (a) energy (b)R^2_{00} (c) R^2_{22} at point B6 ($\lambda^{'}$ = 0.740, Fig.4.2)

Table 4.2: (γ, λ) values corresponding to λ_Z

λ_Z	γ	λ
0.15	0.12247	0.015
0.2	0.1633	0.0266
0.25	0.2041	0.0416
0.3	0.2449	0.06
0.35	0.2657	0.0816
0.375	0.3062	0.0937
0.4085	0.3335	0.1113

OW. The biaxial state is obviously not stable at such parameter points of the Hamiltonian.

4.3 Dispersion Parabola OT

In this section we focus on a trajectory inside the essential triangle which corresponds to dispersion approximation. In terms of the general quadrupolar Hamiltonian, the molecule supports a single oscillator, and the corresponding interaction (which was studied [5]), is written in terms of the single interaction parameter λ_Z as:

$$H = -\epsilon_{ij}\{P_2(\cos(\beta_{ij})) + 2\lambda_Z(R^2_{02}(\omega_{ij}) + R^2_{20}(\omega_{ij})) + 4\lambda_Z^2 R^2_{22}(\omega_{ij})\} \tag{4.3.1}$$

where the symbols have the usual meanings as described in chapter 1. The parameter λ_Z is related to the γ used in this chapter as:

$$\lambda_Z = \sqrt{\frac{3}{2}}\gamma$$

.

Table. (5.2) lists for convenience the values of γ and λ for different points on the parabola, represented by representative values of λ_Z, upto the Landau point T. A cubic lattice of size $15 \times 15 \times 15$ units with periodic boundary conditions was used to perform these simulations. The Metropolis sampling was used for collecting the data to constitute a canonical ensemble of 6×10^5 microstates, after equilibration over 6×10^5 Monte Carlo steps. The WL simulation was then carried out (as per the details of the previous chapter) extensively for fifteen values of λ_Z varying from 0.15 to 0.7. We present the results below.

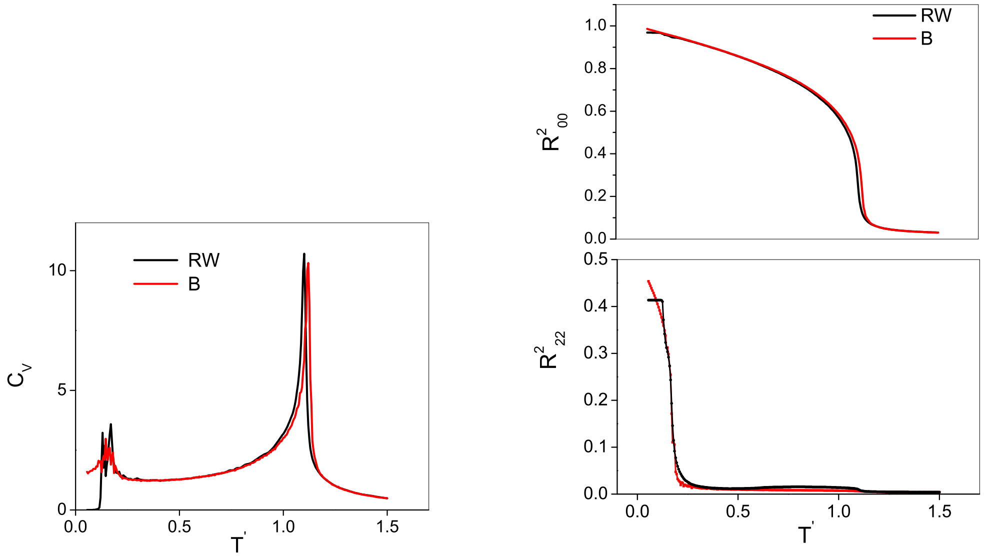

(a) (b)

Figure 4.22: Comparison of (a) specific heat (b) order parameter profiles from B- and RW-ensembles for λ_Z = 0.2

These results are compared in Figs. (4.22) and (4.23) for two values of λ_Z = 0.2 and 0.35. It may be observed from Fig. 4.21 that for the lower value of λ_Z = 0.2, the average values of observables from the two ensembles show good agreement. However, for λ_Z = 0.35, it is seen that though the uniaxial order parameter profiles agree qualitatively, the biaxial order obtained from the RW-ensemble (from WL simulation) shows large deviation from that of the Boltzmann ensemble. Noting from the Table.5.2 that this value of λ_Z is close to the Landau point T on the diagonal IV of the triangle (Fig.4.1), this result is not perhaps surprising. Such deviations should be expected to develop, as the point on the parabola approaches the diagonal, consistent with the findings of the previous chapter at

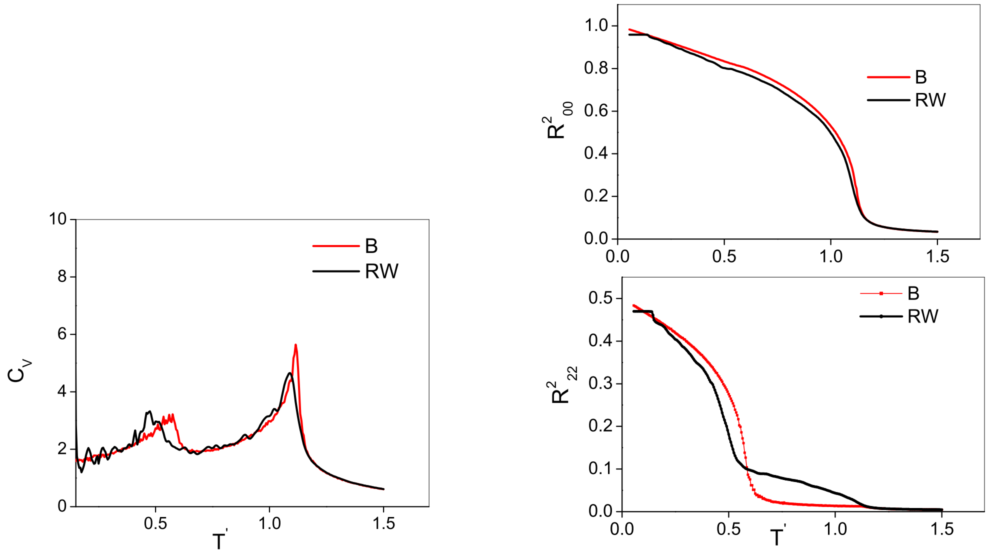

(a) (b)

Figure 4.23: Comparison of (a) specific heat (b) order parameter profiles from B- and RW-ensembles for λ_Z = 0.35

the Landau point T.

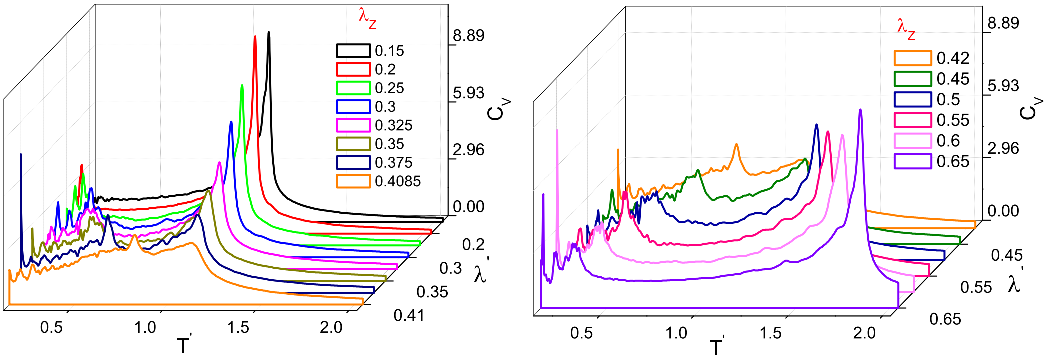

(a) (b)

Figure 4.24: Specific heat for λ_Z values (a) Range: (0.15, 0.4085) (b) Range: (0.42, 0.65) (L=15, RW-ensembles)

We now present specific heat profiles from RW-ensembles, for λ_Z values from 0.15 to 0.65 in Figs. 4.24(a) and 4.24(b). These profiles clearly show the evidence of two transitions in the entire range of λ_Z. Of particular interest is the specific heat profile at λ_Z=0.4085 which nearly coincides with the Landau point at T. We observe two transition peaks in Fig. 4.24(a) at this value. The transition at T_{C1} signifies a $I - N_{B1}$ transition, whereas the low temperature transition at T_{C2} signifies $N_{B1} - N_B$ transition, as concluded in the previous chapter.

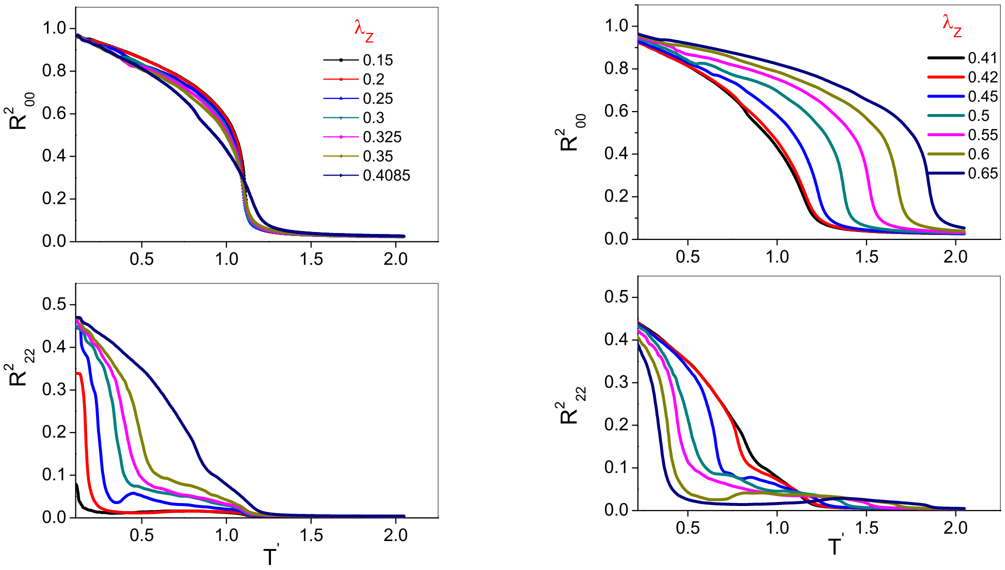

(a)

(b)

Figure 4.25: Order parameter profiles for λ_Z values (a) Range: (0.15, 0.4085) (b) Range: (0.42, 0.65) (L=15, RW-ensembles)

For all the other values of λ_Z, the nature of the intermediate phase can be gauged from the order profiles shown in Fig. 4.25(a), for λ_Z values in the range 0.15 - 0.4085. It may be observed that biaxial order increases in the intermediate phase as λ_Z value increases from 0.15 to 0.4085. The increase is maximum for λ_Z=0.4085, after which it starts decreasing again as shown in the Fig:4.25(b).

It may be observed that the R^2_{22} susceptibility shows a finite and constant increase starting at the transition at T_{C1} for all values of λ_Z, except for λ_Z = 0.2. The susceptibility profiles for the order parameters are shown in Figs. 4.26 - 4.28. Variation of the fourth order energy cumulant V_4 with temperature at different values of λ_Z is depicted in Fig. 4.29. It appears that as λ_Z approaches the Landau point, the low temperature transition shows weak signature of a first order transition. Based on the specific heat and order parameter profiles, we construct the phase diagram along the dispersion parabola, which is shown in Fig. 4.30. This diagram is largely comparable to the mean field phase diagram extensively

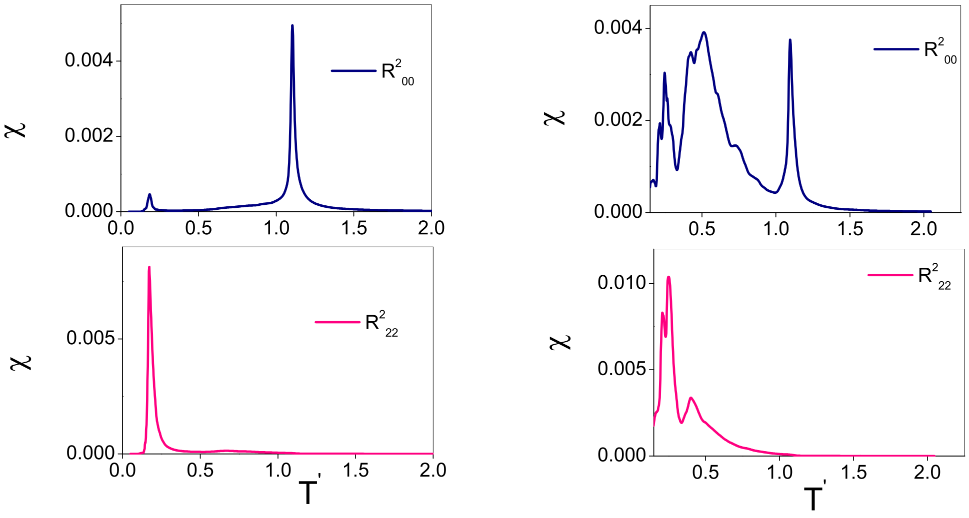

(a) (b)

Figure 4.26: Susceptibilities (χs) of the order parameters for λ_Z values: (a)0.2 (b) 0.25

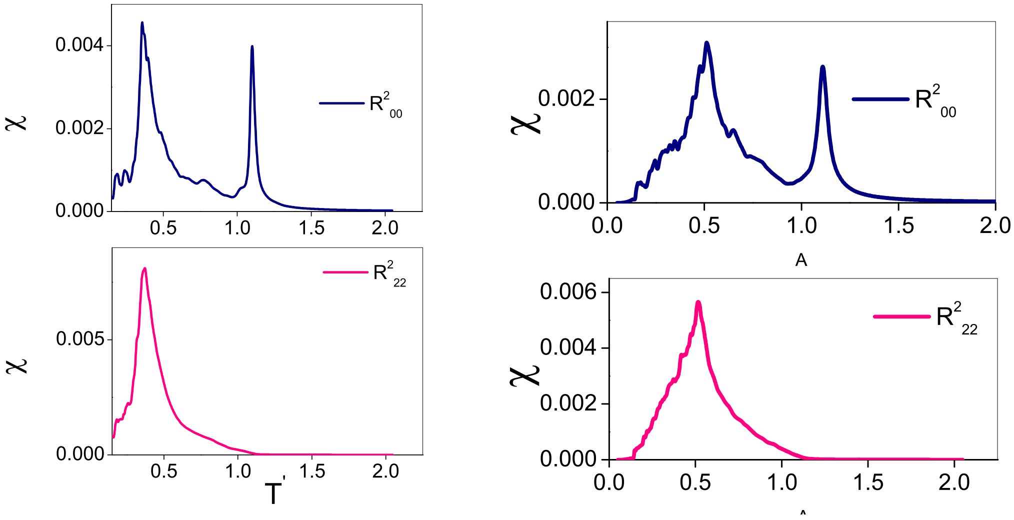

(a) (b)

Figure 4.27: Susceptibilities (χs) of the order parameters for λ_Z values : (a)0.3 (b) 0.35

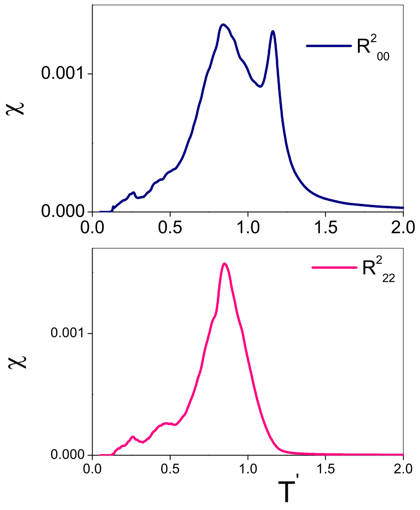

Figure 4.28: Susceptibilities (χs) of the order parameters for λ_Z value 0.4085

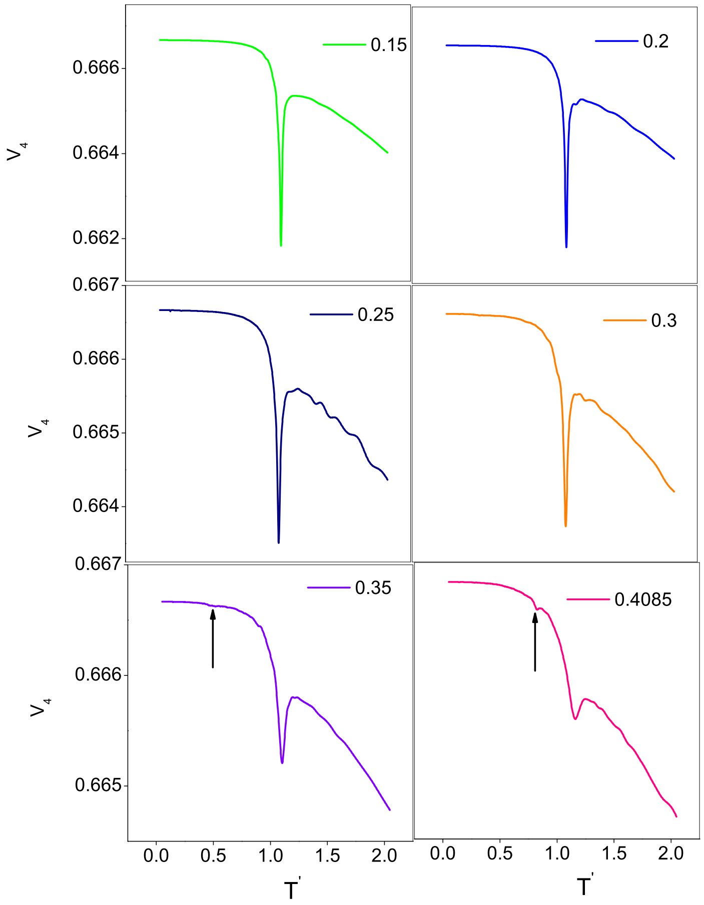

Figure 4.29: Energy cumulants V_4 at various λ_Z values along the path OT (L=15, RW-ensembles)

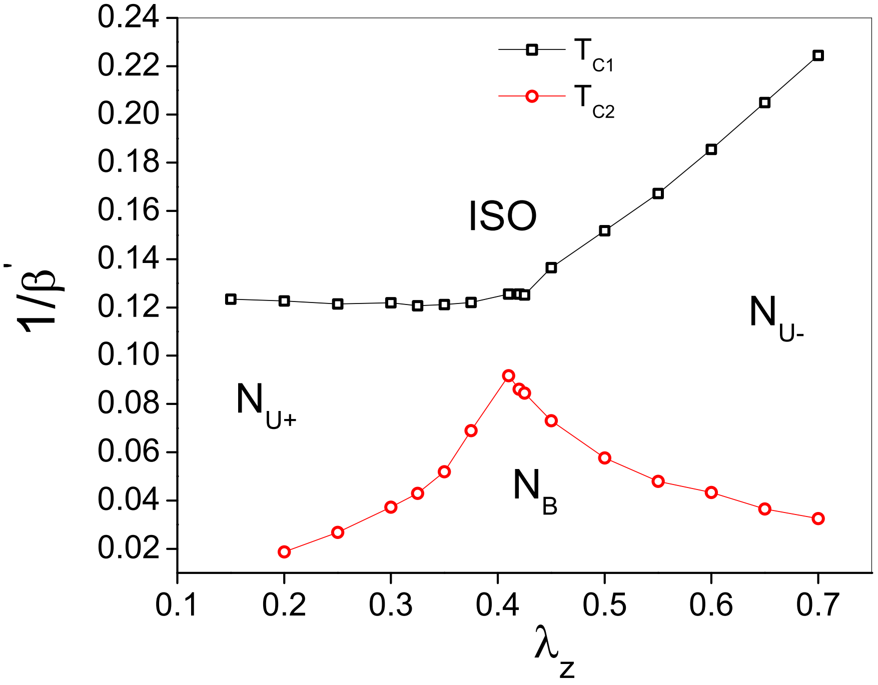

Figure 4.30: Phase diagram along the dispersion parabola from RW-ensembles (L=15)

studied in literature [6] [7] [8] and which was confirmed with Metropolis Monte Carlo simulations [9]. However two major differences are brought out by the present RW-ensembles. Firstly, as was pointed out in the previous chapter, the Landau point now seems to host two transitions in place of a single direct $I - N_B$ transition: it now has an intermediate biaxial phase of low order. Secondly, the symmetry of the intervening phase as one approaches the Landau point T is not clear. Mean field prediction supported by earlier Monte Carlo results suggest a simple and pure uniaxial intermediate phase. Our results indicate that the symmetry of this phase near T is not purely uniaxial, but it does acquire a small but non-zero biaxial character. This discrepancy however vanishes asymptotically as we move away from T, towards the origin O (or to higher values of λ_Z towards 0.7). The curious changes in the symmetry of the intermediate phase (from N_U to $N_{U'}$ in our notation) as one progresses along the parabola towards T prompted a detailed examination of the spatial variation of the orientational correlations of the molecular axes along this path, to be discussed in the next chapter.

4.4 Conclusions

In this chapter, two trajectories inside the essential triangle are explored with entropic sampling method, and compared with MF predictions as well as earlier results base on Metropolis sampling procedure. The first trajectory is a line drawn from apex I of the triangle to the mid point W of the base OV (Fig. 4.1). We refer to the arc length OIW as $\lambda^{'}$, for purposes of discussion. As per MF treatment this line cuts both the trajectories of C_2C_3 and C_1C_3. Thus the phase sequences along this line IW should be qualitatively similar to that on the λ-axis. In particular the direct transition from isotropic to biaxial phase is expected to be interrupted by a uniaxial nematic phase beyond a value as γ increases, and the temperature range of the uniaxial phase should progressively increase, suppressing the second transition temperature, till the line cuts the parabola, at Z (Fig.4.1). Results from mean field treatment in the partly repulsive region on this line IW are not available for direct comparison, even though it is established that biaxial phase would not be stable at the point W [1, 10]. The phase sequences in the present work qualitatively follow this scenario, but with a curious deviation. The intervening ”uniaxial ” phase N_U is not strictly devoid of biaxial symmetry. Indeed all along the line, beyond $K^{'}$ (Fig.4.1), and upto point Z, the onset of the uniaxial order is invariably accompanied by a small, but unmistakable, development of biaxial symmetry. We thus refer to this phase as $N_{U'}$, to make this subtle distinction. This small degree of biaxiality of the $N_{U'}$ phase is temperature independent within that phase, and is also fairly independent of its location in the trajectory beyond $K^{'}$. An examination of the free energy profiles, drawn as a function of both the major order parameters, show interesting features: while the free energy curves show smooth variation of the minima with respect to R^2_{00} as the temperature is varied, the case of R^2_{22} is qualitatively different. These profiles exhibit free energy barriers at low values of R^2_{22}, which could be overcome (thereby pushing the system to access regions of higher and discernible order), only after these initial barriers could be overcome on considerable cooling. Thus these results show a complex free energy surface that develops with decrease of temperature on a typical trajectory inside the triangle. It appears that development of a $N_{U'}$ phase with a small biaxial order (≤ 0.05) is expected, and the degree of this symmetry is restricted by the free energy barriers till the system is permitted to access these regions of biaxial order. Given that such barriers are strongly dependent on the size of the system, it is a plausible conjecture to suggest that in real systems these barriers are not readily overcome (or equivalently, requires significant cooling of the medium), and hence their biaxial order appears to be restricted inherently. Under such circumstances requiring wider temperature ranges to overcome barriers, real systems may have other competing interactions (like translational degrees, influencing the phase sequence qualitatively differently , e.g layer formation). Deviations of real systems from MF predictions [11] could perhaps be understood in these terms.

The second trajectory, the segment of the dispersion parabola OZT within the triangle, is a curiosity. At the origin of the triangle the model collapses to the Lebwohl-Lasher interaction. As the conclusions of the earlier chapter indicated, it appears that the Landau point T hosts the sequences $N_B - N_{B1} - I$, alluding to the presence of a non-uniaxial intermediate phase. Thus, as the set of interaction parameters (γ, λ) are varied to traverse the parabola (through a single parameter λ_Z), the scenario should change qualitatively as to reach the observed phase sequence at the Landau point T asymptotically. It is with this objective that the phase sequences are investigated. We find that for lower values of λ_Z (≤ 0.25), the intervening phase is purely uniaxial (within computational errors), thus the biaxial interaction acting only as a perturbation on the LL coupling. We find that the nature of the intermediate phase changes ($N_U \rightarrow N_{U'}$) as λ_Z increases. We conclude that in the intermediate neighbourhood of T, the phase sequence is : $N_B - N_{U'} - I$. While the simulated phase diagram(Fig.4.30) is similar to the well known data on the parabola, this subtle distinction regarding the nature of the intervening ”uniaxial” phase perhaps need to be made, besides ofcourse the qualitatively different phase sequence at the Landau point.

Bibliography

[1] G. De Matteis, F.Bisi and E. G. Virga, *Continuum Mech.Thermodyn.* **19** 1 - 23 (2007).

[2] F. Bisi, E. G. Virga, Jr. E. C. Gartland, G. De Matteis, A. M. Sonnet and G. E. Durand, *Phys. Rev. E* **73**, 051709 (2006).

[3] G. R. Luckhurst and S. Romano, *Mol.Phys.* **40**, 129 (1980).

[4] F. Bisi, S. Romano and E. G. Virga, *Phy. Rev. E* **75**, 041705 (2007).

[5] G.R. Luckhurst, C. Zannoni, P. L. Nordio, U. Segre, *Mol. Phys.* **30**, 1345 (1975).

[6] R. Alben, *Phy. Rev. Lett.* **30**, 778 (1973).

[7] J. P. Straley, *Phys. Rev. A* **10**, 1881 (1974).

[8] D. K. Remler and A. D. J. Haymet, *J. Phys. Chem.* **90**, 5426 (1986).

[9] F. Biscarini, C. Chiccoli, P. Pasini, F. Semeria and C. Zannoni, *Phys. Rev. Lett.* **75**, 1803 (1995).

[10] G. De Matteis and S. Romano, Phys. Rev. E. **78**, 021702 (2008).

[11] F. Bisi, G. R. Luckhurst, E. G. Virga, *Phy. Rev. E* **78**, 021710 (2008).

Chapter 5

A Study of Pretransitional Behaviour of Biaxial Nematics

5.1 Introduction

The nematic - isotropic (NI) transition is a weak first order transition, a fact which is experimentally corroborated by the observed small changes in latent heat and volume at the clearing transition, as compared to the melting transition from the crystal to nematic phase. Its features are well accounted for by the Landau-de Gennes theory [1]. As a consequence, large pretransitional effects, reminiscent of second order behaviour are expected to be observed in the region very close to the transition. Physical observables like the intensity of scattered light and birefringence in the isotropic phase near the clearing point vary essentially as $(T - T^{*})^{-1}$ where T^{*} is the second order transition temperature [2]. These quantities are observed to diverge at the isotropic-nematic transition temperature T = T_{NI}. In principle T^{*} is not observable because it is preceded by a first order transition at T_{NI}. Thus critical behaviour is observed very close to T_{NI}, which cannot be satisfactorily explained by Landau theory which essentially considers the free energy as a function of the mean order parameter.

A nematic liquid crystal is characterised by the orientational order which develops at the NI phase transition as the uniaxial nematic is cooled from the isotropic phase. The amount of orientational order, which develops in thermal equilibrium, is given by the mean value of the order parameter. However, any disturbance of the system, such as a thermal fluctuation, produces spatial variations of the order parameter. Spatial correlations between the local fluctuations of the order parameter from its mean value influence the thermodynamic functions near a phase transition. The generalized Landau-de Gennes theory (GLGT) of the nematic-isotropic transition assumes these fluctuations to be small, and the generalized free energy density at each temperature is written in terms of the order parameter and its spatial derivatives. The analysis of the the resulting Landau free energy in the Gaussian approximation leads to the calculation of correlation functions of the order parameter tensor [3]. The pair correlation function has an Ornstein-Zernike form [4] and away from the critical point the spatial correlations decay exponentially, whereas nearer to the critical point the correlations become extremely long-ranged, mimicking a power law behaviour , like $(1/r)$. The correlation length $\boldsymbol{\xi}$ is a measure of the distance over which the local fluctuations are correlated, and can be estimated from the asymptotic behaviour of the pair correlation function. The correlation length is practically zero at infinitely high temperature, and diverges as $T \rightarrow T^*$ with a a critical exponent $\nu = 0.5$. This divergent behaviour of $\boldsymbol{\xi}$ gives rise to the pretransitional phenomena mentioned above in the isotropic phase of uniaxial nematics.

A Monte Carlo study of the uniaxial nematic using the Lebowhl - Lasher model [5] as the prototype was instrumental in extracting the isotropic - nematic transition temperature and also the correct order of magnitude of the deviation of T_{NI} from T^*, which is $1°K$. The transitional and pretransitional behaviour of the order parameters and pair correlations were studied and found to be in compliance with Landau-de Gennes theory of phase transitions in liquid crystals [6]. This study assumed the uniaxial nematic to be made up molecules with $D_{\infty h}$ symmetry.

In the light of the recent experimental realisations of the thermotropic biaxial nematic phase, in tetrapodes [7] and bent-core mesogens [8], the aim of this chapter is to explore, as a preliminary exercise, the pretransitional orientational ordering effects exhibited by a biaxial nematic as it is cooled from the isotropic phase through an intervening uniaxial nematic phase to the low temperature biaxial phase, and to estimate correlation lengths and the critical exponents associated with both $I - N_U$ and $N_U - N_B$ transitions.

Theoretically, the critical and multicritical fluctuations in nematic liquid crystals were studied within a mean field approach [9] by considering the order parameter fluctuation modes near the isotropic-uniaxial nematic and uniaxial-biaxial nematic transitions, after the experimental realization of the critical points [10] and critical opalescence in the nematic phase [11]. The critical exponents associated with the uniaxial-biaxial nematic transition in a model made of rod-like and disc-like molecules were estimated within the frame work of Landau - de Gennes theory, and renormalization theory to the first order in the expansion coefficient ϵ. On the experimental front, a recent dynamic light cattering study from orientational order fluctuations in a liquid crystalline tetrapode [12] revealed distinct relaxational modes associated with the uniaxial and biaxial order parameters. The measured linear pretransitional temperature dependence of the measured parameters associated with biaxiality is explained by Landau-de Gennes theory.

For the present simulation in this context, we consider a bulk biaxial nematic made up of molecules of D_{2h} symmetry and the interaction between the molecules is assumed to be in the dispersion approximation for simplicity and convenience. The interaction Hamiltonian is parameterised in the (γ, λ) space, by the dispersion parabola OT of the essential triangle (Chapter3, fig 1) [13]. The Phase diagram for this Hamiltonian [14] predicts a first order isotropic-uniaxial nematic transition at a higher temperature followed by a second order uniaxial-to-biaxial nematic transition at a lower temperature. The biaxial nematic phase at a given temperature and as λ_z is varied, is sandwiched between two uniaxial nematic phases N_{U+} and N_{U-} and a Landau triple point exists where the two second order lines meet the first order line. At that point, a direct second order transition is predicted between the isotropic-biaxial nematic phases [15]. The Landau triple point occurs for large biaxiality parameter $\lambda_Z = \dfrac{1}{\sqrt{6}}$ which corresponds to a switching of the molecular shape from a distorted prolate to distorted oblate ellipsoid. It is observed from the phase diagram that the transition temperature is highest at the triple point. This Landau triple point corresponds to the point 'T' in the essential triangle referred to earlier.

The pretransitional effects associated with the above mentioned transitions is particularly interesting in view of the phase behaviour exhibited by the biaxial nematic on cooling from the isotropic state. The phase diagram of the dispersion Hamiltonian has been discussed in detail in chapter 3 and we note that for $\lambda_Z > 0.2$ the uniaxial state is characterised by a small amount of biaxial order which starts developing at the isotropic - uniaxial nematic transition itself. Thus the uniaxial phase exhibited by the biaxial molecules of D_{2h} symmetry does not appear at the mesoscopic level to be necessarily identical to the conventional uniaxial phase formed due to the alignment of rod like molecules of D_{2h} symmetry. We expect that the pretransitional behaviour in the isotropic phase and uniaxial nematic phase could show possible signatures of this development.

We adopt a lattice-based biaxial Hamiltonian in the dispersion approximation for the study the behaviour of a bulk biaxial nematic sample. We employ Markov chain Monte Carlo methods based on Metropolis algorithm to compute the second rank angular pair correlation coefficients in the three distinguishing directions of the biaxial molecules as a function of distance (in lattice units). The variations of these parameters, at various temperatures bracketing the transitions, quantify the critical behaviour of the system near the transitions. The characterisation of pretransitional signatures is done with chosen values of the intrinsic molecular biaxiality λ_Z of the molecules, spanning the relevant part of the phase diagram for this model [14]. The critical fluctuations in the close proximity of the transitions at various points in the phase diagram are thus obtained and the results are compared. In the following, section 2 briefly introduces the lattice model for the biaxial system and provides details of our simulations. The results are presented and discussed in section 3 and conclusions are presented in section 4.

5.2 Model used and System studied

The lattice model within the dispersion approximation is characterized by the biaxiality parameter λ_Z (chapter 1). The resulting phase diagram predicts, on cooling the sample from the isotropic phase, successive formation of uniaxial and biaxial nematic phases for non-zero values of λ_Z, with the isotropic-nematic transition temperature (all reported in appropriate reduced units) being essentially independent of the parameter λ_Z. Focussing on the selection of the parabola within the essential triangle, the spread of the intermediate uniaxial nematic phase however is diminished gradually with increase in λ_Z, finally culminating in a direct transition to biaxial phase from the isotropic fluid at $(\lambda_Z \sim 0.4)$ as per mean-field predictions and Metropolis based Monte Carlo simulations. The Hamiltonian is given by (Chapter 1, eqn.(1.4.2))

$$H = -\epsilon_{ij}\{P_2(\cos(\beta_{ij})) + 2\lambda_Z[R^2_{02}(\omega_{ij}) + R^2_{20}(\omega_{ij})] + 4\lambda_Z^2 R^2_{22}(\omega_{ij})\} \tag{5.2.1}$$

where ϵ_{ij} is the coupling constant which determines the reduced temperature, $\omega(\alpha, \beta, \gamma)$ are the set of Euler angles, R^L_{mn} are symmetrized Wigner functions, $P_2(cos(\beta_{ij}))$ is Legendre polynomial and λ_Z is the shape biaxiality parameter, which determines the amount of molecular biaxiality.

The phase diagram of this Hamiltonian has a Landau triple point at $\lambda_Z = \dfrac{1}{\sqrt{6}}$. It is known from earlier Monte Carlo simulations [14,15]that the molecules are prolate in shape for values of $\lambda_Z < \dfrac{1}{\sqrt{6}}$ and oblate otherwise. The above expression is conveniently recast as a function of inner products of different vectors specifying the orientations of different molecules (x_i, y_i, z_i) with respect to those of the chosen laboratory frame (X, Y, Z), and is expressed as [15]

$$U_{ij} = -\epsilon\{\frac{3}{2}V_{33} - \sqrt{6}\lambda_Z(V_{11} - V_{22}) + \lambda_Z^2(V_{11} + V_{22} - V_{12} - V_{21}) - \frac{1}{2}\} \tag{5.2.2}$$

Here $V_{ab} = (u_a.v_b)^2$, and the unit vectors u_a, v_b, $[a, b = 1, 2, 3]$, are the three axes of the two interacting neighbouring molecules. λ_Z sets the relative importance of the biaxial interaction in the Hamiltonian, while ϵ (set to unity in the simulations) defines the temperature scale $(T^{'} = \dfrac{k_B T^*}{\epsilon})$, where T^* is the laboratory temperature.

5.3 Simulation Details

A cubic lattice (L=31 in lattice units) with periodic conditions is considered as the bulk sample for simulation. The molecules on the lattice sites are treated as liquid crystal constituents which interact through the nearest neighbour interaction potential given in Eqn.5.2.2. In order to compute the spatial correlations of the molecular axes, a molecule is selected at a random site and the number of neighbours at distances ranging from 1 to 15 lattice units are identified and arranged in successive shells of increasing radius. Markov chain Monte Carlo simulations were used to equilibrate the sample for different experimental conditions, the experimental parameters for each experiment being the biaxiality parameter λ_Z and a given temperature T' (in reduced units) chosen very close to the transition temperature. By adopting this sampling procedure, we conform to the established phase sequence as a function of λ_Z [14]. Simulations were done for 3 sets of λ_Z (0.2, 0.275. 0.35). The isotropic-uniaxial transition temperature T_{NI} is approximately constant (1.1, in reduced units) for all values of λ_Z, but the uniaxial-biaxial transition temperature varies from about 0.15 to about 0.5 as λ_Z changes from 0.2 to 0.35.

A simulation experiment for a given λ_Z consists of cooling the sample from the isotropic phase to the biaxial phase and collecting the relevant data at various temperatures very close to the $I-N_U$ and N_U-N_B transitions. A total of 11 million microstates are sampled at each temperature, out of which 1 million are used for equilibration of the sample at that temperature. At each temperature the correlation between the orientation of the chosen molecule i at a given random site and its neighbor j separated by a distance r_{ij} , having a relative orientation β_{ij} is calculated using the second rank angular pair correlation coefficient

$$G_2(r_{ij}) = \langle P_2(cos(\beta_{ij}))\rangle \tag{5.3.1}$$

The averaging is done over various shells surrounding 15 such random sites at each temperature. The angular correlations are computed for the three molecular axes using Eqn.(5.3.1) in the isotropic state as the $I - N_U$ transition is approached from the high temperature side, at a temperature resolution of 0.001 (in reduced units) very close to the observed transition temperature T_{C1}. the same procedure is repeated at the uniaxial-biaxial transition as the transition is approached from the high temperature uniaxial phase at the same temperature resolution mentioned above. The spatial variation of the correlation function $G_2(r)$ is fitted to the classical Ornstein-Zernike (OZ)form [6]

$$G_2(r) = (\frac{A}{r})exp(-\frac{r}{\boldsymbol{\xi}}) \tag{5.3.2}$$

where $\boldsymbol{\xi}$ is the correlation length in lattice units. This length varies with temperature at the transition as

$$\boldsymbol{\xi} = A(T - T_C)^{-\nu} \tag{5.3.3}$$

where the exponent ν refers to the divergent behaviour of the correlation length in the critical region.

The simulations are done for various values of the biaxiality parameter (λ_Z = 0.0, 0.2, 0.275, 0.35) so as to examine the effect of the degree of molecular biaxiality on the formation of nematic clusters at the $I - N_U$ and $N_U - N_B$ transitions.

5.4 Results and Discussions

For a given λ_Z, as the sample is cooled from the isotropic phase, the spatial correlations $G_2(r)$ for the molecular $\boldsymbol{x}, \boldsymbol{y}, \boldsymbol{z}$ axes are calculated at various temperatures, below and above the isotropic nematic transition temperature. In the following discussion, these are denoted as $GX(r), GY(r), GZ(r)$, respectively. At each temperature, the decay of the correlation function is fitted to the OZ relation in Eqn. (5.3.2) and correlation length at that temperature is extracted, for each molecular axes. These correlation lengths $(\boldsymbol{\xi}_x, \boldsymbol{\xi}_y, \boldsymbol{\xi}_z)$ for $(\boldsymbol{x}, \boldsymbol{y}, \boldsymbol{z})$ molecular axes are then fitted to the power law behaviour in Eqn. (5.3.3) and the exponent ν is estimated. This procedure is repeated covering the $N_U - N_B$ transition as well. The results and the analysis at $I - N_U$ and $N_U - N_B$ transitions are presented in the following subsections.

5.4.1 $I - N_U$ transition

Since the same methodology is applied for collection and analysis of the data at each value of λ_Z, we show a representative analysis of the data for λ_Z=0.35 at the $I - N_U$ transition.

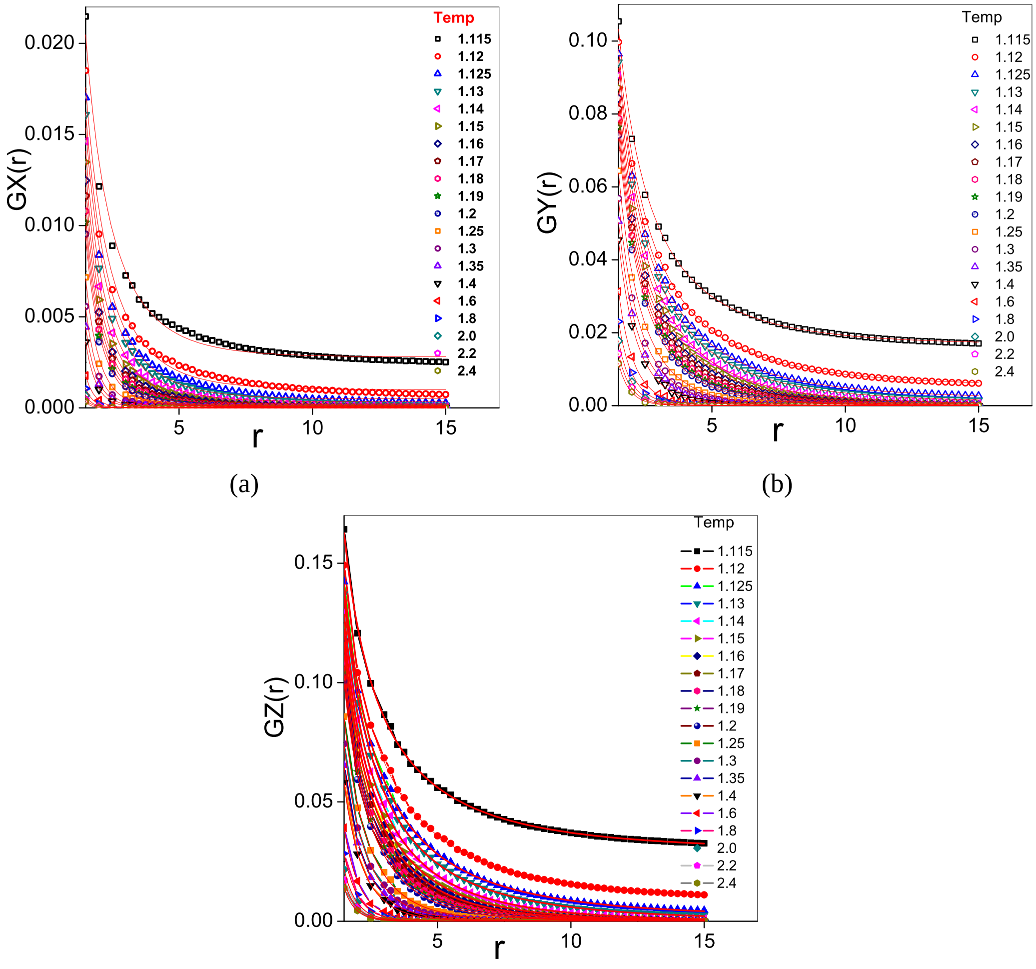

(a) (b)

(c)

Figure 5.1: Spatial variation of angular correlations of different molecular axes near the $I - N_U$ transition temperature ($T^{'}$ = 1.12) for λ_Z=0.35

Figs.5.1(a) - 5.1(c) depict the spatial variation of the correlation function at various temperatures in the vicinity of the $I - N_U$ transition, which are fitted to the Ornstein-Zernike equation in Eqn.(5.3.2) for $\lambda_Z = 0.35$. The extracted correlation lengths at each temperature are plotted as a function of temperature.

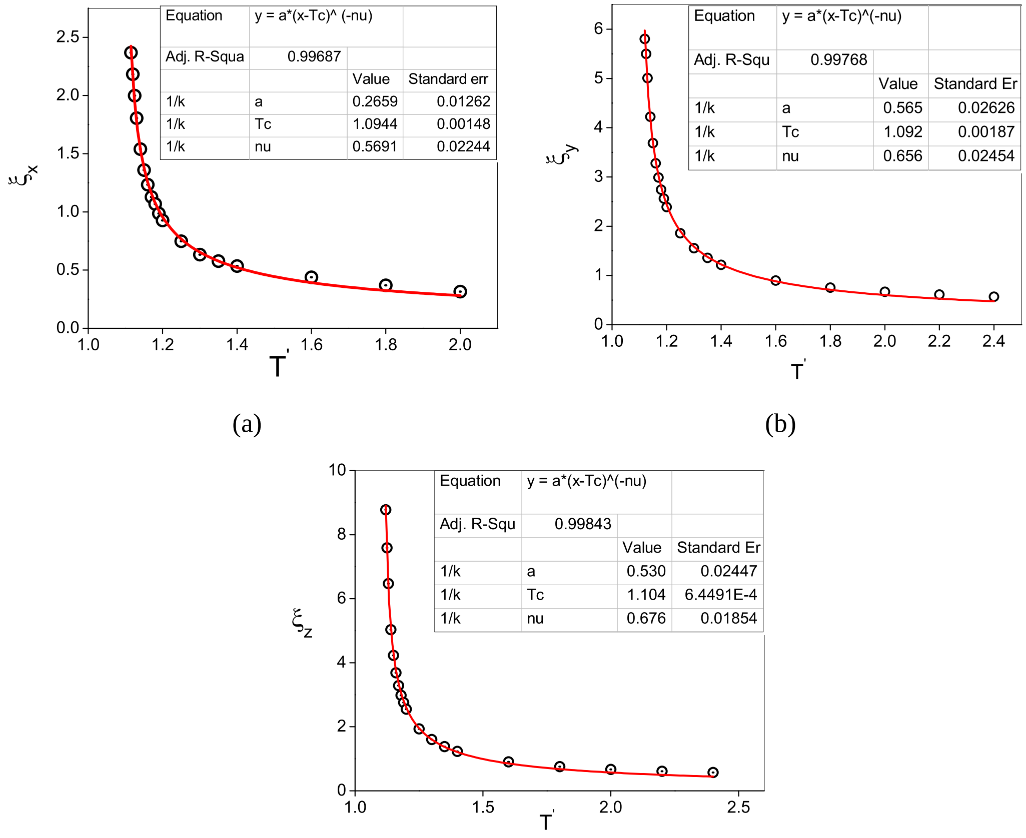

(a)

(b)

(c)

Figure 5.2: Fits of correlation lengths of different molecular axes to the power law behaviour (Eqn.5.3.3 near the $I - N_U$ transition (λ_Z=0.35)

Figs. 5.2(a)-5.2(c) show temperature fit of the correlation lengths to a power law behavior yielding the values of the exponents associated with different molecular axes.

Similar analysis is done at λ_Z = 0.2 and 0.275. The values of the extracted exponents, are tabulated in Tables. 5.1 - 5.3. A comparison of the correlation lengths of the three molecular axes at the $I - N_U$ transition for various values of λ_Z is presented in Table 5.4.

5.4.2 $N_U - N_B$ transition

The fit of the spatial correlations to the Orenstein-Zernike relation at the $N_U - N_B$ transition for λ_Z = 0.35 is depicted in Figs.5.3(a) - 5.3(c). The plots (not shown here) for λ_Z = 0.275 exhibit similar behaviour. However, similar study for λ_Z=0.2 at the $N_U - N_B$

Table 5.1: Critical exponents and estimated T_{C1} values from angular correlations of different molecular axes (λ_Z=0.35)

Molecular axis	$\boldsymbol{\nu}$	$\boldsymbol{T_{C1}}$
$\boldsymbol{x}$	0.569 ± 0.022	1.090 ± 0.00148
$\boldsymbol{y}$	0.656 ± 0.02454	1.090 ± 0.00187
$\boldsymbol{z}$	0.676 ± 0.01854	1.100 ± 6.44E-04

Table 5.2: Critical exponents and estimated T_{C1} values from angular correlations of different molecular axes (λ_Z=0.275)

Molecular axis	$\boldsymbol{\nu}$	$\boldsymbol{T_{C1}}$
$\boldsymbol{x}$	0.588 ± 0.01532	1.104 ± 3.86E-04
$\boldsymbol{y}$	0.595 ± 0.0188	1.090 ± 8.5E-04
$\boldsymbol{z}$	0.621 ± 0.013	1.105 ± 2.4E-04

Table 5.3: Critical exponents and estimated T_{C1} values from angular correlations of different molecular axes (λ_Z=0.2)

Molecular axis	$\boldsymbol{\nu}$	$\boldsymbol{T_{C1}}$
$\boldsymbol{x}$	0.552 ± 0.0048	1.112 ± 5.0E-05
$\boldsymbol{y}$	0.534 ± 0.00325	1.107 ± 7.12E-05
$\boldsymbol{z}$	0.483 ± 0.0181	1.115 ± 1.85E-04

Table 5.4: Correlation lengths for various λ_Z at the $I - N_U$ transition

$\boldsymbol{\lambda_z}$	$\boldsymbol{x-axis}$		$\boldsymbol{y-axis}$		$\boldsymbol{z-axis}$	
	$\boldsymbol{\xi_x}$	$\boldsymbol{T_{C1}}$	$\boldsymbol{\xi_y}$	$\boldsymbol{T_{C1}}$	$\boldsymbol{\xi_z}$	$\boldsymbol{T_{C1}}$
0.2	7.5	1.118	6.43	1.12	7.9	1.12
0.275	5.79	1.117	6.0	1.117	8.77	1.114
0.35	2.3	1.12	5.8	1.12	8.87	1.12

transition, shown in Figs. 5.4(a) - 5.4(c), shows a very interesting scenario. Large fluctuations are observed in the correlation functions $GX(r)$ and $GY(r)$ near the $N_U - N_B$ transition, whereas $GZ(r)$ is unaffected by the transition. Correlation lengths are extracted (as described previously) for λ_Z = 0.35 and 0.275. However, it was not possible to extract the correlation lengths for λ_Z = 0.2 as they could not be fit to OZ equation. Further, a power law fit of the correlation lengths (that could be extracted for λ_Z = 0.35 and λ_Z = 0.275) could not be made satisfactorily for this value of λ_Z, indicating deviations from the expected temperature variation near this transition.

Summing up these observations, it appears that a power law fit, reminiscent of mean-field expectation, could not be made for λ_Z = 0.35 and λ_Z = 0.275 near the $N_U - N_B$ transition. And λ_Z = 0.2 seems to be corresponding to a cross-over region from a perturbed LL model to an established biaxial Hamiltonian. The strong deviation from OZ relation, of the spatial variations of the angular correlations at λ_Z=0.2, in the case of all three molecular axes, seems to be a strong pointer to the manifestations of the crossover.

5.4.3 Temperature Variation of Correlation Lengths

The variation of the angular correlation lengths of all the three molecular axes as a function of temperature at both $I-N_U$ and N_U-N_B transitions for $\lambda_Z = 0.275$ are depicted in Figs. 5.5(a) - 5.5(c) and for $\lambda_Z = 0.35$ in Figs. 5.6(a) - 5.6(c) respectively. It may be seen that the correlation lengths of the short molecular axes double at the low temperature $N_U - N_B$

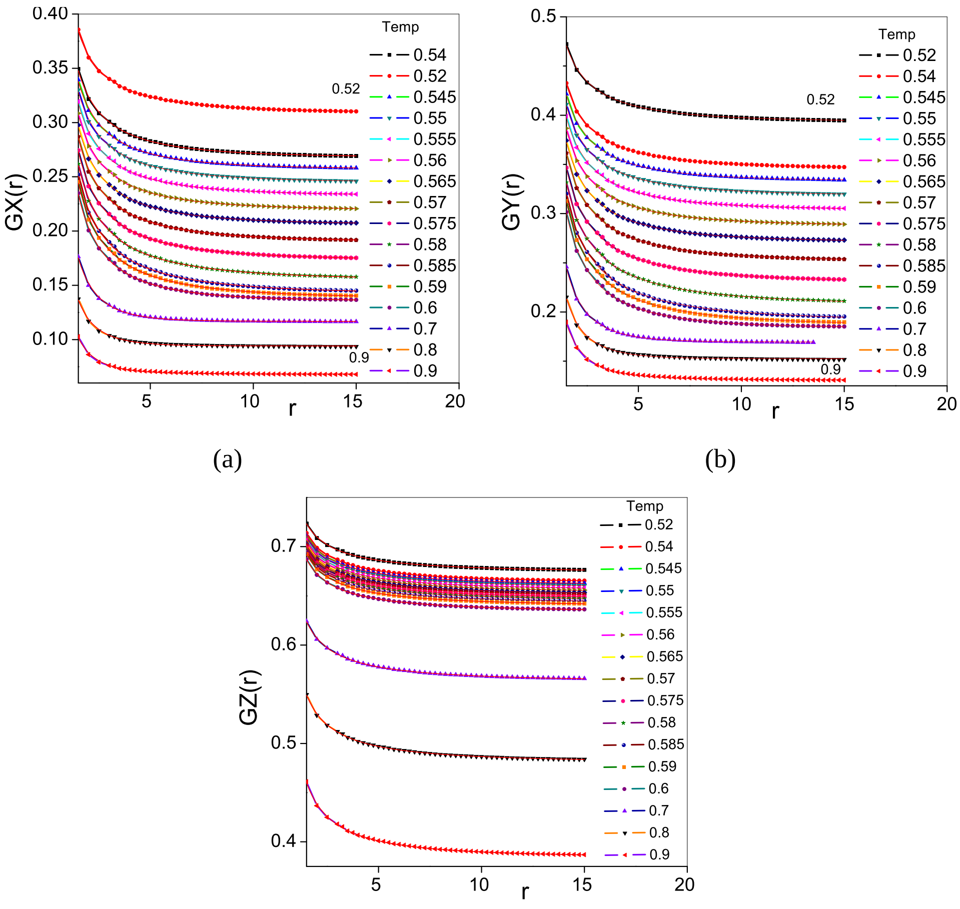

(a)

(b)

(c)

Figure 5.3: Spatial variation of angular correlations of different molecular axes near the $N_U - N_B$ transition temperature ($T^{'}$ = 0.51) for λ_Z=0.35

transition for both values of the biaxiality parameter λ_Z (relative to their values at $I - N_U$ transition), whereas the correlation length scale of the long molecular axis decreases compared to its value at $I - N_U$ transition. These observations are in line with the expectations regarding the effect of condensation of different phases on the ordering of the different molecular axes. This behaviour indicates that the ordering of the molecular long axis ($\boldsymbol{z}$ axis) is achieved initially at the $I - N_U$ transition. As the temperature of the bulk biaxial liquid crystal is further cooled, the short molecular axes are ordered at the $N_U - N_B$ transition. The long molecular axis appears to be unaffected by the low temperature $N_U - N_B$ transition.

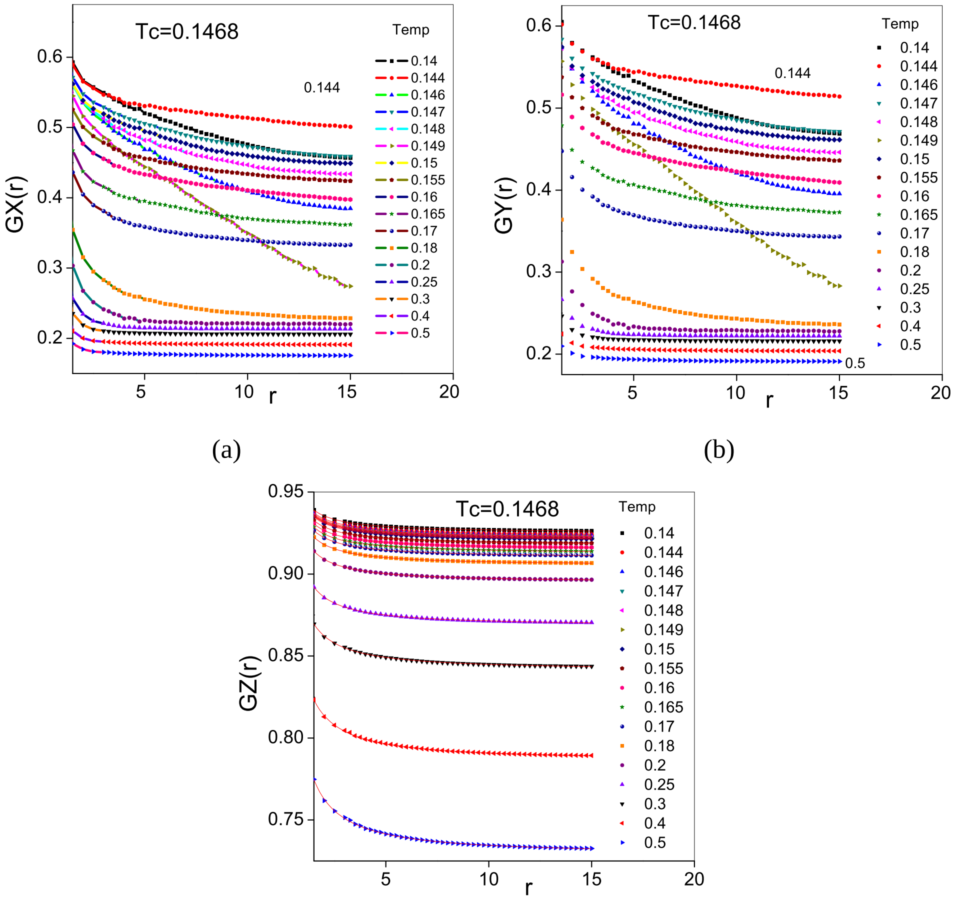

(a)

(b)

(c)

Figure 5.4: Spatial variation of angular correlations of different molecular axes near the $N_U - N_B$ transition temperature ($T^{'}$ = 0.15) for λ_Z=0.2

5.4.4 Effect of the Biaxiality Parameter λ_Z

The above discussion near the $I-N_U$ transition and the results in Table. 5.4 are summarised in Figs.5.7(a) - 5.7(d). A comparative study of the correlation lengths for molecular axes $(\boldsymbol{x}, \boldsymbol{y}, \boldsymbol{z})$ at various temperatures near the $I - N_U$ transition with variation of the biaxiality parameter λ_Z are shown in Figs.5.7(a) - 5.7(d). Referring to Fig. 5.7(a) we find that on comparison with a uniaxial nematic (λ_Z=0.0) which exhibits correlation length scales of 4-5 lattice units near the transition temperature, these results indicate that for a biaxial system, nematic clusters of larger size are formed in the isotropic phase at the transition point. The correlation length scales of the $\boldsymbol{x}$ axes decrease steadily as λ_Z increases from 0.2 to 0.35, as shown in Fig. 5.7(b). The correlation lengths for $\boldsymbol{y}$ and $\boldsymbol{z}$ axes remain relatively the same

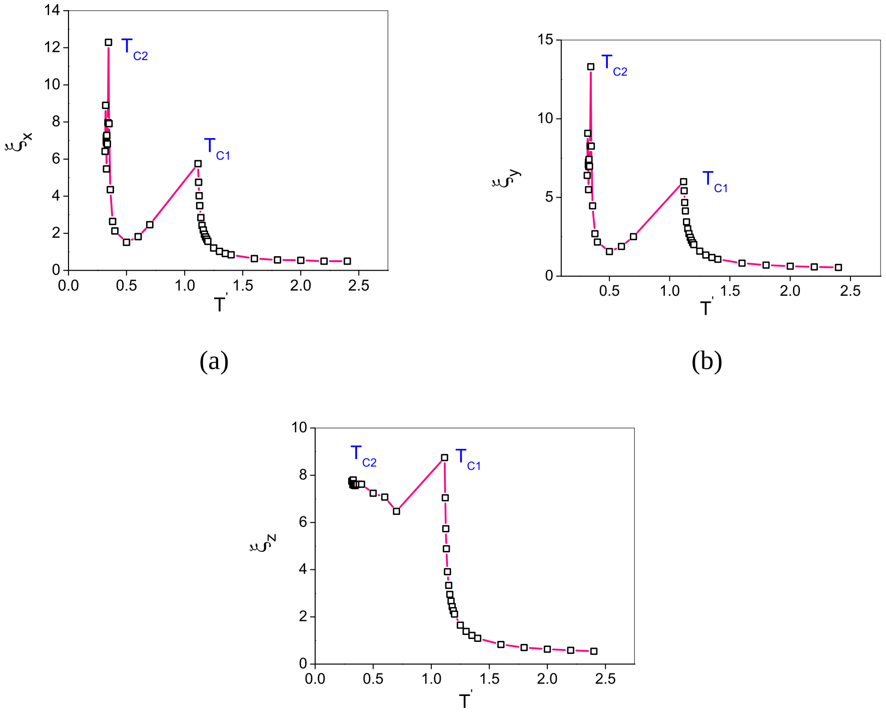

(a)

(b)

(c)

Figure 5.5: Variation with temperature of correlation lengths of different molecular axes covering both transitions for λ_Z = 0.275

for all values of λ_Z.

5.5 conclusions

The characteristic lengths associated with angular correlations of the three molecular axes of a biaxial liquid crystal were estimated in this Chapter using Metropolis based Monte Carlo sampling method. We find that average correlation length of the molecular long axis (z-axes) to be 8 lattice units, at the $I - N_U$ transition. This value is approximately twice that of a uniaxial liquid crystal (4-5 lattice units) reported based on the LL model under identical conditions of lattice size and simulation conditions. The correlation lengths of y- and z-axes are independent of the value of λ_Z at the $I - N_U$ transition. The length associated with the molecular x-axes however is different : It is comparable for λ_Z = 0.2 and 0,275, but significantly decreases for λ_Z - 0.35. The critical exponents for all the three

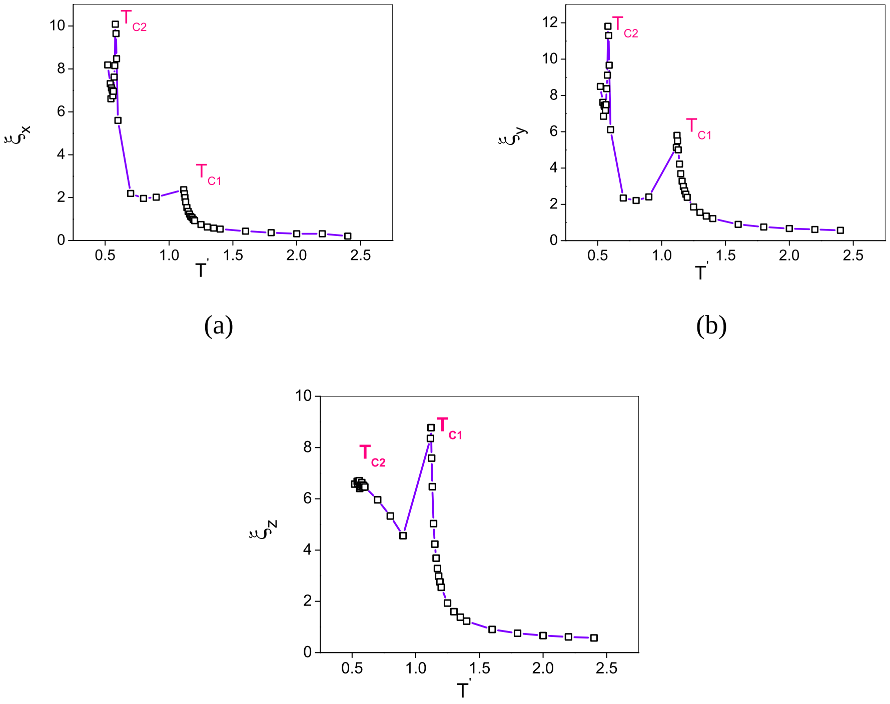

(a)

(b)

(c)

Figure 5.6: Variation with temperature of correlation lengths of different molecular axes covering both transitions for λ_Z = 0.35

axes remain approximately in the range 0.55-0.6 at the $I - N_U$ transition.

The critical exponents could not be calculated at the $N_U - N_B$ transition, since a temperature fit to a power law behaviour was not found possible. Finally, the deviation (from OZ behaviour) at $N_U - N_B$ transition at λ_Z = 0.2 seems to be a manifestation of the cross over region between the perturbed LL model and a strong biaxial Hamiltonian. As this point lies very close to the γ-axis, the biaxial-biaxial coupling term (third term in eqn.5.2.1) and the uniaxial-biaxial coupling term (second term in eqn.5.2.1) have competing effects on the ordering of all the molecular axes, and it appears that unique assignment of corresponding correlation lengths is not feasible.

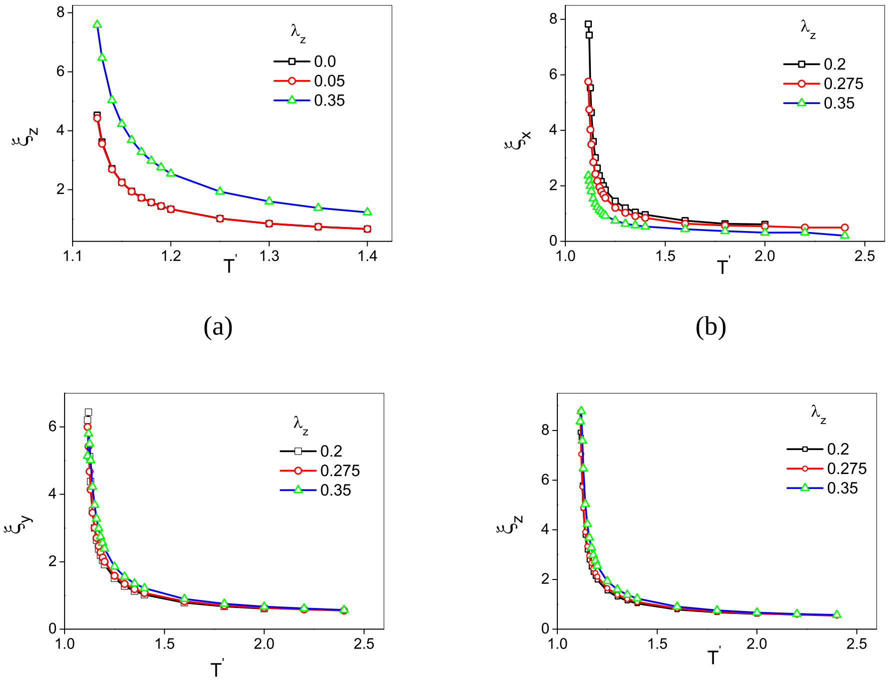

(a) (b)

(c) (d)

Figure 5.7: comparison of correlation lengths at $I - N_U$transition for different λ_Z

Bibliography

[1] P. G. De Gennes,*Mol. Cryst. Liq. Cryst.***12**,193 (1971).

[2] S. Chandrasekhar. *Liquid Crystals*. Cambridge University Press, 2nd edition, January 29, 1993.

[3] E. F. Gramsbergen, L. Longa and W. H. de Jeu, *Phys. Rep.* **135**, 195 (1986).

[4] P. G. De Gennes and J. Prost, *The Physics of Liquid Crystals*, 2nd edition, Clarendon Press, Oxford, 1993.

[5] P. A. Lebwohl, G. Lasher,*Phys. Rev. A* **6**, 426 (1972).

[6] U. Fabbri, C. Zannoni, *Mol. Phys.* **58**, 763 (1986).

[7] K. Merkel, A. Kocot, J. K. Vij, R. Korlacki, G. H. Mehl, T. Meyer. *Phys. Rev. Lett.*,**93**, 237801(2004)

[8] B. R. Acharya, A. Primak, and S. Kumar. *Phy. Rev. Lett***92**, 145506(2004).

[9] Z. H. Wang, P. H. Keyes, *Phys. Rev. E* textbf54, 5249 (1996).

[10] I. Leldis and G. Durand, *Phy. Rev. E* **48**, 3822 (1993).

[11] J. P. McClymer and P. H. Keyes, *Phys. Rev. E* **48**, 2838 (1993).

[12] K. Neupane, S. W. Kang, S. Sharma, D. Carney, T. Meyer, G. H. Mehl, D. W. Allender, Satyendra Kumar, and S. Sprunt, *Phys. Rev. Lett.* **97**, 207802 (2006).

[13] F. Bisi, E. G. Virga, Jr. E. C. Gartland, G. De Matteis, A. M. Sonnet, and G. E. Durand,*Phys. Rev. E* **73**, 051709 (2006).

[14] F. Biscarini, C. Chiccoli, P. Pasini, F. Semeria, C. Zannoni, textit Phys. Rev. Lett. **75,** 1803 (1995).

[15] C. Chiccoli, P. Pasini, F. Semeria, C. Zannoni, *Int. J. Mod. Phys. C.* **10**, 469 (1999).

Chapter 6

Structures and Transitions in a Hybrid Biaxial Nematic Film

6.1 Introduction

The topic of liquid crystals in confined systems continues to be of great interest due to the innumerable applications in the fields of liquid crystal displays (LCDs) [1], colloidal dispersions in nematic matrix [2], photonics [3], LC biosensors [4], to name a few. Liquid crystals are increasingly being used as host materials for colloidal and nanoscopic particles to form ordered structures at micro and nano scales which are used as photonic crystals and metamaterials [5–7]. The tendency of the anisotropic liquid crystal molecules to align parallel to one another aids in developing structural forces between the particles. The understanding of the interfacial properties of a liquid crystal is crucial for the control and improvement of optical devices which employ these soft materials. The surfaces impose boundary conditions on the bulk director resulting in compatible director structures. Usually electric fields are applied to induce textural transitions, providing convenient method of estimating the nematic-surface interaction strengths.

A liquid crystal cell is formed by confining the medium between two surfaces, called substrates. The substrates are typically Indium Tin oxide (ITO) coated glass plates which are pre-treated to obtain the required liquid crystal alignment. This type of surface induced alignment is called anchoring. When the liquid crystal molecules are aligned such that the long axes of the molecules lie parallel to the substrate plane, a planar boundary condition is obtained. On the other hand, if the molecular long axes are perpendicular to the substrate plane, a homeotropic boundary condition is realized. A liquid crystal film confined between two planar substrates which enforce a planar anchoring of the long axis (say, along the laboratory Y-axis) at one surface and a homeotropic anchoring (say, along the laboratory Z-axis) at the other is called a hybrid film. The equilibrium director structures obtained in such films are a result of the various competing mechanisms present due to the antagonistic boundary conditions, the strength of interaction with the substrates, the ordering interactions within the bulk liquid crystal, and the disordering effects due to temperature.

Hybrid films of uniaxial liquid crystals were extensively studied theoretically using Frank elastic theory and Landau-de Gennes formalism [8]. Within the frame work of the elastic theory the director is bent continuously from one substrate to the other. It was shown by Barbero $etal$ [9] that in such films the bent-director configuration occurs only if the film thickness is greater than a critical thickness determined by the elastic constant (in one- elastic-constant approximation) and the surface interaction strength. In thinner cells the director field is uniform with the director aligned along the easy axis of the substrate with stronger anchoring. Pallfy-Muhoray $etal$ [10] showed that that in highly constrained hybrid cells the boundary conditions can also be satisfied by a biaxial configuration, apart from uniform bending of the director field. A structural transition is predicted between the two ordered configurations. Galabova $etal$ [11] obtained the phase diagrams depicting the dependence of the nematic order on the thickness of the cell and the anchoring strength. The stability of different structures in a thin hybrid nematic film was examined within a Gaussian description of order fluctuations by Sarlah *et al* [12]. In a very thin film the director field is not bent smoothly but exhibits a step like change if the anchoring at the surface are strong and comparable in magnitude. A discontinuous structural transition to the bent-director state is predicted with increasing film thickness or decreasing temperature.

Experimental investigations were undertaken to study the effect of confinement on the isotropic-nematic transition temperature, orientational order enhancement and relaxation times [13–16]. Surface force measurement [17, 18] is a recent technique employed to study the effects of confinement.The first evidence of a hybrid to planar anchoring in NLC films (thinner than 100 nm) using externally applicable mechanical constraint was obtained recently using a surface force apparatus [19].

Simulations of confined systems of uniaxial liquid crystals in various geometries [20–23] have played a vital role in verifying the theoretical predictions. Detailed computer simulations were carried out using off-lattice Gay-Berne potentials [24, 25] and lattice models like Lebowhl-Lasher potential [26] to understand the behaviour of such systems. A Monte Carlo simulation study of structures and transitions in a thin hybrid film confirmed the existence of the structural transition between the bent-director state and biaxially ordered non-bent structure [22]. More recently hybrid films of uniaxial nematic were investigated using the conventional canonical Monte Carlo methods [26] and also non-Boltzmann sampling techniques [27]. Based on these simulation results, two transitions are predicted in the film, as a function of temperature. With decrease in the temperature, the first transition occurs from a disordered phase to a phase-biaxial phase at a temperature higher than the isotropic-nematic transition. The second occurs at a temperature lower than this transition temperature, from a phase-biaxial phase to a bent-director nematic phase.

With several recent attempts to realize biaxial nematic materials [28–30], long after their theoretical prediction by Freiser [31, 32], new avenues for their possible use as fast responding bistable devices are now being examined. Thermotropic biaxial nematic phase found in liquid crystalline organo-siloxane tetrapodes [29] and achiral bent-core mesogens [33] has prompted a search for suitability of these materials for fast switching. In the biaxial nematic phase, fast switching between different birefringent states may be possible because the birefringence can be changed by a rotation of the short axes, while the orientation of the long axes could be kept fixed [34]. Recently, it has been confirmed experimentally [35] that the short axis and long axis of bent-core liquid crystal ODBP-Ph-C7 and ODBP-Ph-C12 could be independently switched on the application of an electric field in the biaxial phase. The switching time of the short axis was much faster than the long axis in response to the applied field, as well as during its relaxation. These electro-optical experiments were done on thin cells of thickness 2μm and suitably enclosed within substrates having a pretilt angle of 2^0. The substrates are rubbed such that the long axes are in antiparallel directions. The thin cell gap and the low pretilt angle ensure that the long axis orientation is strongly held and thus promote a surface stabilized biaxial nematic phase. The short axis is randomly distributed around the director in zero field and switches in the same plane as the long axis when the field is switched on. A subsequent molecular dynamics (MD) simulation of the bulk biaxial Gay-Berne fluid under the action of an electric field [36] has shown that the switching of the secondary axis director is an order of magnitude faster than the switching of the primary axis director. Of course, this simulation was done as demonstration on a bulk biaxial fluid.

In a more recent Monte Carlo simulation study [37] of biaxial hybrid films, a medium of biaxial molecules was enclosed within planar substrates percolating hybrid anchoring influences from both sides. The anchoring is such that the orientation of long molecular axis is fixed as planar anchoring on one substrate and homeotropic anchoring on the other. The short molecular axes directions are chosen such that they follow the z-axis rotation from one substrate to the other without introducing any additional twist around the z-axis (see Fig.(6.1)). This arrangement is denoted as type A film for convenience. The simulation study, using Boltzmann sampling techniques, revealed a bent director structure for the primary director in the uniaxial nematic phase, as expected. However the growth of the primary order of the system in the biaxial nematic phase, and the fluctuations of the relevant order parameters in the biaxial phase turned out to vary curiously and needed further study.

In the light of the above observations we investigated this system from different perspectives, and report our findings in this chapter. For example, we investigated the effect of removing anchoring restrictions on the molecular minor axes at both the substrates. Such a film is denoted as Type C film. ('B' has already been reserved to denote a biaxial phase and hence avoided). We investigated in detail with Markov chain Monte Carlo methods the thermal evolution of the above hybrid films for different relative anchoring influences at the substrates. The relevant order parameters and their fluctuations (quantified as their susceptibilities) are measured both as bulk and layer wise properties, as a function of temperature. The effect of variation of the film thickness on the observed parameters is also investigated. Boltzmann sampling is preferred, since its results with a dispersion Hamiltonian model are extensively studied, interpreted and readily understood [38], and are reported to conform to MF expectations in terms of the phase symmetries. In the light of earlier observations on the outcome of employing Boltzmann sampling $vis-a-vis$ WL sampling, the Boltzmann sampling procedure on the dispersion parabola leads to the established $I - N_U - N_B$ phase sequences in the bulk medium, and provides a convenient reference to examine the relative effects of a geometric confinement on its director structures.

6.2 System under study

The system studied here is a planar hybrid film of biaxial molecules. We assign $\{X, Y, Z\}$ axes to represent the laboratory-fixed frame and $\{x, y, z\}$ axes to represent the molecular-fixed frame. We further assign *z* direction to represent the molecular long axis, while the other two molecular minor axes are represented by *y* and *x*. The film is obtained by confining the biaxial molecules between two planar substrates taken to be in the X-Y plane. The substrate planes are positioned at Z=0 and Z=d (in lattice units)in the laboratory Z-direction. The influence of the substrates is simulated by introducing two bounding layers of molecules with the designated, but fixed orientations, referred to in the literature as ghost molecules [39]. We consider the two types of films A and C (as described earlier) which are depicted in Fig. 6.1. The boundary conditions are such that the long axis of the molecules are hybrid-aligned (planar orientation at one substrate and homeotropic at the other), but differ with respect to the x- and y-axes of molecules. The bent primary director structure is retained in both films, which are examined below.

TYPE A FILM In this film, the long molecular axis is anchored so as to experience hybrid boundary conditions at the two substrates (planar orientation at one substrate and

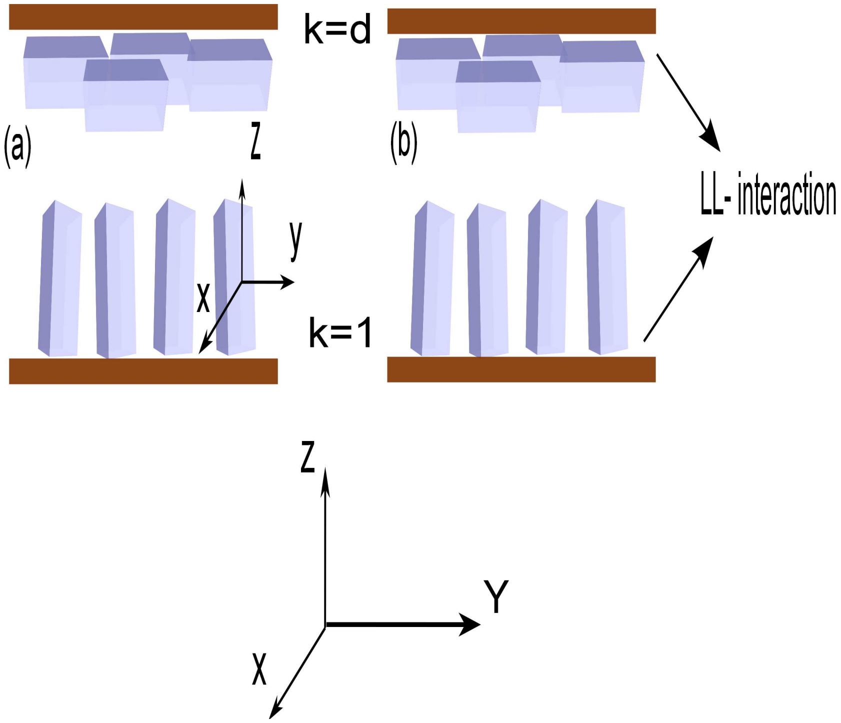

Figure 6.1: (a)Type A Film (b) Type C Film

homeotropic at the other). With biaxial molecules we however still have to choose whether the relative (x, y) directions of the molecules are unchanged while the molecular *z*-axis undergoes a $\pi/2$ turn. One configuration could be that (x, y) axes follow the *z*-axis rotation without a twist around the *z*-axis. We refer to this configuration as type A film, as shown in Fig.6.1. The orientations of the ghost molecules at the two substrates (defining the anchoring directions) are specified by the following:

Substrate 1 : $z \parallel$ Z, $y \parallel$ Y, $x \parallel$ X

Substrate 2 : $z \parallel$ Y, $y \parallel$ Z, $x \parallel$ X

TYPE C FILM The molecular alignment at the two substrates is the same as for a type A film, but the substrate molecules are allowed to interact only with the long axes of the LC molecules, thereby effecting free boundary conditions at the two substrates as far as the *x*-*y* axes of the LC molecules are concerned.

Of the two films, type C film appears to be the easiest to realize since it involves only anchoring of the long molecular *z* axes at the two ends. The other variant (Type A) has boundary conditions which require special preparation of the substrates with appropriately oriented biaxial molecules.

6.2.1 Model Hamiltonian

The biaxial LC molecules are assumed to interact through a pairwise additive lattice Hamiltonian [38] within the dispersion approximation, and is expressed in terms of generalised Wigner rotation matrices as:

$$H = -\epsilon_{ij}\{P_2(\cos(\beta_{ij})) + 2\lambda_Z(R^2_{02}(\omega_{ij}) + R^2_{20}(\omega_{ij})) + 4\lambda_Z^2 R^2_{22}(\omega_{ij})\} \qquad (6.2.1)$$

where $\epsilon_{ij} = \epsilon$ is the coupling constant used to define the reduced temperature, $\omega(\alpha, \beta, \gamma)$ are the set of Euler angles which specify the rotations to be performed in order to bring the laboratory frame of reference in coincidence with the molecular frame, R^L_{mn} are symmetrized Wigner functions, $P_2(cos(\beta_{ij}))$ is the second Legendre polynomial and λ_Z is the shape biaxiality parameter quantifying the degree of molecular biaxiality.

The phase diagram of this Hamiltonian has a Landau triple point at $\lambda_Z = \dfrac{1}{\sqrt{6}}$. It is known from earlier Monte Carlo simulations [38] that the molecules are prolate in shape for values of $\lambda_Z < \dfrac{1}{\sqrt{6}}$ and oblate for $\lambda_Z > \dfrac{1}{\sqrt{6}}$. The value of the biaxiality parameter is chosen at λ_Z=0.35 in this study, as it on one hand corresponds to a high degree of molecular biaxiality, and on the other leads to a wide temperature range of the biaxial phase, on condensation due to cooling [38].

6.2.2 Simulation Details

A planar hybrid film of dimensions $15 \times 15 \times d$ (*d* = 6, 8, 10, 12) layers is considered in the present work. Periodic boundary conditions are applied along the laboratory X and Y directions, so as to minimize finite size effects. The anchoring conditions applied at the two substrates (contained in the X-Y plane) depend on the specific choice of the film (Type A or C), and their relative strengths can be chosen as required. Referring to Fig 6.1, the lower LC layer experiencing homeotropic boundary condition on the long molecular axis is indexed as *k*=1 and the upper LC layer experiencing hybrid boundary condition of the same axis is indexed as *k*=*d*. The LC ghost molecules in the substrate layers (which are adjacent to the two bounding layers of the LC medium) do not participate in the Monte Carlo dynamics. The interaction strength of the long molecular axis at the two substrates are represented by ϵ_1 and ϵ_{nz}, and ϵ_{nz} can be varied relative to ϵ_1 (which is set equal to 1). The temperature T' in dimensionless units is set by the coupling strength ϵ in the Hamiltonian (Eqn.6.2.1).

In each simulation on a particular film, the reduced temperature is varied from 2 to 0.05 in steps of 0.005, and at each temperature the film is equilibrated for 5×10^5 lattice sweeps (runs) while the data are collected over a production run of 5×10^5 lattice sweeps. The quantities computed are the average energy E, the specific heat C_V, the order parameters R^2_{00}, R^2_{02}, R^2_{20}, R^2_{22} as well as their susceptibilities, and layer-wise orientation of the local directors (average orientation over the layer) with respect to the laboratory Z-axis (layer-wise θ) and the azimuthal angle made by the local layer-wise director with respect to laboratory X-axis (layer-wise ϕ). We computed both layer-wise properties (to examine the director structure and its relative changes) as well as bulk properties (averaged over the film) as a function of temperature for a fixed relative anchoring strength and layer thickness. The simulations are then repeated by varying the thickness effecting length scale of the system, and also varying the anchoring strength (ϵ_{nz}) to look for possible anchoring-induced transitions among the different director structures.

6.3 Results and Discussion

For convenience, initially simulation results for films of type C and A under strong anchoring conditions ($\epsilon_1 = \epsilon_{nz} = 1$) are discussed under subsections: (a) Type of the film (b) effect of variation of film thickness. The effect of varying the anchoring strength ϵ_{nz} at the second substrate is discussed under a different subsection: Anchoring transitions.

6.3.1 Type of Film

In this section, the results for a fixed film thickness of 8 layers are presented under strong anchoring conditions. Figs.(6.2) and (6.3) depict the system order parameters of Type C film and their layer-wise variation and corresponding director angles. Figs.(6.4) and (6.5) display similar data for Type A film. The interpretation of the data turned out to be on similar lines in all these films. Hence we discuss the type C film in some detail to provide bench marks for comparison of information from the other film. It may be noted that whenever layer-wise angles of the local directors (with respect to laboratory X or Z axis) are plotted, the data in the isotropic phase, which are automatically generated and plotted during the course of the computation, should be obviously ignored. We henceforth treat any such display of data in the isotropic phase as inconsequential and ignore them for purpose of discussion.

TYPE C FILM

As mentioned earlier, this film corresponds to a hybrid boundary condition on the long axis (z of the biaxial liquid crystal molecules (Fig.6.1), while the molecular minor axes do not interact with the substrate, and experience free boundary conditions. Fig (6.2) depicts the specific heat profile, the system order parameters and their susceptibilities as a function of temperature. It is found from Fig. 6.2(a) that as the temperature is decreased from the isotropic state, two transition peaks are observed in the C_V profile - first at $T_{C1} = 1.021$, and the second at $T_{C2} = 0.522$, which signify the $I - N_U$ and $N_U - N_B$ transitions, respectively. The transition temperatures are lowered in comparison with the bulk transition temperatures at $T_{C1} = 1.117$ and $T_{C2} = 0.5601$, as a result of confinement. Fig. 6.2(b) depicts a comparative study of the growth of uniaxial order R^2_{00} at the $I - N_U$ (T_{C1}) transition as well as at $N_U - N_B$ transition (T_{C2}) and the biaxial order R^2_{22} at the $N_U - N_B$ transition, plotted as a function of temperature. Figs. 6.2(c)-6.2(f) show temperature variation of the four order parameters and their susceptibilities. The uniaxial order parameter R^2_{00} in Fig.6.2(c) starts increasing at T_{C1} and displays a bent-director structure in the uniaxial

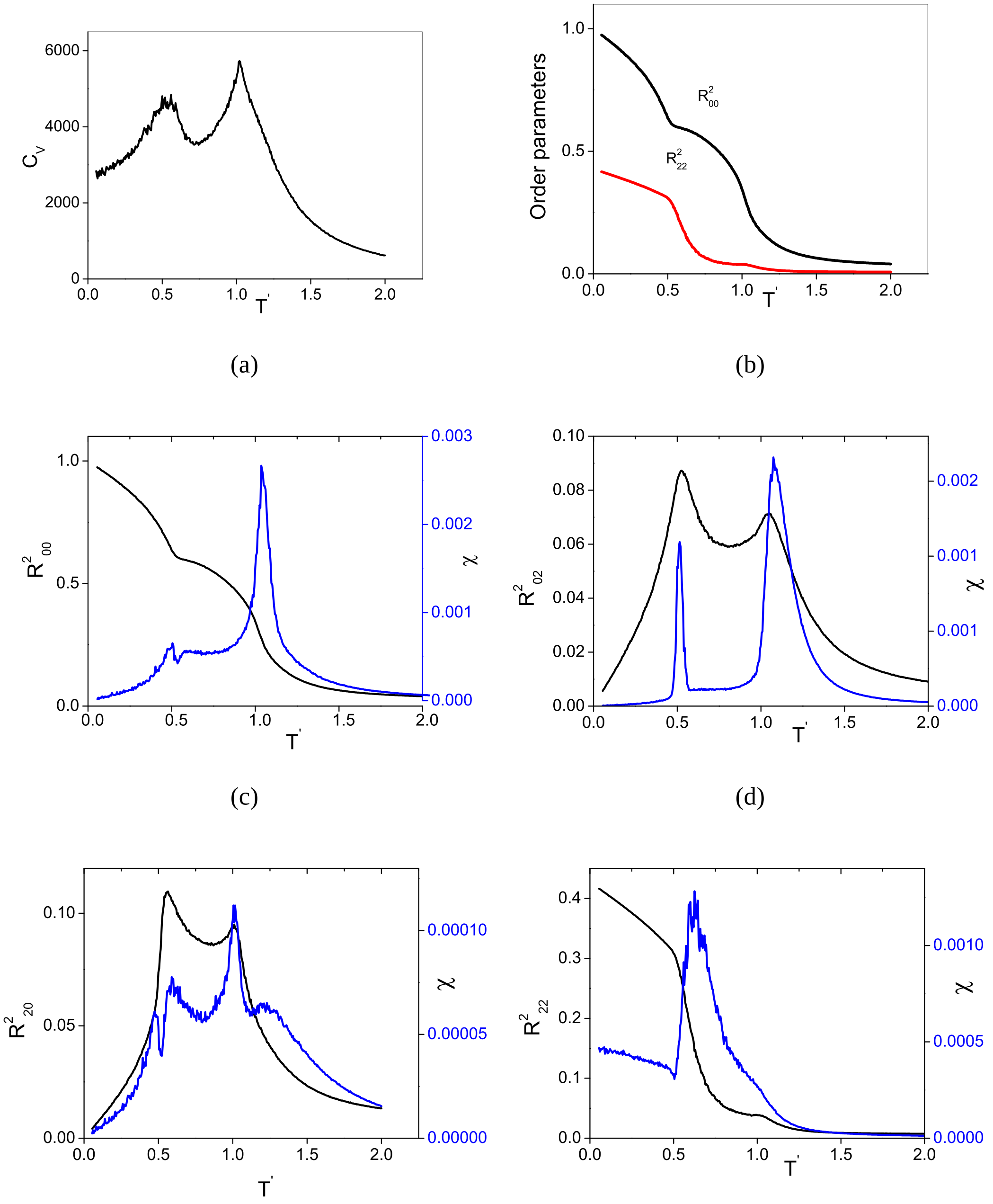

Figure 6.2: Variation with temperature of system properties in Type C film (a) Specific heat C_V (b) Two major order parameters R^2_{00}, R^2_{22} (c)- (f) The four order parameters along with their susceptibilities

nematic phase. The maximum value attained by the uniaxial order is 0.6 in this phase. The slope of the R^2_{00} curve however increases abruptly at the $N_U - N_B$ transition, below which it steadily increases to a maximum value of unity.

The phase biaxiality parameter arising from the non-cylindrical distribution of the molecular long axes, R^2_{20} and the ordering along the primary director originating from molecular minor axes R^2_{02}, are shown in Figs. 6.2(d) and 6.2(e). As compared to their values in a bulk system (without confinement), we observe that these parameters have non-zero values in the uniaxial nematic phase between the $I - N_U$ and $N_U - N_B$ transitions, obviously a clear manifestation of finite confinement. Fig. 6.2(f) shows the biaxial order parameter R^2_{22}. The non-zero value at the onset of the $I - N_U$ transition has been found to be a finite size effect in a bulk system. A significant biaxial ordering is observed only at $N_U - N_B$ transition (T_{C2}), as is also evident from its susceptibility profile, which shows a peak at T_{C2} at this temperature. The layer-wise variations (for the layer index k=1 to d) of some of the useful properties, plotted along with their counterparts corresponding to the total system are shown in Figs.6.3(a)- 6.3(f). It is observed from Fig.6.3(a) that layer-wise R^2_{00} values vary smoothly and do not show the abrupt jump at T_{C2} exhibited by the system value (i.e. average over the film) and the order in all the layers asymptotically reaches the maximum value of 1.0 at the lowest temperature. Layer-wise variation of R^2_{00} also shows that the middle layers (k = 4 and 5), being least influenced by the substrate boundaries, are most effective in contributing to the critical onset of the order at the transition.

The layer-wise R^2_{02} and R^2_{20} are shown in Figs.6.3(b) and 6.3(c). It is observed that they have small, but non-zero values in the uniaxial nematic phase in the middle layers of the film. Fig.6.3(d) depicts the system and layer-wise behaviour of biaxial order. It is observed that in the middle layers R^2_{22} starts increasing from the $I - N_U$ transition itself, but shows a significant increase only at the $N_U - N_B$ transition.

The plots of the layer-wise θ (Z-angle) (angle made by the layer-wise director with the laboratory Z-axis) and layer-wise ϕ (angle made by the layer-wise director with the laboratory X-axis) are shown in Figs. 6.3(e) and 6.3(f). Focusing on the data only below

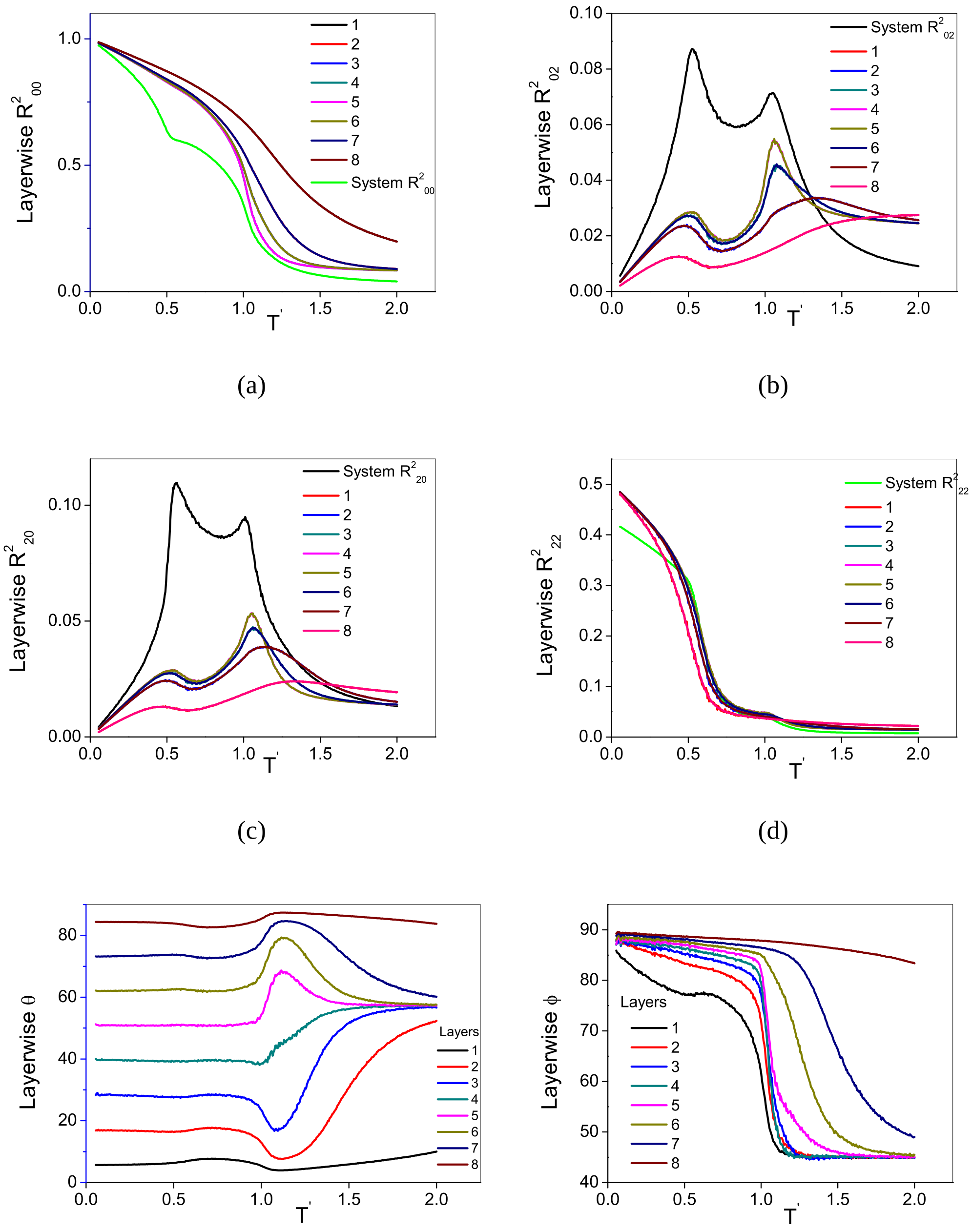

(a) (b)

(c) (d)

(e) (f)

Figure 6.3: Layerwise variation of different properties of the Type C film, with tempertaure: (a) R^2_{00} (b) R^2_{02} (c) R^2_{20} (d) R^2_{22} (e) Angle θ (f) Angle ϕ (see text)

the clearing point, it is observed from Fig.6.3(e) that as the temperature is lowered from the isotropic phase, layer-wise θ values stabilise to certain fixed values after the $I - N_U$ transition. The value of this angle increases monotonically from $k = 1$ layer to the $k = d$ layer, clearly indicating that the layer-wise primary director bends gradually from the lower substrate to the upper substrate, exhibiting a bent-director structure. The layer-wise ϕ angles depicted in Fig.6.3(f) show a sudden flip by approximately 90^0 at the $I - N_U$ transition, particularly in the region of middle layers. This signals the onset of a long range order, essentially confining the primary director to the laboratory YZ plane, as the system is cooled. The layer-wise angle profile also suggests that the bending of primary director takes place confining it to the YZ plane, and is not affected by the $N_U - N_B$ transition. It also confirms the fact that the bent-director structure in the uniaxial nematic phase is purely due to the restrictions on the geometry of the film, under the anchoring conditions imposed.

TYPE A FILM

In this film a biaxial interaction is introduced between the LC molecules and substrate (ghost) molecules, unlike the case of a Type C film. The anchoring orientations of the molecules (with respect to the laboratory axis) are shown in Fig.6.1. Referring to Fig.6.4 it is observed that all order parameter susceptibilities except that of R^2_{22} display fluctuations in the biaxial phase, which are reflected on their (average) order profiles as well. It may be noted that the onset of biaxial order in Type A film occurs only at the $N_U - N_B$ transition unlike in the Type C film. The system and layer-wise variation of the order parameters are shown in Figs. 6.5(a) - 6.5(d). The layer-wise R^2_{00} values in Fig.6.5(a) do not fluctuate in the biaxial phase and attain maximum ordering, unlike the system order parameter. The layer-wise R^2_{02} and R^2_{20} have small, nonzero values in the uniaxial nematic phase, but fluctuate significantly in the biaxial phase, showing the same behaviour as the system values of R^2_{02} and R^2_{20}. Fig 6.5(d) depicts the system and layer-wise biaxial order. It may be observed that the layer-wise biaxial order shows a non zero value at the $I - N_U$ transition and grows gradually, whereas the system biaxial order develops only at the $N_U - N_B$ transition. Both

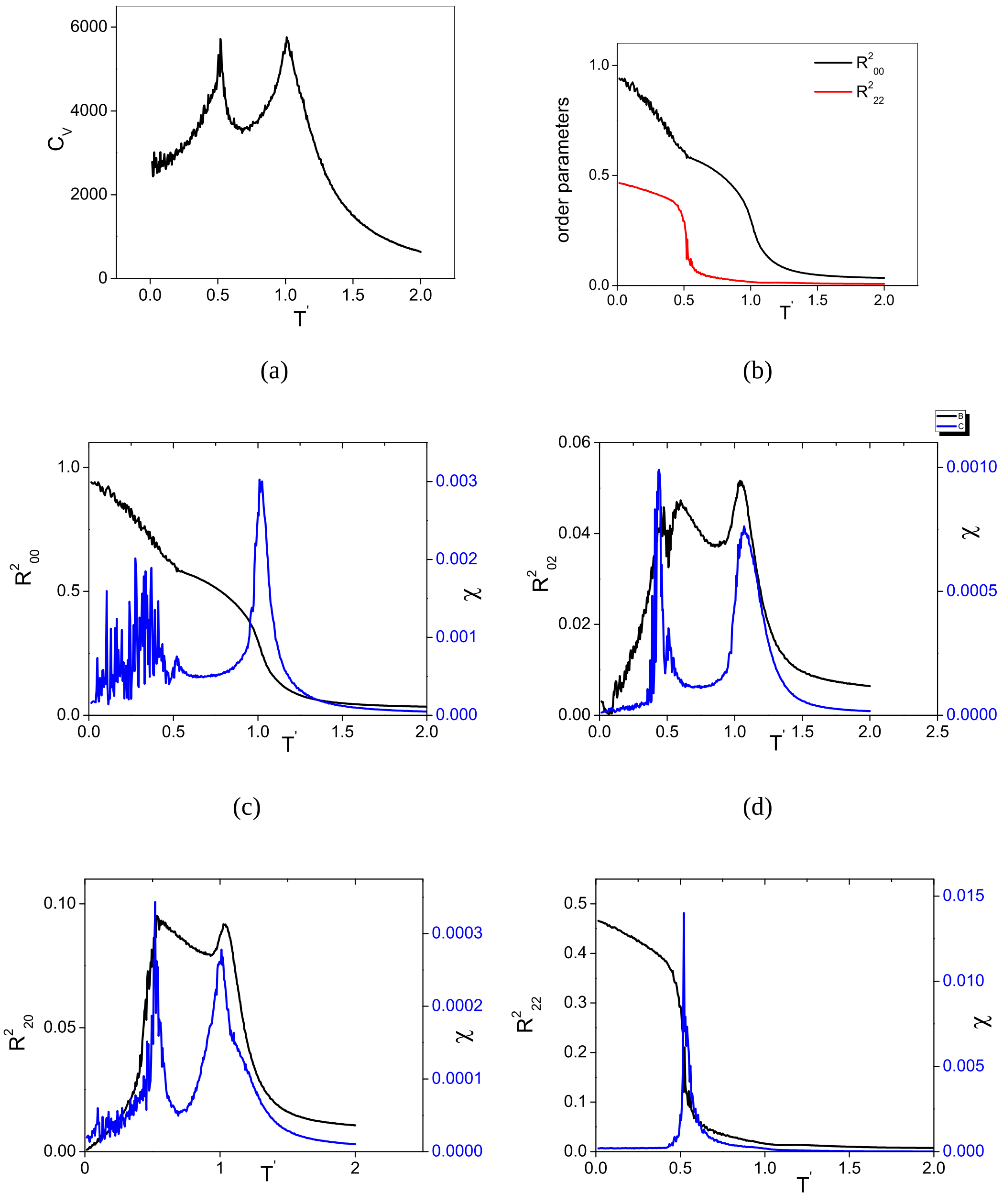

(a)

(b)

(c)

(d)

(e)

Figure 6.4: Variation with temperature of system properties in Type A film (a) Specific heat C_V (b) Two major order parameters R^2_{00}, R^2_{22} (c)- (f) The four order parameters along with their susceptibilities

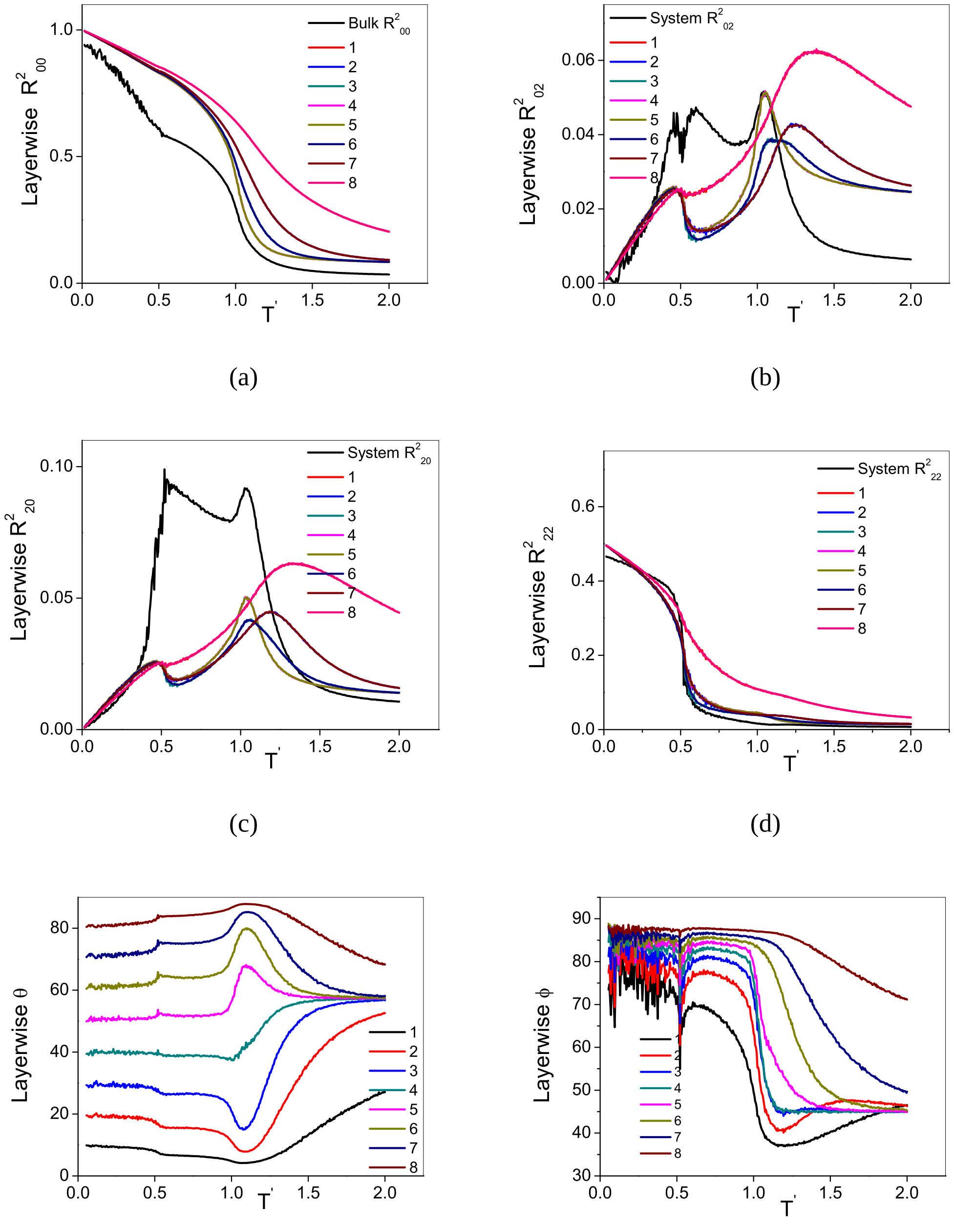

(a) (b)

(c) (d)

(e) (f)

Figure 6.5: Layer-wise variation of different properties of the Type A film, with temperature: (a) R^2_{00} (b) R^2_{02} (c) R^2_{20} (d) R^2_{22} (e) Angle θ (f) Angle ϕ (see text)

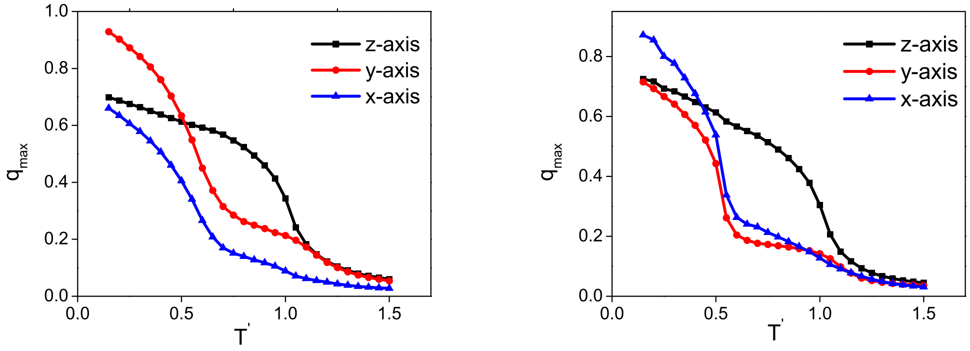

(a)

(b)

Figure 6.6: Variation of maximum eigen values associated with each of the ordering tensors of the three molecular axes (x, y, z), as a function of temperature for (a) Type C film (b) Type A film

develop fluctuations in the biaxial phase similar to the other order parameters.

The layer-wise θ and layer-wise ϕ values shown in Figs. 6.5(e) and 6.5(f) depict a similar gross behaviour as for a Type C film, but fluctuate significantly at the $N_U - N_B$ transition, indicating that while the degree of layer-wise order is relatively stable, its direction however is not.

A discussion on these two films (Type C and Type A, with λ_Z=0.35) seems interesting when the system as well as layer-wise evolutions of R^2_{00} on cooling are examined, as depicted in Figs.6.2(b), 6.3(a), 6.4(b) and 6.5(a). Their system uniaxial order parameters R^2_{00} develop at the high temperature $I - N_U$ transition, and show a sharp increase at the $N_U - N_B$ transition. They tend to a saturation value close to unity at low temperatures, much like the case in a bulk system which does not have geometric constraints from boundary anchoring effects. The layer-wise R^2_{00} values on the other hand (particularly their θ values (Figs.6.3(e) and 6.5(e)), vary smoothly across the second transition pointing to the bent-director structure. This puzzling result regards temperature variation of R^2_{00} at T_{C2}, in conjunction with smooth layer-wise director properties points to a distinct possibility that the order terms contributing to the primary director may be changing at T_{C2} and system-wise R^2_{00} corresponding to the maximum eigen value direction (by operative definition) may simply be reporting this qualitative change in its direction. This clue led to the computation of averaged (over MC steps), maximum eigen values (q_x, q_y and q_z) associated with the three molecular axes (derived from the three system ordering tensors Q_{xx}, Q_{yy} and Q_{zz} respectively), and the directions of their eigen vectors with respect to the laboratory frame, as a function of temperature. The temperature variation of the three eigen values (scaled by 1.5) was accordingly investigated, to resolve this puzzle.

Noting that the standard procedure of computing the R^2_{00} values is to identify the maximum eigen value among all the eigen values of the individual ordering tensors (scaled by 1.5) to get the degree of the uniaxial order, and the associated eigen vector denoting the direction of the primary director, we plotted the temperature evolution of the eigen values for Type C and A films in Fig.6.6. Referring to Fig.6.6(a) for Type C film, it is very interesting to note that the onset of the second transition (at T_{C2}=0.51) leads to a dramatic increase of q_y (maximum eigen value of the molecular y-axis), surpassing the value of q_z (maximum eigen value of the molecular z-axis). This implies that in reality the assignment of the direction of primary director itself changes at T_{C2}. For temperatures above, it is the geometrically averaged bent-director structure arising from the ordering of the molecular z-axes (long axes) with the eigen vector lying in the plane with $\theta = 45°$ (with respect to laboratory Z direction) and $\phi = 90°$ (with respect to laboratory X direction). The primary director is contained wholly in the YZ plane of the bent-director. But the onset of the biaxial phase coincides with the crossing of the q_z and q_y values and what has been observed below T_{C2} as the development of R^2_{00} to unity, unhindered by geometric constraints, is the near perfect ordering of the molecular y-axes. Its eigen vector makes angles $\theta \sim 90°$ (with respect to laboratory Z direction) and $\phi \sim 0°$ (with respect to laboratory X direction), which implies that the molecular y-axis is ordered along the laboratory X-direction. Correspondingly, the eigen vectors of molecular x and z axes are contained in the laboratory YZ plane, mutually perpendicular to each other. Evolution of the angles θ and ϕ of these eigen vectors, at different temperatures and observed as a function of Monte Carlo steps after equilibration, bring out this curious development. We conjuncture that this observation could be of potential use in applications, and will comment further later.

In contrast, Type-A film which imposes boundary conditions on the minor axes of molecules as well at both ends presents a very different scenario. We refer to Fig.6.6(b) showing q_x, q_y and q_z as a function of temperature in this film. At the onset of the second transition ($T_{C2} \sim 0.5$) q_z ($\sim$ 0.617) is higher than the q_x and q_y which have values ~ 0.536 and ~ 0.447 respectively. But on further cooling, q_x crosses the value of q_z (~ 0.632 at a (reduced) temperature $T^{'}$ = 0.433), while q_y remains less than q_z. At very low temperature q_x saturates at $\approx$ 0.87, while q_y and q_z reach a value of $\leq$ 0.72. Eigen vector of q_z makes angle ($\theta \sim 45^0$ with the laboratory Z-direction and $\phi \sim 90^0$ with laboratory X-direction, thereby indicating that the bent-director structure from z-axis term is contained in the YZ plane, as is the case in the high temperature nematic phase. Curiously the eigen vector of q_y makes angles $\theta \sim 45^0$ and ϕ varying between 0^0 to 90^0 as we cool from the uniaxial nematic phase. This appears to be the effect of geometric confinement of the molecular y-axis, imposed by the anchoring on boundary. The molecular y-axis is thus in principle, bent within the laboratory YZ plane, but its direction does fluctuate sibnificantly. The observed fluctuations in the thermal averages of R^2_{00}, R^2_{20} and R^2_{02} order parameters at the onset of the biaxial phase (Figs. 6.4(c) - 6.4(d)) are to be seen as a result of this circumstance. R^2_{22} does not show significant fluctuation since contribution to its ordering is mainly due to the highly ordered molecular x-axis in the perpendicular plane. Our further observation in the next section seems to indicate that this is due to the simultaneous presence of boundary conditions on the molecular x and y axes, as well as the influence of cross coupling term between the uniaxial terms (associated with the molecular z axis) and the biaxial term (associated with the molecular x and y axes) at this high coupling value of λ_Z = 0.35.

Case of vanishing cross-coupling term

In the light of the above contrasting results between the Type C and Type A films, we now investigate their counterparts, say, Type-CY and Type-AY. These correspond to setting the coefficient of the cross-coupling term, λ_Z (2nd term in Eqn.6.2.1) to zero, but otherwise retaining the same boundary conditions respectively. Obviously, this corresponds to choosing a point on the λ-axis on the (γ, λ) plane of the general quadrupolar Hamiltonian at the ordinate value of the dispersion point at λ_Z=0.35. Details of the computations and presentation of observable properties derived are similar to the earlier section, and hence are not reported here.

The variation of the system order parameters along with their susceptibilities are presented in Figs. 6.7(a) - 6.7(d) for the Type-CY film, while Figs.6.8(a) - 6.8(d) depict similar data of Type-AY film. Temperature variation of the θ and ϕ angles (with respect to the the laboratory frame) for each of of the layers are presented in Figs.6.7(e) - 6.7(f) and Figs.6.8(e) - 6.8(f), respectively.

Interestingly it is the Type-CY film that shows effect of frustration on the onset of biaxial phase at $T^{'} \sim 0.5$ (Figs.6.7(a) and 6.7(d) for example). To recall, this film employs a model where there is a uniaxial-uniaxial coupling term and a biaxial-biaxial coupling term, without a cross-coupling interaction. And, the film is anchored at the both ends in a hybrid condition only in so far as the long molecular axes is concerned, with the minor axes experiencing free boundary conditions. In such a film the onset of biaxiality curiously leads to significant fluctuations of all orders, as evidenced by their average values and their variances. Thus neglect of the cross-coupling interactions between the two types of tensor components in the absence of (stabilising) anchoring of the minor axes leads to unstable director structures.

On the other hand, Figs.6.8(a)-6.8(d) (corresponding Type AY film) show that the full dispersion model without the cross-coupling interaction, coupled with compatible anchoring of the minor axes at both the ends, leads to a stable, noise-free director structure in the biaxial phase. It may be noted that a similar smooth variation of the two order parameters, R^2_{00} and R^2_{22}, with temperature is observed in Type C film (presence of cross-coupling term in the Hamiltonian, and only long axes of molecules anchored at the substrate).

To investigate further, we computed the corresponding q_x, q_y and q_z as a function of temperature for types CY and AY films, depicted in Fig.6.9. As in the case of Type C

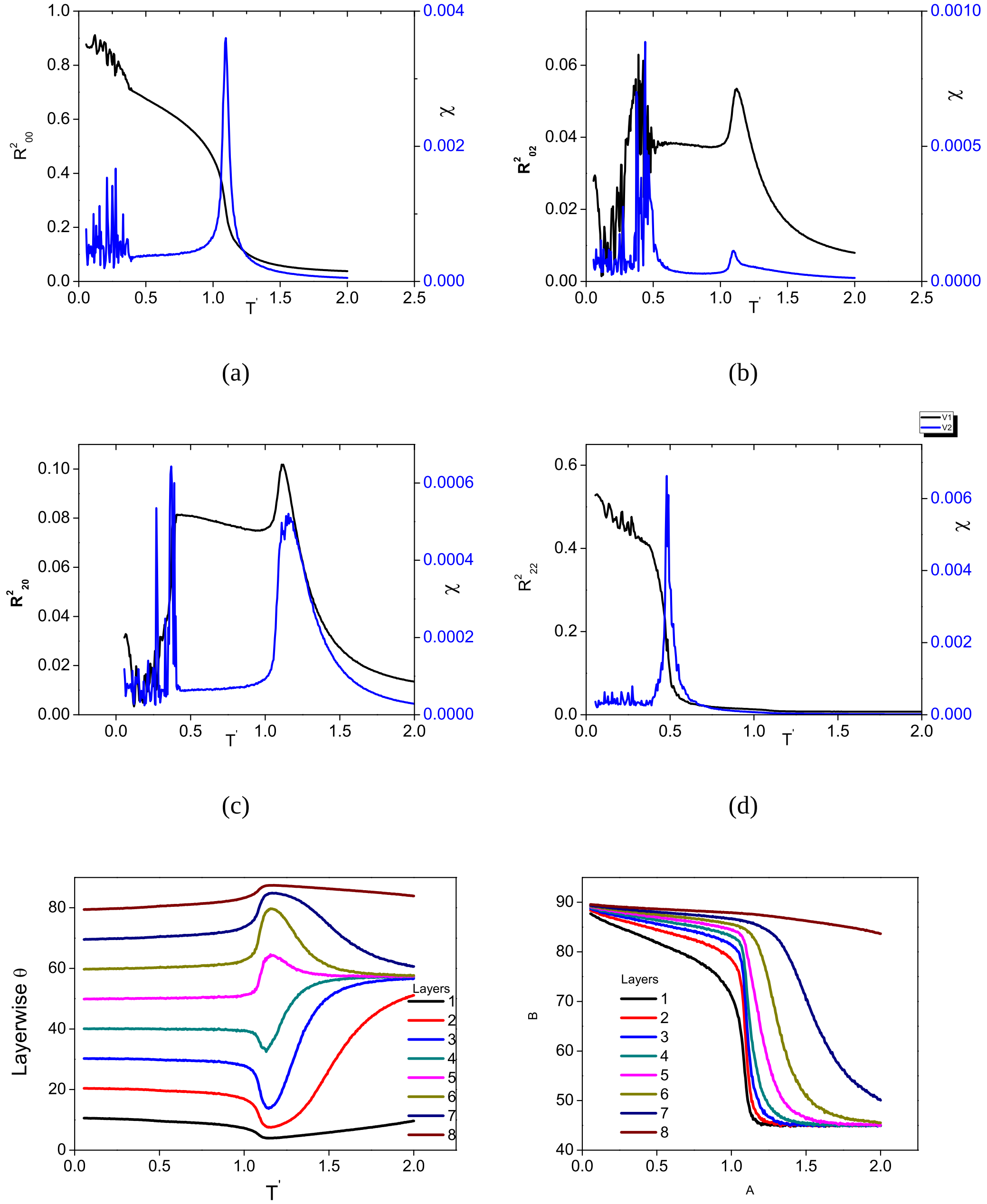

(a)

(b)

(c)

(d)

(e)

(f)

Figure 6.7: Variation with temperature of system properties in CY film (a)- (d) The four order parameters along with their susceptibilities (e) Angle θ (f) Angle ϕ

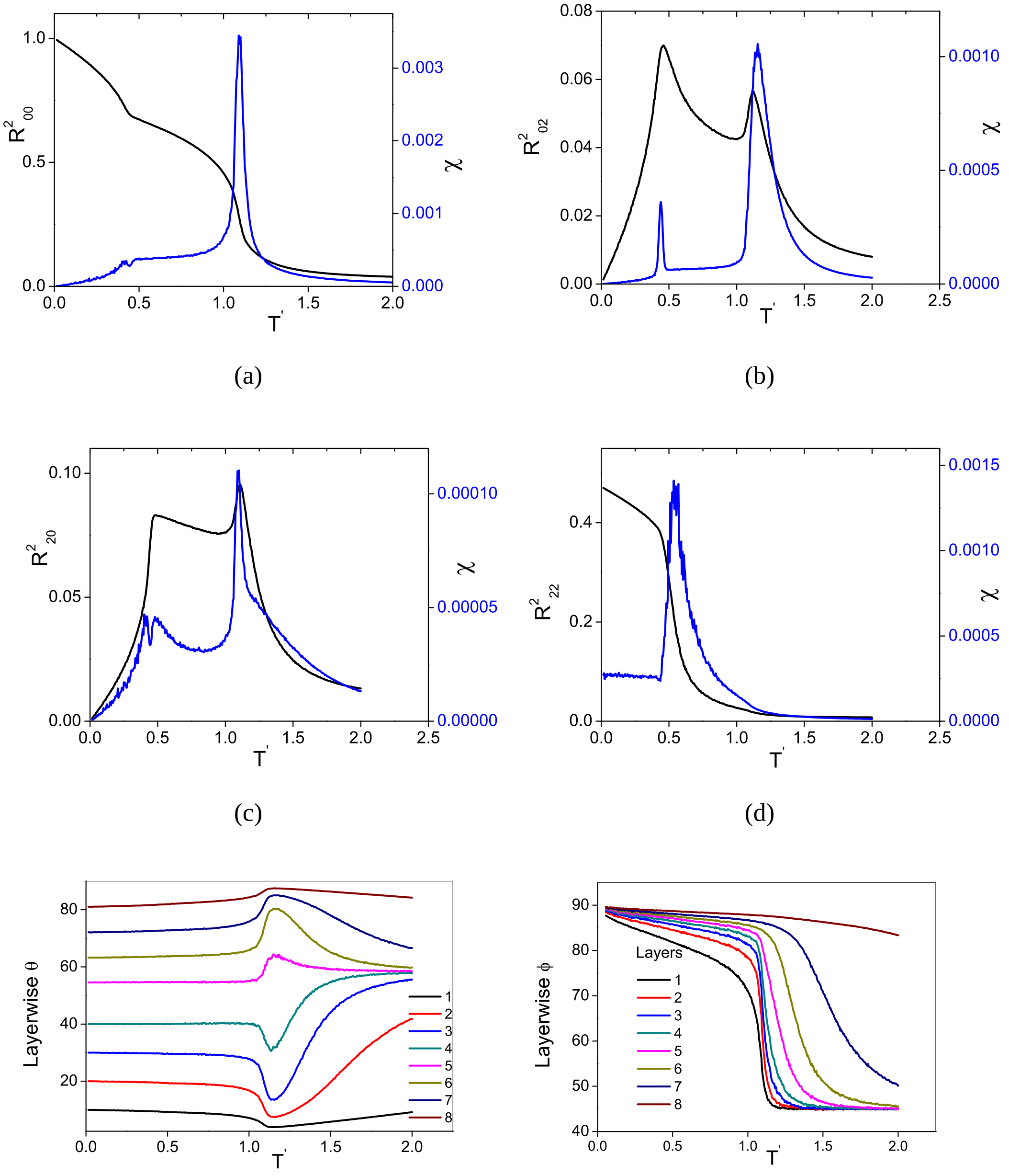

(a) (b)

(c) (d)

(e) (f)

Figure 6.8: Variation with temperature of system properties in AY film (a)- (d) The four order parameters along with their susceptibilities (e) Angle θ (f) Angle ϕ

and Type A films, the sharp increase in the value of R^2_{00} at the second transition is indeed a signature of one of the eigen values of the minor axes exceeding that of the long axis, and thus qualifying as the primary order parameter. In practical terms, the direction of the primary director relocates itself from the bent-director plane, (normal to the plane) after the onset of the biaxial phase.

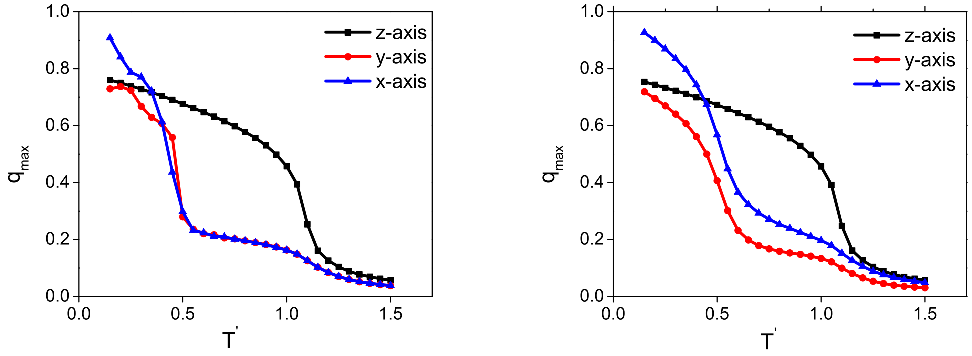

(a) (b)

Figure 6.9: Variation of maximum eigen values associated with each of the ordering tensors of the three molecular axes (x, y, z), as a function of temperature for (a) CY film (b) AY film

Obviously in both the CY and AY films, the hybrid nature of anchoring imposed on the molecular z-axis pins the two ordering eigenvectors to the laboratory YZ plane, while the third director axis (x-axis) coincides with the laboratory X-axis permitting unhindered growth of its order in the low temperature phase.

The variation of these eigen values for the films CY bring out clearly the smooth variation of q_z throughout, the gradual development of noise in the other two eigen values and the very significant fluctuations at the onset of the second transition. This seems to signal that in the absence of anchoring of the minor axes at the substrates, and when the uniaxial and biaxial tensor components of the interaction are decoupled, the long axis ordering develops as a bent-core structure, while the ordering of the other two molecular axes becomes spatially unstable since there is no term either in Hamiltonian or in the surface interaction to fix the orientation of either of these axes bringing stability to their orders. The observed order parameter variation (and their susceptibilities) of this film (Figs.6.7(a)-6.7(d)), in conjunction with their eigen values, support this scenario. The film seems to be characterised by a stable long range order contained in the YZ plane, but fluctuating components q_{xx} and q_{yy} (max eigen values of Q_{xx} and Q_{yy}) as they move in and out of the plane. In this process their system averages suffer varying degree of geometric averaging, leading to rather wildly fluctuating associated molecular orders.

6.3.2 Effect of variation of thickness

In this subsection we present the results obtained as the thickness of the liquid crystal film 'd' is varied. Typical dimensions of the films considered are $15 \times 15 \times d$ where 'd' is set to have values 6, 8, 10, 12 lattice units. These studies are done, under strong anchoring conditions at both the substrates, on two types of films: Film C and film A. Figs 6.10 - 6.11 depict a comparative study of the simulation results obtained as the thickness of the biaxial film is varied as above, for each type of the film. Figs.6.10(a) - 6.10(e) show the effect of varying 'd' on the experimental parameters like C_V, R^2_{00}, R^2_{02}, R^2_{20} and R^2_{22} in the type C film. The specific heat profiles become sharper as shown in Fig. 6.10(a) as the thickness increases (size effect). The uniaxial order parameter R^2_{00} slightly increases in value in the uniaxial phase as the thickness increases, retaining the bent director structure for all thicknesses. The R^2_{02} and R^2_{20} values decrease as the thickness increases (possible size effect). The biaxial order R^2_{22} shows a slight decrease as the thickness is increased and shows a marked increase in the nematic phase itself for a thinner film of thickness 6 lattice units. Figs.6.11(a) - 6.11(e) depict the effect of varying the thickness of the Type A film on the specific heat and the order parameters. The behaviour is similar to a type C film. From the discussion of the earlier section, the measure of R^2_{00} in a film C (all thicknesses) in the biaxial phase reflects the degree of ordering of the molecular y-axis along the laboratory X-axis. However, in film A, the measure of R^2_{00} is due to the ordering of molecular x-axis along laboratory X-axis. In both cases, the onset of biaxiality leads to a re-assignment of the eigen value to R^2_{00} qualifying as its primary director order. Accordingly, the direction

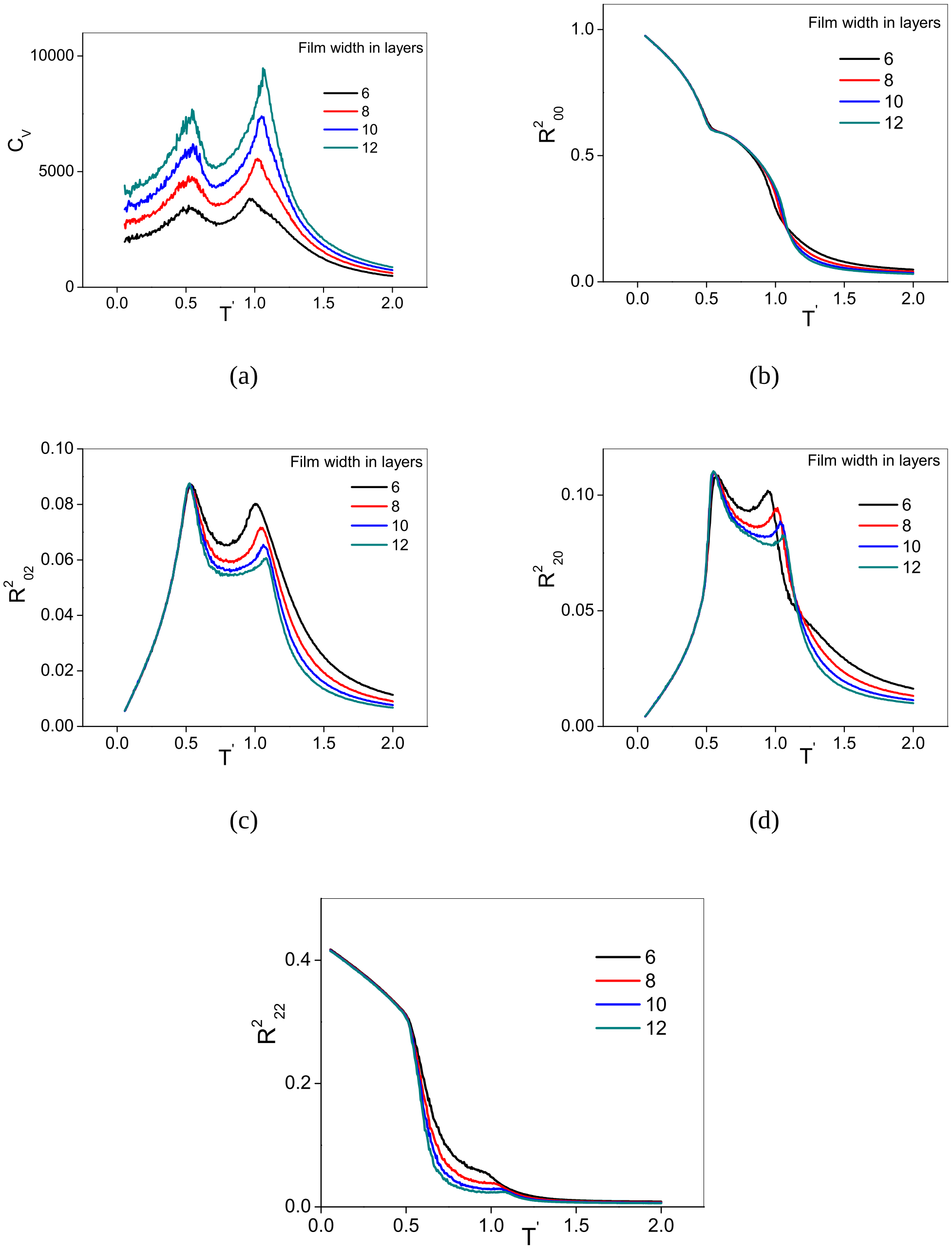

(a)

(b)

(c)

(d)

(e)

Figure 6.10: Variation with temperature of system for different thickness of Type C film (a) C_V; (b) R^2_{00}; (c) R^2_{02}; (d) R^2_{20} (e) R^2_{22}

of the primary director gets relocated.

6.3.3 Effect of variation of anchoring strength

In this section we present the results obtained when the anchoring strength ϵ_{nz}, at the second substrate (imposing planar anchoring along laboratory Y-axis for the long molecular axis), is varied from 0 to 0.6, in steps of 0.1. Each type of film is simulated at these anchoring values (ϵ_{nz}) and the experimental parameters are collected as the film is cooled from the isotropic phase to the biaxial phase. The resulting differing temperature variation of the system order parameters for a given type of film are compared to investigate the influence of ϵ_{nz} on the equilibrium director structures. The plots depicting this study are shown in Figs. (6.12) and (6.13) for Type C and Type A films, respectively. We observe from Figs.6.12(a) and 6.12(d) that for anchoring strengths ϵ_{nz}=0.0, corresponding to a free surface and for a low value of ϵ_{nz}=0.1, the uniaxial order R^2_{00} and the biaxial order R^2_{22} attain maximum values of 1.0 and 0.5, respectively. The model is similar to a bulk sample with free boundary conditions in one direction, and periodic boundary conditions in the other two. For $\epsilon_{nz} \geq 0.2$ the primary director assumes a bent structure and the primary order attains a value with an upper bound of 0.8 for $\epsilon_{nz} = 0.2$. A similar sharp difference is exhibited by R^2_{22} as well (Fig.6.12(d)) where the temperature variation qualitatively changes from $\epsilon_{nz} = 0.2$ upwards. The order parameters R^2_{02} and R^2_{20}, shown in Figs. 6.12(b) and 6.12(c), have very low values at anchoring strengths 0.0 and 0.1, and they also start increasing for anchoring strength $\epsilon_{nz} \geq 0.2$. Thus it appears that the film needs a minimum threshold anchoring strength ($\epsilon_{nz} \geq 0.2$) before director structures and its associated manifestations, transit to the bent geometry. The progressive development of this bent-director structure with the increase of ϵ_{nz} is evident from the gradual decrease of the system primary order (Fig.6.12(a) for example) in the uniaxial phase at any temperature.

We observe from Fig. (6.13) that similar effects occur at ϵ_{nz}=0.2 in Type A film as well. Fig.6.13(a), for example, indicates again the influence of ϵ_{nz} on the equilibrium director structures in this film, culminating in a noisy low temperature R^2_{00}. As was pointed out in

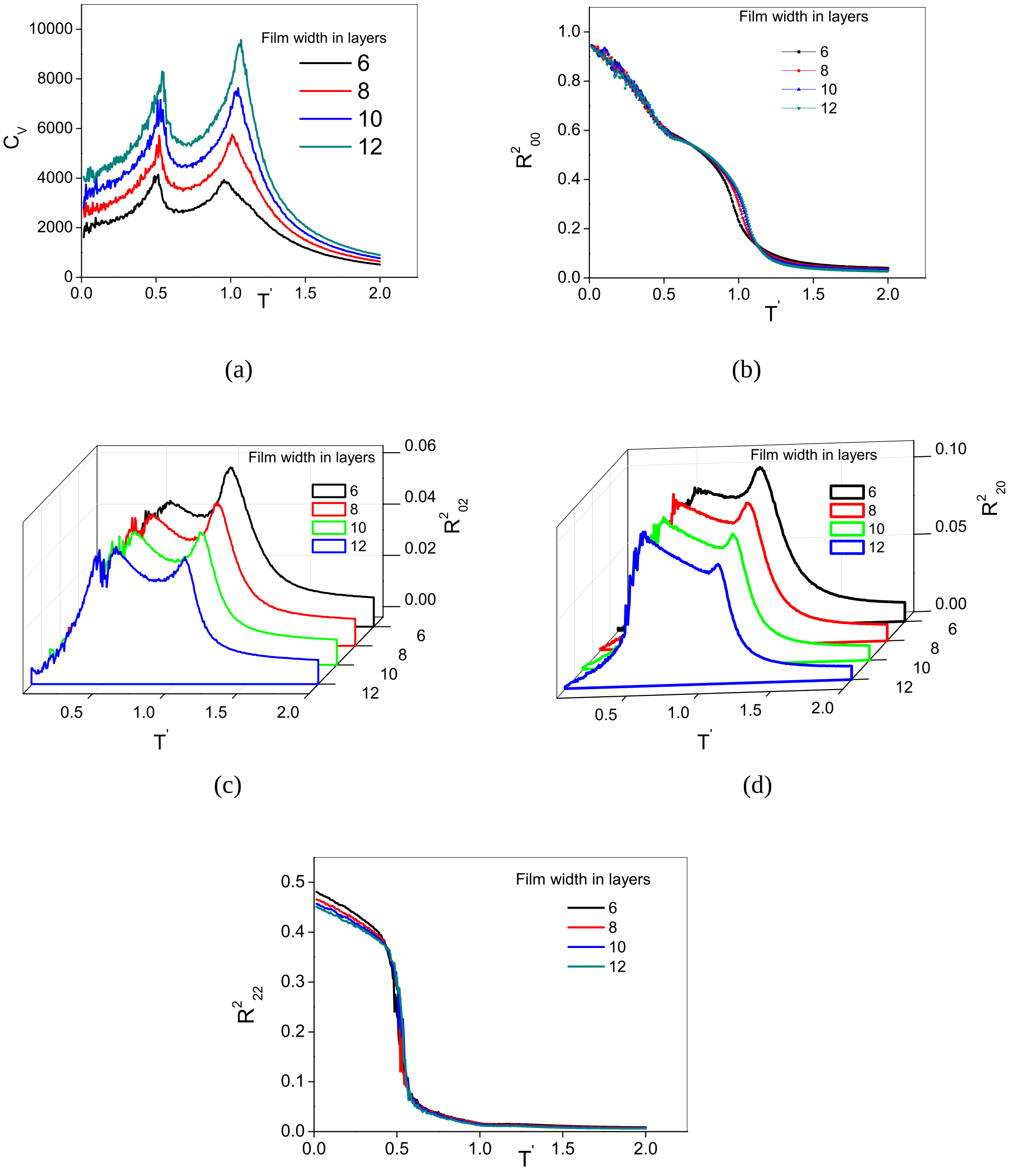

(a)

(b)

(c)

(d)

(e)

Figure 6.11: Variation with temperature of system for different thickness of Type A film (a) C_V; (b) R^2_{00}; (c) R^2_{02}; (d) R^2_{20} (e) R^2_{22}

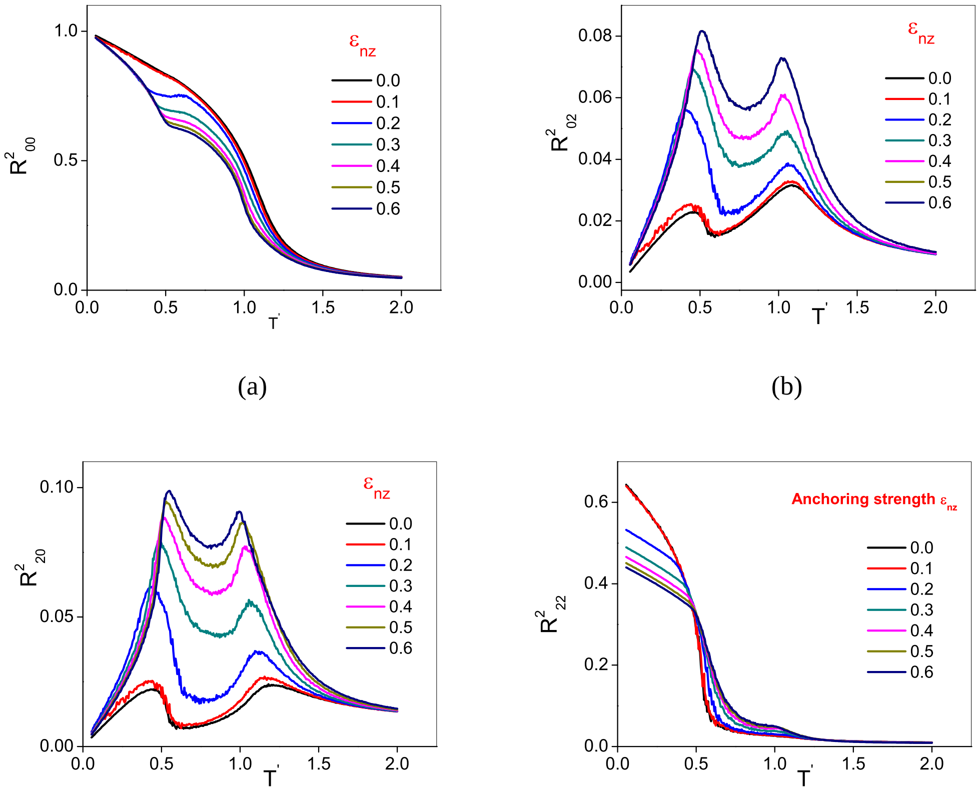

(a)

(b)

(c)

(d)

Figure 6.12: Variation of order parameters with temperature for different anchoring strengths (ϵ_{nz}) in Type C film: (a) R^2_{00} (b) R^2_{02} (c) R^2_{20} (d) R^2_{22}

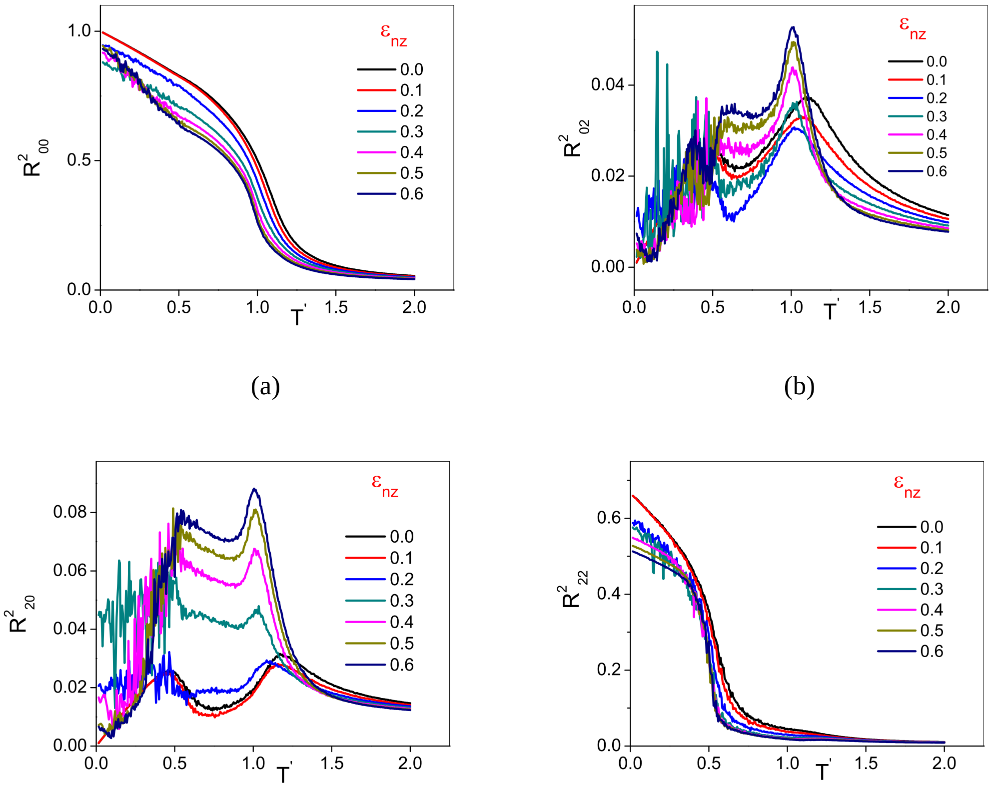

(a) (b)

(c) (d)

Figure 6.13: Variation with temperature for different anchoring strengths (ϵ_{nz}) in Type A film: (a) R^2_{00} (b) R^2_{02} (c) R^2_{20} (d) R^2_{22}

the last section, at the strong anchoring limit (ϵ_{nz}=1.0) the R^2_{00} in the biaxial phase of these two films is determined by the ordering of the minor axes. So as ϵ_{nz} is progressively varied, at some defined value the calmitic axis should be changing over from the eigen vector of $\boldsymbol{Q}_{ZZ}$ to that of $\boldsymbol{Q}_{XX}$ (or $\boldsymbol{Q}_{YY}$). This results in these systems as development of a cusp at T_{C2} as ϵ_{nz} increases.

6.4 Conclusions

Equilibrium director structures in thin planar films, imposing hybrid boundary conditions at the two substrates on the molecular long axes (z-axes), are investigated based on a Hamiltonian model under dispersion approxiamation (at λ_Z = 0.35). Boltzmann sampling is adopted so as to correspond to the established phase sequence involving uniaxial and biaxial phases ($N_B - N_U - I$) in bulk samples. Two different films were considered: Type A which imposes anchoring influences on the minor axes as well as at the substrates; and Type C which does not. Very interestingly, Type C film leads to a stable, noise free, high order parameter value for R^2_{00} deep in the biaxial phase region, and this order is due to the near perfect alignment of the molecular y-axes in a direction perpendicular to the plane hosting the bent director structure associated with the long molecular axes. This scenario is appealing for two reasons: the Hamiltonian model is realistic as it accommodates both the perturbing interactions (last two terms in Eqn.6.2.1), and secondly the substrates are needed to influence suitably only the long molecular axes, which is practical. Under these convenient conditions we find that in the biaxial phase, one can generate an in-plane order of high degree involving one of the minor axes of the molecules, while the bent director from the long axis alignment is locked within the plane due to influence from the substrates. It appears to be a good candidate for further studies of switching with external in-plane fields. Type A film on the other hand is frustrated on entering into the biaxial phase, perhaps due to competing energetic demands of the Hamiltonian and of the surface anchoring involving minor axes.

The second set of films investigated are the counterparts of the above: they retain the corresponding boundary conditions as in Type A and Type C, but the Hamiltonian model is modified though perhaps making it unrealistic. The cross coupling strength in the second term of Eqn.6.2.1 is set to zero, thereby choosing a system on the λ-axis of the quadrupolar Hamiltonian, resulting in these films AY and CY. In this case a stable low temperature director structure (without noise) is obtained in the biaxial phase, and the high degree of ordering (qualifying as R^2_{00}) is again in the direction perpendicular to the plane hosting the bent director structure (of the molecular long axes). The differnce however is that this orientational order belongs to molecular x-axis, unlike the order (from molecular y-axis) in the Type C film. In principle Type C and Type AY films have identical evolution of the director structures, but for this difference. It may be noted that Type AY film is somewhat impractical: the chosen point in the Hamiltonian parameter space rules out any interaction between molecules involving cross coupling of the molecular tensors; and secondly it also requires the substrates be suitably treated so as to enable them to impose specified anchoring influences on all the three axes of the surface LC molecules.

The interesting point from an academic view point however is that a high degree of order, eventually free from the director structure of the other molecular axes, develops in the biaxial phase when any of the following conditions are met: The Hamiltonian permits intermolecular cross coupling of molecular uniaxial and biaxial tensors, but the surfaces do not influence the minor axes (Type C), or the Hamiltonian restricts the interaction only to intermolecular biaxial - biaxial coupling, but imposes suitable (and comparable) anchoring influences on the minor axes (Type AY). Finally the case of Type CY film is curious: here the tensor interactions are decoupled in the Hamiltonian and there are no boundary conditions on the axes involved in the defining of biaxial terms. The result is a relatively free evolution of the orientation of the alignment axes of the $\boldsymbol{Q}_{XX}$ and $\boldsymbol{Q}_{YY}$ terms, resulting in very unstable director configurations.

The effect of the variation of the thickness is marginal and is the same in all the three types of films. It is also found that the sharpness of the C_V peak increases as the thickness is increased (due to size effect). It is found that both the films seem to undergo a transition in their director structures, as the anchoring strength at the planar bounding surfaces ϵ_{nz} crosses the value of 0.2.

In summary, we conclude that the Type C film, involving realistic LC biaxial molecular system with simple hybrid anchoring conditions imposed only on the long axes is a potential candidate to generate a high degree of in-plane order in the biaxial phase. This arises from the long range orientational correlations of the molecular minor axes along the laboratory X-direction, while the film is pinned to a bent director structure(of the other two axes) in the laboratory YZ-plane.

Bibliography

[1] A. Poniewierski and T. J. Sluckin,*Liq.Cryst.* **2**, 281(1987).

[2] Musevic.I, Skarabot.M, Tkalec. U, Ravnik. M and Zumer. S, *Science* **313**, 954(2006).

[3] Tomoki Ikeda,*J.Mater.Chem.* **13**, 2037(2003).

[4] Benjamin Wincure and Alejandro D. Rey, *Liq.Cryst.* **34**, 12, 1397(2007).

[5] Mary O'Neill and Stephen M. Kelly,*Adv. Mater.*,**15**, No. 14, 1135 (2003).

[6] J. C. Loudet, P. Barois ,and P. Poulin,*Nature* **407**, 611 (2000).

[7] M. Draper et al, *Adv. Funct. Mater.* **21**, 1260(2011).

[8] P. Sheng, *Phys. Rev. Lett.* **37**, 1059(1976);*Phys. Rev. A* **26**, 1610 (1982).

[9] G. Barbero and R. Barberi, *J. Phys.(Paris)* **44**, 609 (1983)

[10] P. Palffy - muhoray, E. C. Gartland and J. R. Kelly, *Liq. Cryst.* **16**, 713 (1994)

[11] H. G. Galabova, N. Kothekar and D. W. Allender, *Liq. Cryst.*, 23:6, 803 (1997)

[12] A. Sarlah and S. Zumer, *Phy. Rev. E* **60**, 2 (1999).

[13] G. Barbero, N. V. Madhusudana and G.Durand,*J. Phys. Lett.* **45**, 613 (1984).

[14] Surajit Dhara and N. V. Madhusudana, *Eur. Phys. Journal E* **13**, 401 (2004).

[15] M. M. Wittebrood, Th. Rasing, S. Stallinga and I. Musevic, *Phy. Rev. Lett* **80**, 6 (1998).

[16] S. Stallinga, M. M. Wittebrood, D. H. Luijendijk and Th. Rasing,*Phy. Rev. E* **53**, 6 (1996).

[17] B. Zappone, Ph. Richetti, R. Barberi, R. Bartolino and H. T. Nguyen,*Phy. Rev. E* **71**, 041703 (2005).

[18] G. Carbone *et al,Phys. Rev. E* **83**, 051707/1-6(2011).

[19] Marina Ruths and Bruno Zappone, *Langmuir***28**, 8371(2012).

[20] C. Chiccoli, O. D. Lavrentovich, P. Pasini and C. Zannoni, *Phy. Rev. Lett.* **79**, 4401 (1997).

[21] C. Chiccoli, P. Pasini, Ivan Feruli and C. Zannoni., *Mol. Cryst. Liq. cryst.* **398**, 195 (2003).

[22] C. Chiccoli, P. Pasini, A. Sarlah, C. Zannoni and S.Zumer, *Phys. Rev. E* **67**, 050703(R) (2003).

[23] G. Sai Preeti, V. Vijay Kumar, V. S. S. Sastry and K. P. N. Murthy. *Computational Materials Science* **44**, 180 (2008).

[24] J. G. Gay and B. J. Berne, *J. Chem. Phys.* **74**, 3316 (1981).

[25] Greg D. Wall and Douglas J. Cleaver., *Phys. Rev. E***56**, 4306 (1997).

[26] P. A. Lebwohl and G. Lasher,*Phys. Rev. A* **6**, 426 (1972).

[27] C. Chiccoli, S. P. Gouripeddi, P. Pasini, K. P. N. Murthy, C. Zannoni and V.S.S. Sastry, *Mol. Cryst. Liq. Cryst.* **500**, 118 (2009).

[28] B. R. Acharya, A. Primak and S. Kumar, *Phy. Rev. Lett.* **92**, 145506 (2004).

[29] K. Merkel, A. Kocot, J. K. Vij, R. Korlacki, G. H. Mehl and T. Meyer, *Phys. Rev. Lett.* **93**, 237801 (2004).

[30] J. L. Figueirinhas, C. Cruz, D. Filip, G. Feio, A. C. Ribeiro, Y. Frere, T. Meyer, G. H. Mehl, *Phys. Rev. Lett.* **94**, 107802 (2005).

[31] M. J. Freiser, *Phys. Rev. Lett.*, **24**, 1041 (1970).

[32] M. J. Freiser, *Mol. Cryst. Liq. Cryst.* **14**, 165 (1971).

[33] veena prasad, shin-woong Kang, K. A. Suresh, Leela Joshi, Qingbing Wang and Satyendra Kumar, *J.AM.Chem.Soc.* **127**,17224(2005).

[34] G. R. Luckhurst, *Thin Solid Films*, **393**, 40 (2001).

[35] J. H. Lee, T. K. Lim, W.T. Kim and J. I. Jin. *J. Appl. Phys.* **101**, 034105 (2007).

[36] R. Berardi, L. Muccioli and C. Zannoni,*J.Chem.Phys.* **128**, 024905 (2008).

[37] G. Sai Preeti, Ph.D Thesis, University of Hyderabad, 2009.

[38] F. Biscarini, C. Chiccoli, P. Pasini, F. Semeria and C. Zannoni, *Phys. Rev. Lett.* **75**, 1803 (1995).

[39] P. Pasini, C. Chiccoli and C. Zannoni, *Advances in computer simulations of liquid crystals*, (ed.) P. Pasini and C. Zannoni, Kluwer Acad. Publishers (2000).

.

Chapter 7

Anchoring Transitions in Biaxial Nematic Droplets

7.1 Introduction

Nematic droplets are formed by the dispersion of nematic droplets of low molar mass in a solid polymer matrix. This arrangement, called a Polymer Dispersed Liquid Crystal (PDLC), has been found to be very interesting case to study, from a fundamental research point of view as well as applications. The PDLC system realized decades ago [1–4] have several application in elctro-optic displays in the LCD industry and are used in advanced optical applications like large flexible displays, switchable windows, paper-like displays for electronic books, etc. The electro-optical performance of the PDLCs depend on the elastic properties of the liquid crystal used, the size of the droplet and its shape anisotropy, the anchoring energy at the surface and the orientational structure of the liquid crystal in the droplet. Mean field analysis [5, 6] is employed to study the light scattering from a nematic droplet which enables their use as optical shutters in several opto-electronic applications. The stable phases in these sub-micron sized droplets have been investigated using Landau-de Gennes theory and the dependence on the surface anchoring energy, droplet radius and the sample temperature have been demonstrated [7, 8]. Experimentally the PDLC was studied using Deuterium NMR experiments and polarisation microscopy [9, 10]. Anisotropic diffusion of light in these systems [11] and orientational multiplicity and transitions in these droplets [12] lead to several applications in photonic devices [13], random lasers [14, 15]. Possible use in optically engineered diffractive structures and devices [16] has led to a renewed interest in the PDLC devices.

Studies on topological defects of nematic droplets are interesting from the point of view of mesophases in a confined environment [17]. A topological defect is a configuration of the order parameter that cannot be transformed continuously into a uniform state. It can occur during a symmetry breaking phase transition, under an external field or simply be a necessary aspect of an equilibrium state. PDLC droplets represent practical examples of systems exhibiting topological defects which are of interest in many areas of physics [18–21]. The molecular organisation in a droplet depends on the elastic constants of the liquid crystal used, the interfacial interactions at the nematic-polymer interface, the temperature and applied external electric or magnetic field. It is characterised by the spatial dependence of the director field and the scalar order parameter. The director distributions are very sensitive to the nature of the boundary conditions which in turn depend on the preparation methods used. It is observed in uniaxial nematics that if the molecules are strongly anchored parallel to the surface and the elastic constants for splay, twist and bend deformations do not differ significantly, a bipolar structure results with two point defects on the cylindrical axis of symmetry. However, if the bend elastic constant is smaller than the splay elastic constant, a toroidal structure results. On the other hand, if the molecules are strongly anchored perpendicular to the surface, a radial director distribution is obtained with a point defect in the centre of the drop [8]. Nematic droplets suspended in a isotropic matrix, such as polymer, water, glycerin or nucleating at the isotropic -nematic first order phase transition are examples of systems where surface anchoring results in equilibrium defect structures.

The ratio of the bulk elastic energy to the surface anchoring energy determines the shape of the liquid crystal droplet which is formed. Assuming a spherical droplet of radius R, the elastic energy scales as $|k|R$ (where k is an elastic constant of the nematic medium) whereas the anchoring energy scales as $|w|R^2$ where w is the anchoring coefficient. Usually for a uniaxial nematic the ratio $k/|w|$ is of the order of 1-10 nm, any macroscopic LC nematic droplet is spherical in shape. When the radius R of the drop is small such that $R << k/|w|$, the elastic energy contributes more to the total free energy of the drop, there by inhibiting any spatial variations in the director distribution in the bulk. Hence smaller droplets behave like a bulk nematic at the expense of violated boundary conditions.On the other hand, for large drops such that $R >> k/|W|$, the boundary conditions are satisfied at the surface, leading to a surface induced distortion of the director field in the bulk, resulting in the formation of hedgehog point defect at the centre of the drop. Hence the drop should have a critical radius $R = k/|w|$ (in microns) to observe the formation of this point defect, also called a core in recent literature, in such systems.

Computer simulations have played a very important role in the study of such confined systems in the presence of complex geometries and boundary conditions where analytic solutions are difficult to achieve. Monte Carlo simulations of polymer dispersed liquid crystals composed of uniaxial nematic medium were performed earlier based on Lebwohl-Lasher model [22]. These studies establish that the droplet in its nematic phase and under strong anchoring conditions, is essentially radially ordered except for a small spherical region at the core, which has uniaxial nematic phase [23]. The size of the core region was found to be independent of the size of the actual droplet [24]. Recently,a droplet of uniaxial molecules confined to a radially anchoring boundary was simulated using a Hamiltonian model which explicitly incorporates the elastic properties of the medium as parameters in the Hamiltonian [25] using Monte Carlo techniques [26]. A structural transition in the director field, induced by tuning the anchoring strength at the spherical boundary was reported. It was found that the splay elasticity of the medium mediates the characteristics of the core.

It is expected that the topological defect structure of biaxial nematics will be different from uniaxial nematics in view of the lower symmetry of the biaxial nematics. An earlier theoretical study [27] predicts that a point hedgehog defect should not be stable in a biaxial nematic . It is also hypothesised [28, 29] predicts the formation of a defect core region as in uniaxial case, but the defect would tend to move to the surface.

More recently such a micro-droplet comprising of biaxial molecules was investigated based on Monte Carlo simulations using a lattice model [30], reporting interesting optical textures generated for different molecular biaxiality parameter values λ_Z and qualitatively different boundary conditions under strong anchoring conditions. The interest in the present work is to complement this study with detailed information on director configurations in such a biaxial droplet under radial boundary conditions, as a function of biaxiality parameter λ_Z and temperature, as the anchoring strength at the bounding surface is varied. We adopt the Hamiltonian model used earlier [31] for this purpose, and observe the formation of the droplet (parametrized by the uniaxial and biaxial order parameters) as the sample is cooled from the isotropic phase to the biaxial phase via the intermediate uniaxial phase. We report our results for four different λ_Z values representatively spanning the relevant part of the phase diagram reported for this model [32].

In the second set of computations we investigate the effect of the surface (radial) anchoring strength on the droplet formation at different temperatures in the biaxial phase. These studies also compare the elastic response of the uniaxial phases formed by the inherently biaxial constituents at different λ_Z values (at appropriately high temperatures), with the results on the pure uniaxial system (Lebwohl-Lasher model) providing the reference points for such purposes [26]. In the following, Section 2 briefly introduces the lattice model for the biaxial system and provides details of our simulations. The results are presented and discussed in Section 3, while the main conclusions are presented in Section 4.

7.2 Model and details of simulations

The present lattice model assumes the dispersion approximation, as has been the case with the earlier work [30], thus requiring one parameter λ_Z to assign the biaxiality at molecular level. The resulting phase diagram predicts, on cooling the sample from the isotropic phase, successive formation of uniaxial and biaxial nematic phases for non-zero λ_Z values, with the isotropic - uniaxial nematic transition temperature (all reported in appropriate reduced units) being essentially found to be independent of the molecular biaxiality. The temperature range of the intermediate uniaxial nematic phase however is diminished gradually with increase in λ_Z, finally culminating in the asymptotic limit of a direct transition to the biaxial phase from the isotropic fluid as $(\lambda_Z \to 1/\sqrt{6})$. The Hamiltonian is given by

$$H = -\epsilon_{ij}\{P_2(\cos(\beta_{ij})) + 2\lambda_Z(R^2_{02}(\omega_{ij}) + R^2_{20}(\omega_{ij})) + 4\lambda_Z^2 R^2_{22}(\omega_{ij})\} \qquad (7.2.1)$$

Here, $\omega(\lambda, \beta, \gamma)$ is the set of Euler angles specifying the orientation of the molecule, and ω_{ij} represents the relative orientation of the ij^{th} pair of molecules. R^L_{mn} are combinations of Wigner functions, symmetry-adapted for the D_{2h} group of the two interacting particles [31, 33]. ϵ_{ij} is the strength of interaction between the molecules. We take it to be independent of the choice of the specific pair $\epsilon_{ij} = \epsilon$ and set its value to this constant for nearest neighbours on the lattice, and zero otherwise. The reduced temperature is thus measured in units of ϵ. The above expression is conveniently recast as a function of inner products of different vectors specifying the orientations of different molecules (x_i, y_i, z_i) with those of the chosen laboratory frame (X, Y, Z), and is expressed as [32]

$$U_{ij} = -\epsilon(\frac{3}{2}V_{33} - \sqrt{6}\lambda_Z(V_{11} - V_{22}) + \lambda_Z^2(V_{11} + V_{22} - V_{12} - V_{21}) - \frac{1}{2}). \qquad (7.2.2)$$

Here V_{ab}= $(u_a.v_b)^2$, and the unit vectors u_a,v_b $[a, b = 1, 2, 3]$, are the three axes of the two interacting neighbouring molecules. The value of λ_Z sets the relative importance of the biaxial interaction in the Hamiltonian, while ϵ (set to unity in the simulations) defines the temperature scale $(T = \dfrac{k_B T^*}{\epsilon})$, where T^* is the laboratory temperature.

Simulations on confined systems, based on lattice models, start by carving out the desired geometry from a sufficiently big cubic lattice. One treats the lattice sites within this geometry as liquid crystal constituents participating in the Monte Carlo simulation (namely performing a Markov chain Monte Carlo random walk), while the others are treated as substrate molecules with fixed orientations appropriate to the boundary conditions, referred to in literature as the ghost molecules [34]. The value of ϵ_{ij} involving liquid crystal and substrate molecules (on the condition of being nearest neighbours), relative to that between nearest neighbour liquid crystal molecules (set to unity in the present case), represents the degree of influence of the surrounding medium imposing boundary conditions on the droplet. We focus on the effect of a medium which enforces variable degree of such anchoring in the radial direction towards the centre of the droplet. In the first set of the computations, where we investigate the equilibrium director structures across the phase diagram (by varying temperatures over the liquid crystalline phases at different biaxiality parameter values), we assume strong anchoring, and set the corresponding$\epsilon_{ij}(= \epsilon_s)$ also to be unity. In the second part, we focus on the effect of the variation of this coupling on the director structures in the biaxial phase, at a few temperatures.

A droplet of radius 20 (in lattice units) was considered, carved out of a cube of sufficient dimension, to allow for the ghost molecules. The equilibrium ensembles were constructed following the Metropolis algorithm [35] for different combinations of temperature and biaxiality parameter (in the strong anchoring limit), with typically 4×10^5 microstates being collected to constitute a representative equilibrium ensemble after ensuring equilibration.

In the first set of simulations with strong anchoring condition, λ_Z was chosen at four values (0.20, 0.25, 0.30, and 0.35); this provides essentially constant isotropic-uniaxial nematic transition temperature $(T_{IN_U} \sim 1.1)$, while the transition temperature from the uniaxial to the biaxial nematic phase $(T_{(N_U N_B})$ varied from about 0.15 to about 0.5 as λ_Z changed from 0.2 to 0.35 [31]. The temperature T at each of these λ_Z values is varied from 1.2 to 0.1 in steps of 0.1. The physical parameters of interest in this system are the four order parameters which essentially quantify the uniaxial order $< R^2_{00} >$ (along the primary director), the phase biaxiality $< R^2_{02} >$ (originating from the lack of azimuthal symmetry of the long axes of the molecules), and the molecular contribution to the biaxiality of the medium, $< R^2_{20} >$ and $< R^2_{22} >$. From the data we find that only $< R^2_{00} >$ and $< R^2_{22} >$ have appreciable values and reflect effectively the changes in the configuration of the droplet. For examining the formation of the core closely, we extract from the equilibrium ensembles the values of these parameters (and their variances) for different concentric spheres within the droplet , as the radius of this sphere is varied by a lattice unit starting with an initial sphere of radius 2 lattice units. This helps in the identification of the core region, and its exclusive characteristics, once formed.

The second set of simulations are carried out primarily under the conditions of high molecular biaxiality (λ_Z = 0.35), and in the biaxial region (below $T_{(N_U N_B)}$), for differing values of ϵ_s involving the liquid crystal and substrate molecules. These are varied from zero (free boundary condition on the droplet surface) in steps of 0.05, upto the strong limit value of unity. These form the latter part of the results presented below.

7.3 Results and discussion

Figs 7.1 - 7.4 summarize the variation of different interesting parameters in the limit of ϵ_s=1. Figs. 7.1(a) 7.1(c) depict the temperature variation at λ_Z = 0.35 of the uniaxial order $< R^2_{00} >$, biaxial order due to molecular origin $< R^2_{22} >$ and its susceptibility, all shown as a function of the radius of concentric spheres built within the droplet, while Figs. 7.2(a) - 7.2(c) present in the same format the results for λ_Z = 0.30, 7.3(a)-7.3(c) for λ_Z=0.25 and 7.4(a)-7.4(c) for λ_Z=0.2.

We now focus on the competition between the intermolecular aligning interactions and the disordering surface coupling for moderate anchoring values. We depict in Figs.7.5(a) and 7.5(b), the variation of $< R^2_{22} >$ and $< R^2_{00} >$ across the droplet (averages over spheres of increasing radius) in the biaxial phase (at T = 0.1) at an intermediate value of the anchoring strength ϵ_s=0.25. The variation of susceptibility of $< R^2_{00} >$ across the droplet in the strong anchoring limit, (ϵ_s=0.1) at two representative temperatures within the uniaxial phase, is shown in Figs 7.6(a) and 7.6(b), as the molecular biaxiality parameter is varied spanning the phase diagram of interest.

Finally, the effect of variable anchoring leading to a configuration transition in the biaxial phase is presented in Figs. 7.7-7.8 for λ_Z=0.35. The variation across the droplet of the two order parameters $< R^2_{00} >$ and $< R^2_{22} >$ as well as susceptibility of $< R^2_{22} >$ as ϵ_s is varied between 0 and 0.25 is studied. These represent a subset of the data collected on order parameters and their susceptibility, of different director configurations, under differing conditions of temperature, molecular biaxiality, and anchoring strength.

Focussing on Figs. 7.1(a) (λ_Z = 0.35) and 7.2(a) (λ_Z = 0.30) representing the evolution of the droplet director structure as a function of temperature, we observe that in the temperature region corresponding to the uniaxial nematic phase a core with appreciable uniaxial order but of variable size forms, its size decreasing as λ_Z decreases (from about 10 lattice units in Fig7.1(a) to 7 in Fig7.2(a)).

Figs. 7.3(a) and 7.4(a) show that this value asymptotically reduces to about 4-5 lattice units as λ_Z is decreased to 0.2, and is very close to the value observed in the case of uniaxial molecules (Lebwohl-Lasher (LL) potential) [24]. Thus the uniaxial phases arising from models of different degrees of molecular biaxiality λ_Z seem to enforce significantly different core sizes (all other experimental conditions being the same). These signal subtle changes in the appropriate elastic property of the medium, thus alluding to changes in the elastic properties of uniaxial bulk phases found at different λ_Z values. For example, for a medium of uniaxial molecules such core changes are attributed to changes in the splay elastic energy [26].

Figs. 7.1(b) and 7.2(b) show differing resistances of the medium, as proved by the average biaxiality parameter $< R^2_{22} >$, (within biaxial regime of temperature) to allow the surface induced disorder to percolate to the centre, for the two λ_Z values. At λ_Z = 0.35, for example, a biaxial core forms once a biaxial phase sets in (size estimated to be about 8 lattice units, see Fig.7.1(b)), while a slight decrease of its value to 0.3 shows that this scenario changes qualitatively and only a uniaxial core is possible under these conditions. The results at λ_Z=0.25 and 0.2, shown in figs 7.3(b) and 7.4(b) only confirm this observation.

Figs. 7.1(c) and 7.2(c) show susceptibilities of $< R^2_{22} >$ across the droplet, exhibiting a peak at the interfacial regions between the central core and the surrounding medium. The evidence for the formation of the biaxial core (under strong anchoring limit, ϵ_s = 1.0) at λ_Z = 0.35 relative to 0.30, was further borne out by a comparison of its susceptibility profiles at these two values, depicted in these figures.

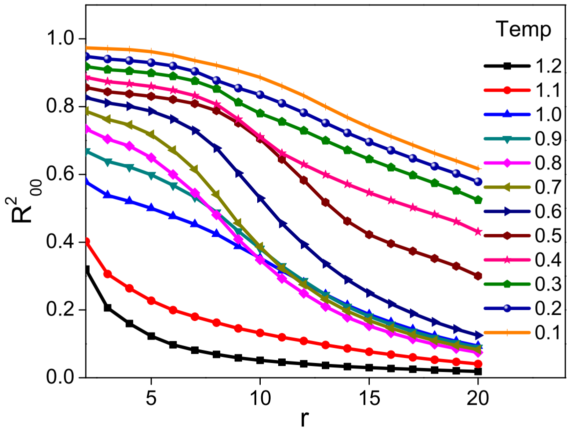

(a) R^2_{00}

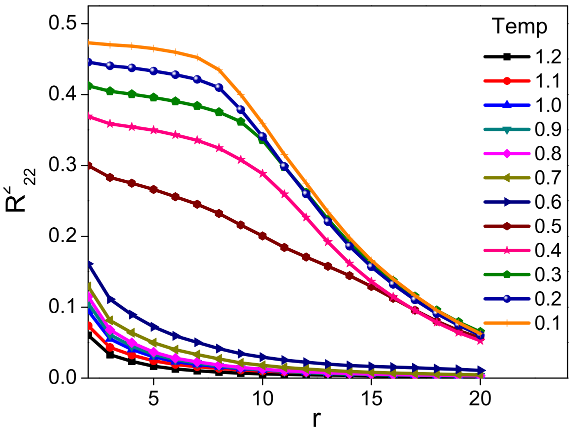

(b) R^2_{22}

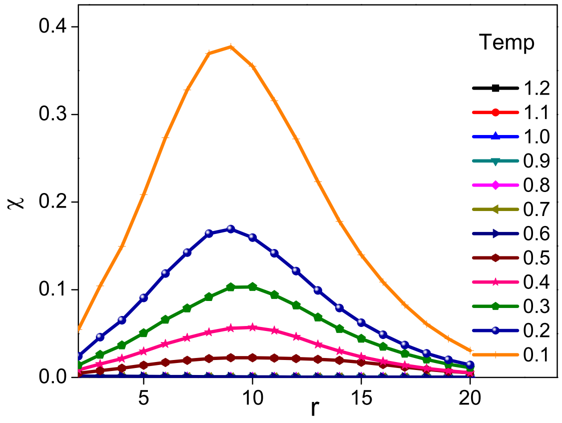

(c) susceptibility of R^2_{22}

Figure 7.1: Spatial dependence of order parameters and susceptibilities at λ_Z = 0.35, at different temperatures

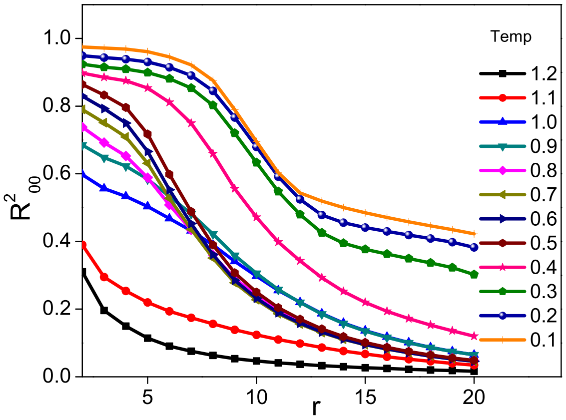

(a) R^2_{00}

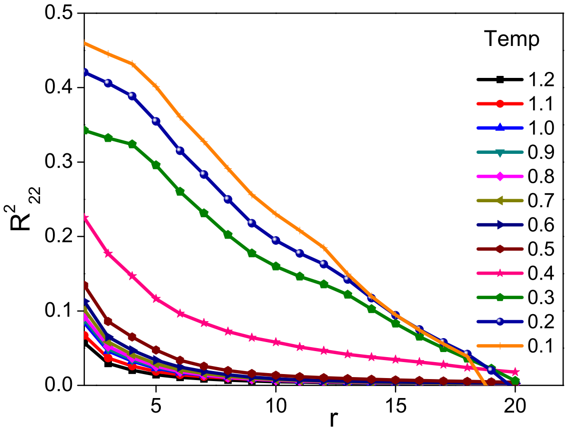

(b) R^2_{22}

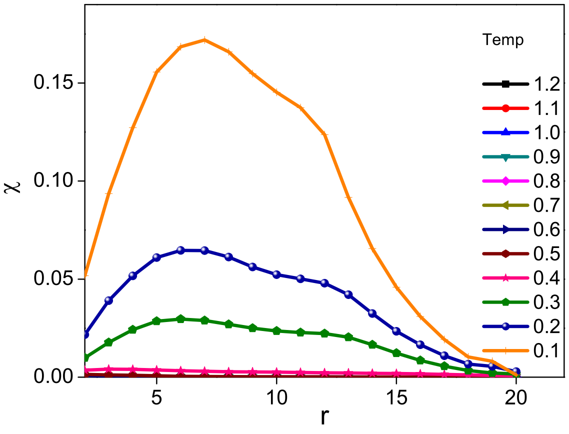

(c) Susceptibility of R^2_{00}

Figure 7.2: Spatial dependence of order parameters and susceptibilities at λ_Z = 0.3, at different temperatures

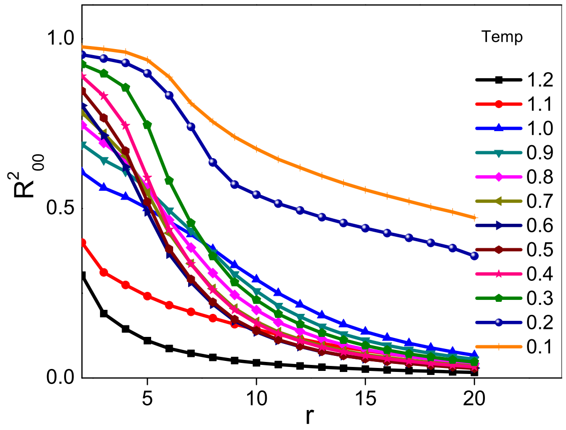

(a) R^2_{00}

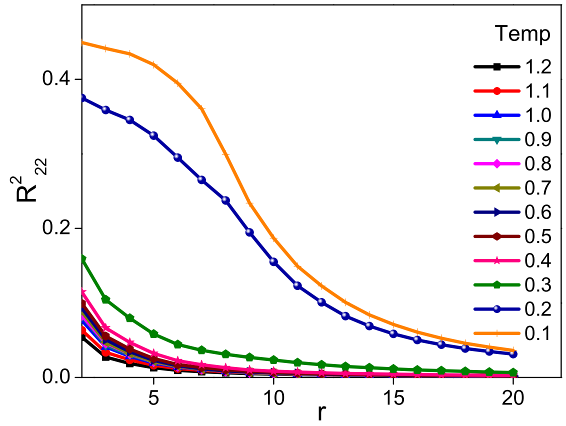

(b) R^2_{22}

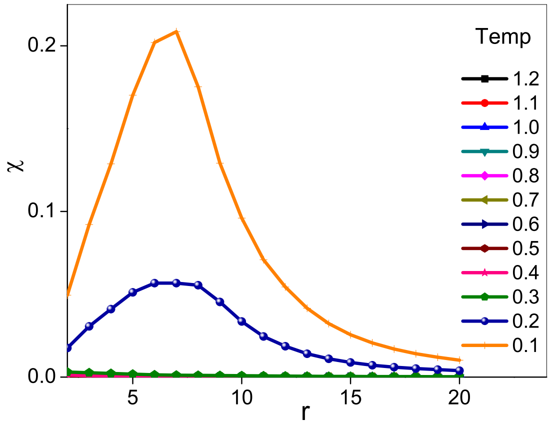

(c) Susceptibility of R^2_{22}

Figure 7.3: Spatial dependence of order parameters and susceptibilities at $\lambda_Z = 0.25$, at different temperatures

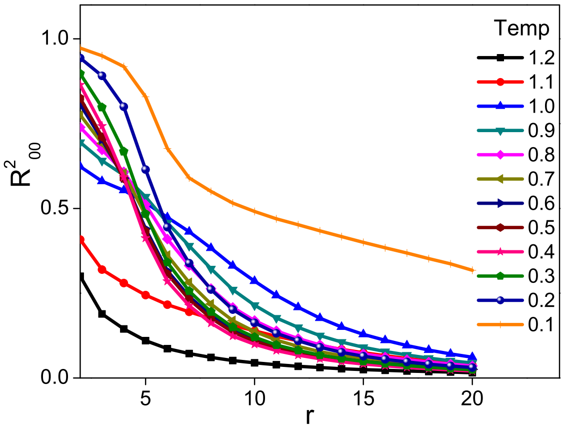

(a) R^2_{00}

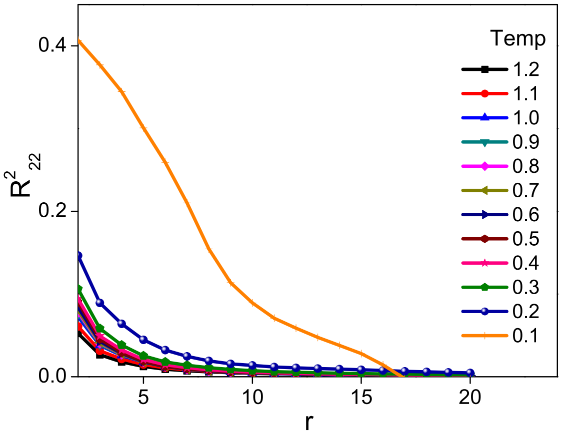

(b) R^2_{22}

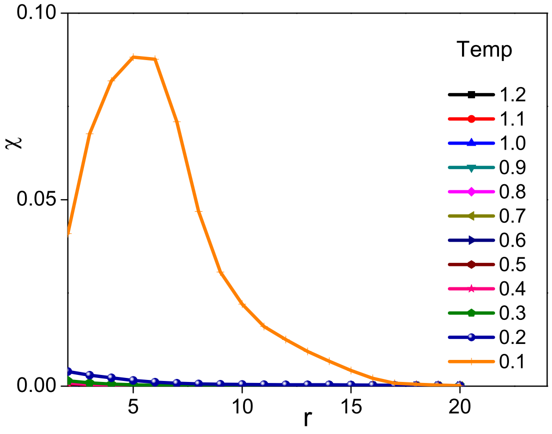

(c) Susceptibility of R^2_{22}

Figure 7.4: Spatial dependence of order parameters and susceptibilities at λ_Z = 0.2, at different temperatures

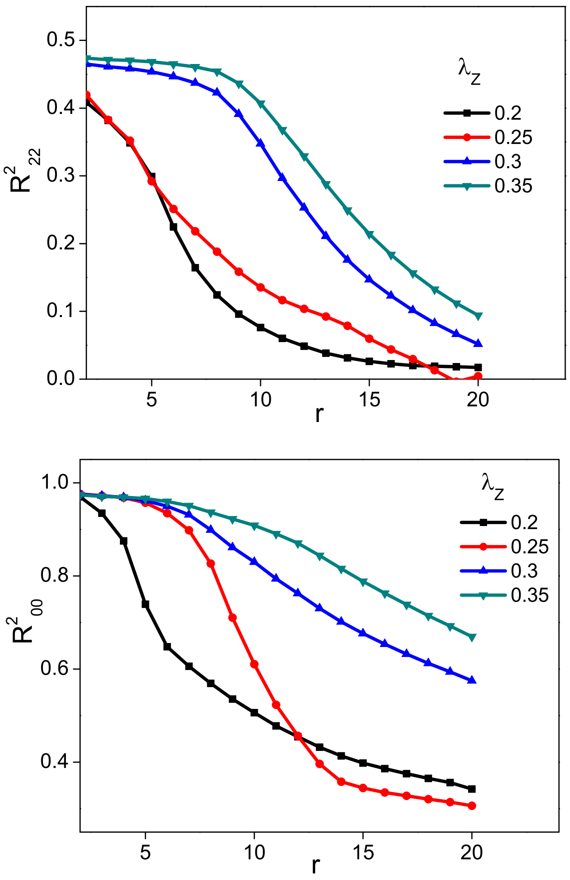

Figure 7.5: Effect of variation of λ_Z on the spatial dependence of (a) R^2_{22} (b) R^2_{00} at T=0.1 and anchoring strength ϵ_s = 0.25

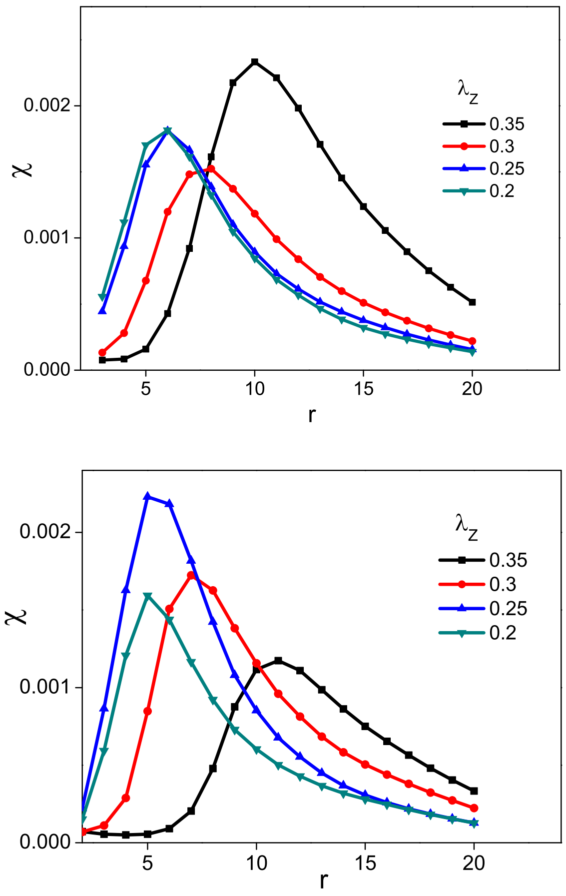

Figure 7.6: Spatial dependence of fluctuations in R^2_{00} for different λ_Z at (a) T = 0.7 and (b) T = 0.6

An interesting contrast is provided in Figs 7.5(a) and 7.5(b), where $< R^2_{00} >$ and $< R^2_{22} >$ are plotted for different concentric spheres at T = 0.1 (lowest temperature simulated in the biaxial region) for different λ_Z values, but for a reduced anchoring strength of ϵ_s =0.25. We immediately see from Fig.7.5(a) that at this reduced degree of surface-induced disorder, the biaxial medium at λ_Z = 0.3 has enough elastic resistance to sustain a biaxial core of a magnitude comparable to that at 0.35. On the other hand, fig 7.5(b) shows that the droplet manages to have a uniaxial core of high order and perceptible dimension for all value of λ_Z, but for the lowest value of λ_Z = 0.2. At this value it tends to the asymptotic LL limit.

In Figs 7.6(a) and 7.6(b) we present a similar comparison of data in the uniaxial phase of

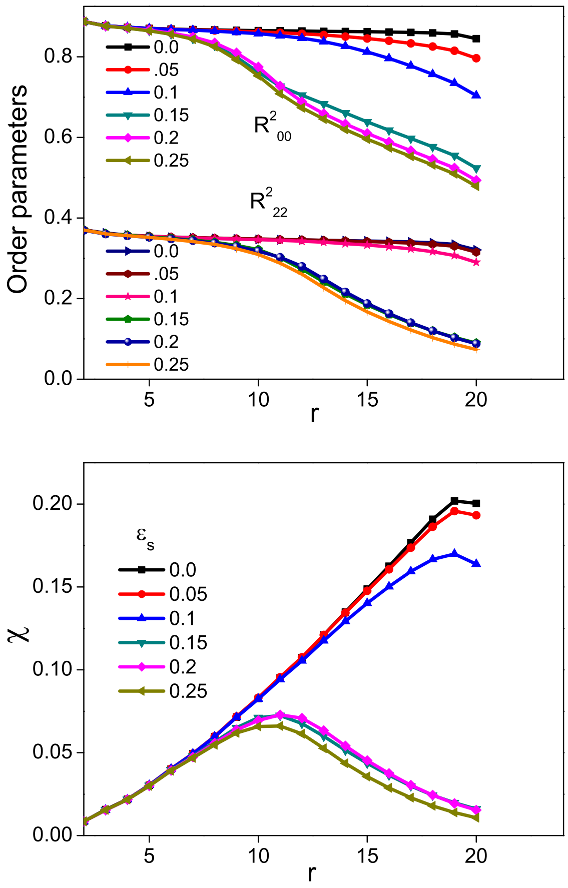

Figure 7.7: Variation of (a) order parameters and (b) susceptibility in $< R^2_{22} >$, bracketing the anchoring transition for various values of ϵ_s at λ_Z = 0.35, T = 0.4

the medium at two different temperatures (T = 0.7 and 0.6), the relevant parameters being the susceptibilities in $< R^2_{00} >$, for different λ_Z values. The location of the interfacial region between the uniaxial core and the rest of the droplet in this high temperature uniaxial nematic phase, and its progressive shift towards outer regions as the inherent molecular biaxiality is increased in the model, are again supportive of the observations made earlier based on Figs.7.1(a) and 7.2(a).

Anchoring Transition We study the formation of the core region in the biaxial phase at two temperatures (T = 0.4 and 0.2) at λ_Z = 0.35, as a function of ϵ_s (varying between 0.0 and 0.25, in steps of 0.05). We present the variation of $< R^2_{00} >$ and $< R^2_{22} >$ for different anchoring strengths, and the corresponding variation of the susceptibility of $< R^2_{22} >$, at T = 0.4 in Fig.7.7, and at T = 0.2 in Fig.7.8. From Fig. 7.7(a) we notice that both the order parameters show a qualitative change in their spatial distribution as ϵ_s changes from 0.1 to 0.15. Fig7.7(b), depicting the spatial variation of the susceptibility in $< R^2_{22} >$, interestingly indicates that the interfacial region forms only when ϵ_s increases beyond 0.1, below which it monotonically increases as the size of the sphere under consideration increases, reaching the edge of the droplet. This is the scenario typically expected in a simple bulk-like medium with weak antagonistic boundary conditions at the boundaries of this geometry. Both these results together indicate that the droplet undergoes a configuration transition at some threshold value lying in between these two values, at this high value of λ_Z. The evidence suggests that at this anchoring induced transition, the droplet splits into a biaxial core region with a size of about 10 lattice units (see Fig.7.7(b)), and the core is characterized by typical value of order parameters: $< R^2_{00} >\approx 0.85$ and $< R^2_{22} >\approx 0.35$, at T = 0.4.

Figs. 7.8(a) and 7.8(b) depict such variations at a lower temperature T = 0.2 (at the same biaxiality parameter). We notice that at this temperature qualitative changes have taken place even at a low value of ϵ_s= 0.05 itself. As may be seen from Fig.7.8(b), $< R^2_{22} >$ shows a dramatic decrease from a nearly uniform biaxial distribution (at a higher value of $< R^2_{22} >\approx 0.45$) of an unperturbed system (ϵ_s= 0), at the slightest of perturbation from the surface. The uniaxial order of the core (with $< R^2_{00} >\approx 0.95$) also shows a qualitative change with this slightest increase in ϵ_s (from 0.0 to 0.05). Further, the profiles of $< R^2_{00} >$ (Fig.7.8(a) also seem to betray the possibility of a second anchoring driven transition also, between 0.15 and 0.20, with such accompanying changes in $< R^2_{22} >$ as well. Fig.7.8(b) brings out the qualitative difference between the same droplet at the two different temperatures more clearly. Unlike at T = 0.4, the susceptibility in $< R^2_{22} >$ shows evidences of an interfacial region (dividing the droplet into two distinct parts) even at ϵ_s = 0.05, supporting the results of Fig.7.8(a).

These observations, coupled with data at this value of biaxiality but at ϵ_s = 1.0 (see

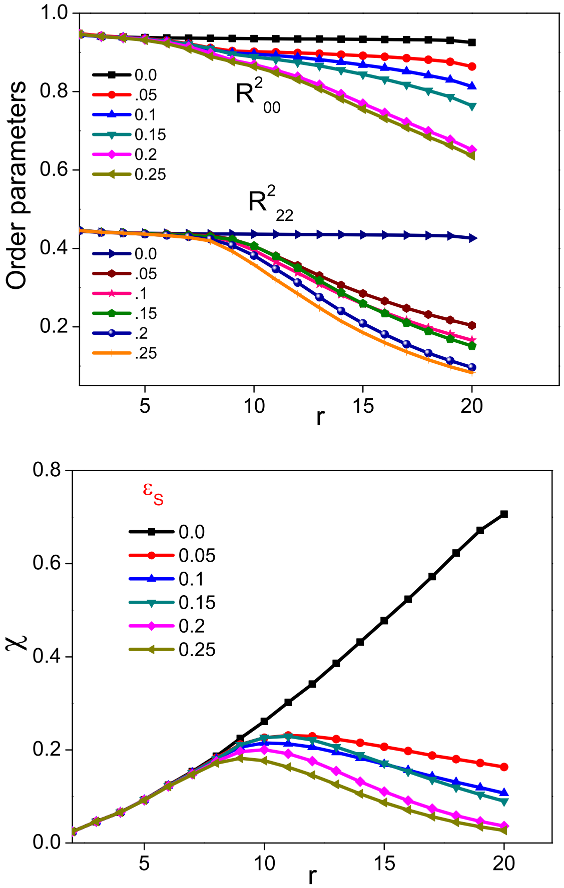

Figure 7.8: Variation of (a) order parameters and (b) susceptibility in $< R^2_{22} >$, bracketing the anchoring transition for various values of ϵ_s at λ_Z = 0.35, T = 0.2

Fig.7.1(b)), suggest that as the biaxiality assumes higher values (at a given biaxiality parameter, say), the droplet is less compatible, from energetic considerations obviously, to even the slightest antagonistic perturbation of the medium from the bounding surface, forcing the medium to undergo anchoring driven transition(s). And the droplet size seems to shrink (though nominally, see Fig.7.1(b), at the strong anchoring limit) as the biaxial order firms up more at low temperatures. This makes an interesting and contrasting comparison with a medium comprising of uniaxial molecules, wherein for a given anchoring strength and big enough droplet, the core grows in size with the decrease of temperature since the corresponding $< R^2_0 0 >$ increases, and so does its elastic resistance.

7.4 Conclusions

We studied a spherical droplet of a liquid crystal comprising of biaxial molecules whose phase diagram includes a low temperature biaxial nematic phase. the extent of which can be varied by a single parameter (λ_Z) in the interaction terms. We investigated the formation of different director configurations, quantifying them with spatial variations of the relevant order parameters and their susceptibilities. We in particular focus on the formation of a central core region bearing the characteristics of the nematic region compatible with the corresponding experimental conditions, spanning the phase diagram (i.e. as a function of λ_Z and T). We examined the spatial variation of the uniaxial ($< R^2_{00} >$) and biaxial ($< R^2_{22} >$) order parameters (and their susceptibilities) to infer about interesting subtle changes in its structure. We supplement this effort by varying the anchoring strength at chosen values of λ_Z (we present results for λ_Z = 0.35 here), and make an attempt to correlate its behaviour under different experimental conditions. We find that the uniaxial phases formed at high temperatures at different λ_Z values are quantitatively different in their elastic behaviour, and tend to the Lebwohl-Lasher behaviour as λ_Z tends to zero. It is also known in the uniaxial regime that a higher inherent order (by, say, lowering the temperature) leads to bigger core (other conditions of anchoring being the same) owing to an increase in the relevant elastic energy density. In the biaxial regime, this does not seem to be true, and if at all it seems to be the opposite [36].

Bibliography

[1] C. P. Crawford *et al.*, Liquid Crystal in Complex Geometries formed by Polymer and Porous Network, Taylor and Francis, London, (1996).

[2] P.Drzaic, *J. Appl. Phys.* **60**, 2142,(1986).

[3] J. W. Doane, N. A. Vaz, B. G. Wu and S. Zumer, *Appl. Phys. Lett.* **48**, 269 (1986).

[4] P. S. Drzaic, *Liq. Cryst.* **11**, 1543, (1988).

[5] S. Zumer, M. Vilfan and I. Vilfan, *Liq.Cryst.* **3**, 947 (1988).

[6] I. Vilfan, M. vilfan and S. Zumer, *Phy. Rev. A* **40**, 4724 (1989).

[7] J. H. Erdmann, S. Zumer and J. W. Doane, *Phy. Rev. Lett.* **64**, 1907 (1990).

[8] S. Kralj, S. Zumer and D. W. Allender, *Phy. Rev. A* **43**, 2943 (1993).

[9] A. Golemme, S. Zumer, J. W. Doane and M. E. Neubert, *Phy. Rev. A* **37**, 559 (1988).

[10] R. Ondris-Crawford *et al.*, *J. Appl. Phys.* **69**, 6380 (1991).

[11] Alenka Mertelj and Martin Copic, *Phy. Rev. E* **75**, 011705 (2007).

[12] Rajesh K. Goyal and Martin M. Denn, *Phy. Rev. E* **75**, 021704 (2007).

[13] M. J. Escuti, Jun Qi and G. P. Crawford, *Appl. Phys. Lett.* **83**, 1331 (2003).

[14] S. Gottardo, D. D. Wiersma, S. Cavalieri and O.Yaroshchuk, *Phys. Rev. Lett.* **93**, 263901 (2004).

[15] H. Harada, M. Nakatsu and H. Naito, *Jpn. J. Appl. Phys.* Part 2, **44** L915 (2005).

[16] G. B. Hadjichristov, Y. G. Marinov and A. G. Petrov, *Mol. Cryst. Liq. Cryst.* **525:1**, 128-139 (2010).

[17] Maurice Kleman and O. D. Lavrentovich, Philosophical Magazine and Philosophical Magazine Letters (2006).

[18] N. D. Mermin, *Rev. Mod. Phys.* **51**, 591 (1976).

[19] S. Chandrasekhar and G. S. Ranganath, *Adv. Phys.* **35**, 507 (1986).

[20] O. D. Lavrentovich and E. M. Terentjev, *Sov. Phys. JETP*, **64**, 1237 (1986).

[21] N. Schopohl and T. J. Sluckin,*J. Phys. France* **49**, 1097 (1988).

[22] P. Lebwohl and G. Lasher, *Phy. Rev. A.* **6**, 426 (1972).

[23] C. Chiccoli, P. Pasini, F. Semeria,and C. Zannoni, *Mol. Cryst. Liq. Cryst.* **212**, 197 (1992).

[24] C. Chiccoli, P. Pasini, G. Skacej, S. Zumer, and C. Zannoni, Lattice spin Models of Polymer Dispersed Liquid Crystals in Computer Simulations of Liquid Crystals and Polymers, Kluwer, Dordrecht, pages 1-23 (2005).

[25] G. R. Luckhurst and S. Romano, *Liq. Cryst.* **26**, 871, (1999).

[26] G. Sai Preeti, N. Satyavathi, K. P. N. Murthy and V. S. S. Sastry, *Liq. Cryst.* **36**, 1379 (2009).

[27] R. Rosso and E. G. Virga, *J. Phys. A: Math. Gen.* **29**, 4247 (1996).

[28] M. V. Kurik and O. D. Lavrentovich, *Sov. Phys. Usp* **31**, 196 (1988).

[29] S. Sukumaran and G. S. Ranganath, *J. Phys II France.* **7**, 583 (1997).

[30] C. Chiccoli, P. Pasini, I. Feruli, and C. Zannoni, *Mol. Cryst. Liq. Cryst.* **441**, 319 (2005).

[31] F. Biscarini, C. Chiccoli, P. Pasini, F. Semeria and C. Zannoni, *Phy. Rev. Lett.* **75**, 1803 (1995).

[32] C. Chiccoli, P. Pasini, F. Semeria, and C. Zannoni, *Int. J. Mod. Phys. C* **10**, 469 (1999).

[33] G. R. Luckhurst and S. Romano, *Mol. Phys.* **40** 129 (1980).

[34] P. Pasini, C. Chiccoli and C. Zannoni, Advances in the Computer Simulations of Liquid Crystals, Kluwer, Dordrecht (2000).

[35] N. Metropolis, A. W. Rosenbluth, M. N. Rosenbluth, A. H. Teller, and E. Teller, *J. Chem. Phys.* **21**, 1087 (1953).

[36] B. Kamala latha, G. Sai Preeti, N. satyavathi, K. P. N. Murthy and V. S. S. Sastry, *Mol. Cryst. Liq. Cryst* **545:1**, 230 (2011).

Chapter 8

Conclusions

The work reported in this thesis is directed towards an investigation of the biaxial liquid crystal system with Markov chain Monte Carlo techniques. A general quadrupolar lattice Hamiltonian model is chosen for examining the phase diagram in bulk systems, and its simplified variant under dispersion approximation is used to investigate the effects of geometric confinement in the biaxial phase. Both these Hamiltonian models have been studied earlier in some detail with molecular field theory as well as conventional Monte Carlo simulations. Monte Carlo strategies for the present work are chosen depending on the requirement. Phase diagrams of bulk systems are examined via entropic sampling procedure, which is geared to obtain the density of states of the system though an elaborate scheme of asymptotically vanishing guided random walk in the configuration space of the variables of the Hamiltonian. The entropic ensemble (ES) of microstates collected during a long random walk guided by the computed density of states, (which are reasonably uniformly distributed with respect to the system energy), are then utilized to extract equilibrium ensembles and hence their average physical properties. The confined systems, simulated with a dispersion model (chosen for its simplicity and established bulk behavior), are investigated employing Metropolis algorithm, which provides algorithmic guidance so as to achieve asymptotically a Markov sequence of microstates representing the equilibrium Boltzmann distribution. The conclusions from these studies are summarized below.

The investigation of the bulk biaxial system along the boundary of the so-called essential triangle, employing entropic sampling technique (Wang-Landau algorithm combined with frontier sampling) has lead to the detection of an intermediate biaxial phase of an inherently low order in certain regions of the parameter space where a direct isotropic-biaxial phase transition has been predicted based on mean-field treatment of the model. The temperature range of the intermediate phase increases gradually along the lambda-star axis, thereby pushing the second transition (whose onset is found to lead to a second biaxial phase with measurable degree of biaxial order) to progressively lower temperatures. An interesting outcome of this work is the observation of two transitions at the Landau point (T on the diagonal), which traditionally is expected to host a direct isotropic-biaxial transition. The origin of this additional phase is attributed to the lack of concomitant development of long range order of the three molecular axes (manifesting as inherent inhomogeneity within the system), arising from the vanishing attractive coupling of short molecular axes at this point. The detection of the low temperature transition peak was made possible with the entropic sampling procedure. This methodology appears to be particularly successful in accessing all microstates associated with the system at a given total energy (within a narrow band of course, approximating to a micro-canonical ensemble of states). In this process, the rare fluctuations of the individual energy components, (while retaining their sum to correspond to the fixed total value) could be captured. It is the presence of these rare states at each such total energy value (particularly in the energy regions corresponding to the intermediate biaxial state reported), that seem to contribute qualitatively differently to the canonical averages, thus manifesting as deviations both from the mean-field expectations and simulation results from the Boltzmann sampling methods.

These studies are extended to encompass more realistic systems by choosing two trajectories in the interior of the essential triangle. The first trajectory drawn from the apex bisects the base of the triangle (line IW depicted in the triangle), whereas the second trajectory is a segment of the dispersion parabola (OZT). The simulation results along the two trajectories confirm qualitatively with the mean field predictions inside the triangle, but with a deviation. Starting from a point $K^{'}$ on the first trajectory, the intervening uniaxial phase in the predicted sequence $N_B - N_U - I$ seems to possess a detectable degree of biaxial symmetry, though very small. We differentiate this phase (which is not in principle uniaxially symmetric anymore) as $N_{U'}$. The free energy profiles obtained in these regions point to the existence of barriers, exclusively to the development of biaxial order, necessitating further cooling in order to access higher (biaxial) order regions. The traversal on this trajectory led to the exploration of the partly repulsive regions of the Hamiltonian parameter space as well. The free energy profiles obtained in this region offer evidences for the origin of the disappearance of the biaxial phase as the biaxial-biaxial coupling strength (λ) tends to zero. The simulations on the second trajectory point to the possible changes in the nature of the intervening uniaxial phase from N_U to N_U' to N_{B1}, as we traverse on the parabola from the origin O of the triangle (case of pure uniaxial coupling among molecular z-axes : Lebwohl-Lasher model) to the Landau point T (case of pure biaxial coupling among molecular y- and z-axes : μ-model at μ = 0).

In order to investigate further these curious observations on the dispersion parabola, we have studied the pre-transitional behavior of the bulk biaxial nematic near the isotropic-uniaxial and uniaxial-biaxial phase transitions at three values of the interaction parameter λ_Z, using the conventional Monte Carlo sampling. The average correlation length of the long molecular z-axes was found to be of the order of 8 lattice units at the isotropic-uniaxial nematic transition. The correlation length for the molecular y-axes was found to progressively increase (and become comparable to that of the molecular z-axes), whereas the correlation length for the molecular x-axes was found to correspondingly decrease, as λ_Z value increases along the parabola. These correlation lengths could not be estimated at the uniaxial-biaxial nematic transition for lower values of λ_Z, as the corresponding spatial functions fail to follow Ornstein-Zernike behavior. In this respect, $\lambda_Z \simeq 0.2$ seems to indicate the cross over region from a perturbed LL model to a strong biaxial interaction Hamiltonian model.

From the above results on bulk systems, it appears that the detection of an intermediate biaxial state but with a very low inherent biaxial order, in certain regions of the Hamiltonian parameter space, could offer a plausible rationale for the experimental difficulties in realizing the biaxial nematic systems. The inference that emerges is that large enough values of γ (promoting cross-coupling between the uniaxial and biaxial tensor components of the neighbouring molecules) could interfere, by suppressing long range orientational correlations of molecular axes, with the process of development of significant onset of biaxial order. That consequent inhomogeneity in the system at a mesoscopic level could be contravening the provisions of the mean-field treatment (and thus accounting for the deviations found in the present work) is at this stage a plausible argument. We feel that further work is needed to investigate this aspect of the problem. From the point of view of entropic sampling technique per se, the demonstration of the power of the algorithm, to seek out rare fluctuations among the different energy components overcoming their internal barriers (at a given total energy within a small band) leading to qualitatively different canonical averages, is noteworthy and new, and seems to be conceptually different from what is generally appreciated hither to from its application to other systems.

The behaviour under confinement was studied by considering a hybrid planar film of biaxial nematic. Two types of films have been simulated employing Metropolis sampling technique based on the dispersion Hamiltonian. The first film is a biaxial nematic confined at planar substrates exerting hybrid boundary conditions such that it imposes anchoring influences on the three molecular axes (Type A film), whereas the second film imposes anchoring only on the long molecular axis (Type C film). The boundary conditions for both films for the long axis promote a bent-director structure for the primary director (of molecular z-axes). Under these conditions we find that in the biaxial phase we can generate an in-plane order of high degree involving one of the minor axes of the molecules, while the bent-director from the long axis alignment is locked within a plane due to the anchoring influence of the substrates. Type C film with free boundary conditions for the short molecular axes (and which seems to be more readily realizable experimentally) promises to be a good candidate for switching experiments with in-plane external fields. Type A film on the other hand is frustrated on entering the biaxial phase. The effects of varying the thickness and the anchoring strength have also been studied in some detail for both the types of films.

A droplet comprising of biaxial liquid crystal molecules, subjected to radial boundary conditions imposed on the molecular z-axes at the spherical boundary, was also simulated employing the Metropolis sampling technique, based on the dispersion Hamiltonian. The formation of different director configurations were studied in this spherical droplet of biaxial nematic for various values of the biaxiality parameter (λ_Z). We find that the uniaxial core regions formed at different values of interaction parameter vary in their elastic behavior. The onset of the biaxial phase leads to the formation of a small biaxial core region (much like in the uniaxial phase), but it exhibits qualitatively different behavior with changes in λ_Z. These results are compared with the earlier findings in similarly confined systems of uniaxial liquid crystal systems. The qualitative differences exhibited by the biaxial droplets with respect to the formation of the core, in relation to their uniaxial counterparts, are obviously linked to the different elastic distortions promoted and sustained by the two different media.

In summary, the thesis presents certain new results on the phase behaviour of biaxial liquid crystal systems, obtained from Monte Carlo simulations guided by entropic sampling procedures. The conclusions thereof seem to have possible bearing on the difficulties in a ready realization of biaxial systems of appreciable order in the laboratory. The study of confined systems, based on conventional sampling methods, is more directed towards potential applications. In the process of these simulations, we also find that the Wang-Landau algorithm (augmented with frontier sampling protocol) exhibits a promising potential in dealing with systems described by multiple order parameters, and modelled by Hamiltonians promoting competing interactions among the microscopic constituents. In this context, the present work is a modest attempt to explore the consequences in one such system.

List of Publications

1. ”Anchoring Transitions in Biaxial Nematic Droplets-A Monte Carlo Study.”

   B. Kamala Latha, G. Sai Preeti, N. Satyavathi, K. P. N. Murthy and V. S. S. Sastry

   Molecular Crystals Liquid Crystals **545:1**, 230-241(2011).

2. ”Polymer Network induced ordering in Biaxial nematic Liquid Crystals: A Monte Carlo study.”

   Lavanya Kunduru, S. C. R. Roshan, **B. Kamala Latha**, K. P. N. Murthy and V. S. S. Sastry

   AIP Conf. Proc. **1349**, 182-183 (2011).

3. ” Detection of an intermediate biaxial phase in the phase diagram of biaxial liquid crystals: Entropic sampling study.”

   B.Kamala Latha, Regina Jose, K. P. N. Murthy and V. S. S. Sastry

   Physical Review E **89**, 050501 (R) (2014).